Chemical reactions on surfaces
-a SFG study

Im Fachbereich Physik
der Freien Universität Berlin
eingereichte Dissertation

Harald Kirsch

Juli 2014

This work was done between October 2010 and July 2014 in the Department of Physical Chemistry at the Fritz-Haber-Institut of the Max Planck Gesellschaft.

Berlin, July 2014

Erstgutachter: Prof. Dr. Martin Wolf
Zweitgutachter: Prof. Dr. Katharina Franke

Datum der Disputation: 11. August 2014

Ich widme diese Arbeit meinen Eltern

Abstract

This thesis focused on the investigation of chemical reactions on surfaces by usage of Sum Frequency Generation (SFG) spectroscopy and Thermal Desorption Spectroscopy (TDS). Understanding of chemical reactions on surfaces is of critical importance for modification and optimization of a variety of environmental and industrial processes, but the complexity of the ongoing reactions under "realistic" conditions often hinders an understanding on a molecular level. The aim of this work was to get insight into these complex chemical reactions by application of appropriate model systems in UHV. These model systems were methane dissociation on a Ruthenium(0001) single crystal and the dissociation of deuterated water(D_2O) on α-Alumina single crystals.

Understanding the interaction of methane with various metal surfaces have shown to be of particular importance for industrial applications, such as the Steam reforming of methane or the Fischer-Tropsch synthesis. Investigating the methane decomposition pathway with our experimental approach allowed the identification of all occurring dissociation(CH, CH_2) and coupling(CCH, CCH_2, CCH_3) products on Ru(0001) in UHV by identification of their characteristic vibrational modes. This was the first experimental observation of CH_2, CCH and CCH_3 during methane decomposition on Ru(0001). These observations provided information about the limiting factors which control the kinetics of stability and formation of the surface species like surface temperature and morphology, adsorbate coverage or co-adsorption of other molecules. Investigation of the CH_2 radical, which is assumed to be important for the Fischer-Tropsch-Synthesis, allowed the determination of its dissociation barrier which is 65 kJ/mol. This is four times higher than previous theoretical studies predicted. By cooperation with the Theory Department of the Fritz-Haber-Institut it was possible to explain this deviation by stabilization effects of co-adsorbed hydrogen. Another focus of this work was the investigation of coupling processes between CH-radicals which lead to CCH_2 formation. Setting up a reaction system by chemical rate equations enabled a qualitative simulation of the surface temperature formation process and provided insight into the underlying elementary reaction steps and their kinetics.

The second part of this thesis focused on the investigation of water/α-Alumina interaction. Water adsorption on these surfaces changes the morphology of the substrate and further affect its chemical properties dramatically. An understanding of this interaction is therefore of importance for environmental chemistry and heterogeneous catalysis. Investigation of water adsorption on α-Al_2O_3(0001) and α-Al_2O_3(1102) in UHV allowed an insight in this interaction on a molecular level. The combination of in-situ water dissociation by applying a molecular beam source and characterization by high resolution vibration spectroscopy allowed the first experimental observations and therefore verification of the, so far only theoretically predicted, single molecular dissociation channels on both surfaces. Furthermore, probing the substrate specific surface phonon modes via SFG allowed the observation of morphological changes due to water adsorption. This could open new channels in the understanding of surface reactivity for water dissociation.

Kurzzusammenfassung

Die vorliegende Dissertation beschäftigt sich mit der Untersuchung von chemischen Reaktionen auf Oberflächen mithilfe von Summen-Frequenz-Erzeugungs (SFG) Spektroskopie und Thermischer Desorptions Spektroskopie (TDS). Das grundlegende Verständnis von chemischen Reaktionen auf Oberflächen ist von großer Bedeutung für die Modifikation und Optimierung verschiedenster Prozesse in der Umwelt und Industrie, jedoch verhindert die Komplexität dieser ablaufenden Prozesse oftmals ein Verständniss auf molekularer Ebene. Ziel der Arbeit war es, Einblick in komplexe chemische Prozesse mittels der Untersuchung von Modellsystemen unter UHV-Bedingungen zu erlangen. In diesem Rahmen wurde die Methandissoziation auf einem Ruthenium(0001)-Einkristall und die Dissoziation von schwerem Wasser(D_2O) auf α-Aluminiumoxid-Einkristallen untersucht. Die Wechselwirkung von Methan auf verschiedenen Metalloberflächen ist von Interesse für verschiedene industrielle Prozesse, wie z.B. die Dampfreformierung von Methan oder die Fischer-Tropsch-Synthese. Im Rahmen der Untersuchung der Methandissoziation wurden alle vorkommenden Molekülfragmente(CH, CH_2) sowie ihre Kopplungsprodukte(CCH, CCH_2, CCH_3) anhand ihrer charakteristischen Molekülschwingungen identifiziert. Dies ermöglichte Einblick in den Einfluss der Oberflächentemperatur, der Adsorbatbedeckung und der Co-Adsorption anderer Moleküle auf die Stabilität und die Bildung der verschiedenen Spezies. Die Untersuchung des CH_2-Radikals, welches für die Fischer-Tropsch-Synthese von Bedeutung sein könnte, ergab eine Aktivierungsenergie für die Dissoziation von 65 kJ/mol, die vier mal grösser ist, als von der Theorie bisher vorausgesagt wurde. Durch Kooperation mit der Abteilung Theorie des Fritz-Haber-Institut war es uns möglich zu beweisen, dass diese Diskrepanz mittels Co-Adsorption von Wasserstoff erklärt werden kann. Ein weiterer Schwerpunkt der Arbeit lag auf der Untersuchung des Kopplungsprozesses von CH-Radikalen, der zur Bildung des CCH_2-Moleküls führt. Mit Aufstellung eines Reaktionssystems von chemischen Ratengleichungen war eine qualitative Reproduktion der CCH_2-Bildung in Abhängigkeit von der Oberflächentemperatur möglich, was einen Einblick in die zugrundeliegenden Elementarprozesse sowie deren Kinetik erlaubte. Der zweite Teil der Arbeit konzentrierte sich auf die Untersuchung der Wasser/α-Aluminiumoxid Wechselwirkung. Wasseradsorption auf solchen Oberflächen induziert morphologische Veränderungen, welche sich auf die chemischen Eigenschaften des Substrats auswirken. Das Verständnis dieser Prozesse ist daher von Bedeutung für die Umweltchemie oder die heterogene Katalyse. Die Untersuchung der Wasseradsorption auf α-Al_2O_3(0001) und α-Al_2O_3(1102) im UHV ermöglichte dabei Einblick in die Prozesse auf molekularer Ebene. Durch Kombination spezieller Probenpräparations-und Charakterisierungstechniken konnten erstmals die theoretisch vorhergesagten Dissoziationsmechanismen von Wasser auf beiden Oberflächen experimentell nachgewiesen werden. Zusätzlich ermöglichte die Spektroskopie substratspezifischer Oberflächenphononen die Beobachtung der durch Wasseradsorption verursachten morphologischen Veränderungen, was einen neuen Einblick in die Oberflächenreaktivität für verschiedenste Reaktionen geben kann.

Contents

Chapter 1

Introduction

Understanding of chemical reactions on surfaces is of critical importance for modification and optimization a variety of environmental and industrial processes. An example of surface reactions in nature is the corrosion/dissolution of solid materials, such as metals and oxides, in the presence of water. An important example of an industrial application is heterogeneous catalysis. These two examples already divided the field of surface chemistry. In case of corrosion or dissolution the ongoing chemical processes are happening at the majority of surface sites. Only the efficiency or rates between different surface sites for a specific reaction differs. In the field of heterogeneous catalysis on the other side, the surface chemistry is normally controlled by a minority of surface sites, so called actives sites, that often dominate the surface reactivity for a given catalyst and a particular reaction. These different types of problems are usually dealt with by different communities employing different tools. Here I employ two principal tools, Sum Frequency Generation spectroscopy (SFG) and a Molecular Beam Source (MBS), typically employed to study 'majority' and 'minority' problems respectively. In this thesis both tools are applied to one paradigmatic minority problem, hydrocarbon chemistry on metals and one majority, oxide/water interaction

While the field of heterogeneous catalysis has been developed in the last 100 years, this development has been almost exclusively driven by empirical testing rather than molecular level insight[1, 2]. Unfortunately, the molecular level understanding of these catalytic driven processes is of critical importance for optimization and development of new desired chemistry, for example the methane conversion during the oxidative coupling of methane on oxide catalysts[3].

One reason for this lack of molecular understanding is that few analytical techniques have interfacial selectivity and a sufficient sensitivity. As mentioned, desired chemistry on solid catalysts occurs at mostly very specific surface sites (active sites),

therefore interfacial selectivity of a spectroscopy method is an advantage. These active sites will fully control the ongoing chemistry, even though their total number on a catalysts surface is usually small [4]. The limited amount of active sites on a catalyst is also the reason for requiring a high sensitivity for your probe. But even with such a high sensitivity, getting insight into the specific reactions at each type of active site is challenging [5]. On industrial used catalysts, like metals on amorphous supporting materials [6, 7], specific reactions are controlled by plenty of different surface structures which shows, depending on their local geometry and electronic structure, different reactivities regarding their reactions. This huge phase space of parameters for a catalytic system thus makes it difficult to gain molecular level understanding.

One way to overcome this hurdle is by reducing the complexity of the real catalyst: creating appropriate model systems. In an attempt to reproduce the essential features of real catalysts, model systems have typically been single crystal surfaces on which chemical reactions under ultra high vacuum (UHV) conditions have been characterized[2, 8, 9, 10, 11, 12]. The advantages of this approach are the possibilities of using atomically well defined surfaces and surface sensitive electron in/out probes as analytical techniques. On these single crystal surfaces, local defects, for example steps, kinks and corners can act as reactive centers and can show comparable selectivity for certain reactions like the reactive centers of real catalysts[4]. By investigation of these reactions in UHV you can possibly learn something about the elementary processes and reaction kinetics of these selective sites. This experimental approach therefore enables the understanding of morphology effects, pressure and temperature dependence, and various other factors influencing the desired heterogeneous chemistry.

However, this approach comes with significant limitations. A famous example for the application of model systems to reduce complexity is the study of the Fischer-Tropsch (FT) Synthesis[13, 14, 15]. The FT-Synthesis describes the formation of long-chain hydrocarbons on transition metal surfaces from a syngas mixture of CO and H_2 [16]. This process has been studied for decades. Nevertheless, the question of where on the surface the reactions happen and which hydrocarbon species are relevant for the carbon-chain prolongation step remains controversial [17, 16, 18]. Clearly, if understanding of systems with reduced complexity in UHV is problematic, this emphasizes the general problem of transferring insight from observed UHV reactions to large scaled industrial systems.

One consequence of investigating reactions by the model system approach might be, that reactions are completely different in their kinetics and thermodynamics [19]. But especially the correct kinetics and thermodynamics are of high interest, because

these are controlling for example the relative stability of surface species, such as hydrocarbon intermediates during the FT process. Without informations about the correct kinetics and thermodynamics of these intermediates a correct understanding of the FT process is impossible. [16, 18].

This problem of transferring insight from model systems is the result of the UHV surface science approach. These differences are usually summarized as the gas pressure and material gap. The pressure gap is the effect of unrealistic low gas pressures on reactions in UHV compared those under realistic conditions. A possible consequence of the pressure gap is that observed reaction paths in UHV and real conditions can differ, due to other molecular species and reaction channels present on the sample surface. An example for such a problem has been reported by Freund and coworkers[20], who found different reaction channels for the reaction of methanol on palladium catalysts in UHV and ambient. One additional disadvantage is also that the investigated system in UHV is usually prepared in thermal equilibrium with a gas phase, which can lead to similar problems.

The material gap is the effect of UHV on the reacting surface itself. The absence of realistic amounts of reactants (high pressure) in UHV will create a different chemical potential for the surface as you have under realistic conditions. This implies that the thermodynamically favored surface structures between real and model systems can differ. An example for such morphological changes can be found in the system of water on α-Al_2O_3(0001) [21]. Alumina surfaces are ubiquitous in heterogeneous catalysis, optics and electronics and a useful model system for complex, environmentally abundant alumino-silicate phases [22, 23]. Because of this importance the water/alumina interaction has been studied experimentally and theoretically for decades. On result of these investigations was the observation of a changing surface structure and reactivity due to water adsorption and dissociation. In this case a molecular understanding of site specific reactions in UHV will give no insight into the surface reactions under realistic conditions.

As should be now clear, the application of model systems to gain understanding of high pressure reaction conditions will be always challenging. Therefore a transfer of knowledge requires a detailed consideration of all system constraints at each condition as well as general cooperation of theory and experiment.

It is fundamental aim of this thesis to demonstrate that by combining tools typically used to study majority and minority type systems, and with judicious application of theory, one can partially overcome both pressure and material gap.

In the first part of this thesis I will address the UHV $\rightarrow$ ambient pressure gap for the model chemistry of methane on Ru(0001) by a special combination of sample preparation and characterization. Preparation of samples with a Molecular Beam

Source allows the preparation of samples directly in UHV. With this technique it is possible to "freeze" adsorbate states which would otherwise decompose in case of sample preparation in thermal equilibrium with gas phase. This will be helpful in probing surface reaction intermediates and their kinetics, that have not been experimentally accessed before. By doing that I am able to gain more insight into some of the open question of the Fischer-Tropsch sythesis. Furthermore using Vibrational Sum Frequency Generation (SFG) as a high resolution optical spectroscopy method allow a detailed insight into population of different molecules at the surface.

The second part of my thesis addresses both the material and pressure gap of single crystals by focusing on the adsorption mechanism of water on α-Al_2O_3(0001) and (1102) by application of similar techniques. While there have been plenty of studies focusing on the interaction of α-Al_2O_3 with water, an detailed understanding of the molecular processes is still missed. A pressure dependent sticking coefficient of water hindered up to now the investigation of low coverages of dissociated water under UHV on these surfaces. This problem will be addressed by deposition of controlled amounts of dissociated water in UHV with our MBS in combination with characterization by SFG spectroscopy for detection of the reaction products. Furthermore the morphological changes during water adsorption will be addressed by SFG spectroscopy of surface phonon modes, which will give insight into the substrate reorganization due to water adsorption.

Chapter 2

Concepts and Methods

Investigation of surface reactions plays an important role in the understanding of various processes such as catalysis or corrosion. The investigation of these reactions is the subject of surface physics and chemistry. The following chapter describes the physical and chemical basis for the scientific work of this thesis.

The observation of controlled surface reactions often requires a high degree of measurement accuracy. It must be even possible to detect just percents of a monolayer of an adsorbate. Therefore even small amounts of background adsorbed molecules interfere with the detection and falsify the results. As an example to get some feeling for the adsorption behavior I will give a few numbers. At a background pressure in the UHV chamber of 1 x 10^{-6} mbar one monolayer of gas molecules per second will adsorb at the surfaces. In order to minimize these effects experiments have to be performed under Ultra High Vacuum(UHV) conditions. Just under these conditions we are able to simplify the investigated chemical reactions at the surfaces to a situation where we could talk about an isolated molecular picture. It is important to mention that "isolated molecule" does not imply we have just one molecule at our surface. Of course, there will always be huge amounts of molecules apparent at a surface. Therefore, the critical point is that we should be able to create situations where the amount of molecules at the surface is small enough that molecules do not interact strongly with each other. To fulfill such a situation the adsorption distance between two molecules must be wide enough to be in this regime. This could be fractions (1-20 %) of a monolayer of molecules. How far such a distance of two molecules should be, so that the chemical interaction is small depends on the investigated system itself. The reason why we wanted to come to the situation of isolated molecules is quite easy explained: it is a typical approach for investigation that you want to understand at the beginning the "pure" interaction of a single molecule with the surface. Then you investigate and try to understand the

interaction of many molecules with each other and with the substrate. By starting at this "simple" situation and increasing the numbers of molecules at the surface it is easier to understand how does coverage influences chemical reactions. On the other hand the investigation of these "simple" situations requires extremely high sensitivities of spectroscopic tools (e.g. optical, electron based or scanning probe), because low amounts of molecules imply small signal intensities. For this purpose we are using an optical technique called vibrational Sum Frequency Generation(SFG). It is a powerful tool for investigation of molecular processes because of its surface sensitivity (which will be more clear later) and its high resolution for vibrational spectra.

As a second technique for probing the populations at our investigated surfaces we are using a shielded Feulnercup Quadrupole mass spectrometer (QMS). By this experimental technique we are able to detect very low amounts of molecules desorbing from the surface in case of a temperature programmed desorption (TPD).
Nevertheless, the transfer of our investigated system e.g. methane dissociation on Ru(0001) or D_2O on Al_2O_3(0001) into the UHV let us face additional problems, which had to be overcome. Especially the dissociative adsorption of the investigated gases in UHV were one of the crucial points for successful investigation of these systems.

To specify all the general ideas and challenges for the experimental work in this thesis I want to give some background knowledge about the physical and chemical constraints which had to be to overcome and the resulting requirements for our experimental setup.

2.1 Introduction into heterogeneous catalysis

A lot of the work done in this thesis focuses on the understanding and modification of catalytic driven reactions on surfaces. Before we will go into detail with these very specific reactions, a general introduction into this topic seems necessary.

Catalyzed reactions are some of the first chemical reactions used by humans. Even 8000 years ago humans generated alcohol by usage of sugar and catalytic reactive enzymes [24]. Specification of these processes as catalysis has been introduced much later in the 19th century by Joens Jakob Berzelius and later on by Wilhelm Ostwald [25]. They gave the definition of catalysis as the increase of the reaction rate by addition of another material which should not be consumed during the reaction. The idea behind this process is that the added material/ catalyst reduces the activation energy of a certain reaction which increases the reaction rate. Thereby, the catalyst forms intermediate complexes with the reactants, so called transition states, but

in the end after further reaction steps the catalyst should be completely restored. Schematically this is shown in Figure 2.1

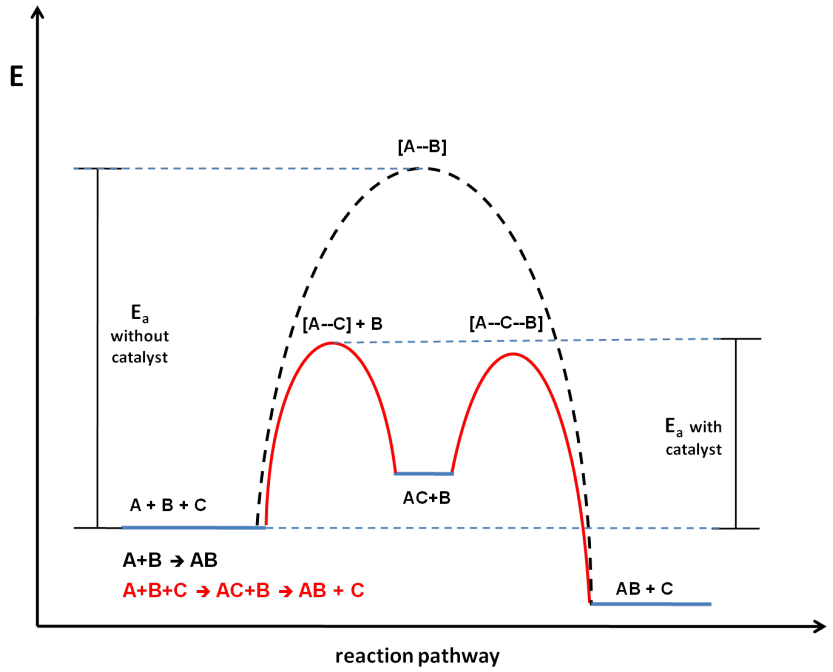

Figure 2.1: Schematic overview of a catalytic reaction of reactants A and B. The catalyst C forms with an intermediate state the reactants, which then further reacts to form the final product AB and the restored catalyst C. As is clear from the scheme, the insertion of the catalyst into the system dramatically reduces the activation barrier, e.g. the energy needed to run the reaction, which increases the reaction rate.

If A and B react together without the presence of a catalyst, as shown in Figure 2.1, the reaction barrier which they have to overcome is quite high. That slows down or even completely suppresses the reaction. The presence of a catalyst changes this dramatically. The catalyst will form some intermediate state with one of the reactants. The activation barrier for the intermediate formation is much smaller, then for the direct conversion. In a second step this intermediate state forms an additional *complex* with the reactant B which triggers the coupling of A and B to AB and the regeneration of catalyst C. Both formations of the complexes [A–C] and [A–C–B] will have a certain activation barrier, but just the larger one will be the rate determining step for the formation of AB. This means the formation of AB has a much lower barrier in presence of the catalyst C. The increase of the reaction rate depends on the energy difference between barriers for the intermediate state with and without the catalyst. It has been found that the reaction rate depends exponentially on the barrier size. The general theory behind reaction rates will be

given later in Section 2.4.1.

Generally, catalysis can be separated into two different types: *homogeneous* and *heterogeneous*. In case of homogeneous catalysis the reactant and the catalyst have the same physical state e.g. as a liquid. The enzyme driven conversion of sugar to alcohol is an example for this type of reactions. For heterogeneous catalysis reactant and catalyst will have different physical states. Normally you have a solid state catalyst and gas or liquids as reactants.

It is not possible to overestimate the importance of catalysis for industry, society and environment. Approximately 90 % of all used chemicals today are formed by catalytic driven processes and nearly all of these by heterogeneous catalysis [26]. Furthermore, many applications for pollution reduction in industry or in a normal car are controlled by catalytic reactions like the conversion of $CO + \frac{1}{2}O_2 \overset{Pt}{\rightarrow} CO_2$. In case of the catalyst in a car you have a porous material like Al_2O_3 in a honeycomb structure on which reactive materials like platinum, rhodium or palladium were deposited. The conversion takes place on these metal clusters[27]. In this case the Al_2O_3 is just the supporting material for the actual catalyst. For other catalytic reactions metal oxides in general and Al_2O_3 in particular could be the catalysts themselves [28]. A famous example for catalysis on oxides is the ammonia synthesis on Fe(II/III)-oxide, which based on the reaction of molecular nitrogen and hydrogen to form ammonia and was developed by Fritz Haber and Carl Bosch at the beginning of the 20th century[1, 2]. This synthesis is one of the most important applications of catalysis because it allowed the synthetic production of fertilizers, which was not possible before. Before this, just naturally produced fertilizer e.g. guano was used, whose limitation for feeding the increasing population of the 20th century is quite obvious.[29]

Another example for oxides as catalysts is the Claus Process for generation of sulfur from hydrogen sulfide in a fixed bed Al_2O_3-reactor.[28] This reaction is the most significant gas desulfurizing process and is still in usage since its invention in 1883.

It should be now clear that the understanding of catalysis either on metals or on metal oxides is of particular interest for science and industry and has been the topic of research for over 100 years. As already mentioned before this thesis focuses on two fields: firstly the catalytic system of CH_4 dissociation on Ru(0001), which is a good model system for the investigation of hydrogen abstraction from hydrocarbons and higher hydrocarbon formation[8, 12]. Secondly the water dissociation on Al_2O_3, which is a widely used catalyst or supporting material for catalysis and whose interaction with water is of particular interest for surface chemistry.

2.2 Adsorption and desorption of molecules on surfaces

In the following paragraph I will discuss the different adsorption mechanisms of molecules on surfaces and their relationship to the chemical reactivity. Finally, I will give some brief introduction into the spectroscopy method which depends on thermal induced desorption of molecules: the thermal desorption spectroscopy or thermal programmed desorption (TDS or TPD).

2.2.1 Physisorption and Chemisorption of molecules

One of the crucial points for investigation of surface chemical reactions is the fact that molecules must be adsorbed at a surface. This could happen in two ways: physisorption and chemisorption.

Physisorption is the result of Van-der-Waals forces between surface and adsorbate. Its energies are normally lesser than 50 kJ/mol [30]. The main issue is thereby that physisorption does not induce strong changes in the properties of the adsorbed molecule.
For chemisorption of a molecule it is necessary to have an overlap between the electronic orbitals of the molecule and the surface. This overlap could induce a weakening of the internal bindings of the molecule and end up in a dissociation of the molecule. The remaining fragments will have a chemical binding with the surface. Normally the energies of chemisorption are greater than 50 kJ/mol. Chemisorption is an activated process where the activation energies can vary in a wide range. To emphasize the energetics I will discuss a chemisorption process at the following example by two types of molecules, called A_2 and AB.

In case of low temperatures both gases will physisorb at the surface as you can see in Figure 10.1. If physisorption would be the only adsorption channel an increase of the internal energy (for example by thermal heating) above the zero energy line of the gas-phase would induce desorption of the molecules into gas-phase. But as you can see the chemisorption well and the physisorption well of A_2 have the crossing point below the zero line. This means that at low temperatures A_2 would adsorb molecularly and with increased temperature it would overcome the small barrier (see E_{A2}), dissociate and would chemisorb. In such a situation the physisorption state is called a precursor state for chemisorption.

For AB this process is slightly different. As clear from the graph the crossing point of chemi- and physisorption is above the zero energy line. This is the reason why molecular adsorption of AB followed by heating of the surface would always

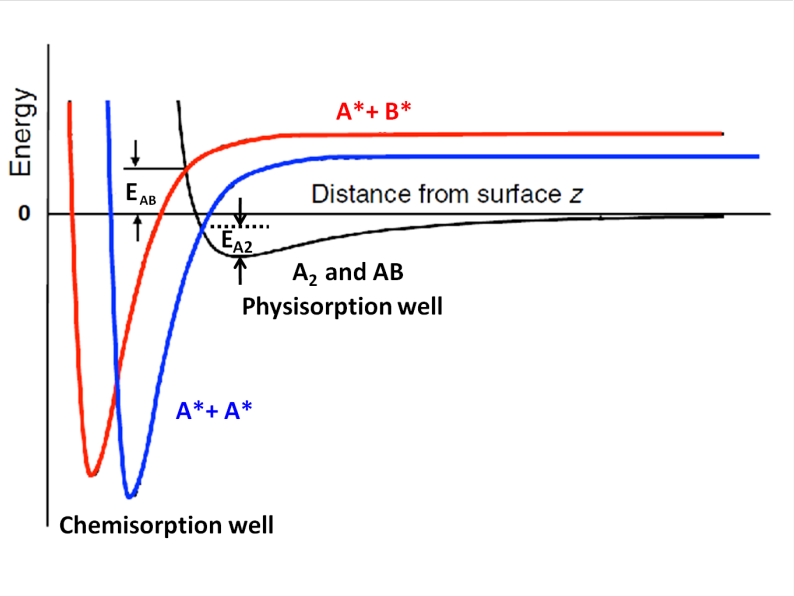

Figure 2.2: Qualitative discussion of chemisorption and physisorption on the example of two different molecules A_2 and AB

end up with desorption. If we want to adsorb AB from the gas-phase at surface temperatures that are high enough to provide the energy for chemisorption we have to overcome an energy barrier, which shown in the graph as E_{AB}. Actually, this kind of adsorption behavior we observed in our experiments for methane on Ru(0001). This is the reason why dissociative adsorption of methane on many metal surfaces is studied using High-Pressure-Cells (HPC)(low sticking coefficient, but many molecules) or a molecular beam source (MBS)(low amount of molecules, but high sticking coefficient).The MBS allows us to overcome the activation barrier, shown in Figure 10.1, directly out of the gas-phase by creation of methane molecules with enhanced kinetic.

One general issue by talking about adsorbed molecules at surfaces is the coverage of the molecules. If all adsorption sites of a surface are saturated by a molecule we talk about one full monolayer. In the following thesis we will often describe adsorbate concentrations in "fraction of a monolayer" (Θ). Θ is determined as:

$$\Theta = \frac{N_{ads}}{N_{max}}$$

N_{ads} is the number of adsorbed molecules at the surface and N_{max} is the total number of adsorption sites. After saturation of a monolayer, molecules get adsorbed in a multilayer. Multilayer adsorption is always a physisorption process and the desorption energy of these molecules are lower than the desorption energy of the

monolayer.

2.2.2 Desorption of molecules

Generally, the desorption of molecules from surfaces is determined by breaking of the adsorbate/substrate interaction, nevertheless it is chemi- or physisorbed. To induce this breaking process we have to add energy to the adsorption system which must be higher than the adsorption energy of the molecule. For the energy transfer into the system, several ways of stimulating the desorption process are possible. These are thermal driven desorption, but electronic or vibrational induced desorption processes can also occur. The easiest and most applicable way for initiation of a desorption process is the thermal driven desorption process, because control of the sample temperature is a normal degree of freedom for each UHV setup. Therefore, intensive work on the description of such a thermal driven desorption processes have been performed within the last century. This ended up with the Polanyi-Wigner equation(PW) which is a suitable tool to understand, describe and simulate the desorption spectrum of a system[31]. This theoretical description allows us to get information about population and energetics of adsorbates on a certain surface. Furthermore it provides insight into adsorbate interaction and morphologic effects on the desorption spectrum. The spectroscopic method which is based on this desorption process is called Thermal Desorption Spectroscopy (TDS). It is used in this thesis because of its huge applications for adsorbate analysis. Below we will derive the Polanyi-Wigner equation(PW), which is necessary for the understanding of desorption spectra.

For investigation of desorption we monitor the time dependent change of coverage, called the desorption rate:

$$v_{\mathrm{des}} \;=\; -\dot{\Theta} = \; -\frac{d\Theta}{dt} \tag{2.1}$$

In case of a n-order process, we get

$$-\,\dot{\Theta} \;=\; -k_0 \cdot \Theta^n \tag{2.2}$$

k_0 is thereby the rate constant and n the kinetic order of desorption. The order of desorption can be predicted to some extend by the number of elementary steps that are involved in the process. Normally, molecular desorption has a desorption order of one, whereas recombinative desorption has an order of two. For a more detailed definition of the rate-constant several expressions have been found in the end of the 19‘th century to describe the kinetics of a certain process (e.g. desorption, dissociation, reaction ...) acceptably. Just to give some examples these were the

Arrhenius expression, the Harcourt-Esson equation or the Kooij equation [32]. At the beginning of the 20'th century the only one-parameter equation which was still in usage was the Arrhenius equation. Actually, this was not the case because this equation described the empirical data in the best way. This equation was accepted because it provided insight into how a reaction proceeds, which was of certain interest [32]. Therefore we will use the Arrhenius equation for description of the rate constant. This formula follows from kinetic theory and connects the rate-constant quantitatively to the temperature.

$$k_0 \ = \nu(\Theta) \cdot e^{\left(-\frac{E_{\mathrm{A,des}}}{R \cdot T}\right)} \tag{2.3}$$

In this equation $\nu(\Theta)$ is called the preexponential frequency factor. It could be interpreted as the number of attempts per second of an adsorbed molecule to desorb from the surface. It is usually in the range of 10^{13} Hz, which is due to the lattice vibration of a solid [33]. In the exponential part $E_{\mathrm{A,des}}$ is the activation energy of a desorption process and R is the gas-constant. With this we get for the desorption-rate[31]:

$$v_{\mathrm{des}} \ = \ -\frac{d\Theta}{dt} = \nu(\Theta) \cdot \Theta^n \cdot exp\left(-\frac{E_{\mathrm{A,des}}}{R \cdot T}\right) \tag{2.4}$$

This is called the Polanyi-Wigner equation (PW) and is the fundamental tool for investigation and simulation of desorption processes.

2.2.3 Temperature Programmed Desorption

Above we derived the Polayi-Wigner equation (PW) which is necessary for description of thermal induced desorption processes. Equipped with this tool we want to understand the physics behind the Thermal Desorption Spectroscopy (TDS). The method is also often called Temperature Programmed Desorption (TPD). TPD is a spectroscopy method where the desorption of molecules from a given surface as a function of surface temperature is monitored. You can see in the PW equation that you get insight into the energetics of the thermodynamics of a surface. Therefore, it is a common technique for investigation of adsorbates. In a practical way one can apply a linear heating ramp to the adsorbate/substrate system and detect with a quadrupole mass spectrometer the increase of the partial pressure. If the pumping speed of the used UHV setup is large compared to the partial pressure increase of the desorption the measured partial pressure is proportional to the desorption rate. Then the area under the measured TPD curves is proportional to the number of desorbing molecules[34]. This can be shown by calculation. Let us assume that a

chamber of volume V has a pumping rate S. Molecules from the chamber surface will desorb with rate L. There are molecules left in the chamber with the density of c_g and the sample has a surface area of A_s, from which molecules desorb with desorption rate $v_{des}(t)$. The time dependence of the desorptionrate is given by the heating ramp

$$T_s \;=\; T_0 \;+\; \beta t$$

T_s is the sample temperature and β the heating rate. The change of molecules in the gasphase in given by

$$V\frac{dc_g}{dt} \;=\; A_s v_{\mathrm{des}}(t) \;+\; L \;-\; c_g S \tag{2.5}$$

Definition of V, S and L see above. We can assume that S and L are constants, which means no desorption happens. Then we will get

$$V\frac{dc_g}{dt} \;=\; L \;-\; c_g S \tag{2.6}$$

In equilibrium, the solution is therefore

$$c_{gs} \;=\; \frac{L}{S} \tag{2.7}$$

This leads to a pressure in case of no desorption

$$p_s \;=\; k_B T_s c_g \;=\; \frac{k_B T_s L}{S} \tag{2.8}$$

A pressure change by desorption of molecules from the sample could be described as

$$\Delta p \;=\; p \;-\; p_s$$

The relationship between pressure change and desorption-rate could now be described as:

$$V\frac{d\Delta p}{dt} \;+\; S\Delta p \;=\; k_B T_s A_s v_{\mathrm{des}}(t) \tag{2.9}$$

In case of high pumping speed, the first term on the left side could be neglected because $\frac{d\Delta p}{dt} \approx 0$ and we get for the change

$$\Delta p \;=\; \frac{k_B T_s A_s}{S}\; v_{\mathrm{des}}(t) \tag{2.10}$$

Under the given constraint that the pumping speed is huge compared to the pressure change during desorption(what is the case for our UHV setup) we can estimate that changes in the pressure are direct proportional to the desorption rate.

Spectra which were gained by monitoring the partial pressure in order of the sample temperature can give now insight into the properties of the bonding between

adsorbate and substrate. Also the shape of desorption spectra can give information about desorption order or (in special cases) defect concentrations. A zero order desorption process (not shown) is an coverage independent process, as clear from the PW equation. The TPD signal of different coverages of such a case have always the same rising edge and the desorption maximum is followed by a sharp cut to zero. For first and higher desorption order processes, this changes and will be emphasized in the following graph‘s 2.3 where I will demonstrate the effect of desorption order by simulation of desorption spectra with the PW equation for the first and second order.

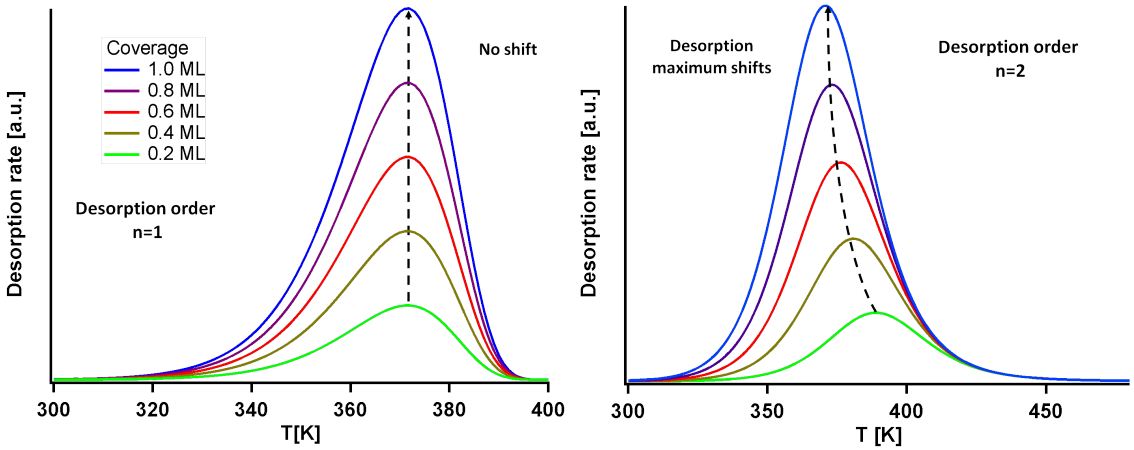

Figure 2.3: Figure show the simulated dependence of the spectral shape of a TDS spectrum on the desorption order and coverage. Spectrum were simulated with the PW equation by assumption of a preexponential factor ν of 10^{13} and a desorption energy of 100 kJ/mol. While first-order desorption show an asymmetric shape to the low temperature tail, second-order reaction were symmetric or show an high temperature tail. Furthermore the dependence of the desorption maximum on the coverage of a certain sample with second-oder kinetics gets emphasized.

Figure 2.3 shows a series of simulated desorption spectra in dependence of the desorption order and coverage. The spectra were simulated by using Equation 2.4 with an assumed preexponential factor of ν of 10^{13} Hz and a desorption energy of 100 kJ/mol. You can see clearly the effect of desorption order and coverage. First order kinetics show an asymmetric shape to the low temperature tail and have a constant maximum desorption temperature. Second order kinetics will be symmetric around the maximum or show a desorption tail to higher temperatures. In this case you can observe a coverage dependent shift of the desorption maximum, as marked in the Figure b). In simulation, the shape and symmetry of the peaks is determined by the math behind. In a real adsorption system this depends on the way how a molecule adsorb at the surface. If you have molecular adsorption in your system it will show first order kinetics in the desorption spectrum. In case of

dissociative adsorption of molecules the system will show second order kinetics. At this point we have to mention that the order of desorption for a real system is not the only determining factor for the desorption shape. It could have also contributions from surface morphology on the desorption spectrum. Therefore it is important to mention that a symmetric shape of a TPD signal does not generally imply a dissociative adsorption. Nevertheless, even with these restrictions it is obvious that TPD spectroscopy is a powerful tool for investigation of adsorbate systems. With this technique we are able to learn something about the kinetics and thermodynamic of our adsorbates. Unfortunately, it is necessary to remove the molecules from the surface to learn something about the system. We are just able to observe situations after the molecules have left the surface. If we want to learn something about our molecules adsorbed at the surface we need an additional tool. In my thesis this tool was Vibrational Sum Frequency Generation and will be introduced in the next section.

2.3 Vibrational Sum Frequency Generation (SFG)

The investigation of molecules, which have left the surface (as it is the case for TPD), gives only barely information about the situation while the molecules are adsorbed at the surface. A powerful tool for an in-situ investigation of an adsorbate system would be vibrational spectroscopy, which has the needed properties mentioned above. Vibrational spectroscopy methods being possible to perform in UHV and in ambient (necessary for D_2O/Al_2O_3) would be IR-Reflection Adsorption spectroscopy and vibrational Sum Frequency Generation (SFG). Thus we chose SFG as our additional tool for investigation of the different adsorption systems in the following thesis. It is a nonlinear optical vibrational spectroscopy method [35]. In comparison to other optical vibrational spectroscopies like IR-Reflection Absorption Spectroscopy (IRAS), SFG shows some advantages. By a convenient choice of the visible up-conversion pulse the detected SFG light will be in the visible spectrum of light and much easier to detect. This is due to the fact that the detection efficiency of CCD-cameras is much higher for visible light than for IR[36]. Generally, vibrational IR-spectroscopy methods are quite powerful tools for the characterization of chemical reactions and species. The reason for this based on the fact that the vibrational frequencies of certain molecules depend on its intermolecular potential. Therefore it allows to gain insight into the binding energy and geometry. Additionally, this kind of optical vibrational spectroscopy has the advantage of having a high resolution and it could be performed in a way which not changes the system during the measurement. In contrast to SFG, conventional linear optical spectroscopies monitor in their spectra

contributions of substrate‘s bulk and adsorbed molecules. In our investigations we are interested in molecules and reactions just at surfaces. Therefore, sum frequency generation spectroscopy is a perfect choice for the investigations because of its interfacial selectivity. This effect is based on the inversion symmetry of our used single crystals and will be later explained more detailed [37, 35].
Below I will briefly introduce the reader into linear and nonlinear optics. This knowledge enables understanding of second order nonlinear processes happening at the interface in case of sum frequency generation.

2.3.1 Linear and Nonlinear Optics

Before starting a discussion of the SFG-process, a general introduction into linear and nonlinear optics should be given. In linear optics light induces in a media a polarization P, which is linearly proportional to the applied electric field E of the light.

$$P = \epsilon_0 \chi \cdot E \tag{2.11}$$

In this equation χ describes the linear optical susceptibility of the media and ϵ_0 the permittivity of free space. If the applied electric field of the laser-pulse becomes strong this linear approximation of the polarization is no longer correct. Then higher order terms in the polarization have to be taken into account [35]. For the description of this higher order terms the Taylor series can be used and we will get:

$$P = P^{(1)} + P^{(2)} + P^{(3)}... \tag{2.12}$$

$$= \epsilon_0 \chi^{(1)} E(r,t)^{(1)} + \epsilon_0 \chi^{(2)} E(r,t)^{(2)} + \epsilon_0 \chi^{(3)} E(r,t)^{(3)}... \tag{2.13}$$

In this equation $\chi^{(1)}$ is the linear susceptibility and is a scalar. All the higher terms of $\chi^{(i)}$ are the susceptibility of the i-order and have a tensor form. The in this thesis used spectroscopic technique SFG is a nonlinear optical process of second order. Like all $\chi^{(2)}$-processes it is forbidden in media with inversion symmetry. This will be shown in the following section [37].

Assuming two incident laser beams at the surface with the electric fields $E_1 cos(\omega_1 t)$ and $E_2 cos(\omega_2 t)$ overlap at the same time and space they induce a second order polarization $P^{(2)}$ in the media . This could then be written as

$$P^{(2)} = \epsilon_0 \chi^{(2)} \cdot (E_1 cos(\omega_1 t) + E_2 cos(\omega_2 t))^2 \tag{2.14}$$

If we further rewrite this equation we will get

$$\begin{aligned} P^{(2)} = \frac{1}{2}\epsilon_0\chi^{(2)}\left[E_1^2(1+cos(2\omega_1)t) + E_2^2(1+cos(2\omega_2)t)\right] \\ +\epsilon_0\chi^{(2)}\left[E_1E_2(cos(\omega_1+\omega_2)t + cos(\omega_1-\omega_2)t\right] \end{aligned} \tag{2.15}$$

This equation shows that the polarized media itself can act as a light source because of its nonlinear response. The oscillating polarization can emit light at the frequencies of $2\omega_1$, $2\omega_2$, $\omega_1+\omega_2$ and finally $\omega_1-\omega_2$. This emitted light corresponds to several nonlinear processes which are: second harmonic generation(SHG) (for the input beams ω_1 and ω_2), sum frequency generation(SFG) ($\omega_1+\omega_2$) and difference frequency generation (DFG) (ω_1 - ω_2). We will focus on the SFG part, where ω_1 corresponds to a 800 nm beam and is called ω_{VIS}. ω_2 corresponds to an IR beam which is called ω_{IR}. For all of the mentioned processes described above we have energy conservation. Therefore so we can write for the SFG

$$\omega_{SFG} = \omega_{Vis} + \omega_{IR} \tag{2.16}$$

Furthermore this process contains momentum conservation parallel to the surface. We get for the momentum:

$$k_{SFG}sin\beta_{SFG} = k_{Vis}sin\beta_{Vis} + k_{IR}sin\beta_{IR} \tag{2.17}$$

where β_{SFG}, β_{Vis} and β_{IR} are the angles with respect to the surface normal. That implies that the angle of the emitted SFG light depends on the angle of both incoming beams and their frequencies.

The surface sensitivity of the $\chi^{(2)}$-processes will be clearer right now. Generally, you can divide nonlinear media into two groups depending on their internal symmetry. On one hand you have media which are centrosymmetric, what implies an inversion-symmetry and on the other hand media with a broken inversion symmetry. In case of a centrosymmetric crystal the crystal must be symmetric by $x \to -x$. If we look on the induced polarization in case of SFG we will see the effect of an inversion symmetry easily. We have

$$P^{(2)} = \epsilon_0\chi^{(2)} \cdot E_1(t)E_2(t) \tag{2.18}$$

If we change the sign of the incoming electromagnetic field the polarization must change its sign, too. But due to the inversion symmetry of the medium the $\chi^{(2)}$ is insensitive to this transformation [38]. We get

$$-P^{(2)} = \epsilon_0\chi^{(2)} \cdot [-E_1(t)]\,[-E_2(t)] \tag{2.19}$$

The only way both Equations 2.18 and 2.19 can be fulfilled is, if $\chi^{(2)} = 0$. Followed from that the $\chi^{(2)}$ for media with inversion symmetry will be always equal zero. The bulk of some single crystals (as we used in our experiments) is such a media. Therefore, the bulk of our used single crystals will never generate SFG. In case of an interface between the crystal and vacuum inversion symmetry is broken and we have $\chi^{(2)} \neq 0$: a SFG-process can happen. Therefore, SFG is a surface sensitive spectroscopy method.

Because some SFG-measurements of this thesis have been performed on a metal surface I will briefly discuss the influence of a metal substrate on the SFG response. The presence of free electrons in the metal surface influences the vibrational spectrum by the interaction of the electrons with the applied electric field of the Laser. This interaction creates an additional selection rule for SFG. If the transition dipole oscillates parallel to the surface the transition dipole respectively the corresponding molecular vibration will not be visible in a SFG as well as in an IR reflection vibrational spectrum [39]. The reason for that is the created image dipole in surface, which will cancel the effective dipole of a molecular vibration. This could be easily seen in Figure 2.4.

Dipoles which are perpendicular to the surface will be enhanced by the same process because the overall-dipole for this vibrational mode will be stronger.

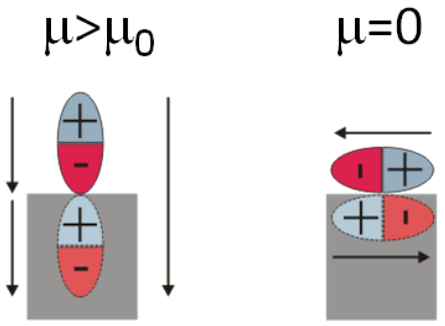

Figure 2.4: Selection rule for SFG spectroscopy on a metal surface. Dipoles which are parallel to the surface will be canceled out by the image dipole in the surface. In contrast, dipoles that are perpendicular to the surface will be enhanced by the same process, because the overall-dipole for this vibrational mode will be stronger. Figure taken from literature [39]

With this information about nonlinear optical effects at surfaces in general we can go more into detail of the SFG process and the practical issues for the spectroscopy itself.

2.3.2 SFG vibrational spectroscopy

Within the last decade SFG as a vibrational spectroscopy method has been established and widely used for many applications. It is obvious that for the detection and identification of molecules during chemical reactions vibrational spectroscopy is quite useful. In a practical manner the SFG process could be described as it is done in Figure 2.5.

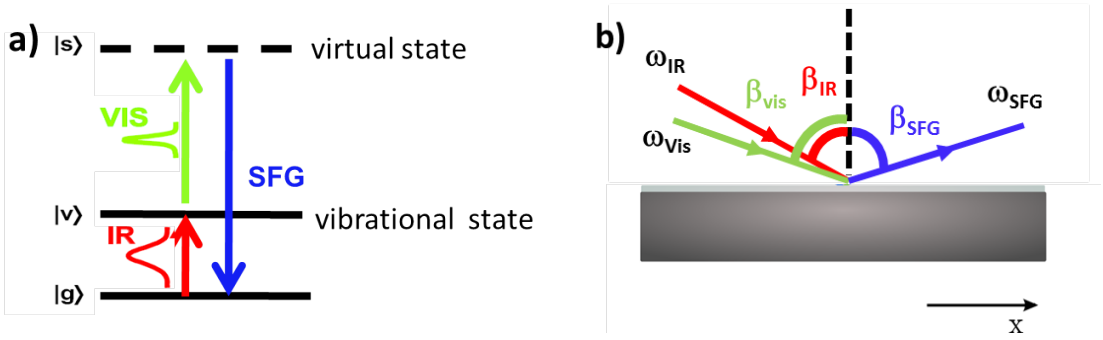

Figure 2.5: Three-level-picture of schematic SFG process

Figure 2.5 a) shows that the incoming IR beam can excite a molecular vibration at the interface. A second beam which will be in the visible region (800nm) is overlapped in space and time with the IR-beam and excite the SFG process in the system. The energy and momentum conservation is shown in Figure 2.5. In our performed experiments we used a broadband IR-pulse which has normally a FWHM of 150 cm^{-1} and a narrow-band 800 nm up-conversion pulse. In Equation 2.19 we showed that induced polarization of a medium is proportional to the intensity of the incoming beams. Therefore the generated intensity of the SFG-process can be expressed by the following formula:

$$I_{SFG} \propto \left|P^{(2)}_{SFG}\right|^2 \propto \left|\chi^{(2)}_{NR}\right|^2 I_{Vis} I_{IR}(\omega) \tag{2.20}$$

$$I_{SFG} \propto \left|P^{(2)}_{SFG}\right|^2 \propto \left|\chi^{(2)}_{NR} + \chi^{(2)}_{R}\right|^2 I_{Vis} I_{IR}(\omega) \tag{2.21}$$

The SFG- intensity is proportional to the intensity of both incoming laser beams. The $\chi^{(2)}_{eff}$ includes all the informations about the system. This could be polarization and geometrical dependent factors of the interaction of the applied electric field with adsorbed molecules. This part is called the resonant contribution in the $\chi^{(2)}_{eff}$. Furthermore, $\chi^{(2)}_{eff}$ will also include some frequency independent non-resonant response which will be called the non-resonant contribution of the created SFG light. Thus we can split our $\chi^{(2)}_{eff}$ in two different components[40, 41, 42]

$$\chi^{(2)}_{eff} = \chi^{(2)}_{NR} + \chi^{(2)}_{R} \tag{2.22}$$

If the applied Laser light of the IR-beam does not match any vibrational excitation of the adsorbed molecules at the surface the $\chi_R^{(2)}$-term will be zero, as clear from Equation 2.23 . Then the signal will be dominated by the non-resonant term. In such a case the spectrum will be a picture of the IR-beam which has in our case more or less a Gaussian shape. Nevertheless it is very important to mention that in case of a resonant transition the intensity depends also on the coverage of the adsorbed molecules, respectively the number of oscillators. First, we will look now from a microscopic point of view. In such a case the resonant term $\chi_R^{(2)}$ of the second order susceptibility $\chi_{eff}^{(2)}$ can be described by the sum of the averaged molecular hyperpolarizability β_q over the resonances q

$$\chi_R^{(2)} = \sum_q N \langle \beta_q \rangle \tag{2.23}$$

where N is the number of molecules at the surface [43, 44]. In case of several resonances the total hyperpolarizability can be given as

$$\beta_{lnm,q} = \frac{\langle g \left| \alpha_{lm} \right| v \rangle \langle g \left| \mu_n \right| v \rangle}{\omega_{IR} - \omega_q + i\Gamma} \tag{2.24}$$

The (lmn) represents in this case the coordinate system of the molecule, while α_{lm} and μ_n are the Raman and dipole vibrational transition elements [43, 44]. The g and the v are standing for the ground and first vibrational state of a molecule, as already shown in Figure 2.5 a). Equation 2.24 show the selection rule that a vibrational mode of a molecule must be Raman and IR active. A second important issue that you can see is that $\chi_R^{(2)}$ is proportional to the number N of the molecules. The intensity of the emitted SFG is then (as clear from 2.21) proportional to N^2. This will be important for some later analysis of our data.

Followed from Equation 2.24 we can use the following equation for a macroscopic description of the resonant part of the nonlinear susceptibility $\chi_R^{(2)}$:

$$\chi_R^{(2)} = \sum_q \frac{|A_q|}{\omega_{IR} - \omega_q + i\Gamma} \tag{2.25}$$

A_q is the amplitude of the resonance q, ω_q is the center-frequency of the resonance and Γ is the bandwidth of it. These are the fitting parameters. For the fitting a homogeneous Lorentzian profile was applied[45, 38, 40, 46]. This expression has been found to work out fine for description of resonances in SFG data. As a full description for the effective nonlinear susceptibility of second order $\chi_{eff}^{(2)}$ for our fitting model we get

$$\chi_{eff}^{(2)} = \chi_{NR}^{(2)} + \sum_q \chi_R^{(2)} = |A_{NR}| \, e^{i\phi_{NR}} + \sum_q \frac{|A_q|}{\omega_{IR} - \omega_q + i\Gamma} \tag{2.26}$$

Attached to the non-resonant amplitude is a phase factor. By inserting 2.26 into Equation 2.21 we will get for the intensity of emitted SFG light following macroscopic description:

$$I_{SFG} \propto \left| |A_{NR}| \, e^{i\phi_{NR}} + \sum_q \frac{|A_q|}{\omega_{IR} - \omega_q + i\Gamma} \right|^2 I_{Vis} I_{IR} \tag{2.27}$$

The practical usage of this equation will be shown in the experimental section, where a schematic way of data analysis will be shown at an example.

2.3.3 Broadband SFG spectroscopy

After the introduction of SFG as a useful vibrational spectroscopy method I will give in this section some necessary restrictions about the way how we wanted to get information out of a system by this spectroscopy method. It is already clear by the title that we are using a SFG-method which is called broadband vibrational SFG spectroscopy. The origin of this name is founded in the fact that we use a broadband IR-pulse for the generation of SFG at the surface. Broadband means in this case a FWHM of about $150\,\mathrm{cm}^{-1}$. The great advantage of such a pulse-width is that we are able to monitor several vibrational transitions at the same time without tuning of the pulse to a new spectral region. If the vibrational frequency of a molecule is covered by the IR frequency of the pulse the corresponding SFG spectrum will be resonantly enhanced at this frequency. The spectrum will show a peak. Because we are performing our measurements in the frequency domain the measured bandwidth of a certain resonance is a convolution of its natural bandwidth with the bandwidth of the VIS pulse. This means, if the bandwidth of the VIS is larger than those of the resonance, the convoluted bandwidth will be determined by the VIS pulse and we lose information. Therefore, we have restrictions to the up-conversion pulse (the 800 nm) if we do not want to lose information out of the SFG data because of poor resolution. We use for the up-conversion a narrow-band 800 nm pulse with a FWHM between $5\,\mathrm{cm}^{-1}$ (for the measurement on Ru(0001)) and $17\,\mathrm{cm}^{-1}$ (on the Al_2O_3 surfaces). The origin of this different bandwidth depend on the different energies of the pulses which we had to use for spectroscopy. That will be clearer when we will discuss the way of generation of these pulses later on in the experimental section. In case of Ru(0001) a pulse energy for up-conversion between 7-12 μJ was sufficient, while in case of the alumina surfaces we had to use a pulse energy of $40\,\mu J$. Figure 2.6 show in the lower panel a broadband IR-pulse and in the upper panel a resonantly enhanced SFG-spectrum. For the spectrum of the IR pulse the SFG wavelength has been already converted to the corresponding IR frequencies. The practical way of

the conversion will be explained later on in the experimental section.

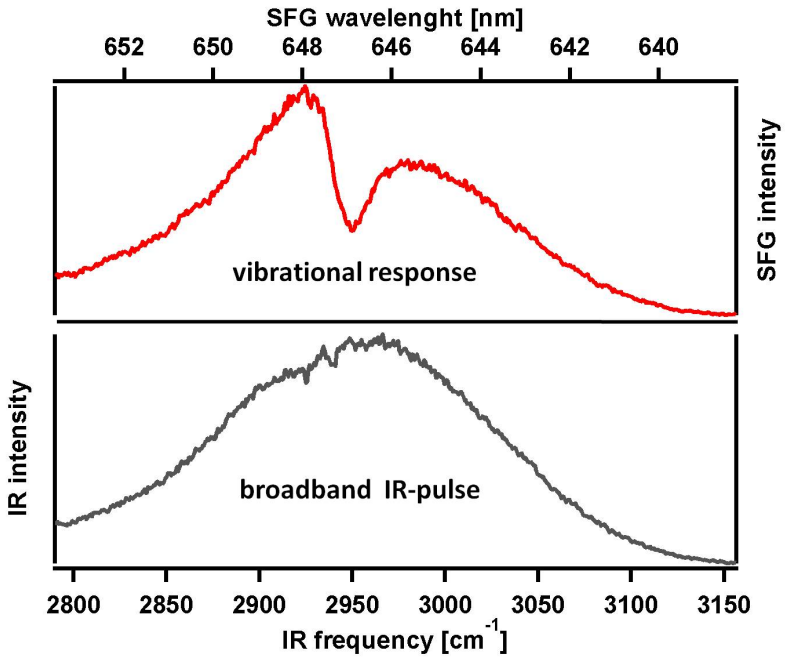

Figure 2.6: Example for the Broadband SFG process on a Ru(0001) single crystal. The clear peak in the upper panel corresponds in this special case to CH_2, adsorbed on the Ru(0001) surface. The lower panel shows the SFG spectrum of a bare Ru(0001) surface. It is the so called non-resonant background (NRB). This NRB is directly proportional to I_{IR}, so you can say it is a picture of this pulse. Generally, the measured SFG wavelength, either with or without resonance, is in the visible range as you can see it in the top panel for CH_2 on Ru(0001). The conversion from the SFG wavelength to the much more interesting IR wavelength is done afterwards and will be explained later on in the experimental section. The reason for the conversion is that we are interested in the vibrational modes of adsorbed molecules to gain information about the adsorbates. These vibrational modes correspond to the modulated IR frequency of our IR pulse.

2.3.4 Molecular orientation and polarization dependency of SFG intensities

The real SFG intensity depends on many different components as shown in Equation 2.26 and 2.26. Some important components whose influence has not been discussed yet, are the dependence of the SFG signal on the angles of the incoming laser-beams, the molecular orientation and the polarization. General insight into these factors allows a prediction for the SFG intensity, which could be useful for some measurements. In the following paragraph we will introduce the theory behind this method.

Generally, the way how these aspects of an interfacial system are related to the SFG intensity has been already discussed and described in detail in literature [47, 48, 49, 50, 51]. At this point we just wanted to reproduce the formalism for simulation and interpretation of a vibrational SFG response measured in order of polarizations and their dependence on the molecular orientation, as it has been already shown in [22]. We will describe the following math with focus on the example of water(D_2O) on the α-Al_2O_3/vacuum interface because this is the system where this formalism is relevant for

For this case sum frequency field can be given by the Maxwell's equation

$$I_{SFG}(\omega_{ir}) = \frac{8\pi^3\omega_{SFG}^2}{c^3 cos^2\beta_{SFG}} \left|\chi_{eff}^{(2)}\right|^2 I_{vis} I_{ir}(\omega_{ir}) \tag{2.28}$$

in which $I_{SFG}(\omega_{ir})$ is the intensity of the generated sum frequency field (which is a function of the frequency of the incident infrared), c is the vacuum speed of light, β_{SFG} is the angle of the reflected SFG field with respect to the surface normal, I_{vis} is the intensity of the visible field and $I_{ir}(\omega_{ir})$ is the intensity of the incident infrared. Beside $\chi_{eff}^{(2)}$ which is the macroscopic nonlinear susceptibility all of the mentioned parameters are under the control of the experimentalist or physical constants.

$\chi_{eff}^{(2)}$ contains all sample specific information. Because the used crystal surface has macroscopic $C_{\infty v}$ symmetry, 7 of the 27 elements of $\chi_{eff}^{(2)}$ are nonzero and just 4 are independent. In a laboratory frame in which (x,y) is the plane of the crystal surface and z the surface normal these are $\chi_{zzz}^{(2)}$, $\chi_{xzx}^{(2)} = \chi_{yzy}^{(2)}$, $\chi_{xxz}^{(2)} = \chi_{yyz}^{(2)}$ and $\chi_{zxx}^{(2)} = \chi_{zyy}^{(2)}$. We further know that all beams propagate in the x-z plane and *s* indicates polarization perpendicular and *p* parallel to the x-z plane. In this coordinate system we can write expressions which relate the experimentally controllable parameters like the beam polarizations and angles to the $\chi_{eff}^{(2)}$ [22]. In the following part we discuss only the combinations ppp and ssp, because these are the relevant combinations for this thesis. For $\chi_{eff,ssp}^{(2)}$ and $\chi_{eff,ppp}^{(2)}$ the relevant equations are,

$$\begin{aligned}
\chi_{eff,ssp}^{(2)} &= L_{yy}(\omega_{SFG})L_{yy}(\omega_{vis})L_{zz}(\omega_{ir})\sin\beta_{ir}\chi_{yyz}^{(2)} \\
\chi_{eff,ppp}^{(2)} &= -L_{xx}(\omega_{SFG})L_{xx}(\omega_{vis})L_{zz}(\omega_{ir})\cos\beta_{SFG}\cos\beta_{vis}\sin\beta_{ir}\chi_{xxz}^{(2)} \\
&\quad -L_{xx}(\omega_{vsf})L_{zz}(\omega_{vis})L_{xx}(\omega_{ir})\cos\beta_{SFG}\sin\beta_{vis}\cos\beta_{ir}\chi_{xzx}^{(2)} \\
&\quad +L_{zz}(\omega_{vsf})L_{xx}(\omega_{vis})L_{xx}(\omega_{ir})\sin\beta_{SFG}\cos\beta_{vis}\cos\beta_{ir}\chi_{zxx}^{(2)} \\
&\quad +L_{zz}(\omega_{vsf})L_{zz}(\omega_{vis})L_{zz}(\omega_{ir})\sin\beta_{SFG}\sin\beta_{vis}\sin\beta_{ir}\chi_{zzz}^{(2)}
\end{aligned} \tag{2.29}$$

where $\sin\beta_k$ is the incident angle for the beam k and $L_{ij}(\omega)$ are the Fresnel coefficients. The Fresnel coefficients for a certain material describe the reflection and transmission

index of a certain wavelength for this material. The coefficients can be rewritten as,

$$L_{xx}(\omega) = \frac{2\cos\gamma_\omega}{\cos\gamma_\omega + n_{Al_2O_3}(\omega)\cos\beta_\omega} \tag{2.30}$$

$$L_{yy}(\omega) = \frac{2\cos\beta_\omega}{\cos\beta_\omega + n_{Al_2O_3}(\omega)\cos\gamma_\omega} \tag{2.31}$$

$$L_{zz}(\omega) = \frac{2n_{Al_2O_3}(\omega)\cos\beta_\omega}{\cos\gamma_\omega + n_{Al_2O_3}(\omega)\cos\beta_\omega}\left(\frac{1}{n'(\omega)}\right)^2 \tag{2.32}$$

in which β_ω is the incident angle of the beam at frequency ω, $n_{Al_2O_3}(\omega)$ is the refractive index of α-Al_2O_3 at frequency ω, γ_ω is the refracted angle at frequency ω (i.e. $\sin\beta_\omega = n_{Al_2O_3}(\omega)\sin\gamma_\omega$) and n' is the interfacial refractive index. We have to note at this point that these coefficients depends only on experimental geometry (e.g. angle of incoming IR and VIS beams) and the refractive index of both bulk phases and the interface. They have no contribution from the nonlinear optical properties of the material.

As we have shown in Equation 2.23 and 2.24 the effective nonlinear susceptibility in the laboratory frame $\chi^{(2)}_{ijk}$ can be connected to the hyperpolarizability $\alpha_{i'j'k'}$ of the molecule. In case of a slow-motion approximation is given as (the physical meaning of slow-motion approximation is explained below):

$$\chi^{(2)}_{ijk} = \frac{1}{2\epsilon_0} N_s \langle R_{ii'} R_{jj'} R_{kk'} \rangle \alpha_{i'j'k'} \tag{2.33}$$

in which $\langle R_{ii'} R_{jj'} R_{kk'} \rangle$ is the ensemble averaged transformation matrix between molecular and laboratory coordinates in the *slow motion limit*: in which the angle of individual molecular groups with respect to the surface normal (θ) does not change on the timescale of the inverse line width [22]. Calculating the $\langle R_{ii'} R_{jj'} R_{kk'} \rangle$ matrix for each of the relevant $\chi^{(2)}_{ijk}$ terms gives,

$$\begin{aligned}
\chi^{(2)}_{yyz} &= \chi^{(2)}_{xxz} = \frac{1}{2\epsilon_0} N_s \alpha^{(2)}_{z'z'z'} \left[\left\langle sin^2\theta\ cos\theta \right\rangle (1-r) + 2r \left\langle cos\theta \right\rangle\right] \\
\chi^{(2)}_{xzx} &= \chi^{(2)}_{zxx} = \frac{1}{2\epsilon_0} N_s \alpha_{z'z'z'} \left(\langle\cos\theta\rangle - \langle\cos^3\theta\rangle\right)(1-r) \\
\chi^{(2)}_{zzz} &= \frac{1}{\epsilon_0} N_s \alpha_{z'z'z'} \left[r\langle\cos\theta\rangle + \langle\cos^3\theta\rangle (1-r)\right]
\end{aligned} \tag{2.34}$$

in which N_s is the molecule number, $\alpha^{(2)}_{z'z'z'}$ is the hyperpolarizability along the molecular axis z' (the only non-zero components of α^2 were the $\alpha^{(2)}_{z'z'z'}$ and the $\alpha_{z'z'z'}$ component of the hyperpolarizability), r is the hyperpolarizability ratio ($r = \frac{\alpha_{y'y'z'}}{\alpha_{z'z'z'}}$) and θ is the angle of the molecule with respect to the surface normal. With this information we are able to predict in case of known molecular orientations the dependence of the relative SFG intensity on the experimental geometry and polarization.

2.4 Thermodynamic description of adsorption systems

The following sections should give the reader some general informations about the theory of Thermodynamics of chemical reactions which are necessary for the understanding of this work. The reader should get some deeper understanding for applied analytic tools which were important for simulation and understanding of the investigated adsorption systems.

Within the last centuries scientists tried to find correct descriptions for thermodynamical systems, which were suitable in their handling giving insight into the thermodynamics and kinetics of occurring processes. Especially the thermodynamic formulation of transition states during reactions where of crucial importance for the understanding of occurring reactions. This theory for understanding was given by the Transition-State theory by Wynne-Jones and Eyring, which is discussed in Literature [32]. But what does an activated complex, respectively a transition state mean? In the prior part an activation barrier or energy for a chemical reaction was mentioned often. This barrier could be understood as the amount of energy a system has to overcome to drive a certain reaction. The energy could be introduced into a system by many ways e.g. thermally or by irradiation with light. The connection between the free energy of reactants, products and the transition state will be clearer in the following sketch 2.7:

We can see in this figure that the free energy between the reactants and the products are different. In this special case we observe a change of the standard internal energy ΔU^0 between the initial and the final-state of $\Delta U^0 = -100\ Kcal/mol$. To reach the final state the reactants have to pass through the transition state. The transition state could be understood as an activated complex and its standard internal energy U^0 is much higher than that of the initial state. Therefore, the free energy change of this reaction path is $\Delta U^0_{TST} = 300\ kcal/mol$. This is the activation barrier the reactants have to pass for their reaction pathway. The rate constants for such a process can given by Eyring theory as follows [32]:

$$k = \frac{k_B T}{h} K_c^+ \tag{2.35}$$

K_c^+ is thereby the concentration equilibrium constant of an activated complex and its variation with temperature is defined as

$$\frac{d(ln\ K_c^+)}{dT} = \frac{\Delta^+ U^0}{RT^2} \tag{2.36}$$

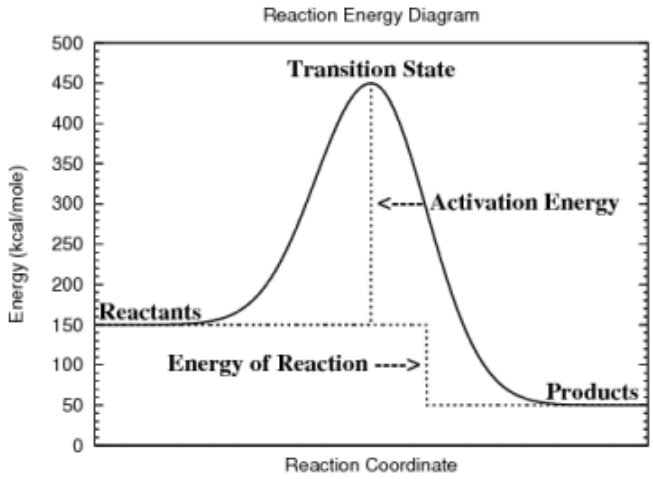

Figure 2.7: Activated complex in Transition State Theory. The figure shows the different energy levels of the initial, the transition and the final state of a chemical reaction. In case of the shown reaction path the final state is energetically more favored which makes this reaction path more likely.

Δ^+U^0 is the standard change of the internal energy between ground and transition state and is the by theory calculated value for the dissociation barrier. By taking Equation 2.35 and 2.36 we get for the rate expression in this case

$$\frac{d(ln\ k)}{dT} = \frac{RT + \Delta^+U^0}{RT^2} \tag{2.37}$$

For a better understanding of the value of Δ^+U^0 its connection to the standard enthalpy of activation is given by $\Delta^+H^0 = \Delta^+U^0 + P\Delta^+V^0$. The quantity Δ^+V^0 is called the standard change of volume between the initial state and the transition state. In case of a single molecular reaction (which is the interesting case for us) there is no change of volume in the activated complex and the equation reduces to $\Delta^+H^0 = \Delta^+U^0$.

Now we have a valuable definition for the chemical rate constants of a certain process. The problem was to connect empirical parameters to this formalism. From 1850 - 1900 several equations, derived from Van't Hoff's Three-Parameter equation, tried to solve the problem of connecting real parameters to the undefined parameters of Van't Hoff. The Three-Parameter equation was :

$$k = AT^m e^{-\frac{B-DT^2}{T}} \tag{2.38}$$

We showed already in the section of adsorption and desorption of molecules that the Arrhenius equation was the only surviving one-parameter equation (as a simplification

of Van't-Hoffs formula). It is already given in Equation 2.3:

$$k \; = A \; e^{\left(-\frac{E_{\mathrm{Act}}}{R \cdot T}\right)} \tag{2.39}$$

This equation is called the Arrhenius equation and describes the quantitative dependence of the rate-constants on an activation energy E_{act}. T is the temperature and R is the gas-constant. Furthermore, the Arrhenius expression includes the pre-exponential factor A. From the collision theory in a gas it can be understood as the total number of collisions between molecules per second. Either they react or not. The factor has some temperature dependency but the relatively small changes of A in an experimentally investigated temperature range allows the rough assumption of A being temperature independent.

However, the Arrhenius expression of a rate constant was not the best expression. But it has been shown that the energy E_{Act} in the Arrhenius equation is related to the height of the reaction barrier ΔU^0_{TST}, as shown in Figure 2.7. Thus experimentalists had a tool to describe their empirical observation and connect them to thermodynamic quantities.

Nevertheless we have to compare this practical treatment of an activated process with a theoretical description of such a system. This is necessary for understanding and comparison of theoretically calculated values to experimentally derived values. In the following thesis we will often compare our results to theoretical work which has investigated the same system. Unfortunately, there will often be differences between both cases. Comparison of the math behind can help to constrain the deviations between both.

The expression in Equation 2.39 could also be written as:

$$\frac{d(ln \; k)}{dT} \equiv \frac{E_a}{RT^2} \tag{2.40}$$

Comparison of the Arrhenius expression in Equation 2.40 with the theoretically derived description in Equation 2.37 gives for the activation energy by Arrhenius:

$$E_a \; = \; \Delta^+ U^0 + RT$$

Because $\Delta^+ U^0$ (respectively $\Delta^+ H^0$) is the theoretically calculated barrier, experimentally derived values will have a difference of RT to calculated values.

Experimental determination of a rate constant is done by monitoring the changes of concentration in a time interval of a certain molecule in order to the reaction temperature. By using the Arrhenius plot method we derive certain parameters from the measured data like the activation energy of a process. To do so we plot ln(k) of 1/T. In case of a temperature independent pre-exponential factor the data points

should be plotted on a line. If that is the case it seems reasonably to conclude that the given assumptions are correct. By fitting the plot with a linear fit we derive out of the slope the activation energy E_{Act}. The practical treatment of the data and the method will be shown later. We use this method for the analysis CH_2 conversion on a Ru(0001) surface.

Next, we wanted also to learn something about the population of different reaction states during a reaction. This is done by setting up rate equations for a certain process which couple the rate-constants to the rate of a reaction and therefore to the population of the different states.

2.4.1 Chemical rate equations and reaction kinetics

As it is clear from the description of the TPD and SFG, our spectroscopic tools allow us to gain some insight into the population of molecules at the surface. TPD gives us information about the total coverage at the surface which is monitored by desorption. Unfortunately, it has the disadvantage that possible intermediate states at the surface could not be distinguished. These intermediate states are of special interest for the investigations of hydrocarbon conversion. On the other hand SFG as vibrational spectroscopic technique gives us information about the different population of molecules. This quantitative insight is based on the connection of the observed signal intensity to the number of molecules ($I_{SFG} \propto n^2$). To understand the population of different kinds of molecules a formalism for simulation and analysis of the signal would be useful, which connects thermodynamic quantities with observable parameters. This tool is given by chemical rate equations which allows the simulation of the kinetics of a certain reaction. The rate of a reaction is given as [32]

$$v_i \;=\; \frac{dc_i}{dt} \;=\; \sum_{j=1}^{N_R} \nu_{ij} k_j \;\prod_{k=1}^{N_j} c_k^{\nu_{kj}} \tag{2.41}$$

In Equation 2.41 v_i is the reaction rate and c_i is the concentration of certain species. ν_{ij} are the stoichiometric coefficients of species i of a reaction. k_j is the rate-constant and N_R is given by the number of occurring reaction steps. N_j is determined by the number of products. Equation 2.41 is the most general form of a chemical rate equation. In a more practical way we will adopt this general expression for a more specific description of the reaction.

$$[A]\;[B] \;\rightleftharpoons_{k_{diss}}^{k_{reac}}\; [C] \tag{2.42}$$

Equation 2.42 describes a generic reaction with no intermediate steps where two reactants are combined to form one product. These kinds of coupling reactions often

takes place at surfaces. Because these coupling reactions will reach an equilibrium we must also include the pathway of a back reaction. The certain equilibrium state (where forward and backward rate are equal) of such a reaction is determined by the height of the reaction barriers between the both states as well as the relative free energy of the states. Therefore the barrier for forward and backward reaction will normally not have the same size, because the free energy of both states is different.

If we apply Equation 2.41 on a reaction as shown in Equation 2.42, the time dependent concentration of the reactants is given by

$$v_{A,B} = \frac{d[A][B]}{dt} = -k_{reac}[A]^x[B]^y \tag{2.43}$$

The general idea of putting up a rate-equation can be described as follows. Information about some parts of the system like the rate-constant, which can be determined experimentally, allows you to predict the speed of a certain reaction. If the rate equation formalism accurately describes the underlying chemistry of a certain reaction the predicted rates should agree with experiment. Therefore, the rate equation enhances the understanding of the system.

The main part of information is included in the rate-constant. Information about this parameter allows a better insight into the system and its limitations. Furthermore it allows to model the reaction path and predict certain stabilities of molecules in order of temperature or time.

2.5 Experimental setup

Above we have learned the theoretical background of physical and chemical processes investigated within the frame of this thesis. In the following part I will describe some technical details with a particular emphasis on nonstandard techniques. The dissociative sticking of methane or water under UHV conditions or the required laser system for high resolution spectroscopy of the different adsorbed species gave us a detailed lists of requirements for the experimental setup. In the following sections the reader will be introduced into the different technologies we were using to reach the aim of a detailed understanding of the occurring processes.

2.5.1 The UHV setup

Most of the performed experiments during this thesis were done under UHV conditions. The vacuum in our ultra high vacuum (UHV) setup was created by pumping a stainless steel chamber with a series of connected pumps. These were, in order, a membrane pump for a pressure of about 1 mbar followed by two turbomolecular pumps. With

these pumps the chamber can reach a base pressure of $2 \cdot 10^{-10}$ mbar. By starting at ambient conditions this process can take even weeks. A common way of shortening this time is by heating of the chamber to elevated temperature (approx. 120 C) and keep it at these temperatures for at least 24 hours. By increasing the temperature of the chamber you exponentially increase the desorption rate of adsorbed molecules at the walls of the chamber. This will reduce the pressure at low chamber temperatures. The pressure in the chamber was monitored in the pressure range from 10^{-4} to 10^{-10} mbar by a Bayard-Alpert ionization pressure gauge.

Attached to the chamber were several devices for investigation and preparation of clean surfaces in UHV. For dosing the gases (e.g. CH_4, D_2O, Ar, CO etc.) we have the ability to choose from three different sources. For a temporarily increase of the background pressure we use a commercial leak valve to increase the background pressure. For more controlled dosing in UHV we employed a pinhole dosing system. It can be positioned in front of the sample and dose through a 5 μm hole. By doing that you can reach locally a 10 times higher pressure at the surface than you have as background pressure. This reduces poisoning of the UHV by adsorption of the dosed gases on the walls of the chamber [52].

As a third dosing technique we connected to the chamber a three-stage supersonic molecular beam source (MBS) based on previously published designs [53, 54]. This source was necessary to enhance dissociative sticking of certain gases in the UHV, where normal dosing methods would not be successful for chemisorption. Details of this source will be given in the next section.
To quantify the total number of molecules on a surface we applied TPD spectroscopy as an additional technique. Therefore a feulnercup quadrupole mass spectrometer (LM500, Spectra) was attached to the UHV-chamber. For testing the quality of the sample cleaning and preparation procedure a combined 4-grid LEED/AES spectrometer (ER-LEED digital, VSI) was used. For cleaning purposes of the sample a Sputter-gun for sputtering the sample with Ar^+-ions was mounted on the chamber. The UHV chamber was connected to a laser table to enable SFG measurements of samples in vacuum. Figure 2.8 should give an overview about the mounting of the different parts to the UHV chamber.

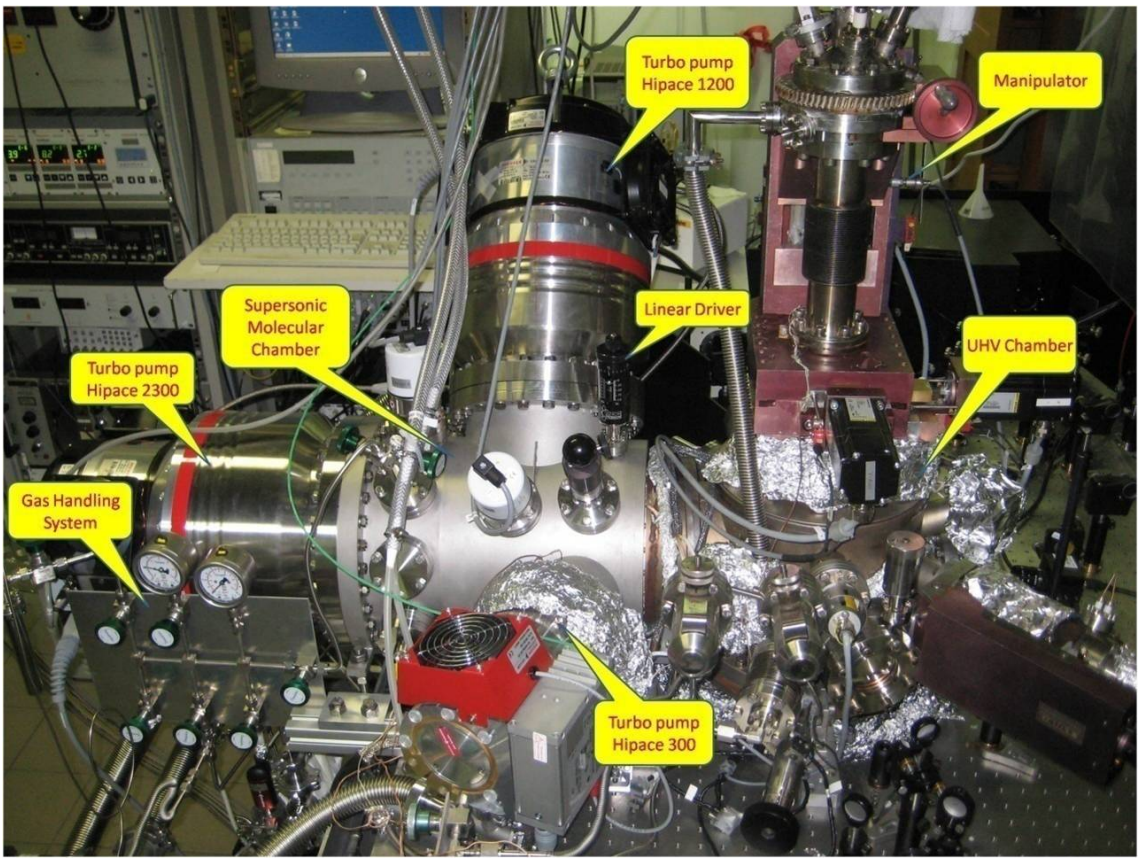

Figure 2.8: UHV setup used in our lab. Generally, the setup could be described in two parts. On the right side, we can see the UHV chamber, where analysis of our samples was performed. On the left side, we can see the molecular beam chamber, with its attached pumps. As you can see, three turbo pumps of different size differentially pump the MBS . This differential pumping decreases the partial pressure between each chamber in the MBS dramatically and hinders main chamber poisoning. Figure taken from literature[55]

2.5.2 Sample mounting and preparation

In this section I will describe the preparation procedure of the Ru(0001) and Al_2O_3 samples, to end up with a well defined sample surface free of contaminations. Both types of samples were fixed to a copper sample-holder (see Figure 2.9), which is mounted to a cryostat and connected to a manipulator that allowed movement in to x, y and z direction with computer controlled stepper motors. Furthermore we were able to rotate the cryostat and therefore the sample for 360°. Between the copper legs of the sample holder the samples were clamped by wires or on a foil to increase thermal conductance. The middle post of the sample holder depends on a solid copper block. The end of this block was mounted to the cryostat (see Figure 2.9). The side of the copper block which is in contact with the cryostat is highly polished and covered by a thin gold foil to guarantee good thermal conductance. This was important for sample cooling.

For several measurements resistance heating of the sample was important. Therefore we needed the copper legs electrically isolated (between which the samples were mounted) to apply a voltage and current to them. This would heat up the wire or foil where the sample was mounted to. Therefore the copper legs were electrically isolated by a thin sapphire plate from the middle post copper block. The reason for electrical isolation is based on the fact that the cryostat was electronically grounded over the UHV chamber. For preparation of the Ru(0001) sample temperatures above 1250 K were necessary. This was not possible with our resistance heating unit. To overcome this problem an Electron beam heater was mounted behind the sample. By this we were able reach temperatures of 1550 K by electron impact on the sample. The sample was grounded and in close vicinity of the filament heated by a current of 3.5 A and set to a negative potential of typically -1000V. [39]

Ru(0001)

The Ru(0001) single crystal used in experiments was circular (2mm thick, 8mm diameter) and cut from a single crystal rod. It was polished until reaching an accuracy of ≤ 0.5 °[39]. The sample was clamped by two tantalum wires to the holder as shown in the Figure 2.9. By this mounting we were able to reach temperatures between 120K-1500K by cooling with liquid nitrogen and by heating. Temperature control was done by two pairs of k-type thermocouples which were spot wielded to the edge of the sample.
The Ru(0001) crystal was cleaned before all measurements by 20 min Ar^+-sputtering. The Ar-ions were accelerated by a potential difference of 500 V. The sputter current which was observed during sputtering with a Fluke power-meter was ≈ 5 μA. As

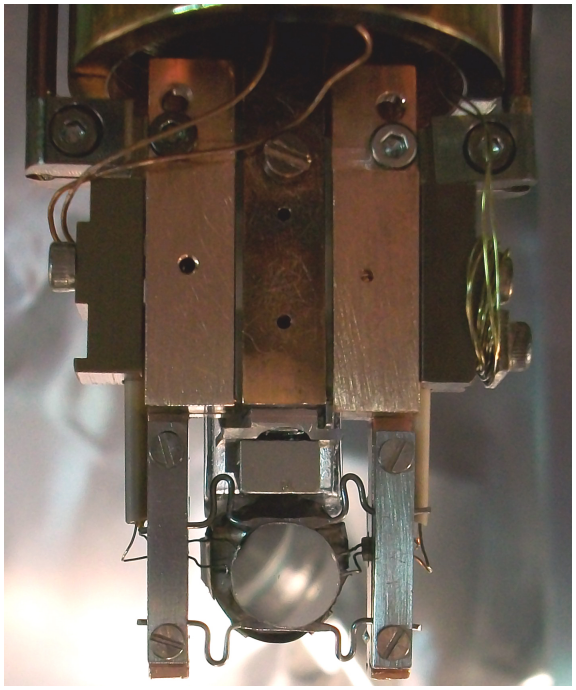

Figure 2.9: Photograph of the copper made sample holder. In this case, a Ru(0001) single crystal was mounted to the holder by two tantalum wires. Figure taken from [39]

a typical gas pressure we used 10^{-5} mbar of Ar as background pressure for the sputtering process. After sputtering we annealed the sample at 1260 K for 10 minutes in a 10^{-7} mbar oxygen background pressure. High temperature annealing in oxygen was required for two reasons. First of all the annealing process reduces the roughness of the sample by a reorganization of the surface structure. Doing this in an oxygen atmosphere has an additional advantage. It has been shown that subsequent annealing of Ruthenium guides to a situation where carbon from the bulk diffuses to the surface [56]. This can hinder or reduce the reactivity of such a surface. By keeping an oxygen background pressure during annealing the carbon gets oxidized to CO which immediately desorbs. Finally the cleaning cycle was finished by heating the crystal up to 1510 K and cooling it afterwards. It has been shown by prior workers that such a preparation creates a well defined, (by sharp hcp-LEED pattern) carbon free and defect less surface[57]. After such a treatment the sample was ready for investigation.

α-Al_2O_3(0001)

For the investigation of the α-Al_2O_3(0001) in UHV we require a sample mounting that allows to control temperature between 130 and 1200 K. This temperature region is determined by needed temperatures for sample preparation.This was done by

following previous authors and create a *sandwich* of two α-$Al_2O_3(0001)$ crystals attached to a 0.01 mm thick Tantalum foil. They were secured by Tantalum clips [58]. The tantalum foil was clamped between the two copper-legs, shown in Figure 2.9. The rest of the mounting stayed the same as before.

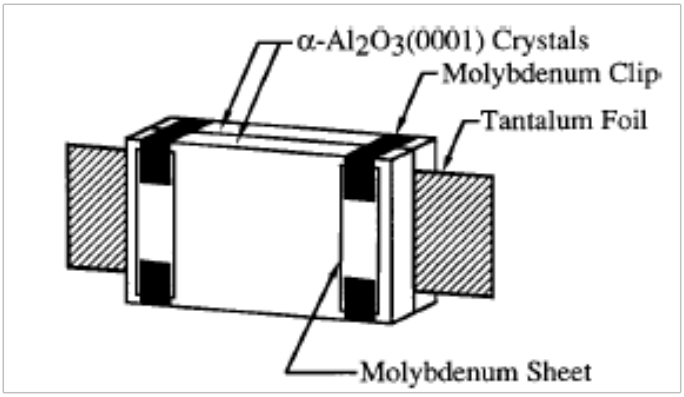

Figure 2.10: Schematic view of sample mounting in case of $Al_2O_3(0001)$ crystal. We followed previous workers on this topic and adopted their way of mounting to our setup by clamping two crystals on a thin Tantalum foil. Figure taken from literature [58]

The α-$Al_2O_3(0001)$ interrogated in this arrangement was a high surface area dimension of commercially available 10 x 15 x 0.5 mm^3 crystals and polished on one side with a roughness < 0.5 *nm* (Princeton Scientific Corp). Analog to the Ru(0001) sample setup measurement of the sample temperature ($T_{Al_2O_3}$) was done by two Chromel/Alumel thermocouples, which were attached to the crystal edges with ceramic glue (Cerabond 605). The thermocouples were connected to a temperature controller (Model 340, Lakeshore). The temperature controller was also connected to a resistance heating unit. By attaching two thermocouples to the crystal‘s opposite sides we ensured that the sample was heated homogeneously (temperature differences in the plane of the sample surface are < 5 K).

For sample cleaning and preparation we adopted previously reported recipes that have been shown to produce a (1×1) Al-terminated surface [58, 59]. This surface has been found to be the thermodynamically most stable arrangement of an $Al_2O_3(0001)$ under UHV conditions, which is also in agreement with theory[21]. Because of constraints of our technical equipment we changed the prior recipes slightly. For being confident with the result of preparation e.g. a carbon free and well defined (1×1) Al-terminated surface we used the the combined 4-grid LEED/AES spectrometer (ER-LEED digital, VSI) to check the quality of our prepared samples.

Before mounting the sample in the UHV chamber we placed it for 30 minutes

in a supersonic bath with methanol, dried it with Nitrogen and then rinsed it with milli-pure water for 30 minutes. Mounting this sample in the UHV with no further preparation produced a sample surface containing carbon contaminations in Auger Electron spectroscopy (AES). To remove the carbon we sputtered the sample with 1.5 KV and 3 x 10^{-5} mbar Argon for 30 minutes at different spots. Sputtering at such voltages has been shown to produce oxygen vacancies in this surface [59]. Therefore we annealed the sample at 1040 K for 30 minutes in an atmosphere of 5 x 10^{-6} mbar of Oxygen. Figure 2.11 shows that this treatment leads to a sample that produces a sharp (1×1) diffraction LEED pattern and shows no carbon contamination in an AES measurement.

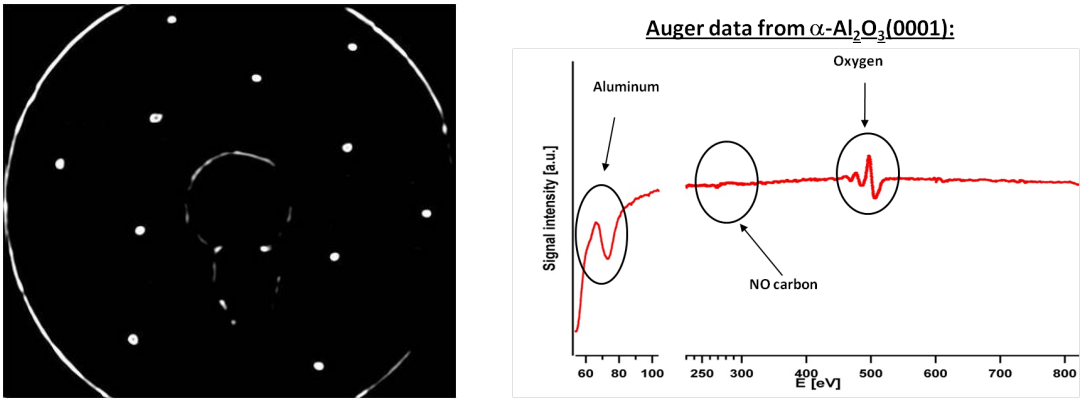

Figure 2.11: (left)LEED and (right)Auger spectra of a sputtered and annealed α-$Al_2O_3(0001)$ crystal; LEED spectrum is taken at 118 eV. As it is clear from the picture, the LEED spectra show a nice (1×1) structure, which could be attributed to the Al-termination of the surface. This pattern has been observed already for this surface by others [58, 60]. (right) Auger spectra of sputtered and annealed sample show the typical lines of Aluminum and Oxygen.The resonance of carbon at 284 eV is absent

α-$Al_2O_3(1102)$

The third kind of sample we investigated was α-$Al_2O_3(1102)$ single crystals. Generally, the sample was treated equally like the α-$Al_2O_3(0001)$. Therefore I will not repeat the mounting and preparation way and conditions. After preparation we took similar to the α-$Al_2O_3(0001)$ a LEED spectrum to crosscheck the surface structure as well as an Auger spectrum to check for impurities at the surface.

Figure 2.12 clearly shows the characteristic LEED pattern of the α-$Al_2O_3(1102)$ surface. In contrast to the (0001)-surface the 1x1 structure apparent from the figure has its origin in an oxygen termination of the surface.

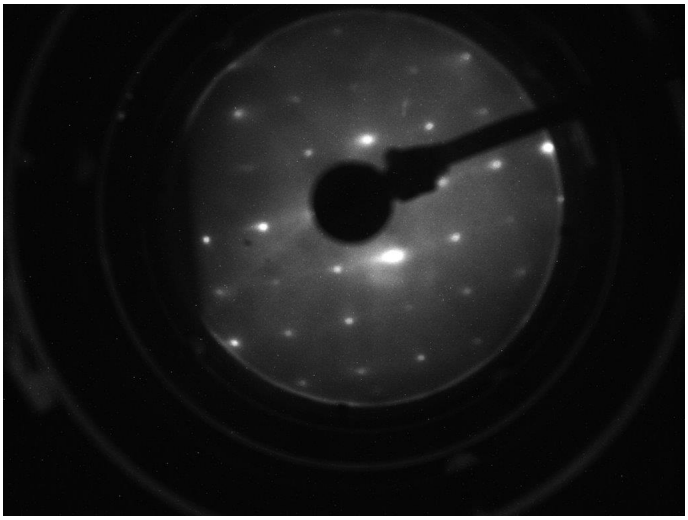

Figure 2.12: LEED spectrum of a sputtered and annealed α-Al_2O_3(1102) crystal; LEED spectra is taken at 120 eV. The LEED spectra show a nice (1×1) oxygen terminated structure. This pattern has been observed by others for this surface [58, 60]. Auger spectrum of such a sputtered and annealed sample shows the typical lines of Aluminum and Oxygen and the AES looked similar to this of the (0001) surface.

2.5.3 The molecular beam source

As mentioned a three stage molecular beam source (MBS) was attached for dosing purposes to our UHV system. In Section 2.2.1 we already discussed the problem for some gases to create significant populations of dissociatively adsorbed molecules under UHV conditions. As an example I have emphasized with Figure 10.1 that dissociative sticking could sometimes be just possible in UHV if certain gases have already some higher internal energy.

We applied for this purpose a MBS in our setup. The idea behind this source was to generate an adiabatic expansion from a high temperature nozzle. The gas molecules dosed at the surface will have a high kinetic energy. The enhanced kinetic energy of the molecules will help to overcome the initial adsorption barrier for dissociative adsorption. The dissociative sticking coefficient i.e. the adsorption probability for a single molecule could be increased by this method by about 5 orders of magnitude between 300 K and 800 K of nozzle temperature at a fixed surface temperature [12].

Because we were not interested into the exact kinetic energy of our dosed gases we just used the setup qualitatively/intuitively for the dissociative adsorption. Therefore, I will skip the details of its construction and the full thermodynamic description of this process. It is just important to mention that we were able to gain dissociative adsorption of methane and water in our system under a certain setting of the MBS .

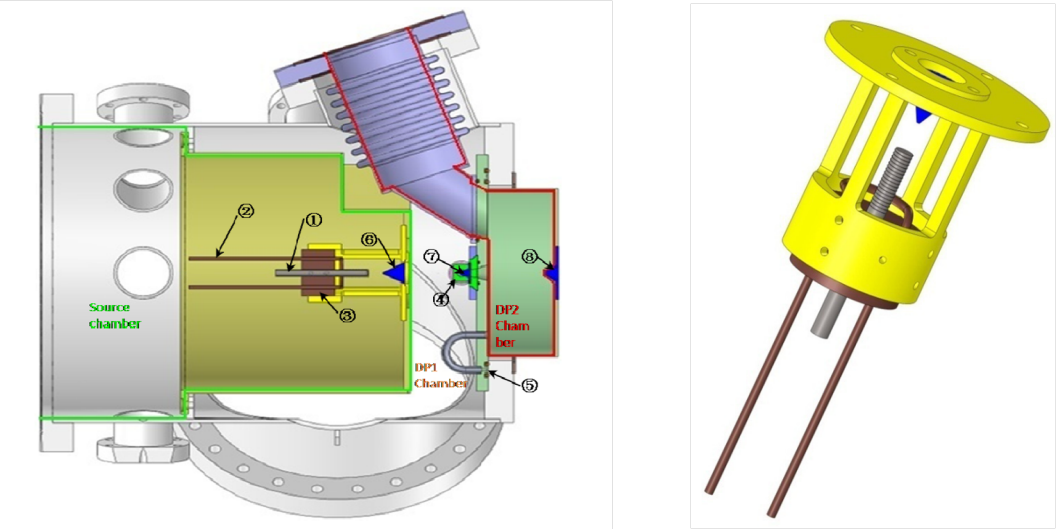

Figure 2.13: drawing of the MBS, used in our setup. The Molecular beam chamber is divided into three different chambers which are all differentially pumped by turbo-pumps. The three stages of the MBS are separated by skimmers with a diameter of about 1 mm. Because of this small diameter always most of the cone shaped beam from the nozzle will be cut by the skimmer and a small fraction can pass through. This has the effect that between the different stages of the source there will be a pressure difference of several orders of magnitude. By such a treatment a molecular beam of a diameter of about 8mm [55] enters the main chamber for analysis. The partial pressure increase in the analysis chamber during dosing is too small for poisoning of the vacuum chamber. The nozzle itself is made by titanium and covered by ceramic glue (Cerabond 605). Finally it is surrounded by a heating wire. The maximum nozzle temperature reachable in this design is 950 K.

This will be mentioned later in the relevant section.

Nevertheless, I want to discuss at this point the difference of a MBS to a high pressure cell (HCP) for sample preparation. Others overcame the problem of dissociative adsorption by usage of a HCP for methane adsorption on transition metal surfaces [8, 9]. Unfortunately this preparation technique of radicals at surfaces allows just the generation of thermally equilibrated dissociation species. This could be a problem if one is interested in initial dissociation steps of molecules. It has been found that methane has on Ruthenium a surface temperature dependent sticking coefficient[12]: at higher surface temperatures the chance for dissociative sticking is much higher than on colder. This trend can be rationalized by noting that in this scenario the surface provides the necessary energy for the C-H bond-breaking (as shown in Figure 10.1), if a molecule comes near enough to the surface to be trapped by the surface potential. Under UHV conditions it is rather unlikely that a CH_4 molecule dosed at the surface without kinetic energy will come near enough to the surface to adsorb. This happens because the density of gas molecules at

low pressure is quite small e.g. the repulsion of the molecules to each other is much smaller than the repulsion from the surface potential. It is energetically more favorable to stay in the gas phase. Of course, the dissociative sticking coefficient is not equal zero. On the other hand the relatively small amount of impinging molecules together with a sticking coefficient of 10^{-12} emphasizes that nearly no dissociative adsorption will happen in human lifetime. This situation changes if you increase the pressure of CH_4 by a factor of 10^{10}. Even a tiny sticking coefficient of 10^{-12} will create adsorbed species because of the huge amount of gas-molecules. But the molecules will be in thermal equilibrium with the surface. The needed energy for the initial dissociation step will be completely provided by the substrate. Because the initial barrier is quite high elevated surface temperatures helps in this case the dissociative sticking. But after the first dissociation step the surface can still transfer energy to the molecule. Depending on the surface temperature this induces further dissociation. In case of the MBS the gas-molecules will get some parts of the needed energy to overcome the initial barrier directly by the source (what implies that a lesser surface temperature is needed).This energy is gone after the first dissociation. This effect is of certain interest for us, because of the creation of a metastable and non-equilibrated distribution of dissociated species. Watching it to return to equilibrium with an increasing temperature allows us to evaluate the kinetic barriers of conversion. Therefore we learn something about the thermodynamics of the system.

2.5.4 The Laser setup

After all the information about the SFG spectroscopy it is now time to introduce the Laser system which is required for the spectroscopy. The exact process of pulse generation and the full description of the laser itself is already intensively discussed in previous theses of other authors[39, 61]. Therefore, I will briefly summarize the key points of the setup in this section. The generation of the intense ultrashort 800 nm pulses bases on a commercial Ti:sapphire oscillator (Vitesse; Coherent, Inc.), which seeds a regenerative and multipass amplifier (Quantronix-Titan II-amplifier; Quantronix/ Excel Technology Europe). For pumping the amplifiers we employ two pulsed Nd:YLF lasers from Quatronix.

Ti:sapphire laser are widely used solid-state lasers. This is the case, because of its strong adsorption band around 490 nm and its spectrally broad fluorescence (670-1070nm).[62] The absorption at $\approx$ 500 nm allows the pumping of the lasing medium by an argon or a frequency-doubled Nd:YLF laser. the latter one was the case in our setup. Normally, the amplification of a Ti:sapphire reaches its maximum

at around 800 nm.

Using this amplifier system we generated 800 nm pulses with an approximate pulse length of 110 fs at 400 Hz. The delivered pulse energy was 4 - 4.5 mJ. 70 percent of this power was used to pump an OPG/OPA (Light Conversion) providing tunable broadband-IR pulses (bandwidth 130-150 cm^{-1} (FWHM)) with energies of 10-15 μJ and duration of $\approx$ 150 fs. The residual 800 nm pulse from the OPA/OPG process was used for creation of the 800 nm up-conversion pulse by spectrally narrowing it in a homebuilt pulse shaper (shown in Figure 2.14). By doing this we obtain pulses of 0.3 - 1.1 nm in bandwidth (verified using a fiber spectrometer, HR2000+; Ocean Optics). The different bandwidth have their origin in different used pulse energies (e.g. different slit-width in the pulse shaper as shown in Figure 2.14) for SFG at the two samples.

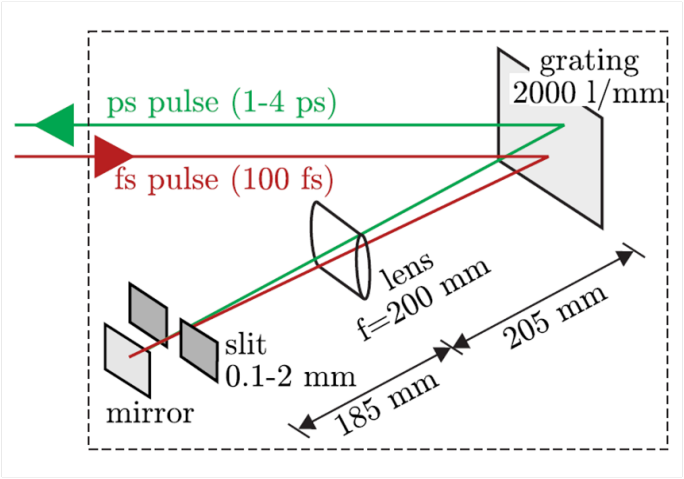

Figure 2.14: Schematic view of our homebuilt pulse-shaper, used in our Laser setup. The incoming short laser-pulse get dispersed at a grating into its frequency components (Vis pulse Gaussian shaped between 790-810 nm). By moving the slit we can choose the center-frequency of 800 nm of the dispersed pulse and with the slit-width we determine the energy of the chosen pulse. With increasing slit-width we increase the pulse energy by taking more frequency components, which were not exactly 800 nm. Thereby we increased the bandwidth of the VIS pulse (e.g. decrease of resolution of the setup). Scheme taken from [39]

After generation, the IR and shaped 800 nm (hereafter abbreviated VIS) beams were propagated through a $\lambda/2$ wave plate, certain polarizer combinations and were focused on the surface with certain incident angles. The appropriate choice of the geometry we wanted to perform measurement in the UHV chamber depended on the general aim of the measurement. As has been already discussed in Section 2.3.4, the measured SFG intensity of a certain resonance depends on the molecular orientation and the experimental geometry, e.g. the incident angles of the the

IR/VIS. If the molecular orientation is known, possibly by calculation, we were able by the in Section 2.3.4 described mechanism to predict the intensity of a vibrational response depending on the experimental geometry. Our UHV main chamber provides two different geometries for SFG spectroscopy. The common used geometry has incident angles of 70° and 75° (geometry 1) for IR/VIS. Furthermore we can also perform measurements at 37° and 35° (geometry 2), relative to the surface normal. Additional geometries were not possible because of the limited number of flanges with view-ports. In nearly all cases we performed our measurements at geometry 1 and ppp-polarization, because the signal intensity were the best and the handling of the system was easier. Later on I will always mention at each dataset the experimental frame behind this measurement.

After generation the SFG signal on the sample in UHV, the light is collimated, propagated through a $\lambda/2$ wave plate, a polarizer combination and several filters to remove the reflected VIS light. Then it got focused into a spectrometer and dispersed,via a grating (1800 g/mm) across an ICCD camera (Princeton Instruments). Because the spectrometer did not directly connect the dispersed signal to a certain wavelength it was necessary to calibrate the spectrometer. The calibration of our spectrometer was done using a LOT Pen-Ray Ne-lamp, which has known emission lines in the spectrum. With this emission lines we were able to connect a certain wavelength to each pixel on the CCD chip. The exact termination of the center-frequency of our 800 nm up-conversion pulse allowed to relate a distinct IR-frequency to the measured SFG wavelength. This was possible because of the already shown and explained energy conservation for the SFG process (as shown with Formula 2.16). As a crosscheck we could also directly observe distinct absorption lines of a polystyrene sample and calibrate the IR wavelength on the known absorption maxima of polystyrene. Both procedures gave the same IR frequency after calibration. Finally the experimental spectral resolution of our setup is determined by the bandwidth of our VIS pulse (as explained in the SFG section, because of a convolution of the bandwidth of the VIS pulse and the natural bandwidth of the resonance). The spectral resolution was 5-17 cm^{-1} for FWHM depending on the energy for up-conversion.

2.5.5 SFG measurements and data analysis

To finish the required background section for understanding of this thesis we will slightly discuss the way how data achievement and analysis has been done and what was the best way of SFG data fitting. Generally, the performance of SFG measurement requires several steps. The most important point is thereby to distinguish the contribution of the substrate in the measured signal from those of observed molecular

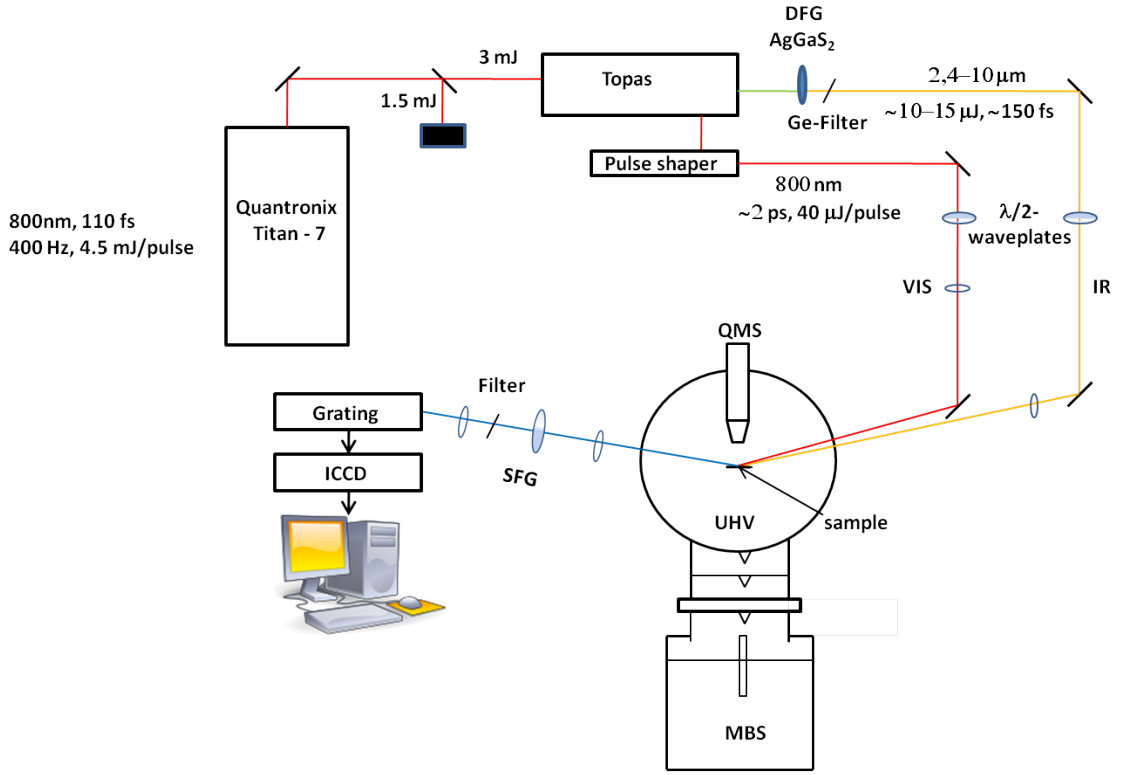

Figure 2.15: Schematic overview of the experimental setup. Shown is the experimental geometry 1, which was used for most of the measurements. In geometry 1 generally the used polarization combination was *ppp*. For geometry 2, *ssp* was the manner of choice.

responses. This is done by measuring two spectra (see Formula 2.27). The first spectrum thereby is the spectrum of the surface with the molecules attached to the interface. Afterwards the sample gets heated to elevated temperatures. This induces desorption of the molecules and the clean surface is left. Than a second spectrum was measured which is normally called the non-resonant background. This spectrum is due to the spectral shape of the IR-beam.

Analysis of the SFG data was done by fitting the data using Equations 2.44 and 2.45. This was done by using an implemented analysis program in Igor Pro (Wavemetrics). We constrained the fit by assuming the phase of the nonresonant contribution to be zero. In line shape analysis we further assume that the phase of each resonance is independent of temperature as long as we are performing the measurement always at the same surface temperature. In our fitting Algorithm we are able to constraint the fitting variables to certain region, which makes physically sense. The fitting algorithm optimizes afterwards these values for the best overlap between the fit and the data. Afterwards, the values for the best fit will be shown by the program in a table. For testing the sensitivity of the fitting program, we

fitted the data with initial guesses for amplitude that vary over several orders of magnitude and phases between 0 and 2π. It has been shown that the resulting fit is relatively insensitive to these choices. Initial guesses for ω_q that vary by > 35 cm^{-1} from a realistic value can lead to non-physical local minima. I will show here once again the fitting equation for the data, as already derived in the SFG-section:

$$I_{sfg} \propto \left|\chi^{(2)}_{eff}\right|^2 I_{vis} I_{ir} \tag{2.44}$$

$$\chi^{(2)}_{eff} \propto |A_{NR}| \; e^{i\phi_{NR}} + \sum_q \frac{A_q}{\tilde{\nu}_{ir} - \tilde{\nu}_q + i\Gamma_q} \tag{2.45}$$

Chapter 3

Methane(CH_4) and Ethylene(C_2H_4) decomposition on Ru(0001)

Life in first world countries requires access to many materials composed of specific longchain hydrocarbons. Often these materials have been synthesized from ethane and ethylene which was extracted from natural gas [138]. Because methane is $\approx$ 10x more abundant in natural sources than ethane or ethylene [138] an efficient manner of converting methane into either of these C_2 species (or of course even longer chains) is of high interest for industry. This causes that the prize per carbon atom from methane to ethane is doubled [82]. Therefore it is highly attractive to find energetically favorable and low cost ways for the conversion of methane to higher hydrocarbons. This is the reason why catalytic dissociation and coupling of methane and other hydrocarbons on various metals and oxides play an important role in many investigations of science and industry.

One of the first applications for industrial usage is for this the Steam-Reforming process (SR) of methane on Ru- and Ni-based catalysts. Thereby methane(CH_4) and water steam (H_2O) react under high pressure and temperature by formation of syngas mixtures containing carbon monoxide(CO) and hydrogen (H_2). This syngas could be later on used for formation of higher hydrocarbon in the Fischer-Tropsch synthesis(FT). During the FT synthesis CO and H_2 react on a catalytic active surface by formation of CO_2 and C_xH_y [181, 8, 10, 9, 117]. This process will be discussed more detailed in the next chapter.

Therefore many investigations in the field of catalytic dissociation on transition metal surfaces (Ni, Ru, Rh..) have taken place within the last decades. [8, 10, 9, 117]

Industry focused thereby on empirical optimization of these reactions to gain a high yield of C_xH_y compounds during the FT synthesis. Unfortunately, the conditions which have been found to give the best yield hinders the mechanistic understanding of the occurring reaction during the process. These conditions are large scaled reactors with high temperature and pressure as well as high surface area and defect rich catalytic substrates. One problem is the huge amount of possible C_xH_x combinations which hinders a complete understanding of surface reactions. The observation and identification of formation and dissociation steps and species during Steam-Reforming are one of the first steps to understand and manipulate the ongoing processes.

For approaching the understanding of the processes a simplification of the system is necessary. Therefore scientists used model systems like single crystals under UHV conditions to get insight in the molecular reactions on surfaces. In our case we used a Ru(0001) crystal. Ruthenium is the topic of this investigation because of its special properties. To be closer to the industrial approach Nickel catalysts would be the right choice. This is the favored material for steam reforming process because it is a cheap material. On the other hand it is known to have problems of deactivation by carbon poisoning. Ruthenium is much more expensive but it is the most active surface and much more stable. This makes it to a good model system under lab conditions. Furthermore it has been found that the chemistry and physics taking place at both surfaces for interaction with hydrocarbons are qualitatively the same[12, 118]. Here we focus on the reactions of methane(CH_4) and ethylene (C_2H_4) on the Ru(0001) crystal.

To emphasize the open questions of this system which will be the topic of this chapter I will show some problems of prior work on this topic. It is quite clear that the chemistry which is important for SR as well as FT cares about the addition or removal of hydrogen from various hydrocarbon compounds. Therefore, the investigation of the CH-stretching region is one of the most powerful tools for understanding the occurring reaction. It is clear that different CH-containing species have their characteristic resonances in this spectral region. These characteristic resonances should allow the correct assignment of the different products in a reaction path. Unfortunately prior work focusing on this field of reactions on single crystals had a poor resolution for resolving the ν_s of different C_xH_y species [9, 8, 10, 13, 85]. To be more specific by showing this lack of insight in a practical problem, let us focus on some work performed on CH_4 dissociation on Ru(0001) at elevated temperatures (T_{Ru} = 400 K-700 K) [9]. They observed two different sets of loss features in their high resolution electron energy loss spectroscopy measurements (HREELS) [9]. These loss features were attributed to the presence of CH and CCH_2 at the surface. CCH_2 (vinylidene) is concluded to be the coupling product of two CH

radicals. Unfortunately they were not able to identify the distinct ν_s of CCH_2 in the CH-stretching region which would be more than useful for a detailed understanding of the coupling reactions. The reason of interest in CCH_2 followed from the assumption that CCH_2 is the direct precursor for non-oxidative low temperature methane coupling for formation of C_2H_6 [85, 11, 67, 68, 63]. It is clear that there is still a lot of work to do for an detailed understanding of these comparably simple reactions in UHV. This understanding is without any doubt necessary as a framework for a correct description of more complex reactions on real catalysts under realistic conditions.

Compared to prior investigations one difference of this work was that it focused on the missed spectral assignments in the CH-stretching region. The high spectral resolution of the used vibrational spectroscopic technique (SFG) should allow to distinguish all different modes of different molecules at the surface. For the correct assignment of the species to the observed vibrational modes, the adsorption system of methane and ethylene were investigated. Both gases have some similar intermediates during dissociation. That makes it to a rational approach to compare the spectral resonances in their dissociation pathways what should allow the correct assignment of the different C_xH_x species and modes. Comparison of these adsorption systems together with a discussion of prior results by others should enable the complete identification of the occurring reaction steps.

3.1 Methane dissociation on Ru(0001)

3.1.1 Assignment of the CH radical

For an understanding and therefore control of methane dissociation it is important to start at surface situations which are easy to understand and interpret. Therefore the sample was prepared in a way, which have been found to show the spectral assignment of just one species at surface: the single CH-molecule. To create such a surface we followed reports of prior investigators. They saw a single resonance in their HREELS spectrum in the CH spectral region by preparation of their sample in a high pressure cell (HPC) at 350 K surface temperature. They connected it with the presence of CH-molecules at the surface, which in agreement with others [8]. In our case we used our MBS for dissociation of the methane and dosed 20 min CH_4 seeded in He at T_{Ru} of 350K. For the nozzle temperature 830K was chosen. At such a nozzle temperature the adiabatic expansion of the molecular beam will have enough kinetic energy to dissociate methane on the sample surface under UHV conditions, as already reported by [117]. The gas pressure in the nozzle was 4 bar.

After the dosing the surface temperature T_{Ru} was rapidly decreased to 100 K. The cooling rate was approximately 100 K per minute. At this temperature alignment of the SFG beam-line was performed. The frequency range of the IR wavelength was centered to the spectral region of CH at 3000 cm^{-1} [8, 118]. The IR beam had an energy of approximately 9-11 μJ and the VIS 9 μJ. With these settings the setup had a resolution of about 5-7 cm^{-1} in our measurements. Measurements of a sample prepared and analyzed in this manner gave the SFG spectra as shown in Figure 3.1. For all measurements within this chapter we applied ppp-polarization and geometry 1 for the incoming beam (75° and 70 °).

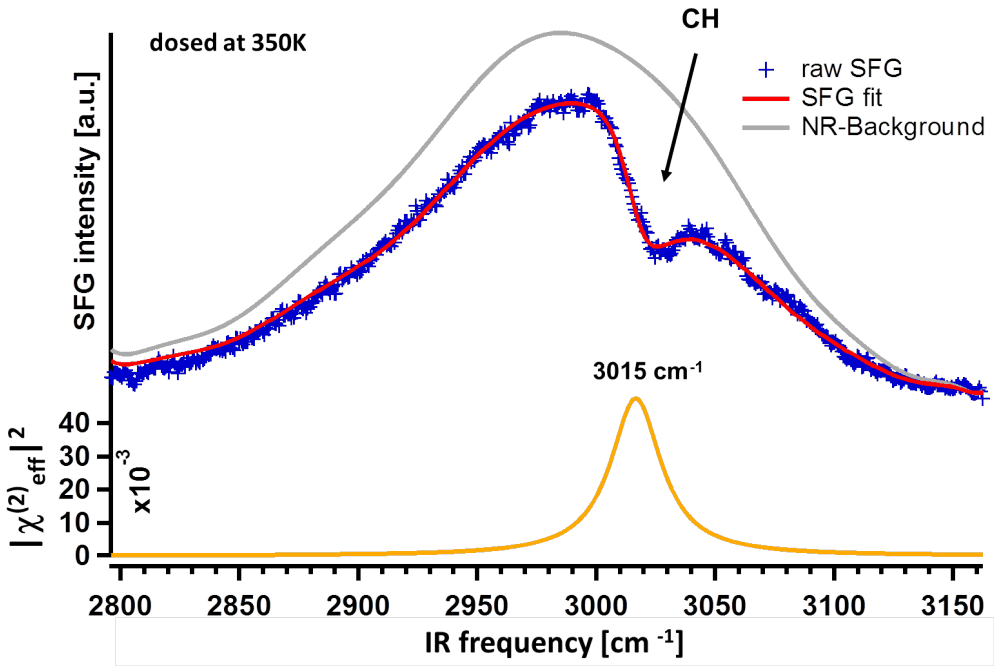

Figure 3.1: Spectrum shows CH species created by dosing methane with T_{Ru}= 350 K and T_{Nozzle}=830 K at the Ru(0001) surface. The SFG intensity is plotted over the IR frequency. The gray line corresponds to the non resonant background, the blue crosses to the experimental data and the red line to the fit of the data, done with the fitting model, given in Equation 2.45. The resonance at the bottom of the graph was given by the fitting model.

As you can see in Figure 3.1 the SFG signal is dominated by a single vibrational response which centered around 3015 cm^{-1} . This is in agreement with observations of others which reported the ν_s of CH at 3010 cm^{-1} on Ru(0001) [190, 8]. Prior work furthermore showed that CH is thermally stable up to 650 K [8]. We can thus test our assignment of the 3015 cm^{-1} resonance to CH by heating the sample to this temperature followed by cooling down to 110 K. Doing this the observed resonance was partially stable up to 600 K before it disappears. The disappearance could be explained by further dissociation of CH to carbon and hydrogen. Because of the

high surface temperature, the hydrogen desorbs, while the carbon remains and forms graphite/graphene [8, 9, 13]. From both the frequency and thermal stability of the resonance at 3015 cm^{-1} you can conclude that Figure 3.1 shows the spectral response ν_s of CH on Ru(0001).

Because knowledge of the carbon coverage of a sample is important for the understanding of spectral responses (as you will see later) the carbon coverage of the samples were checked after each measurement. This is done by relating a fully covered monolayer of carbon to a monolayer of carbon monoxide. For CO it is known that one carbon monoxide molecule adsorbs per Ru atom at the surface (1 ML = 1.58 x 10^{19} sites m^{-2} on Ru(0001) [12]). Carbon coverage was quantified after each measurement by dosing O_2 at 300 K followed by temperature programmed oxidation (TPO). The carbon at the surface will react with the dissociatively adsorbed oxygen by formation of CO, which then desorbs with increasing temperature. The desorbed CO was detected by our Feulnercup QMS. The number of desorbing molecules is proportional to the area under the desorption peak which got monitored by the QMS. Coverage calibration is finished by comparison of the TPO signal with the desorption signal of a saturated CO layer adsorbed at room temperature. This signal corresponds to 0.68 ML of carbon adsorption sites at the surface [150, 4]. To clarify our meaning of coverage once again: in the following sections it will be often talked about the coverage of CH_x molecules at the surface. One monolayer of carbon corresponds thereby to one CH_x molecule per Ru atom at the surface. This procedure is shown practically in Figure 3.2.

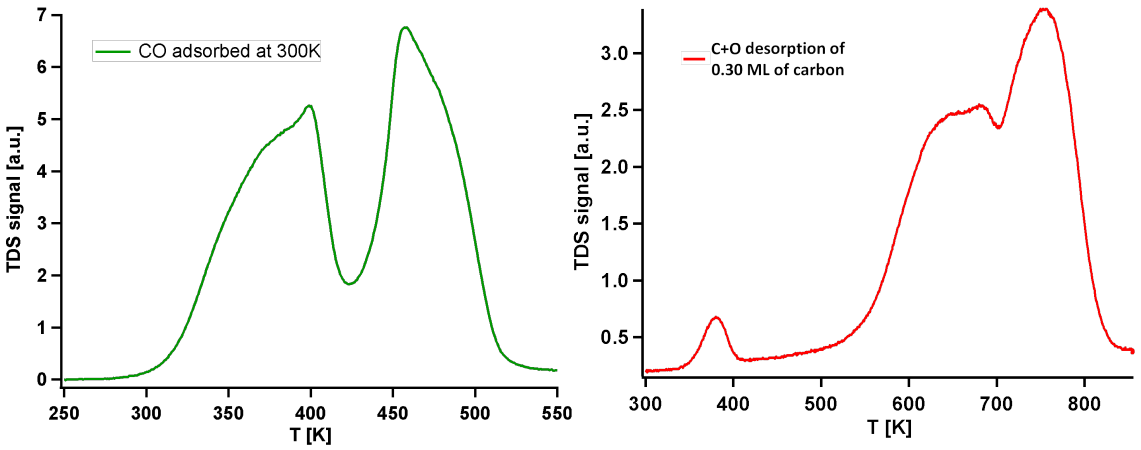

Figure 3.2: Figure a) show the thermal desorption spectra of CO, adsorbed on Ru(0001) at 300K. It show the typical double peak structure, as known from literature.[150] and corresponds to a surface coverage of about 0.68 ML or carbon. Fig. b) show the TPO desorption of the sample, shown in 3.1. Comparison to the CO desorption spectrum determine the sample coverage with about 0.30 ML of carbon.

Figure 3.2 a) shows the typical thermal desorption spectrum of a saturated layer of CO at room temperature. This saturation of CO corresponds to a coverage of 0.68 ML[150] and is used to calibrate the TPO spectra. Figure 3.2 b) shows the typical TPO spectra of a sample with a low coverage of carbon compounds (about 0.30 ML). After dosing of oxygen at 300 K, a heating ramp of 100 K/min was applied and the desorbing CO was monitored with the QMS. At this coverages one cycle of oxidation is enough to completely remove all carbon from the surface. In the case of higher coverages it is often necessary to repeat the TPO cycle several times for removal (and quantify) all carbon at the surface. The feature around 400 K in Figure 3.2 b) has its origin not in a C+O reaction at the surface but rather the molecular adsorption of CO from the background-pressure of the chamber.

3.1.2 Low temperature dissociation of CH_4 on Ru(0001)

After gaining knowledge about the correct assignment of CH at the surface (which is obviously just a first step) now the interconversion and formation of various C_xH_y species should be studied. On the one hand dissociation of methane at surface temperatures of 400 K or higher would be interesting. In this region more complex molecules have been reported[9, 10, 117, 106] but no spectral responses ν_s of the corresponding molecules beside CH have been found yet. On the other hand there has been no work performed for the observation of initial dissociation steps of methane on Ru(0001) which should take place at the surface temperatures below 350 K. That it should take place below 350 K is clear from the last section because dissociation of CH_4 at 350 K produces just CH at the surface: the end of the dissociation pathway of methane (CH_4 $\rightarrow$$CH_3$$\rightarrow$ CH_2 $\rightarrow$ CH) [11]. This subsection will focus on the dissociation of methane at low surface temperatures.

One reason why prior investigations of this system have not explored this portion of dissociation pathway is the low sticking coefficient of methane on a Ruthenium surface at temperatures below 300 K. Under these conditions Goodman and coworkers[9] observed hardly any dissociative sticking of methane in their HPC.

Information about surfaces temperatures at which CH_3 and CH_2 is probably stable can be found in literature. Zhou et al. [190] reported in their work that CH_3 on Ru(0001) was stable up to 190 K when it was produced by thermal decomposition of adsorbed CH_3I. At temperatures above 190 K CH_3 decomposed to CH_2 which was thermally stable up to 290 K. In case of higher coverages (35% of carbon or more) they reported also the presence of CCH_3 at the surface, which they explained as a coupling product of CH_2.

With this background we tried to modify our molecular beam source in a way that it is possible to access dissociative sticking at a surface temperature of 190 K. Therefore the temperature of the nozzle was increased to 970 K (which was the upper limit for our setup). This enhances the translational energy of the impinging molecules and therefore increases the sticking coefficient. A more detailed discussion of increasing sticking coefficients with nozzle temperature will be given in the next chapter where the low temperature dosing conditions will be investigated in detail.

Unfortunately, it was not possible to observe dissociative sticking at T_{Ru}= 190 K. So the surface temperature was increased during dosing to T_{Ru}=250 K. By dosing for 30 minutes at 250 K a clear and sharp response in the spectral region of CH could be observed, as you can see in Figure 3.3

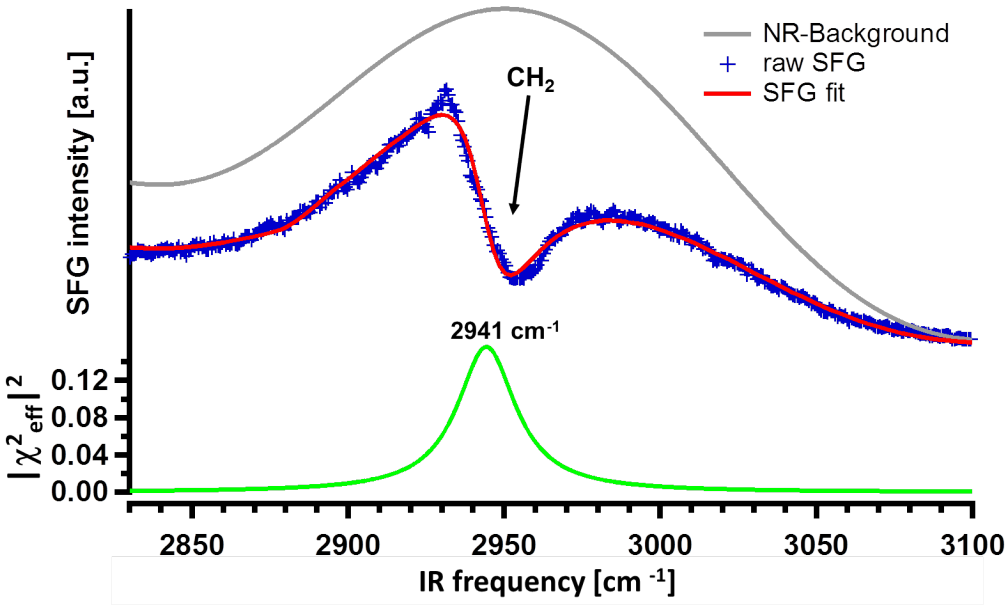

Figure 3.3: CH_2 (Methylene) species created by methane dissociation at the Ru(0001) surface. The SFG intensity is plotted over the IR frequency. The dosing conditions were T_{Ru}= 250K and T_{Nozzle} = 970K. The gray line is the non resonant background, the blue crosses the experimental data and the red line corresponds to the fit of the data, done with the fitting model given in Equation 2.45. The gas pressure in the nozzle during dosing was constantly at 4 bar. The identification of the resonance as the ν_s of CH_2 follows from the comparison to the related system in literature [144, 190]

First of all it should mentioned that such a resonance at this vibrational frequency has never been observed before by methane dissociation on Ru(0001). The center-frequency of this peak is at approximately 2940 cm^{-1}. The coverage of the sample has been determined by the same procedure as already described in the last section. By dosing for 30 minutes you reached a total carbon coverage of 15-18%. It is important

to mention that dosing longer further increased the coverage but the increase is just 2% by dosing twice the time. For the sake of completeness Figure 3.4 shows the TPO signal of a sample, prepared as described. In this case one oxygen cycle is enough for a complete removal of the surface carbon.

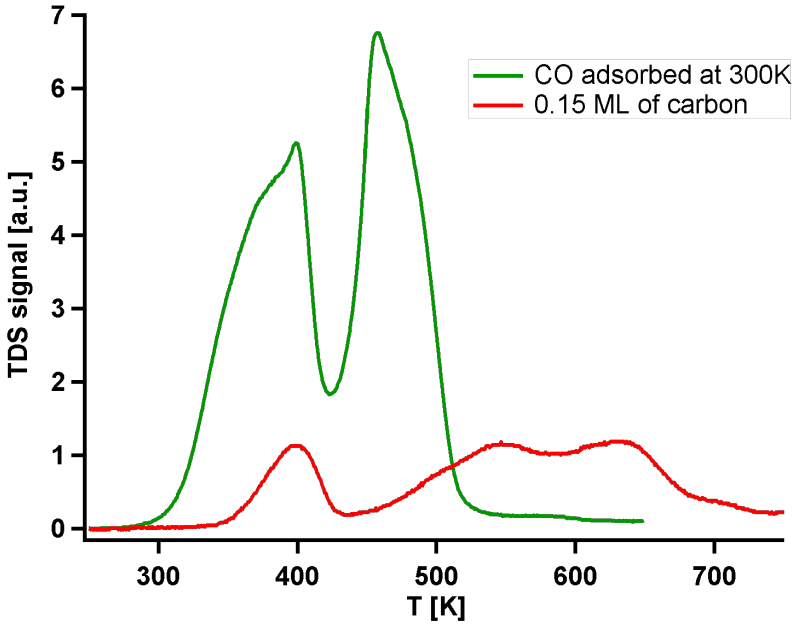

Figure 3.4: The figure shows the desorption spectrum of the C+O recombinative desorption of surface carbon. Compared to fig. 3.2 the desorption signal is much weaker. Once again the desorption feature around 400K has its origin in molecular CO, which got adsorbed from the background during the dosing process. The coverage corresponds to approximately 13-16 % of a ML.

Identification of this resonance is done by comparison of its thermal stability and center frequency to prior work about CH_3I and CH_2N_2 dissociation on Ru(0001) [144, 190].

First, let us have a look at the thermal stability of this resonance. Heating the surface after dosing to temperatures above 300 K causes a complete disappearance of the resonance. Instead of the resonance at 2940 cm^{-1} a new resonance at 3010 cm^{-1} appeared which can be identified as the ν_s of CH (spectrum not shown). The fact that there were no other intermediate states observable suggests that the peak at 2940 cm^{-1} can be contributed to a precursor state of CH e.g. CH_3 or CH_2. Zhou and coworkers[190] reported that CH_2 is partially stable up to 290 K. This thermal stability fits well with our result suggesting that the peak corresponds to CH_2. Other investigations reported measured frequencies of CH_2 in good agreement with us [144, 190]. The actual value of one of these frequencies for CH_2 were found at 2940 cm^{-1} by HREELS studies of CH_2N_2 on Ru(0001) [144]. In HREELS studies of Zhou et al.[190] about CH_3I on Ru(0001) they found the ν_s of CH_2 at 2920 cm^{-1}

what is also near by. By comparison of their observations of thermal stability and vibrational frequencies to our system it seems likely that CH_2 was produced at the surface.

As an additional verification of the CH_2 observation we dosed for a longer time to increase the surface coverage of our sample. Zhou et al. [190] reported for high coverages the formation of CCH_3 at the surface. By generating a higher surface coverage of CH_2 by dosing longer it should be possible to reproduce this observation. For a given dosing time of 60 minutes you got a spectral response of the sample, as shown in Figure 3.5. The coverage of the sample was about 18% ML of carbon. As

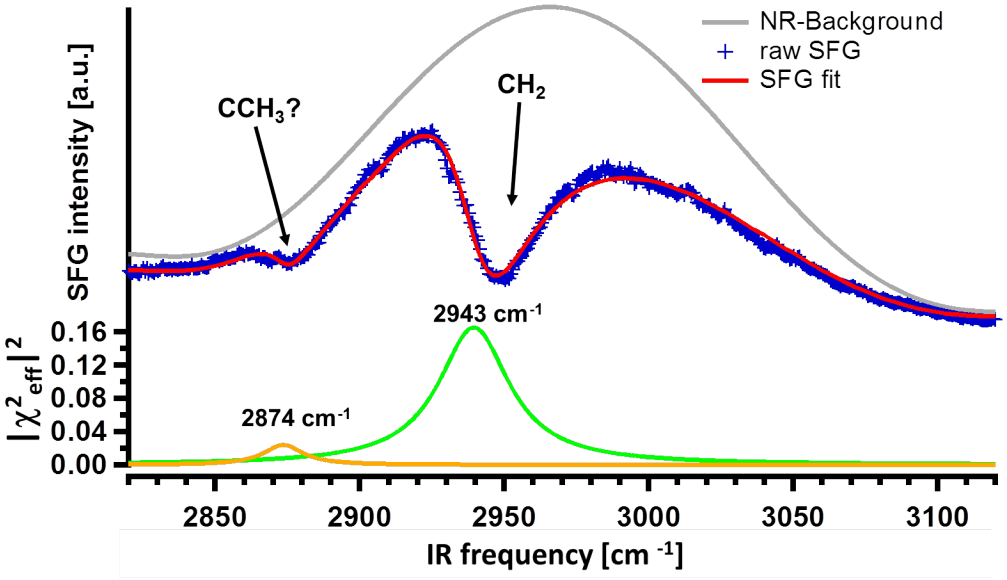

Figure 3.5: Spectral response of a Ruthenium surface, which has been dosed with the MBS for 60 minutes at 250K. Beside the already observed spectral response, which is contributed to the ν_s of CH_2, you observe a new peak, which is relatively small and centered around 2875cm^{-1}.

you can see in this figure, dosing for longer times at 250 K surface temperature induces an additional spectral response which is centered at 2875 cm^{-1}. In the literature you find the symmetric stretch of CCH_3 on Ru(0001) identified at 2880 cm^{-1} [126]. There, they investigated the dissociation pathway of ethylene on Ru(0001) with reflection adsorption infrared spectroscopy (RAIRS), where CCH_3 is known to be a common dissociation product. The center-frequencies of both resonances agree well. Therefore we concluded to have CCH_3 at the surface under these dosing conditions. Testing this conclusion will be done later in this chapter by comparison of the observed spectral response of CCH_3 to the spectral response of dissociated ethylene on the sample. The data will be presented later and verify the conclusion.

By taking all the observations e.g. center-frequency, stability and other combination products into account it is reliable to say that Figure 3.3 shows the spectral response of CH_2 molecules.

With the investigation of surface chemistry it is also always important to take surface morphology into account. Therefore, it would be useful to discuss the adsorption sites of the molecules briefly at this point. The total amount of carbon and the fact that it is still not saturated at this coverages suggested that the CH_2 molecules were mainly adsorbed on terraces. In fact it could not a be defect bound species because the step density (which should be the dominant defect type) on such a surface should be 2-3% or lower [12] (defects cannot be completely suppressed even in case of a perfectly prepared sample). Nevertheless, this is the first experimental observation of CH_2 produced by methane dissociation. A more detailed discussion of this observation and its implications will follow later on in this thesis. This section should just clarify the spectral assignment of all observed CH containing species.

3.1.3 High temperature dissociation of CH_4 on Ru(0001)

The low temperature region methane dissociation pathway was discussed in the last section. To complete the understanding of methane dissociation it is necessary to investigate also the high temperature decomposition of methane. This has been already intensively investigated by others but there are still some open questions like the correct spectral assignment of the ν_s of CCH_2.

For preparation of these more complex samples the same settings for the nozzle as for preparation CH molecules were chosen but the surface temperature was increased to T_{Ru}=400 K. The increased surface temperature enhances dissociative sticking which should make it possible to achieve higher carbon coverages. Dosing for 30 min created a coverage of 60% of a monolayer. By monitoring the spectral region of CH it was possible to observe new spectral features, which were not present on samples prepared at lower T_{Ru}, as you can see in Figure 3.6.

First of all you can clearly identify the stretching mode of CH at about 3020 cm^{-1}. Compared to the ν_s of CH at a coverage of 30% of ML the spectral response has blue shifted by 5 cm^{-1} but is still in acceptable agreement with literature [8, 9]. A qualitative discussion of the observed coverage dependent spectral shift in the CH region will be given in a following chapter. Inspection of Figure 3.6 clearly shows additional resonances at 2917 cm^{-1} and 2960 cm^{-1}. This observation was quite unexpected. Prior work of others reported two different sets of loss features in their high resolution electron energy loss spectroscopy measurements (HREELS) for samples prepared at 400 K surface temperature in a HPC. Losses at 790 cm^{-1}

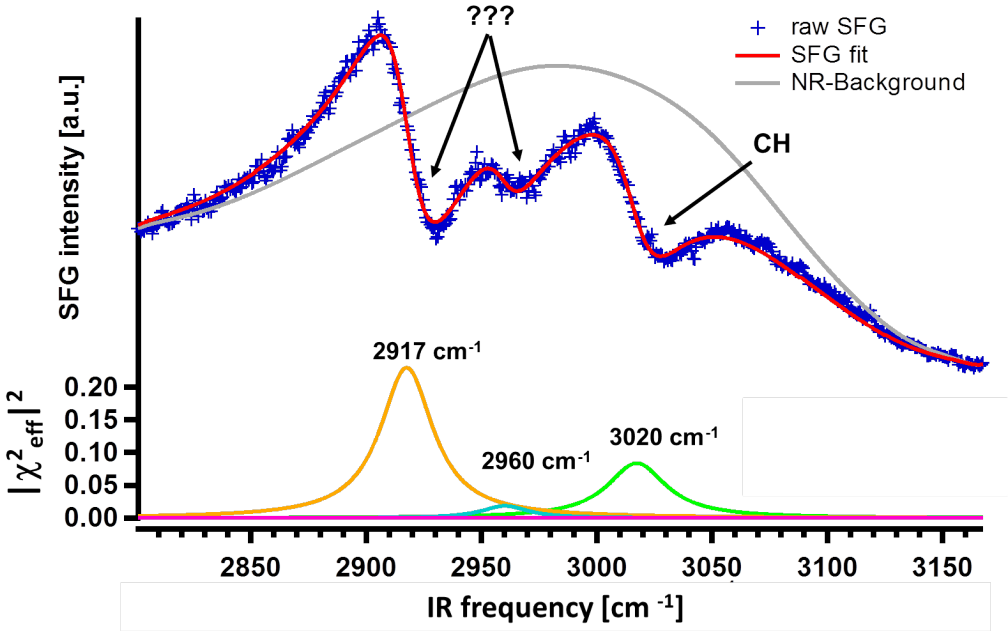

Figure 3.6: Spectral response of a Ruthenium surface, which has been dosed with the MBS for 30 minutes at 400 K. Besides the already observed spectral response of CH , you could clearly distinguish two new spectral features. One dominant feature centered at 2917 cm^{-1} and a much weaker one at 2960 cm^{-1}.

and 3000 cm^{-1} were attributed to the bending and stretching mode of a single CH molecule and were present in the temperature range from 400 K to 650 K[9]. The second set of losses at 1160 cm^{-1} and 1395 cm^{-1} were assigned to the CH_2 bending mode of a vinylidene (CCH_2) and the stretching mode of the corresponding C=C double bond[8, 10]. The corresponding CCH_2-stretch resonance in the CH-stretching region was not observed.

Following from this prior work one of the two unassigned resonances in Figure3.6 should arise from CCH_2 molecules at the surface. But this did not explain the observation of an additional resonance. A possible candidate, whose presence would make sense as a dissociation product of CCH_2 would be CCH (acetylene). Unfortunately, it is not possible at this point to make any comment about which resonance corresponds to which molecules at the surface. For testing this hypothesis and understand the coupling of CH molecules better we will switch to a system where ethylidene and acetylene have been reported to be observable in the dissociation pathway: the adsorption and decomposition system of ethylene on Ru(0001) [132].

3.2 Ethylene dissociation on Ru(0001)

Ethylene belongs to the most important basics in chemical engineering and industry and is a good model system for hydrocarbon chemistry because it is easy to prepare samples with ethylene in UHV. Furthermore it is a desired product of methane coupling [132, 126]. Therefore the interaction of ethylene with transition metal surfaces has been intensively studied for decades to gain insight into the occurring catalytic reactions at surfaces. Especially the understanding of its coupling and dissociation mechanisms is of large interest for scientists but the reaction pathways and intermediates are not fully understood and identified yet. One important example for the lack of clarity is the missing spectral assignment of CCH_2 in the CH-stretching region.

One advantage of investigating hydrocarbon chemistry in UHV by adsorption of ethylene is based on its handling conditions under UHV. While it is necessary for the investigation of CH_4 to apply a HPC or a MBS to gain dissociative adsorption this much easier for ethylene(C_2H_4). It has been shown that at temperatures lower than 150K C_2H_4 adsorbs molecularly on a Ru(0001) surface and then subsequently decompose at higher surface temperatures [137, 132]. Of course, it is obvious that this property of ethylene is not important for us since we are using a MBS. But C_2H_4 decomposition by subsequent annealing of the Ru(0001) crystal to higher temperatures is a practical way to produce C_2H_x compounds on a surface. Therefore CCH should be one of the intermediates in this process [132]. For the preparation of samples with C_2H_4 a Pin-Hole doser system was used which was connected to an external gas-system (described in 2.5.1).

The following set of figures present a series of measurements in which C_2H_4 at T_{Ru}=100 K was adsorbed and subsequently flashed the surface to higher temperatures.

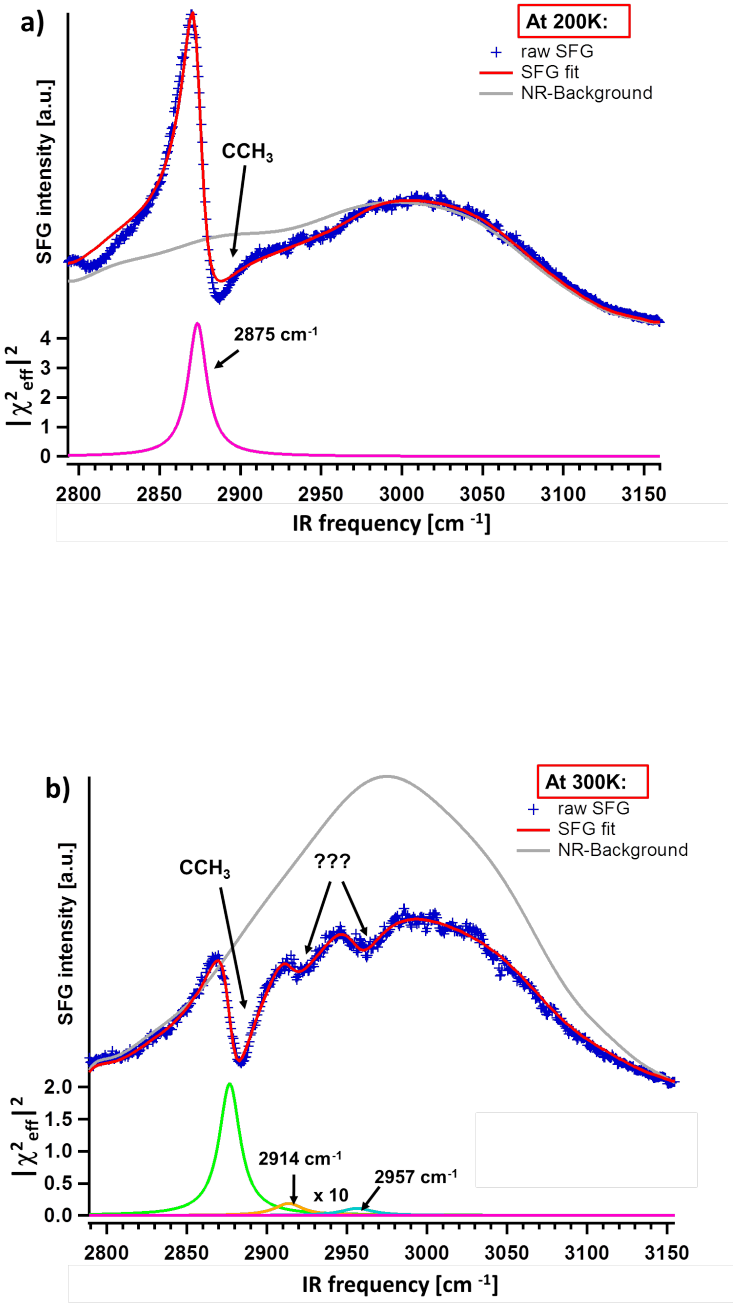

Figure 3.7: The figures a) and b) show the CH spectra of a Ru surface after dosing with ethylene at 100 K and flashing to 200 K and 300 K. Chester et al. reported the observation of a single species at temperatures of 200 K [126]. At this temperature, you can see a single species at the surface, with the same center-frequency as the reported frequency of CCH_3 ($2880\,cm^{-1}$) [126]. At 300 K, two additional features appear in the spectrum with the same center frequencies seen during methane decomposition in Figure 3.6

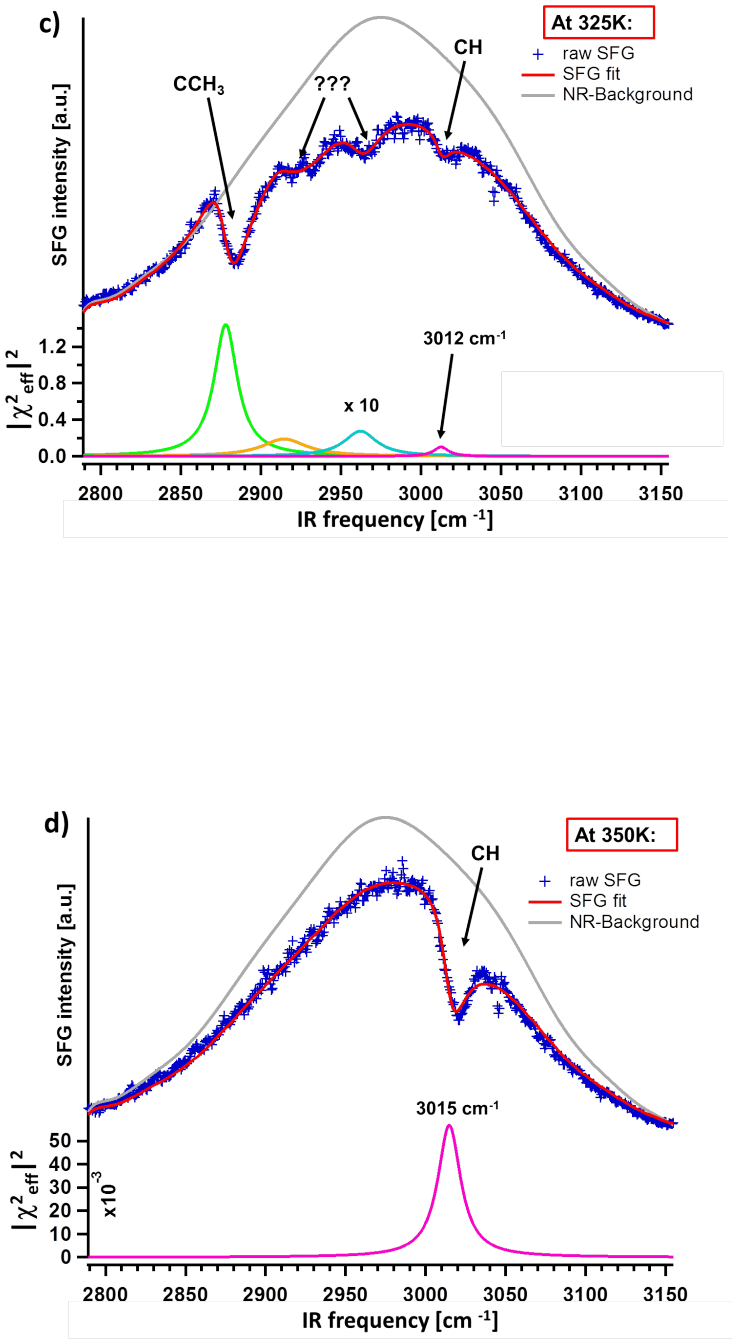

Figure 3.8: The figures c) and d) are the CH spectra of ethylene flashed to 325K and 350K. As can be observed at these higher annealing temperatures four distinct features are present at the surface in Figure c). At temperatures of 350 K or higher, all C_xH_x compounds seems to be completely converted to CH.

Figure 3.7 and 3.8 show the obtained SFG spectra of C_2H_4 adsorbed at 100 K surface temperature and subsequently flashed to higher temperatures. The surface has been shown to saturate with C_2H_4 by dosing two minutes with a gas pressure of 1 mbar in the external gas-system [114]. While dosing the pressure in the UHV chamber increases to from 3×10^{-10} to 5×10^{-9} mbar. The pressure in front of the dozer (at the sample surface) will be approximately one order magnitude higher. A surface, prepared in this way will has a carbon coverage of approximately 30-35 % of a monolayer [114].

For a deeper understanding of the spectra let us compare the data with the literature. Chester et al. [126] observed that C_2H_4 adsorb on Ru(0001) dissociatively by formation of CCH_3 at surface temperatures of 180 K. This species had a vibrational frequency of the ν_s of 2880 cm^{-1} in their system. Analogous to them we observe a single species with a frequency of 2876 cm^{-1} at temperatures of 200 K. Based on this assignment you can attributed this resonance to CCH_3. Further heating to 300 K changed the spectrum dramatically. Two new resonances appeared at 2914 cm^{-1} and 2957 cm^{-1}. Both center frequencies were nearly identical to those observed while methane decomposition at 400 K, as shown in Figure 3.6. It was already supposed that these could be contributed to CCH_2 and CCH. The identical frequencies suggest that for both cases the resonances corresponds to the same molecules. Annealing to intermediate temperatures of 325 K changes the relative intensities of the resonances and the symmetric stretch of CH appear till everything got decomposed to CH at 350 K. Such a spectrum is more or less identical to those gained by methane dissociation at 350 K.
For a correct assignment both systems will be discussed and compared with the literature (for methane and ethylene) in the next section, as it seems clear that in both systems are unobserved spectral features.

3.3 Discussion and comparison of spectral observations

Up to this point it was possible to identify several spectral features in the decomposition pathways of methane and ethylene. Nevertheless, there are still some resonances left where the corresponding molecule is not clear. First let us summarize up what was observed. In the methane decomposition pathway the ν_s of a single CH molecules was clearly identified at 3015 cm^{-1}. In the low temperature decomposition pathway the resonances of CH_2 at 2940 cm^{-1} and CCH_3 at 2880 cm^{-1} were identified. The presence of the CCH_3 has been found additionally in the ethylene decomposition

pathway where it was identified by its center frequency and thermal stability in comparison to prior work [132, 126]. In this system it had a much stronger signal than in the low temperature methane decomposition pathway. Thus in both CH_4 and C_2H_4 decomposition the center-frequency of CCH_3 has been observed and was found to have a CH-stretch frequency of $\approx 2875\,\mathrm{cm}^{-1}$.

A problematic point is the assignment of the remaining observed resonances during methane and ethylene decomposition at 2917 cm^{-1} and 2960 cm^{-1}. In CH_4 decomposition the presence of CCH_2 has been reported but the CH-stretch mode of the molecule was not observed/ resolved [8, 10, 13]. Under comparable preparation conditions we observed two additional resonances in the spectrum which suggests that one of them must have its origin in the symmetric stretch of CCH_2. Because no other molecules were observed under similar conditions by others one could argue that we possibly see the symmetric and the asymmetric stretch of CCH_2. But there are two arguments against this interpretation:
1.) It has been observed for most C_xH_x species[114] that the symmetric and the asymmetric stretch vibration were shifted $> 100\,\mathrm{cm}^{-1}$ relative to each other and not just $40\,\mathrm{cm}^{-1}$.
2.) Furthermore, it must be referred back to the metal selection rule which is shown in 2.4. If the CCH_2 is adsorbed in a standing and more or less symmetric way (as reported by [132]) the asymmetric stretch vibration would create an image dipole parallel to the Ru-surface. This would cancel the effective dipole out and the ν_{as} would not be SFG active.

It thus seems more likely that a third, up to now unobserved, molecule is present at the surface. A candidate would be CCH which seems intuitively possible as a dissociation product of CCH_2. The fact that it has not been observed yet during methane dissociation could be based on the lower spectroscopic resolution of prior investigations. The measurements performed in [8, 9, 10, 114] had a vibrational resolution of 60-80 cm^{-1} in their HREELS, while we have a resolution of 5-7 cm^{-1}. Additionally the total amount of produced CCH was possibly to low for detection. Generally we can assume that on the in Figure 3.6 shown surface much more CCH_2 than CCH should be present, because [8] and others observed just CCH_2. As shown in Equation 2.23 the signal intensity of SFG is proportional to the number of molecules at the surface. Compared to the resonance at $2960\,\mathrm{cm}^{-1}$ we could connect the resonance at $2914\,\mathrm{cm}^{-1}$ to the more populated species, due to the much higher intensity. This works under the assumption of comparable hyperpolarizabilities of CCH_2 and CCH. This is just a rough estimation because different molecules will have different hyperpolarizabilities and therefore a different spectral response. But we assume that between CCH_2 and CCH they are not so different. Going this line

ν_s **of**	CH_4 **/ Ru(0001)**	**ther. stab.**	C_2H_4**/ Ru(0001)**	**ther. stab.**
CH	$3015 \pm 3\ cm^{-1}$	> 600 K	$3012\ \pm 5\ cm^{-1}$	> 600 K
CH_2	$2943 \pm 5\ cm^{-1}$	max. 290 K		
CCH	$2960 \pm 3\ cm^{-1}$	max 565 K	$2957 \pm 5\ cm^{-1}$	max.350 K
CCH_2	$2917 \pm 6\ cm^{-1}$	max 565 K	$2914 \pm 6\ cm^{-1}$	max.350 K
CCH_3	$2875 \pm 6\ cm^{-1}$	max.330 K	$2875 \pm 3\ cm^{-1}$	max.350 K

Table 3.1: This table shows the stretching frequencies of various C_xH_x species produced during CH_4 or C_2H_4 dissociation. The temperature next to the frequencies show the maximum thermal stability of the observed molecules. The uncertainties attached to the resonances followed from the observed differences in the center frequencies derived from different datasets.

of argumentation the resonance at $2914\,\mathrm{cm}^{-1}$ should correspond to CCH_2 and the resonance at $2960\,\mathrm{cm}^{-1}$ to CCH.

With the hypothesis that two unknown resonances correspond to two different molecules at the surface let us return to C_2H_4 on Ru(0001). As mentioned we observed four distinct features (see Figure 3.8), with two already identified as CCH_3 and CH. The remaining resonances were identical in their frequencies to those shown in Figure 3.6. In contrast to the methane system CCH has been observed by others in this system while CCH_2 has not. In particular Weinberg et al. [114] reported the symmetric stretch of CCH at $2960\,\mathrm{cm}^{-1}$ which corresponds to one of the resonant frequencies observed in the CH_4 decomposition pathway which was already suggested to be CCH. The fact that CCH_2 has not been observed in ethylene decomposition on Ru(0001) before could be explained analogous to CCH in the methane system by a low spectral resolution and sensitivity. In ethylene decomposition CCH_2 shows just a weak resonance and CCH is more pronounced in the spectrum while in CH_4 decomposition the situation is reversed.

Overall it is reliable to assume that CCH_2 as well as CCH were observed in both pathways. Furthermore, it was possible to determine the ν_s of both with a high resolution. All obtained values and corresponding thermal stabilities are listed in Table 3.1.

As clear from the table the derived frequencies from different systems for the same molecules are equal within uncertainty. The observed thermal stabilities of the molecules in both systems corresponds well with the reported values for the investigated system. The reader may wonder why the same molecules show such a dramatic differences in thermal stability when they produced in different ways.

This effect is induced by differences in coverage and will be discussed later on in this thesis.
To summarize, this work is the first experimental observation of CH_2, CCH and CCH_3 in UHV produced by methane dissociation. Additionally we were able to resolve the ν_s of CCH_2 in the CH-stretching region.
For ethylene decomposition on Ru(0001) we were able to partially verify prior observations for the dissociation and extended the prior suggested dissociation pathway by the presence of CCH_2. This has been already suggested by work function measurements of others[132] but not proved experimentally yet.

With this information about our adsorption systems and the correctly assigned species we can start to further investigate how changes in temperature and surface morphology influences the transformation between different hydrocarbon species. Thereby we will focus on the influence of molecules to each other regarding their thermal stability and center-frequencies, but also the influence of co-adsorbed molecules and morphological issues in the ongoing reactions.

Chapter 4

$CH_2 \rightarrow$CH conversion and implication for C_1 coupling chemistry

After the first introduction of the methane and ethylene adsorption systems in the last chapter, we will focus now on more specific issues we observed. In this chapter we will focus on the experimental observation of methylene (CH_2) stability on Ru(0001) and discuss the implications of this stability on various processes. The aim is to understand, what the thermodynamics and kinetics behind the stability of this CH_4 derived radical are and how they are influenced by surface morphology.
Chemistry of single carbon compounds (C_1) on transition metal surfaces (Ru, Rh, Ni, Pt..) is important for applications such as the steam reforming of methane ($CH_4 + H_2O \leftrightarrow CO + 2H_2$) and the Fischer-Tropsch (FT) synthesis ($CO + H_2 \leftrightarrow C_xH_y$) [181, 8, 10, 9, 117, 16]. Because of the economic importance of these already industrially used techniques, much work has been performed in the past. The results of this prior work highlights the great importance of the relative stability of surface bound CH_x radicals for both processes. For a more specific understanding of the role of CH_x radical chemistry, the main mechanisms of the FT-process will be briefly introduced.

The FT-process is thought to contain three different steps on the way of long-chain hydrocarbon formation. The first step is the dissociation of CO at the catalysts surface, including the removal of the produced oxygen by formation and desorption of water. The second step is assumed to be partial hydrogenation of the carbon atoms, followed by coupling of these C_1 compounds. There are several reaction routes for this chain-growth mechanism proposed: either CO insertion induced chain-growth or via CH or CH_2 coupling. The last step in the FT process is the termination of the

chain and the desorption of the molecule.

Prior work has shown the strong dependence of the chain-growth mechanism on the existence and thermodynamic stability of the CH_x radicals. Recent theoretical work has shown, that this three step process is best described by the so-called Sachtler-Biloen mechanism(S-B) [16]. In this S-B mechanism chain-growth occurs via coupling of CH_x radicals. While chain-growth by addition of these C_1 compounds seems clear, identifying the relevant building block has proven challenging. Product distribution and isotope studies suggests that adsorbed CH_2 is the key intermediate for coupling and prolongation of chains [17], but other experiments and theory finds this species highly unstable[18]. Alternative growth mechanisms with adsorbed CH radicals or C as the fundamental building blocks of higher hydrocarbons have been suggested [17].

The observation that nobody has found stable CH_2 on Ru(0001) by methane dissociation before is in agreement with this argumentation. The absence of CH_2 on Ru(0001) was rationalized by invoking a low barrier for dehydrogenation and a greater stability for CH than for CH_2[17]. Van Santen and coworkers [18] verified this hypothesis by calculation. They found for a single CH_2 radical an activation barrier energy of 16 kJ/mol for dissociation, while the barrier for CH was six times higher. This barrier of CH_2 is sufficiently low to suggest CH_2 being important for C_1 coupling reaction, because the chain prolongation reactions show activation energies, which are at least several times higher[16]. Literature[131] calculated the activation barrier of coupling of two CH_2 groups on a planar Ru(0001) surface, as follows:

$$CH_2 + CH_2R \rightarrow CH_2CH_2R \quad ; E_a = 119kJ/mol \; ; \; Ru(0001)$$

The R in the formula corresponds to a remaining saturated hydrocarbon chain with a CH_2-group at one end as the reactive coupling center. As you can see, the activation energy for coupling of these molecules on a planar surface is nearly ten times higher than the CH_2 dissociation barrier. This suggests that CH_2 is an unlikely building block for chain prolongation, because it would dissociate before coupling to longer chains. Even if we assume the coupling reaction to occurs at a step (steps are thought to be the active center for FT on catalysts [16]), prior theoretical work has calculated an activation barrier of 59 kJ/mol for $CH_2 + CH_2R \rightarrow CH_2CH_2R$ for this reaction. This value is still four times higher than the CH_2 dissociation barrier on a planar surface[131]. Unfortunately there a no barriers calculated yet for the dissociation of CH_2 at Ru(0001)-steps, which could greatly differ to the plane surface. Calculation for a stepped Ru(1120) surface have shown that CH_2 is the most stable species at this surface with an activation barrier of 52 kJ/mol for the dissociation[16].

As one could see, there are still open questions, which could probably change

the picture of the dominating processes during the FT-process. Also the differences of equilibrium conditions to non equilibrium conditions will be discussed, as most experiments and calculations were performed with thermally equilibrated surfaces. Ignoring the equilibrium with a H_2 gas-phase in calculations have shown stabilization effects for CH_x compounds, which would not have been stable as isolated molecules on a clean surface [16, 14]. Nevertheless, the plan is to investigate the properties of "our" produced CH_2 at the surface to understand the thermodynamics and kinetics of this radical. Because this work focuses on CH_x chemistry, it is clear that any gained insight should be of relevance for all processes that rely on CH_x stability.

For investigation of the CH_2 →CH conversion process, the already introduced Arrhenius plot method for the analysis of the data is applied (see Section 2.4), which is a common method for determining the activation barriers in chemical processes.

4.1 Experimental quantification of CH_2 →CH + H barrier

The following section will introduce the reader to the practical treatment of an Arrhenius analysis, which was performed with the setup. Before performing the measurements, a cleaning cycle for the Ru(0001) sample was performed, as discussed in Section 2.5.2. For the sample preparation of a CH_2 covered Ru(0001) sample, the surface should be prepared in a way that a high number of CH_2 groups are apparent but a low number of other carbon containing molecules. Two experimental parameters can be altered to control the surface speciation (which kinds of species apparent at the surface), the sample temperature while dosing and the dosing time. The nozzle temperature could be possibly seen as a third parameter, but it mainly changed the kinetic energy of the impinging CH_4 molecules and therefore increased the dissociative sticking, but it does not much influences the surface speciation. If the sample temperature is too low, the sticking coefficient will decrease for dissociative sticking[12] and the coverage of CH_2 will be too low for analysis. If the temperature is too high, the coverage will be good for measurements, but it could cause further dissociation while dosing[8]. Following prior investigators [190] a temperature of T_{Ru}= 250 K with 30 minutes dosing is found as the optimum conditions for CH_2 generation. All data shown in the following section were collected under these conditions. The carbon coverage of samples, prepared in this manner, was 16-18 % of a ML (as shown in Figure 3.4). This suggests that the dissociation process of CH_2 on terraces is investigated, because the density of defects at this surface should be less than 2-3% [12].

After preparing CH_2 covered samples, the sample got cooled to 110 K using liquid nitrogen and characterized using the sum frequency generation setup (see Section 2.5.4). For the CH_2 measurements an IR pulse energy of ≈ 10 μJ and an 800 nm up-conversion pulse energy of 12 μJ was used. Control experiments showed that there is no change in surface speciation under these conditions, even in the time span of one day. After a the first characterization of the sample the laser-beams were blocked and the sample got heated to a certain temperature with a ramp of 100 K/min. After reaching the desired temperature, the sample was kept there for 5 minutes before cooling it rapidly to 110 K. After reaching this temperature the sample was characterized again by SFG. The reason for keeping the elevated temperature for 5 minutes based on the idea, that the time (5 min) at a certain temperature should be comparably long to the time it takes to reach this temperature with the given heating ramp or cooled to 110 K. Changes in the surface speciation should happen during the sample is at the given temperature and not while the heating ramp. Under these experimental conditions it is acceptable to assume this, since the ramping time is short compared to the baking time. A graphical overview of the process is given in Figure 4.1

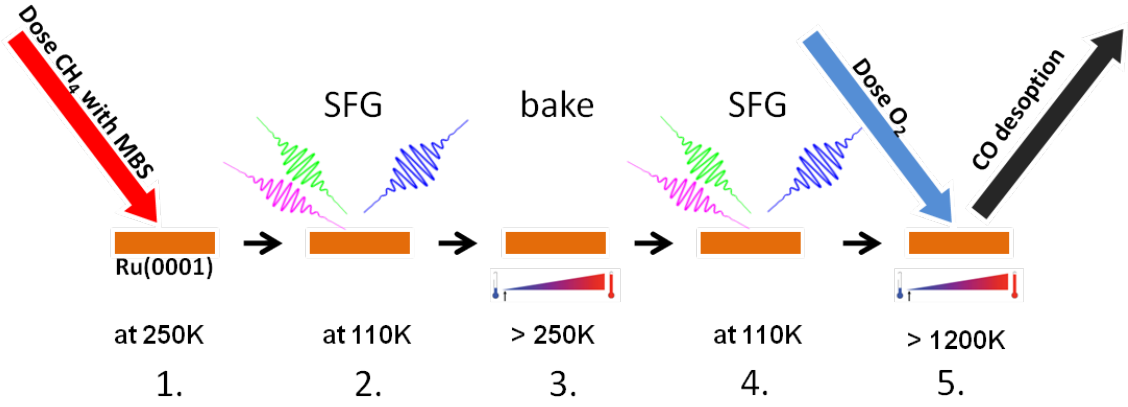

Figure 4.1: This scheme shows the experimental pathway used for our measurements for an Arrhenius based analysis of the population conversion from CH_2 →CH. In step 3 we chose temperatures between 250 and 285 K in approx. 5 K steps. Each cycle from 1. to 5. was finished by flashing of the sample to 1510 K to ensure that no oxygen was left on the surface, which could influence subsequent preparations.

As you will see later on, this treatment of the sample shows that the intensity of the observed CH_2 response decreases as a function of the annealing temperature (step 3.). Because the spectral intensity of the resonance is proportional to the population, it is possible to relate the decreases in intensity at a certain annealing temperature to the decrease in population. The exact way of doing this is given in the next section.

4.2 Arrhenius analysis of CH_2 →CH conversion

After the discussion of the experimental procedure, here it will be shown how to analyze the data to obtain the activation barrier for CH_2 →CH conversion. The theoretical background of this method is already discussed in Section 2.4, therefore we will focus on the application of this approach to our system. Figure 4.2 shows the obtained signal before and after the heating cycle for a baking/annealing temperature of 273 K. As you can see in Figure 4.2, the signal intensity clearly decreases after heating the sample to a certain temperature. This set of measurements was performed for each data point, which is given in Table 4.1

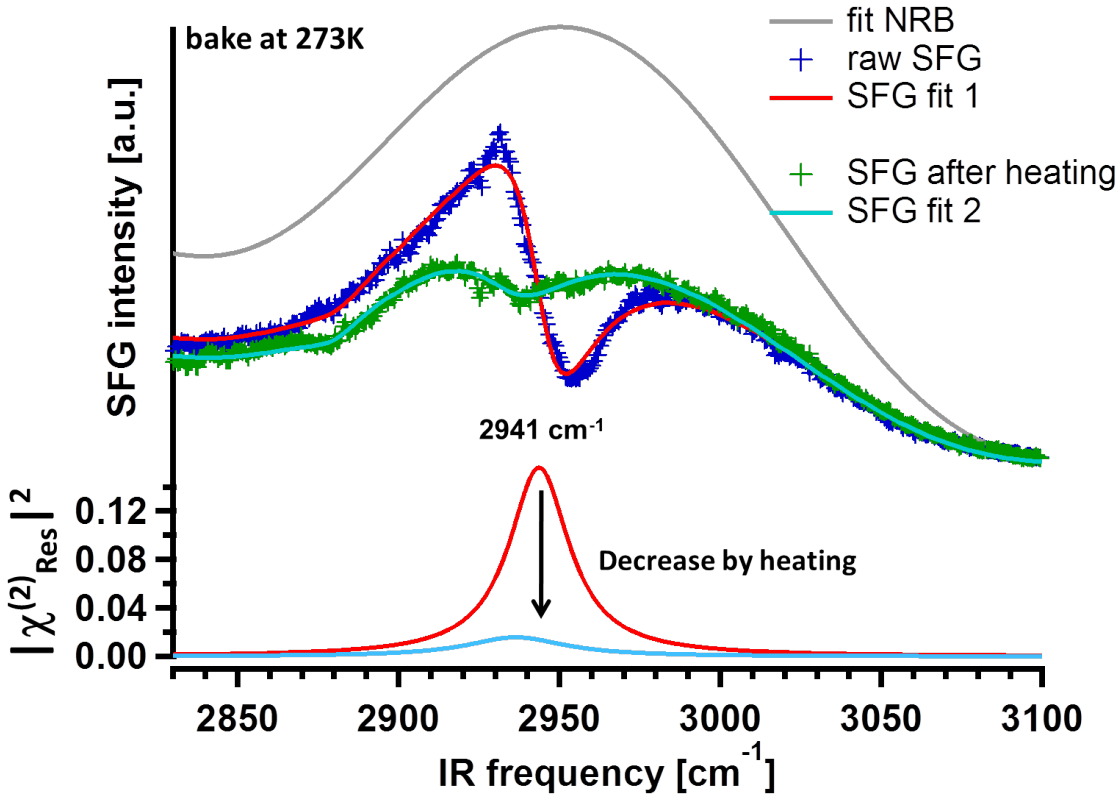

Figure 4.2: An example of the temperature dependent decrease of the SFG response of a sample prepared with CH_2. In this case the baking temperature for step 3 (see Figure 4.1) was 273 K. From the decrease of the signal intensity we can obtain the relative amount of converted CH_2, as described in the text. Plotted is the SFG intensity over the vibration frequency.

By fitting the data (employing the line shape model discussed in Section 2.5.5), we can extract the signal intensity of the resonances before and after heating. By doing this for all measured baking temperatures, you get the values, listed in Table 4.1.

The value of N^2 in Table 4.1 is the resonance intensity after the baking relative

Baking Temp in K	**A_1 before Baking**	**A_2 after Baking**	N^2
245	3.601	3.494	0.97
250	2.492	2.295	0.95
255	2.347	2.203	0.94
258	2.949	2.502	0.85
260	1.747	1.104	0.78
260	3.160	2.943	0.78
263	4.290	3.580	0.83
265	1.941	1.246	0.64
268	2.270	1.295	0.57
270	3.555	2.471	0.69
270	1.763	1.240	0.70
270	2.250	1.411	0.62
273	2.452	0.873	0.35
275	3.781	1.271	0.34
280	4.294	0.847	0.20
285	2.174	0.200	0.09

Table 4.1: The table shows experimentally extracted values for the intensity of the CH_2 resonance before and after heating to a certain temperature. Values of A_1 and A_2 are proportional to the Amplitude × FWHM of a certain resonance and are results of the fits. N^2 is by definition A_2 / A_1

to the intensity before. It is defined as

$$N^2 = \frac{A_2}{A_1}$$

To get the proportionality of the molecule population before and after heating, we have to take the square-root of N^2 because $I_{SFG} \propto N^2$. This number will now give us some information about the relative number of molecules, which are left at the surface after heating. Because the rate constant of a dissociation reaction described by a Arrhenius plot depends on the number of converted molecules at a certain temperature in a certain time, we must take

$$\Delta n = 1 - N$$

for the Arrhenius plot.

For the investigated system the disappearance of CH_2 after heating was explained with the CH_2 →CH + H reaction. Therefore, one can assume to observe a single molecular reaction happening on the surface which should be a first-order process for the conversion (the influence of the reaction order and the possible temperature dependence of the pre-exponential factor is discussed in Appendix 10.1). In such a case the Arrhenius description of the reaction is given by:

$$\left[\frac{\partial CH_2}{\partial t}\right] = -k[CH_2] = -A \cdot e^{\frac{-E_a}{RT}}[CH_2] \tag{4.1}$$

R is the universal gas-constant and $[CH_2]$ is the averaged number of molecules at the surface during a baking process:

$$[CH_2] = \frac{1+N}{2}$$

Of course, this value is just an estimation, but it is not possible to determine the exact number of molecules at the surface at every moment, so we use this approximation. To constrain the effect of this approximation, it was tested by inducing small changes and but there was not a strong influence on the final result of this parameter. By assuming that the pre-exponential factor A is temperature independent (a reasonable assumption, as discussed in Appendix 10.1), we can rewrite Equation 4.1 to:

$$ln\left(\left[\frac{\partial CH_2}{\partial t}\right]\left[\frac{1}{[CH_2]}\right]\right) = ln\left(\frac{\Delta n}{[CH_2]}\right) = -\frac{E_a}{RT} + const \tag{4.2}$$

For extracting the activation energy we plot $ln\left(\frac{\Delta n}{[CH_2]}\right)$ over $\frac{1}{T}$. If our assumptions are correct, the data-points should be plotted on a line. The slope of the line would

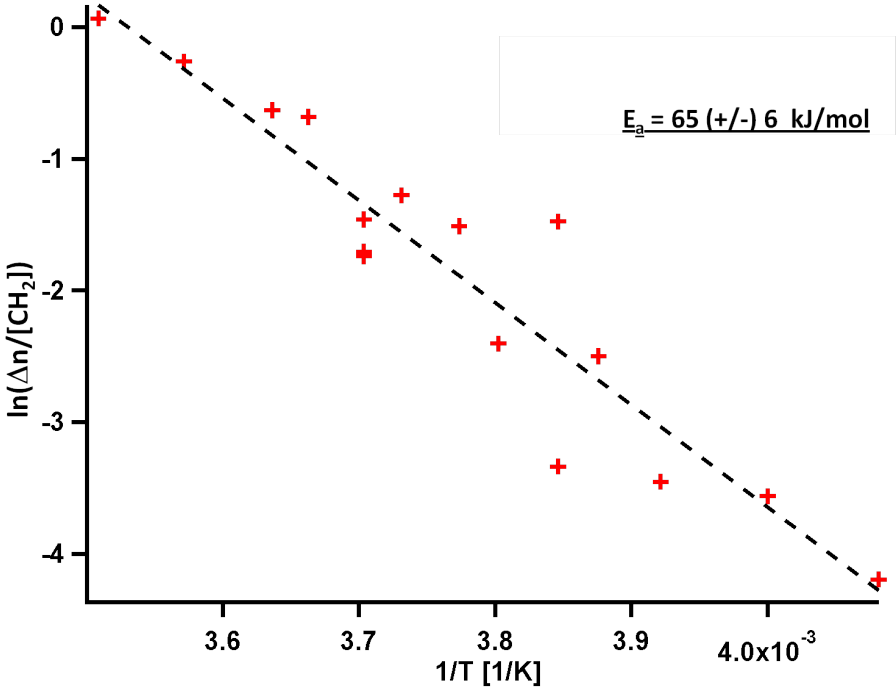

Figure 4.3: This graph shows the Arrhenius plot for the conversion of CH_2 to CH. The linear trend in the data is clearly obvious and verifies our assumption for the reaction order. The slope of the attached fit is determined as $-E_a/R$. Multiplication of the slope by the gas constant R gives the activation barrier of the process.

be given by $-E_a/R$. By multiplying the slope with R you get the activation barrier for the dissociation process. Plotting the data from Table 4.1 in this way gives Figure 4.3

As you can see in Figure 4.3, you can clearly identify a linear trend in the data, suggesting that our assumptions for the pre-factor and averaged coverage in the analysis are acceptable. The error attached to the activation energy, followed from the linear fit and is the standard deviation of our fitted dataset. By this method, you get an activation barrier of about 65 kJ/mol for this process. This result was unexpected, as you can see by comparison with the literature.

Van Santen and coworkers have calculated a barrier of 16 kJ/mol for the CH_2 →CH+ H reaction on Ru(0001) [18, 19]. For a better overview about the methane decomposition pathway, Figure 4.4 shows the calculated pathway of CH_4 on a Ru(0001) surface [65].

These calculated results are a reason, why CH_2 was not considered to be the main building block for higher hydrocarbon formation in the FT synthesis. CH_2 seemed not to be stable under the high temperate conditions, necessary for FT-process. Our experimental observation is now in contradiction to the theoretically calculated barrier, because our result is 4 times higher than the predicted one.

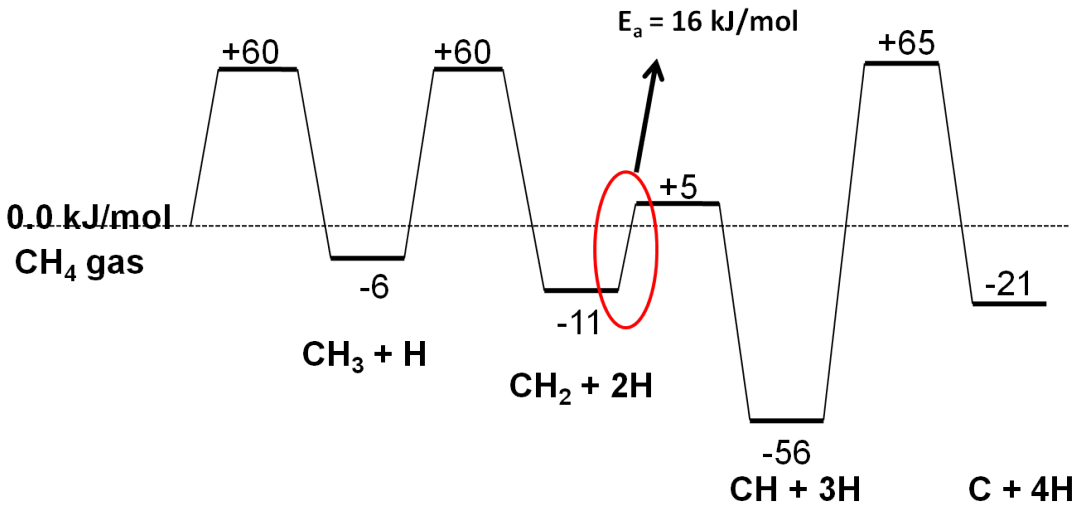

Figure 4.4: Dissociation pathway of CH_4 with calculated adsorption energies for ground-states and transition-states for dissociation. Values taken from [65]. Xing et al. considered in their calculation the remaining hydrogen at the surface, while van Santen and coworkers did not. This hydrogen does not alter the quantitative picture.

One possible explanation for this experiment/ theory discrepancy is that our dosing procedure leads to the investigation of CH_2 at defects. But this can be excluded by considering two facts:
1.) the observed signal increases with increasing coverage (adsorption site is not saturated) and
2.) the amount of carbon is nearly by a factor of ten higher than the normal defect(step) density (max 2-3% of a monolayer) on such a Ru(0001) surface [12]

As a second possibility for explaining the deviations, we have to discuss the meaning of the by Arrhenius analysis gained values to theoretically calculated values for activation barriers. Actually, this was already done in Section 2.4, where it was shown, that the theoretically calculated value, which is due to the standard change of internal energy Δ^+U^0 and the experimentally derived value for E_a differs at least by a factor of RT from each other (see for full derivation in Section 2.37). At 300 K, the factor RT is approximately 2.5 kJ/mol, so this difference could not explain the huge deviation.

Another explanation for the deviation could base on the fact, that the experimentally and the theoretically investigated systems differ in some major ways. In literature [18] they calculated the dissociation barrier for a single CH_2 molecule in a 2x2- cell. This corresponds to a carbon coverage of 0.25 ML, which would be in the regime of our measured carbon coverage for samples prepared with CH_2 (we had about 0.18 ML of carbon, as shown in Section 3.1.2). While the carbon coverage is

similar in experiment and theory it seems likely that our system might also contain larger amounts of co-adsorbed hydrogen. The experimentally investigated system could even contain enough co-adsorbed hydrogen to saturate the four available adsorption sites in a 2x2-cell. This would be in contrast to the theoretical investigations, which always chose situations for the CH_2 dissociation where at least one favored adsorption site for hydrogen was free (CH_2 →[CH + H][18] and [CH_2 + 2H]→[CH + 3H][65]). The reason, why I focus on the issue of co-adsorbed hydrogen is based on some prior work of Neurock et al. [19] which reported dramatically changed energetics of some kinds of hydrocarbon chemistry on catalytic surfaces in case of co-adsorption hydrogen. Prior TPD studies have shown that hydrogen, co-adsorbed with hydrocarbons, leaves the Ru(0001) surface by recombinative desorption at temperatures higher than 300 K[114]. Our measurements are performed clearly below 300 K (see Table 4.1). This implies for the system, that you are starting with a sample, where the hydrogen from the initial dissociation steps of CH_4 is co-adsorbed. Furthermore, it must be taken into account that hydrogen, produced in the hot nozzle, may also be present at the surface. As mentioned in the Methods section, nozzle temperatures above 860 K (970 K was used for dosing CH_2) can lead to dissociation of the methane by formation of H_2 and carbon[136]. While the hydrogen adsorption was not quantified due to this effect, we observed blocking of our nozzle by carbon over time. Finally, a small H_2 contamination in our seeding gas (He 6.0) can also play role, as will be cleaed upr below.

The following estimation should emphasize that even small contributions of hydrogen in the molecular beam are enough, to generate a surface coverage of (CH_2 + 3H) per 2x2-cell. The main reason for the importance of small hydrogen contributions in the molecular beam can be found in the crucial difference between the sticking coefficient of methane and hydrogen, dosed with the MBS and adsorbed at 250 K surface temperature. Therefore, the sticking coefficient of CH_4 for the investigated system will be estimated first. Afterwards it will be compared to the sticking coefficient of H_2 on Ru(0001).

Egeberg et al. [12] reported that the sticking coefficient of CH_4 adsorbed at 300 K gas temperature on a Ru(0001) surface at a surface temperature of T_{Ru}= 250K will be s_{CH_4}=10^{-12} - 10^{-13} . Larsen et al. [117] reported for the effect of nozzle temperature (kinetic energy) on the sticking coefficient following: an increase from 300 K to 950 K -1000 K should increase the sticking coefficient by six orders of magnitude. Therefore one can estimate to have a maximum sticking coefficient of s_{CH_4}=10^{-6} at our conditions. On the other hand, Danielson et al. [91] reported for the sticking coefficient of hydrogen at these sample temperatures a value of s_{H_2}=10^{-1}. A positive effect of the MBS on the dissociative sticking of H_2 have not been included

in this value.

For reaching a level of saturation so that four adsorption sites in the 2x2-cell are occupied by CH_2 or H, you need one additional H-atom from the molecular beam per dissociatively adsorbed CH_4- molecule. By comparison of both sticking coefficients you see, that only 0.0005% of the CH_4 in the nozzle has to dissociate to reach such a saturation level. This corresponds to a contamination of 5 ppm H_2 compared to the CH_4 molecules (5 H_2 per one million CH_4) in the molecular beam. The observation of macroscopic effects of methane dissociation in the nozzle (nozzle blocked by carbon compounds) suggests this regime of contamination. In addition, our as seeding gas used Helium 6.0 (Westfalen AG, Muenster) has an impurity of 0.1-0.5 ppm H_2. Because the ratio of He/CH_4 is 20/1, this could easily explain 20% or more of the required contamination in the molecular beam. Both effects could therefore explain a not neglectable contamination in the molecular beam.

Taking this estimation for the Hydrogen it is absolutely valuable to assume, that the initial coverage before dissociation is about (CH_2 + 3H) per 2x2-cell, as long as the surface temperature is below 300 K.

But why is this important for the barrier?

Van Santen and others [18] have shown that hydrogen and CH_x radicals prefer both threefold hollow sites for adsorption [18]. These threefold hollow sites could be either fcc or hcp-sites. A 2x2- cell contains 4 fcc and 4 hcp-sites. The different adsorptions sites will be more clear in Figure 4.5. If adsorption of an isolated CH_2-

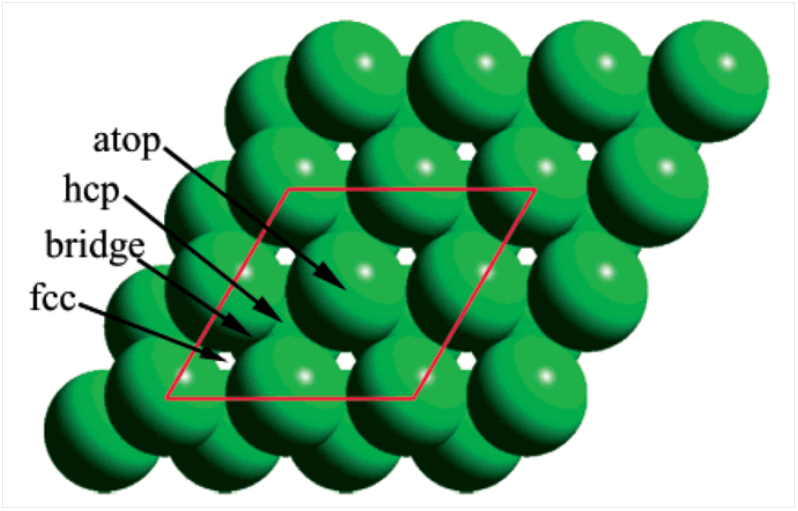

Figure 4.5: This Figure shows the different adsorption sites on a Ru(0001) surface. The red frame highlights the 2x2-cell in the figure. As you can see, fcc and hcp sites are both threefold hollow sites at surface. The only difference between both sites is the subsurface Ru-atom below the hcp adsorption site. Figure taken from literature [99].

radical would happen, it would prefer a hcp-site for adsorption because this site is

$\mathbf{CH_2}$	**H**	**H**	**H**	$\boldsymbol{E}_{\mathrm{hcp}} - \boldsymbol{E}_{\mathrm{fcc}}$ (kJ/mol)
hcp	–	–	–	-17.0
hcp	hcp	–	–	-4.2
fcc	fcc	fcc	–	4.8
fcc	fcc	fcc	fcc	11.0

Table 4.2: Energetically preferred adsorption site for CH_2 and H atoms on a (2×2) supercell of Ru(0001) as a function of the number of H atoms. The last column shows the energy difference between most stable configurations of CH_2 at hcp sites and at fcc sites for a given number of hydrogen atoms. As it is clear from the table, in case of higher hydrogen coverage, CH_2 changes its preferred adsorption site from hcp to fcc. Table taken from our paper[109]

17 kJ/mol more favorable (see Table 4.2) in adsorption energy than the fcc site. This was calculated by coworkers from the Theory department of the FHI.

Our hypothesis is that this adsorption behavior and the connected kinetics for dissociation changes drastically, if co-adsorption of (CH_2 + 3H) happens in a 2x2-cell. To evaluate this hypothesis we asked coworkers from the theory department of the FHI, to perform DFT calculations. They focused on the coverage dependent adsorption geometry and energy, as well as on the activation barrier for the transition state of dissociation reactions. In the low coverage regime (co-adsorption of 0, 1 or 2 H-atoms per 2x2-cell), they found similar behavior as van Santen in their calculations[18]. But changing the coverage to a situation of (CH_2 + 3H) per unit-cell seems to influence the energetics of the system dramatically. All calculated relevant values are listed in Table 4.2 and 4.3.

Let‘s start with the preferred adsorption site. In case of co-adsorption of CH_2 and 3H per 2x2-cell, both prefer the same adsorption site in a 2x2-cell, the fcc-site. See Table 4.2.

The corresponding adsorption energy difference between different adsorption sites is listed in Table 4.2 in the last column. The surface state in which CH_2 and each of the 3 H atoms are all adsorbed at fcc sites is 11 kJ/mol more favorable than the state in which they are all adsorbed at hcp-sites. To be clear in this point: 11 kJ/mol is not the needed energy to transfer one H atom into a corresponding hcp-site. This is the adsorption energy difference between (CH_2 + 3H) being adsorbed in a fcc or hcp-site. All corresponding values, calculated by our coworkers and given in Table 4.2 will be published in [109].

(CH_2 + 3H) corresponds to a coverage of 1 ML. As we can see, the case of co-adsorption with sufficiently high coverages have already an affect on the preferred adsorption site of CH_2.

reaction	$\boldsymbol{E}_{TS} - \boldsymbol{E}_{IS}$ (kJ/mol)	$\boldsymbol{E}_{FS} - \boldsymbol{E}_{IS}$ (kJ/mol)
CH_2 →CH + H	11.2	-49.0
CH_2+H→CH + 2H	10.8	-35.0
CH_2+2H→CH+ 3H	12.4	-39.5
CH_2+3H→CH+ 4H	47.4(61.8)	39.6(53.1)
CH_2+3H→CH+ 2H + $H_{2,gas}$	88.4 (95.6)	-44.8(51.8)

Table 4.3: Calculated reaction barrier(middle column) and reaction heat (right column) for CH_2 dissociation with different numbers of H-atoms in a (2×2)-cell of Ru(0001). E_{IS}, E_{TS}, E_{FS} are the total energies of initial state, transition state and final state respectively. For each stoichiometry the most stable configuration of the reactants is considered to proceed the reaction. The reason why the total energy of the final state (FS) of Line 2 and Line 5 were different (since both states have effectively just CH+2H adsorbed), is based on the different adsorption sites. The FS in Line 2 contains adsorption in hcp-sites, while the FS in Line 5 the adsorption in fcc-sites. The values of Line 4 and 5 reflect the free energy pathways calculated by including harmonic vibrational free energy to the total energy for each structure. This lowers the energies in line 4 and 5. The huge difference in the final state of line 5 is explained by fact, the the H_2 molecule in the gas phase have also translational and rotational modes to the already included vibrational mode. The uncorrected values are given in the brackets behind. Details available in [109].

We suggest that in case of saturation of four threefold adsorption sites (fcc or hcp) the thermodynamics and kinetics of the CH_2 dehydrogenation changes radically. For testing this hypothesis, our coworkers calculated the total energy difference of the system before and after the dissociation for the high and the low coverage case. The results are given in Table 4.3

As the reader can see, Table 4.3 shows the total energy differences of the different states during dissociation, namely the initial state, transition state and final state respectively (E_{IS}, E_{TS}, E_{FS}). For the low coverage regime (0, 1 or 2 H atoms co-adsorbed), the dissociated state is energetically favorable by at least 35 kJ/mol (last column in Table 4.3). The barrier for dissociation (middle column in Table 4.3) is always between 10-12 kJ/mol. Therefore dissociation of CH_2 is energetically favorable.

In case of CH_2 dissociation co-adsorbed with 3 H atoms, the situation changes dramatically. After the dissociation, the CH and 3H-atoms would be adsorbed in fcc-sites and the additional H-atom, produced by the dissociation, would adsorb in a hcp-site, because all four fcc-sites in the (2x2)-cell are already blocked (line 4 in Table 4.3). This increases the barrier for dissociation to 47 kJ/mol, because the adsorption of the additional H-atom at the hcp-site is energetically highly unfavorable. This

value has been corrected for vibrational contribution (as mentioned in the subset of Table 4.3). The uncorrected value for the barrier is 61.8 kJ/mol. The corrected energetics, including the barrier for the transition and final state for such situation, are shown in Figure 4.6.

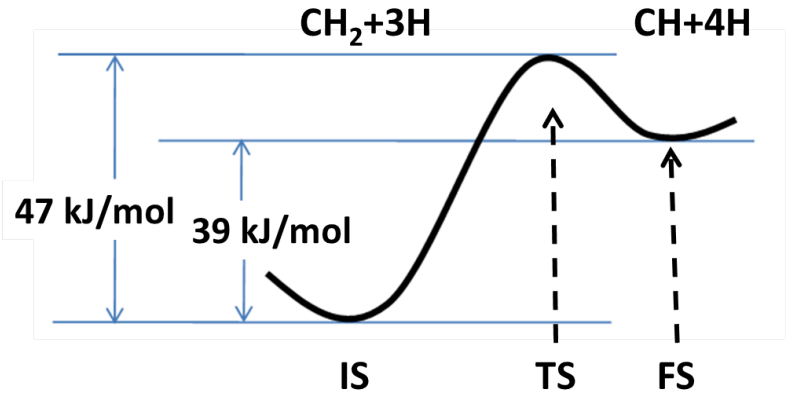

Figure 4.6: This figure shows the energetics of dissociation in case of high coverages at the surface. The adsorption of CH+4H is 39 kJ/mol more unfavorable than CH_2+3H. This induces an activation barrier for the dissociation process of 47 kJ/mol.

As the reader can see the activation barrier for dissociation is ≈ 47 kJ/mol under this conditions, which is much nearer to our measured value of 65 kJ/mol than van Santen‘s calculated value of 16 kJ/mol. Unfortunately, this pathway is unlikely to be the explanation for our observation. The energetics of the final state are so unfavorable (because it is an up-hill reaction) that the adsorbed CH would react back with a co-adsorbed hydrogen to produce CH_2 again. Than we should see no depletion of our measured CH_2 signal.

The way to address this problem can be found in the total energy of the final state. As already said, it is energetically extreme unfavorable to co-adsorb a H-atom in a hcp-site, if all fcc-site were blocked. It seems therefore more likely to include the possibility of a recombinative desorption of H_2. By including this process the energetics of the dissociation changes once again, as shown in the line 5 in Table 4.3. The barrier for dissociation of CH_2 even increases to 88.4 kJ/mol (because desorption requires some energy) respectively 95.6 kJ/mol without including the vibrational contribution. The final state is in this case highly favorable by a 44.8 kJ/mol lower free energy compared to those of State 0. This means no back reaction can take place. The free energy of state 3a (see Figure4.7) is calculated by taking also the translational and rotational contributions for H_2 molecule in the gas phase into account(i. e. taking into account that its free energy is lowered by $2\mu_H$, compared to the uncorrected value in the bracket). To visualize this trend, Figure 4.7 shows the

total free energy of the different states of the pathway with and without desorption, including the activation barriers.

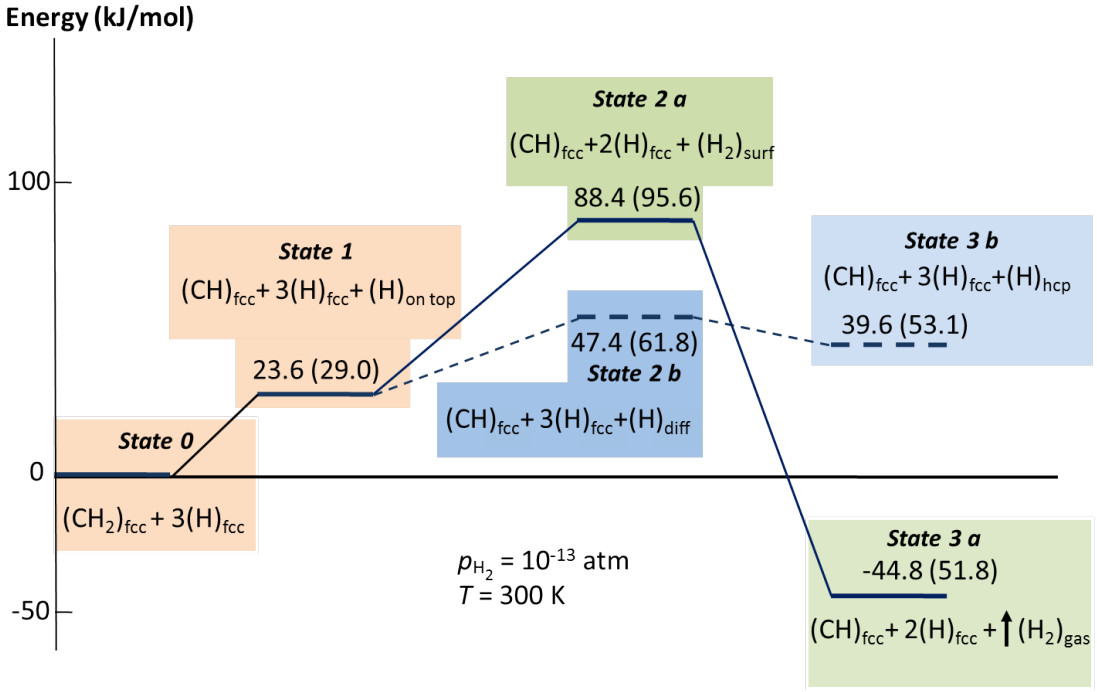

Figure 4.7: Calculated dissociation of CH_2 + 3 H in a 2×2- supercell mode. To simplify the reading, the reaction is divided into 4 steps. State 0 describes the initial condition before dissociation. State 1 reflects the system directly after dissociation, but the system is not relaxed, since the produced H-atom is adsorbed in an on-top position off a Ru-atom. Now the reaction can proceed in two ways. **Way1(no desorption)**: the H-atom has to diffuse across the surface, which requires some energy, as shown in the energy increase between State 1 and State 2b. Finally it relaxes in the energetically unfavorable State 3b, with the H-atom adsorbed at a hcp-site. **Way2(with desorption)**: in this pathway the on-top H-atom forms a H_2-molecule with a nearby H-atom from a fcc-site, which is the step between State 1 and State 2a. Between State 2a and 3a the H_2 molecule desorb and the final State has a total free energy, 44.8 kJ/mol lower than the initial state (State 0). This pathway is therefore energetically favorable. Note: the values in the brackets are without lowering of the energies by vibrational contribution [109] .

Figure 4.7 shows two different possible pathways for CH_2 dissociation, where only one pathway would cause CH_2 depletion. The other pathway without hydrogen desorption would end up in a back reaction. The whole process contains several additional steps, regarding their adsorption geometry. For purpose of a better overview, the graph focused on the main steps, which reflect the reaction pathways. It is the conclusion that the reaction pathway of CH_2 dissociation, which includes H_2 desorption, was experimentally investigated because no back reaction of CH+ H to form CH_2 was observed in the system. The calculated overall activation barrier of such a process is with 88.4 kJ/mol still in acceptable agreement with our measured value of 65 kJ/mol. This conclusion gets also supported by a known overestimation of PBE functionals for calculation of atomization energies of H_2. In the NIST database this overestimation is given with 20 kJ/mol for the used functional of our coworkers. If this would be the case here, the theoretical calculated value and the experimental derived value would be nearly identical.

Nevertheless, you can state that theory and experiment are in agreement with each other, when considering the correct initial conditions of the system.
Let‘s have a brief summery at this point, before coming to further implications of this work. We investigated the dissociation of CH_2 and derived an activation barrier for dissociation of 65 kJ/mol out of our temperature dependent dissociation measurements. This observed barrier is by a factor of 4 larger, than the one predicted from theory for an isolated molecule on Ru(0001)[18]. In an attempt to understand this disagreement we ask our coworkers for new theoretical calculation of this system focusing on the effects of co-adsorbed hydrogen. The calculations have shown that co-adsorption of hydrogen, up to a point where a critical coverage of (CH_2 + 3H) per 2x2-cell were reached, changes the thermodynamics and kinetics of the CH_2 dissociation reaction dramatically. Our experimental conditions suggests that we are at such a critical coverage point. At this coverage the computational derived value for dissociation is 88.4 kJ/mol which is in acceptable agreement with the experiment.

4.3 Interpretation of observed CH_2-stability

After getting some insight into the conditions, when CH_2 is stabilized at the surface, it is necessary to discuss the implications of this observation for "real" hydrocarbon chemistry. In contradiction to experiments and calculations [14, 19] which have shown CH_2 as an unstable molecule and excluded it therefore of being the chain building block in FT, we have shown in our setup that it is possible to create situations where CH_2 is sufficiently stable. Therefore it should be also considered for coupling reactions. At this point, you can try to compare "real" systems to scientifically

investigated systems. For the case of FT synthesis under realistic conditions huge amounts of hydrogen can access the surface, because the used ratio of CO to H_2 in the syn-gas mixture is $\approx$ 1:2 [69]. If this would be the case, this can influence the CH_2 stability in a way that it is getting important for the understanding of the whole process.

One can find for example in literature a possible hint that stabilization of CH_2 can play a role for the FT-process. Goodman and coworkers [13] investigated the formation of hydrocarbons by CO+H_2 reaction under more realistic conditions (high temperature and pressure in the reaction chamber). After the reaction of the sample at 600K in the syn-gas the sample was immediately cooled down and transferred into the UHV, where HREELS measurements were performed. Without subsequent heating of the sample in UHV they were able to observe a vibration band at 1400 cm^{-1}, which they attributed to the CH- scissor mode of a CH_2 containing species at the surface. Flashing of the surface in UHV to 500K removed the peak from the spectrum. Under these experimental conditions it is reasonable to assume, that only two different C_xH_2 species could be apparent at the surface: CCH_2 and CH_2. Other measurements by this group[8, 9] and by us (see chapter 3) have shown that CCH_2 is stable up to 550 K on Ru(0001) with a surface coverage of 60 % ML. Together with our observation of increased stability of CH_2 in case of hydrogen co-adsorption it is a possible interpretation that these measurements have shown CH_2 production by carbon hydrogenation on the Ru(0001) surface. The fact that at conditions, where the mode at 1400 $^{-1}$ can be seen, a vibrational band at 1160 cm^{-1} corresponding to the C=C stretching mode cannot be observed, emphasizes this interpretation. At conditions, where CCH_2 was found at the surface, always both resonances appeared in the HREELS spectrum [8]. The absence of this C=C stretching mode in their spectra [13] suggests that they saw CH_2, which have been prepared under FT-conditions. Nevertheless, all of these indirect evidences can not be verified in the frame of this work.

To relate our conclusions about unanticipated CH_2 stability to FT synthesis it is necessary to revisit the literature in more detail. We have shown that under special circumstances CH_2 could be stabilized at terraces. The main question is whether CH_2, produced at terraces, can be important for the chain-growth and reactivity of a catalyst. Theory has shown that coupling reactions on terraces have higher activation energies compared those at steps[16]. Table 4.4 presents the calculated energetics of fundamental coupling reaction of hydrocarbons on the plane Ru(0001) surface compared to steps on this surface.[131]

As you can see, theoretical calculation emphasizes that defects/steps were favorable for nearly all coupling reactions of the various C_1 compounds. Therefore,

	Ru-step	**Ru(0001)**		**Ru-step**	**Ru(0001)**
C+C	101	146	$CH+CH_2$	116	94
C+CH	**41**	97	CH_2+CH_2	**57**	119
$C+CH_2$	54	104	CH_2+CH_3	135	174
CH+CH	92	84			

Table 4.4: Shown are the activation energies for the main C-C coupling on Ru(0001) at steps and terraces. All values are given in kJ/mol and taken from [131]. Coupling of reactive carbon with CH seem to be energetically most favorable from their calculations. Nevertheless, other coupling reactions, as CH_2 coupling were not so much worse in their energetics for coupling. The energetically most favorable were marked bold in the table.

steps could be seen from the theoretical point of view as the active centers for FT-catalysis.

This behavior of defect driven catalysis is not unknown in chemistry[94]. Another famous example of chemistry that is completely defect driven is N_2 dissociation on Ru(0001)[4]. In this case only a few percents of surface sites, e.g. steps, are thought to completely dominate the dissociation reaction. For FT-synthesis this could also be the case. If this suggestion about a completely defect driven process is true, CH_2 produced at terrace sites should not have a valuable influence on the FT- reactivity.

In contrast to this theoretical prediction of the reaction centers is the experimental work of Brady and Petitt[17]. They showed that the manual deposition of CH_2 groups on the Ru- surface (by adding CH_2Cl_2 into the syn-gas of FT synthesis) increased the formation of higher hydrocarbons. It is likely to assume that CH_2 produced by CH_2Cl_2 dissociation will be mainly deposit at terrace sites because of the low barrier for dissociative adsorption at both terraces and steps (dissociation takes place at temperatures below 250 K at all sites).

A possible way how to connect the results of the calculations and the experimental observations would be the inclusion of surface diffusion into the reaction route. The idea behind this could be described as follows: CH_2 from terrace sites diffuses above the surface, gets trapped at a step and react to longer chains up the point, where the termination of the chain happens. Then it leaves the surface. This mechanism could play a role under three conditions:

1.) The amount of CH_2 at terraces, which can diffuse to a defect site, must be large compared to the amount of defect sites
2.) The barrier for diffusion must be small compared to the activation barrier for hydrogenation of C and CH at defects

3.) The activation barrier for diffusion must be small compared to the activation barrier for coupling of C or CH at defects

Calculation of Ciobica et al. have shown that the diffusion barrier of CH_2 on Ru(0001) is approximately 23 kJ/mol[86]. As shown in Table 4.4, all activation barriers for coupling of C_1 compounds are much lager than this diffusion barrier. Furthermore, also the barriers for hydrogenation of C or CH can be expected to be larger[16]. This implies, that in case of an external source of CH_2, as it was the case by CH_2Cl_2 addition into the syn-gas[17], this could explain their experimental observation of enhanced chain growth. From this point of view, it is reasonable to assume that CH_2 at terraces can play a role in the FT-synthesis.

The remaining question is, whether CH_2 plays a role in the "real" FT-process where no additional CH_2 will be inserted into the system. There, CH_x compounds must be generated by CO dissociation and carbon hydrogenation. Van Santen and coworkers found by their calculations that the dissociation of CO on Ru(0001) at mono-atomic steps is the rate determining reaction in FT with a barrier of 90 kJ/mol. In comparison, the same reaction on terraces has a barrier of 180 kJ/mol [87]. This implies that the FT- process starts at steps. There would be now two questions for us:

A.) would at steps generated C or CH diffuse onto terraces?
B.) would have the hydrogenation of C as well as CH similar thermodynamics and kinetics at steps and terraces ?

It is problematic, to give a correct answer for these complicated questions. Let us discuss first question A. Generally we can assume that diffusion barriers for leaving defects will be higher than those for diffusion across a terrace. The lower coordination of the substrate atoms at defects creates a stronger overlap between the electron orbitals of the substrate and the molecules, what induces therefore a stronger bonding. On the other hand you must take into account that the high temperature during the FT synthesis should enable diffusion of all carbon compounds at all surface sites. Otherwise no chemistry could take place because the surface would be deactivated after initial adsorption of molecules.

The discussion of question B is connected with the problem that there are no calculated values for hydrogenation of C_1 groups at steps available to the best of our knowledge. What can be compared are the activation barriers for hydrogenation on a Ru(1120) (i.e. a stepped surface)[16, 88] to those of the plane surface of Ru(0001)[131, 16]. While the hydrogenation of a single carbon atom is energetically more favorable at steps (the barrier is 55 kJ/mol) than at terraces (barrier is 75 kJ/mol), the effect

of steps on the hydrogenation of a CH molecule is not that big. Hydrogenation of CH at steps is only 10 kJ/mol more favorable than at terraces (51 kJ/mol vs. 61 kJ/mol). These calculated barriers did not include the effect of hydrogen saturation of the surface (saturation means in this purpose coverages of hydrogen, which strongly changes the kinetics and thermodynamics). This could even shift these barriers to lower values. In the work of Van Santen [16] they already see strong differences for the hydrogenation on the Ru(0001) terrace in order of hydrogen coverage. Half of the coverage nearly doubled the activation barrier for hydrogenation of CH. Comparable effects have been also reported by Neurock et al. [19], who found that high coverages of hydrogen in surrounding of C_xH_y lowers the activation barrier for hydrogenation. Nevertheless, it is necessary to mention that all of the coupling and hydrogenation barriers were small compared to the dissociation barrier of CO. This suggests that all of these reactions could happen at the same time, only with a different efficiency. Seen from this point, terrace bound and by hydrogen stabilized CH_2 can play a role in the FT synthesis.

Since the effect of defects on occurring chemistry was discussed at length, it would be interesting to investigate also CH_2 at steps. Therefore, we tried to separate the spectral response of CH_2 at steps from those at the terraces, to understand, whether kinetics and thermodynamics of the CH_2→ CH + H reaction were different from those at the plane surface.

4.4 Arrhenius analysis of CH_2 at defects(steps)

After the detailed investigation and discussion of CH_2 created on terraces, it is clear that the investigation of CH_2 at defect sites would be interesting too. Egeberg et al. have shown in their paper[12] that short time exposure of Ru(0001) to methane in a HPC saturates a limited number of surface sites which they identified as steps. They came to this conclusion by deposition of Au-atoms to the surface which are known to grow at step-edges and therefore block these sites. Differences in Temperature Programmed Oxidation experiments they performed indicated, that approximately 2-3% of the surface were steps, which were deactivated for methane decomposition after Au-deposition.

Our approach to create a sample with adsorbed CH_2 only at steps was to dose for a short time with the MBS: a nozzle temperature of 830 K for 5 min with T_{Ru} = 350 K. By doing this we were able to observe in the SFG spectra a new species at surface, which was not seen before. A peak at 2925 cm^{-1} appeared in the spectra (To remind the reader: the center-frequency of CH_2 at terraces was ≈ 2940 cm^{-1}, as shown in Section 4.2). The surface coverage of a sample prepared in that way were

about 3-5 % of a ML of carbon, which corresponds to the given values of Egeberg for the step density.

Assignment of this peak to CH_2 at defects follows for several reasons. First of all, the spectral intensity saturates at carbon coverages in the regime of the defect density. Dosing longer did not increase the intensity of this peak. Only a second peak in the spectrum appeared, which could be identified as the ν_s of CH at 3010 cm^{-1} (see Figure 3.1 in Section 3.1.1). Furthermore, heating of the sample to temperatures above 380 K directly converted the species into CH, which suggests that it is a precursor of CH. Even keeping a sample with this species for 15 minutes at 350 K leads to disappearance of the 2925 cm^{-1} peak and appearance of the CH. As the last evidence, we saw the same peak by our low temperature dosing experiments (T_{Ru} = 250 K) for short dosing times (5 min). With increasing dosing time the peak started to grow and build up the resonance, which we know to be CH_2 at terrace sites. To demonstrate the similarity of both species regarding their spectral response, we compare them in Figure 4.8.

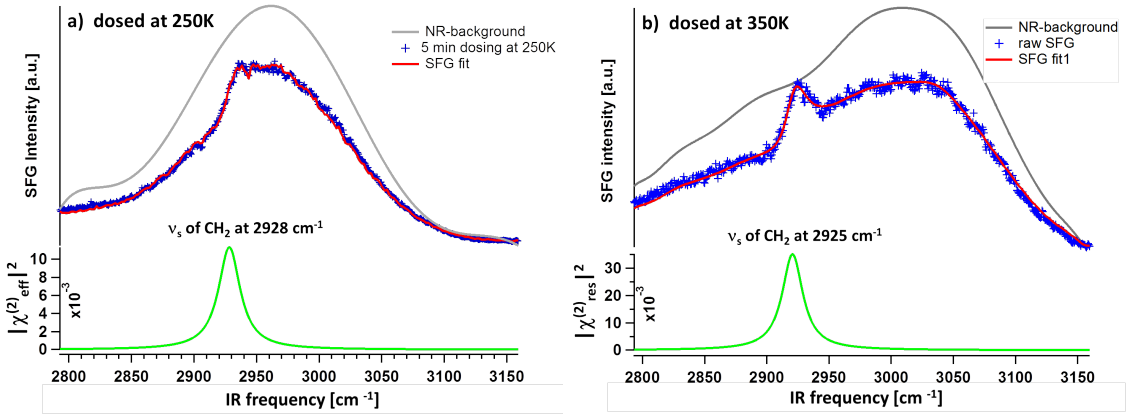

Figure 4.8: Comparison of spectral response of Ru(0001) surface, at different sample temperatures. a) was prepared by 5 minute dosing at a surface temperature of 250K. b) was prepared by 5 minute dosing at 350K. Both the center frequency and thermal stability of the spectral feature were comparable for the two preparations.

As you can see in Figure 4.8 at low coverages both peaks appear nearly at the same position. Just the intensities of both are different. This has the origin in the fact that in case of a 5 minute dosing time in graph a), the defects were not saturated. This happens at longer dosing time of about 8 minutes. Unfortunately we can observe that longer dosing times and saturation of this feature induces a further shift of the center-frequency compared to graph b) for a few more wave-numbers to about 2932 cm^{-1} (the uncertainty of these measurements was $\approx$ 4 cm^{-1} and based on the low signal to noise ratio). One could argue this implies that the observed species were

not the same. On the other hand, you have to take into account that the situation at the surface it not identical. By dosing at a surface temperature of 350 K it is reliable to assume that all defects were saturated (because of higher sticking coefficient for methane at defects [12]). Only few other molecules (mainly CH at terraces) would be co-adsorbed (co-adsorption of H or CO is lowered or completely suppressed, since hydrogen desorbs at 300 K [114] and CO starts to desorb at 300 K [150]). Therefore, a more or less clean surface with CH_2 at defects is investigated. By doing the same at 250 K surface temperature, you will have co-adsorbed H, CO and possibly some CH or CH_2 at terrace sites. Especially the effect of CO on the spectral response is thereby important. It is known that CO co-adsorbed with hydrocarbons induces a blue shift in the vibrational spectrum of the hydrocarbons in the CH-stretching region.[115] The origin of this blue-shift based on dipole-coupling effects of the adsorbates. For the case of dipole-dipole coupling of the CO on Ru(0001) similar effects have been reported [84, 151, 161]. In our system we have to assume, that while dosing at 250 K the amount of CO co-adsorbed from the background of the chamber will accumulate and could be one reason for the shift. Here it must be referred back to Figure 3.4 which showed the C+O desorption spectrum for a CH_2 covered sample, where always a small peak around 400 K was observed which had its origin in molecular adsorbed CO from the background. In literature [84] they have shown, that even 1-2 % of a ML of CO can induce shifts of several wavenumbers. The effect of other co-adsorbed molecules is hard to quantify, but a following chapter will focus more on coverage dependent frequency shifts. Taking all these facts together it is reliable to assume that Figure 4.8 a) as well as b) show CH_2, which is adsorbed at steps on Ru(0001).

With this information about the species it is now the aim to derive the activation energy for dissociation of CH_2 adsorbed at steps out of the SFG data. Therefore the same Arrhenius plot treatment was applied, as already introduced above. For the required series of measurements the sample was prepared at T_{Ru} = 350 K and 830 K nozzle temperature. The relative high surface temperature of 350 K compared to CH_2 at terrace sites (T_{Ru} = 250 K) was chosen, because the CH_2 seemed to be still stable under this situation (as you can see in Figure 4.8). Furthermore, it is clear that under these experimental situation no hydrogen will be co-adsorbed, because hydrogen desorbs from the surface at temperature above 300 K [137, 114]. This suggests that these observed CH_2 species are not stabilized by hydrogen co-adsorption and the observed thermal stability is the result of characteristics of the adsorption site.

After dosing the sample was cooled to 100 K for spectral characterization. The full procedure for the method is already introduced in a prior section (see Section 4.1) and summarized in Figure 4.1. For this measurements baking temperatures between 330 K and 380 K were used.

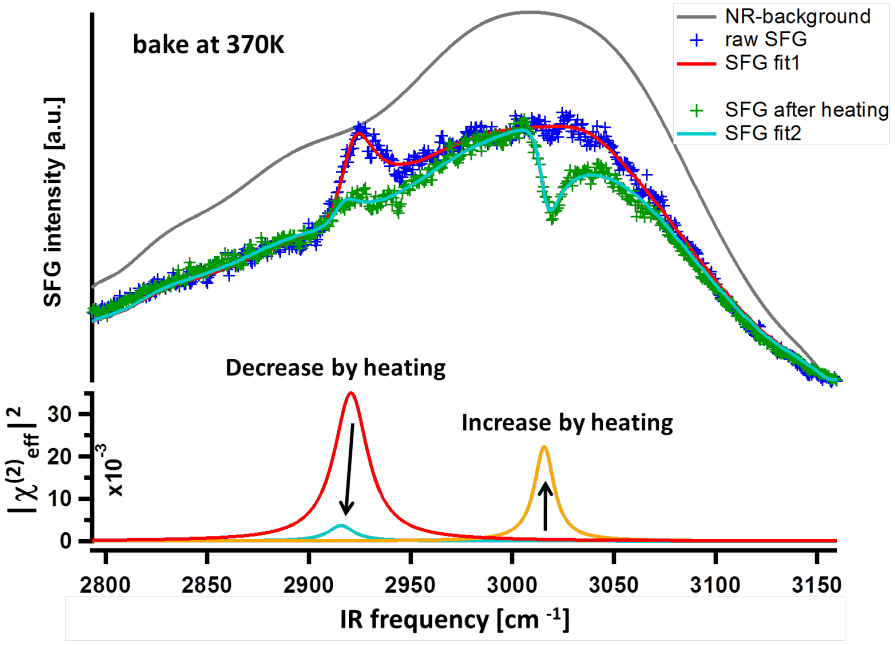

Figure 4.9: This figure shows the experimentally gained spectra for a sample with CH_2 at defects, which has been treated similar as shown prior section and Figure 4.2. As quite clear from the spectrum, annealing of the sample to a temperature of approximately 370 K induce a strong decrease in signal intensity of the CH_2, together with the appearance of the ν_s of CH at the surface.

As shown in Figure 4.9 we observe again a strong signal dependence on the surface temperature. Interestingly, it was possible to see the small signal of CH in the spectrum after the heating. This is in contrast to our prior measurements, shown in Figure 4.2, where after the heating process the signal of CH was absent at annealing temps below 300 K. A valuable explanation of this observation is that the relative IR-intensities of CH co-adsorbed with and without hydrogen in the surrounding are different, which will have a strong effect of the SFG-intensity. This observation has been found by our coworkers from the Theory department. They calculated the IR-intensity of the stretching modes of different CH_x radicals on Ru(0001) in order of coverage. In their calculation they included the effect of high hydrocarbon coverage as also the effect of co-adsorbed hydrogen. Their calculations have shown, that the IR intensity of a CH molecule decreases amazingly (by a factor of 10) in case of co-adsorbed hydrogen. The IR intensity of CH_2 on the other hand has been found to be relatively independent of co-adsorbed molecules. That can clearly explain the differences in spectral responses at low and high temperatures. Their results of calculation will be topic of a further publication.

Nevertheless, as it is clear from Figure 4.9, it is possible to perform the Arrhenius plot method at this adsorption system with an acceptable resolution. The relatively

Baking Temp in K	A_1 **before Baking**	A_2 **after Baking**	N^2
330	1.935	1.089	0.563
335	1.032	0.753	0.73
340	1.597	1.144	0.716
345	1.425	0.765	0.537
350	1.888	0.911	0.483
350	1.625	0.833	0.51
355	1.32	0.822	0.623
360	1.329	0.705	0.530
360	1.507	0.427	0.283
365	1.447	0.39	0.282
370	1.431	0.397	0.277
370	1.447	0.39	0.26
375	1.158	0.172	0.149
380	1.346	0.048	0.036

Table 4.5: Table show the from experiment extracted values for the intensity of the CH_2 resonance before and after heating to a certain temperature. Values of A_1 and A_2 are given from our line shape model and were proportional to the Amplitude × FWHM of a certain resonance. The N^2 is given by (A_2/ A_1)

small intensity of the resonance compared to that of CH_2 on terrace sites produces a higher signal to noise ratio. Performing the measurement cycle, which is shown in Figure 4.9, at different baking temperatures creates a dataset shown in Table 4.5. Given these quantities we were able to create an Arrhenius plot, shown in Figure 4.10.

The Arrhenius analysis of this data gives a value for the activation barrier of dissociation, which is 45 (+/-) 6 kJ/mol. Unfortunately the uncertainty of the dataset was much bigger than in our prior analysis, but the linear trend in the shown data is still obvious. The value of 45 kJ/mol for the activation barrier of dissociation is an interesting result for this system. For interpretation of this value we should have several informations in our mind. Preparation of a sample, as was done is this dataset, created a situation where CH_2 is adsorbed at the surface only at low coverages compared to our data describing CH_2 on terrace sites. Additionally, there were no hydrogen co-adsorption because of the higher surface temperature. Under these situations, CH_2 on terrace sites has an activation barrier for dissociation of approximately 16 kJ/mol [18, 86], as you can see in Figure 4.4. This implies that the dissociation barrier at defects is 3 times higher than st terrace

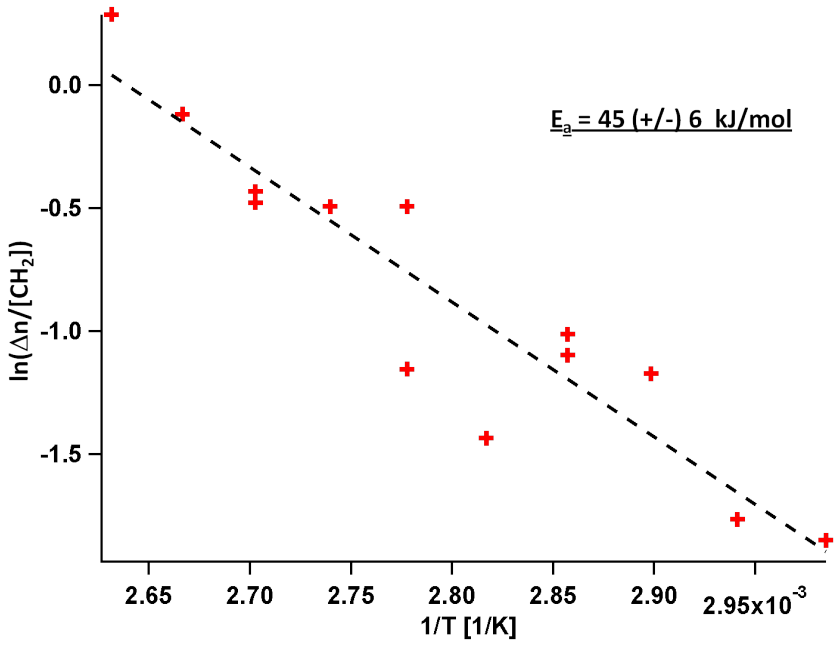

Figure 4.10: Graph show the Arrhenius plot for conversion of CH_2 to CH at defects. Compared to the Arrhenius plot of CH_2 to CH , the noise or uncertainty of the dataset is much bigger. This is due to the smaller spectral intensity of the resonance which increases the uncertainty of the fits. Nevertheless, you can identify a linear trend in the data and derive out of the dataset an activation barrier for the conversion of 45 kJ/mol.

sites under approximately equal conditions. As mentioned above, there is to the best of our knowledge no theoretical or experimental work available that focuses on the kinetics/thermodynamics of CH_x dissociation on Ru(0001) steps. This makes it hard to compare our values to others. But once again the dissociation of methane on Ru(1120) could give us some hints. On this surface, CH_2 has an activation barrier for dissociation of about 52 kJ/mol [16, 88]. Because the Ru(1102) surface could be possibly seen as a stepped surface the value for the activation barrier on this surface could eventually be comparable to those of Ru(0001) steps: then it is in good agreement with our result.

4.5 Interpretation and discussion of CH_2 on terrace and defect sites

Here I want to discuss our findings regarding their implication for the understanding of prior work. We observed in our measurements that CH_2 at defects is much more thermodynamically stable than at terrace sites. Furthermore, a dissociation barrier

for CH_2 at defects of 45 (+/-) 6 kJ/mol was observed, which is three times higher than at terraces under similar conditions. This observation implies that even in case of equilibrium conditions, defect bound CH_2 can play a role in the FT-synthesis. Additionally, there were also other findings regarding the surface mobility of the species. With the valuable assumption, that CH_2 on terrace sites at low coverages without hydrogen co-adsorbed would be unstable and dissociate (dissociation barrier $\approx$ 16 kJ/mol [18]), one must assume that each CH_2 species which diffuses away from the defect site would immediately dissociate. The fact, that this species can be observed more or less stable at 350 K, leads to the conclusion that CH_2 at steps must have for the step→terrace diffusion a much higher barrier than CH_2 at terrace sites have for diffusion across a terrace. This is reported to be 26 kJ/mol[86]). If both CH_2 types (step and terrace) would have the same diffusion barrier, the defect bound CH_2 would be mobile at room temperatures and at 350 K the mobility would even increase. This would cause the dissociation of the CH_2 by diffusion from a defect to a terrace site and it should not be possible to observe it. Following this argumentation, this implies that the diffusion barrier of CH_2 at steps must be in minimum case from the same size of the dissociation barrier, or higher. As a conclusion from this you could be actually not sure, whether we have derived out of the Arrhenius analysis of CH_2 at steps an activation barrier for diffusion of CH_2 away from the defects or for dissociation of CH_2 at steps.

Generally the observations made in this work could give some new insight into the field of FT-synthesis and the question of whether CH_2 is a reactive group for coupling reactions of hydrocarbons. With this up to now unobserved effects of co-adsorbate's on the thermal stability, new reaction routes for some of the coupling reactions could be considered for the correct explanation of the complex chemistry happening during the FT-process. Thereby two different formation routes of CH_2 while the FT process must be considered. On the one hand the formation of CH_2 via hydrogenation of carbon (which should start at steps). On the other hand the formation of CH_2 by re-adsorption of methane which is a common by product during the FT-synthesis [92]. This re-adsorption could probably occur at defects as well as at terraces. Re-adsorption of this CH_4 on terrace sites could then create CH_2 groups (due to the high partial pressure of H_2), which could diffuse to steps and further react to longer hydrocarbon chains. The positive effect of CH_2 deposited on terrace site has been already demonstrated by Brady and Pettit[16]. Possibly, this effect can also play a side roll in the concurring reaction paths of FT synthesis.

Chapter 5

Investigation of CH coupling induced CCH_2 formation

In Chapter 3 and 4 we discussed the implication of my work for the understanding of the chain growth step in the Fischer-Tropsch synthesis. Despite the FT-synthesis it is obvious that the direct conversion of methane without transformation into syn-gas would be desired chemistry . Here I will focus on the direct coupling processes of methane at comparably low surface temperatures. A general problem for this kind of chemistry is the energy efficiency and the lifetime of operating catalysts. The direct conversion of methane into higher hydrocarbons like pyrolysis operates only at elevated temperatures of 1200 K or more [178]. Thereby the coupling reaction occur directly in the gas-phase. Performing the coupling reactions on a catalytic surface reduces the working temperature, for example in case of the oxidative coupling of methane (OCM) to 1100 K. Used catalysts for the OCM consists of various metal oxides which contains reactive oxygen-centers for hydrogen abstraction from the methane. The remaining CH_3^*-radical could couple with other radicals and followed by desorption into gas-phase. The efficiency of conversion is about 25 % for C_{2+} hydrocarbon groups[3].

Later on, the investigation of low temperature coupling reactions of methane became more prominent [148]. It has been found that the catalysts for OCM decreased their reactivity for coupling reactions over time. This was explained by poisoning effects (for example coke formation) and a reduced amount of reactive centers due reorganization and deactivation of the surfaces at high temperatures. Therefore many investigations wanted to discover other pathways for methane coupling which operates at lower temperatures. That would be energetically more favorable and reduces deactivation processes of the catalyst due to high temperatures [134].

The problem of this low temperature methane coupling reactions is the up to

now relatively low efficiency for the coupling reactions. The efficiency is about 15-20 % of ethane and higher hydrocarbon yield. Therefore much experimental and theoretical work has been performed on the understanding and improvement of the ongoing coupling reactions since the first experimental observation in the 80's [68, 159, 102, 10, 116]. During the last decade Goodman and coworkers identified the main building block for ethane production on Ru-single crystals for the low temperature coupling reaction [85]. They suggested the relatively stable vinelydene (CCH_2) intermediate to be the direct precursor state for hydrogenation and ethane production during methane coupling. Figure 5.1 is a summery of their observations. In Goodman's understanding the methane coupling process contains two important

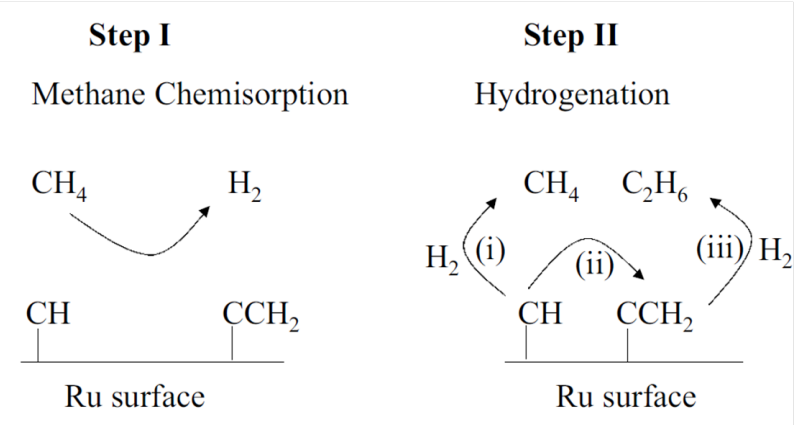

Figure 5.1: The scheme summarizes the experimental observed hydrocarbons groups produced during CH_4 activation on Ru(0001). Goodman and coworkers suggested CCH_2 to be the precursor state for ethane and higher alkanes production in the low temperature methane coupling reaction. Hydrogenation of the CCH_2 should result in a desorption of an alkane/alkene. Figure taken from literature [85]

steps. The first step is the dissociative adsorption of methane, as shown in Figure 5.1. The optimum temperature for dissociative adsorption has been found to be 500 K on Ru single-crystals [10]. This temperature optimum for the first step follows from two constraints: the dissociative sticking coefficient of methane increases with temperature while the thermal stability of the resulting hydrocarbon compounds decreases.

After reaction of the Ru-surface with methane at 500 K two different C_xH_x species have been identified: CH and CCH_2 [8, 10, 13]. Because CH would have to polymerize and hydrogenated to be important for ethane production, CCH_2 is suggested to be the precursor. But even there has been performed plenty of work on this topic, it has been found challenging to identify the correct stretching frequency of CCH_2 in CH-stretching region. This missed observation is an obvious lack of knowledge for the system if you are interested in the understanding of the formation

channels for the suggested precursor state.

It was have already shown in previous chapters that it was possible to identify and distinguish all the different carbon containing groups in the CH-stretching region (see Chapter 3). Especially those which are present at the surface under preparation conditions similar to those of Goodman. With this capability it would be nice to gain a deeper understanding of CCH_2 formation via CH coupling on Ru(0001).

5.1 CCH_2 formation by CH coupling

In the following section will be a discussion of the influence of several parameters on the formation of CCH_2. These parameters will be the surface temperature and the surface coverage of hydrocarbon containing groups. Later on you will see that both factors have a certain influence on the observed signal of CCH_2 in our SFG spectra.

At the beginning we will start with comparison of two samples which had comparable carbon coverage. Only the preparation temperatures where different. Figure 5.2 a) shows the spectral response of a sample which was dosed by the MBS at T_{Ru}= 350 K for 40 minutes and had coverage of 54% ML. Figure 5.2 b) shows the response of a sample which has been dosed at T_{Ru}= 400 K for 20 minutes and had a coverage of 58% of carbon ML. It is clear that both sample are in a regime of comparable surface coverages. By comparison of the spectral responses Figure 5.2 a) nearly shows a single resonance ν_s of CH at 3013 cm^{-1}, while b) also contains small contributions of CCH_2 at 2919 cm^{-1} and CCH at 2960 cm^{-1} in the spectrum. This

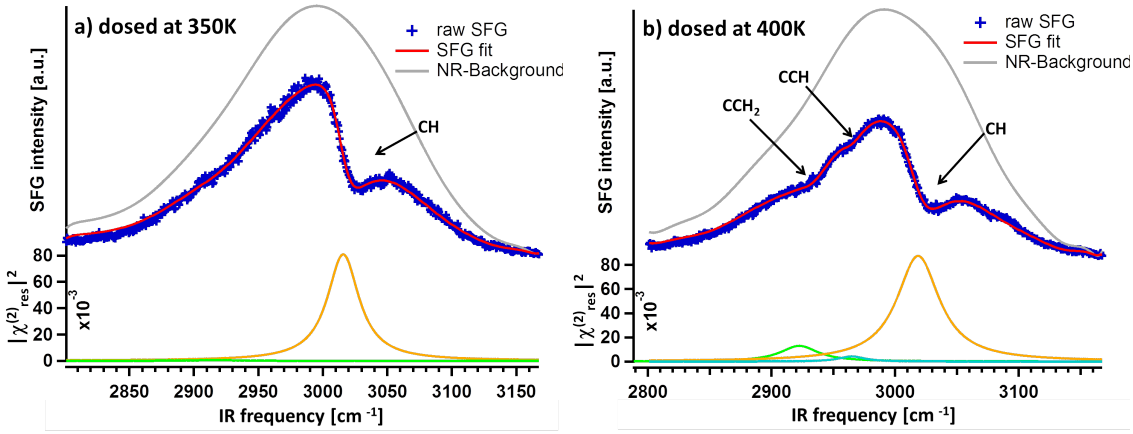

Figure 5.2: The graphs a) and b) show the relative SFG intensity plotted over the frequency. Both samples were prepared with similar coverages, but at different surface temperatures. In case of preparation at 400K additional resonaces apprear in the spectrum.

observation suggests that the formation of CCH_2 by the coupling of CH requires more energy than could be provided by the surface at 350 K. At 400 K this situation

seems to be changed because CCH_2 (and CCH) was more prominent in the spectrum. Beside the obvious dependence on the surface temperature it is valuable to assume that surface coverage plays an important role in CCH_2 formation. It was already proved in the last chapter that blocking of adsorption sites plays a role in stabilization of C_xH_x compounds at the surface. There the stabilization of CH_2 happened by co-adsorbed hydrogen. We suggest that blocking of adsorption sites by other carbon containing groups should have a similar effect.

Furthermore, a higher coverage should also result in more collision events and therefore in an enhanced CCH_2 formation. Let us compare the sample with 58% of a carbon ML to a sample also prepared at 400 K but with 78 % of a carbon ML to validate this conceptual model. Figure 5.3 shows that the relative intensity of the CCH_2 resonance amazingly increases with carbon coverage. The relative intensity of

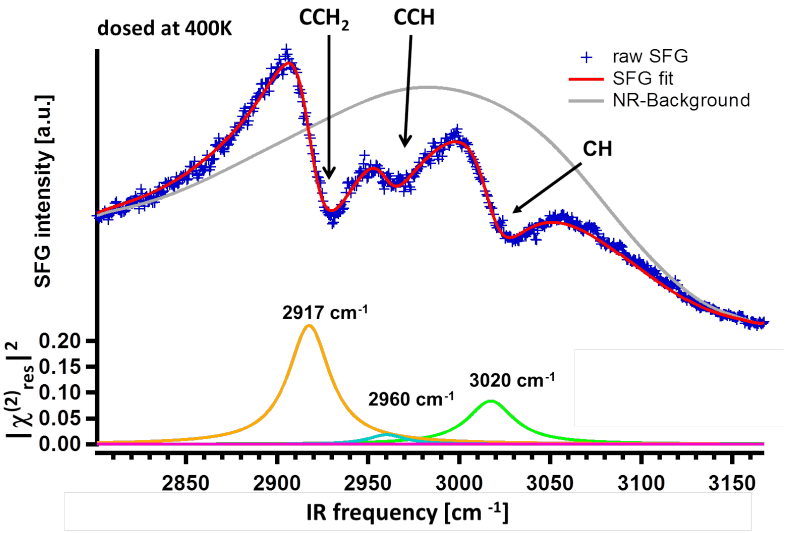

Figure 5.3: Coverage dependency of CCH_2 formation. Investigated sample had a coverage of ≈ 80 % of a ML carbon. The resonance intensity of CCH_2 changed in this case over-proportional compared to Figure 5.2 b). The intensity of the CH-stretch is nearly the same between both samples, while those of CCH_2 is one order of magnitude higher.

CCH_2 compared to CH did not scale linearly with increasing coverage. This verifies the assumption that higher coverages support CCH_2 formation.

It is an interesting question whether the presence of CCH Figure 5.3 is the result of CCH_2 dissociation ($CCH_2 \rightarrow CCH + H$) or of coupling between CH and C. The formation barrier of CCH at terrace sites by coupling of CH and C has a calculated value of 97 kJ/mol [131] (see Chapter 4). This barrier is just slightly higher than the barrier for CH+ CH coupling (barrier of 85 kJ/mol [131]) which suggest both formation path are likely. The barrier heights for the coupling of the different hydrocarbon groups at the surface were already listed in Table 4.4.

Against the suggestion of CCH being produced by coupling is the fact that the observed spectral intensities of CCH_2 and CCH had nearly always the same ratio to each other, even though they were prepared at different temperatures and coverages. For comparison you can look at Figure 5.2 b) and 5.3: both sample were prepared at same temperature but with different dosing times and coverages. The CCH_2/CCH ratio between both samples was comparable. If CCH would have been produced by C and CH coupling there should have been preparation conditions (e.g. dosing time, surface temperature, nozzle temperature) where the relative intensity ratio between both resonances would have changed. This means the relative ratio to each other should depend on preparation conditions what was not the case within my experimental framework.

Because of that, CCH is assumed to have its origin in the dissociation of CCH_2. Changing the seeding gas from He to H_2 should hinder the dissociation process of CCH_2 by a permanent flux of Hydrogen from the molecular beam.

In the last chapter stabilization effects of co-adsorbed hydrogen on C_xH_y groups were already shown. These stabilization effects had their origin in blocking of hydrogen adsorption sites which could either happen by carbon, hydrocarbon species or by hydrogen itself. That is the reason why carbon coverages plays an important role for stabilization of coupling products. We have shown during the last chapter that blocking of favored hydrogen adsorption sites changes the thermodynamics of a surface dramatically. This makes dissociation of CH-bonds much more unlikely.

The idea behind blocking of the adsorption sites by using Hydrogen as seeding gas of the MBS is as follows. Literature reported that adsorbed hydrogen desorbs at temperatures above 300 K. Because of the dosing at 400 K normally no hydrogen should be apparent at the surface and therefore should influence the relative C_xH_x stability.

But by usage of hydrogen as the seeding gas for the MBS the beam contains 95% of hydrogen which induce a permanent flux on the surface. This flux may inhibit dissociation effects. To evaluate the plausibility of this scenario I estimated the amount of Hydrogen which is impinging the surface per adsorption site and second. Therefore it is necessary to estimate the flux of Hydrogen in the molecular beam. From the literature you can estimate the centerline beam flux of hydrogen in the MBS by the following formula [55]:

$$I_{Ideal} = \frac{\kappa}{\pi} \quad F(\gamma) \cdot n_0 \sqrt{\frac{2kT_0}{m}} \left(\frac{\pi d^2}{4}\right) \tag{5.1}$$

I_{Ideal} gives the centerline beam-flux in units of $molecules\ cm^{-2}\ s^{-1}$. n_0 is the molecule density in the nozzle, T_0 is the nozzle temperature, m is the mass of molecules and d

is the diameter of the nozzle. k is the Boltzmann constant. $F(\gamma)$ is determined by the heat capacity ratio γ of the used gases and given by

$$F(\gamma) = \left(\frac{\gamma}{\gamma+1}\right)^{1/2} \left(\frac{2}{\gamma+1}\right)^{1/(\gamma-1)} \tag{5.2}$$

κ is a unit-less experimentally derived value for a certain seeding gas, which is called peak factor. Furthermore we need to know for Equation 5.1

$$n_0 = \frac{p_0}{RT_0} \quad ; \quad F(\gamma) = 0.513 \qquad and \qquad \kappa = 2 \quad (values\ for\ H_2) \tag{5.3}$$

The values are taken from [55]. At a nozzle temperature of 860 K, a pressure in the nozzle of 4 bar and a diameter of the nozzle hole of 35 μm we can estimate an ideal flux of about 5.7 x 10^{19} molecules $sr^{-1}s^{-1}$. The unit sr is the abbreviation of steradian. A sample surface which is 30 cm away from the nozzle get the following flux:

$$I_{H_2} = I_{Ideal} \cdot 95\% \frac{1}{(30\ cm)^2} \ = \ 6 \cdot \ 10^{16}\ molecules\ cm^{-2}\ s^{-1} \tag{5.4}$$

With a number of 1.58 x 10^{15} adsorption sites on Ru(0001) per cm^{-2} [4] it is obvious that there will be a permanent exchange of hydrogen at the surface.

Let us have a look on a sample which has been prepared by dosing with a gas mixture of CH_4/H_2 (5%/95%). By dosing 20 minutes at a surface with 400 K surface temperature you get a sample with a coverage of 87% carbon ML and a vibrational response as shown in Figure 5.4. As clear from inspection of the Figure 5.4 the spectrum did not show any feature of CCH. Therefore you can conclude that seeding with hydrogen suppresses dissociation of CCH_2. If this conclusion would be correct subsequent annealing without dosing with hydrogen should create CCH by CCH_2 dehydrogenation/dissociation. Annealing the sample of Figure 5.4 up to a temperature of 535 K followed by cooling and a next spectroscopic characterization gives a sum frequency spectrum as shown in Figure 5.5:

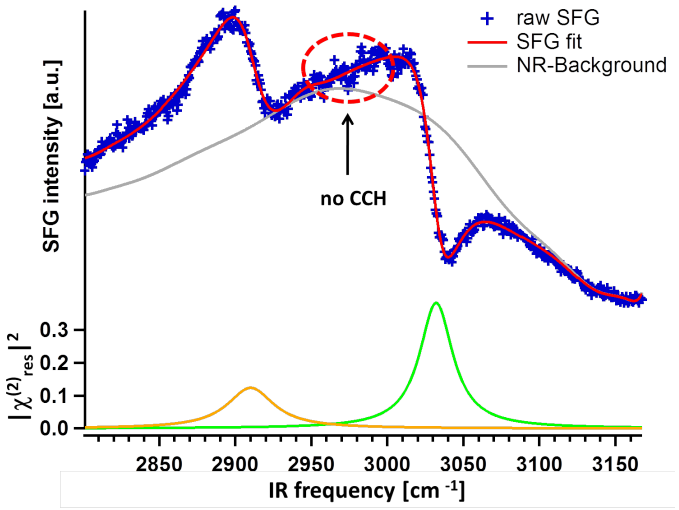

Figure 5.4: The Figure shows the SFG response plotted over the frequency of a sample prepared with Hydrogen as seeding gas. The sample temperature was 400 K which is above the hydrogen desorption temperature [114]. The change of the seeding gas should have two effects. The lower mass of the seeding gas creates a situation in the molecular beam,where the CH_4 molecules will have enhanced kinetic energy[53]. Therefore it is possible to have higher carbon coverages with a shorter dosing time. The second effect of the hydrogen is the observed suppression of CCH in the vibrational spectrum. We attributed that to saturation effect of hydrogen adsorption sites by hydrogen from the source. This should hinder CCH_2 dissociation and thus suppressing CCH formation.

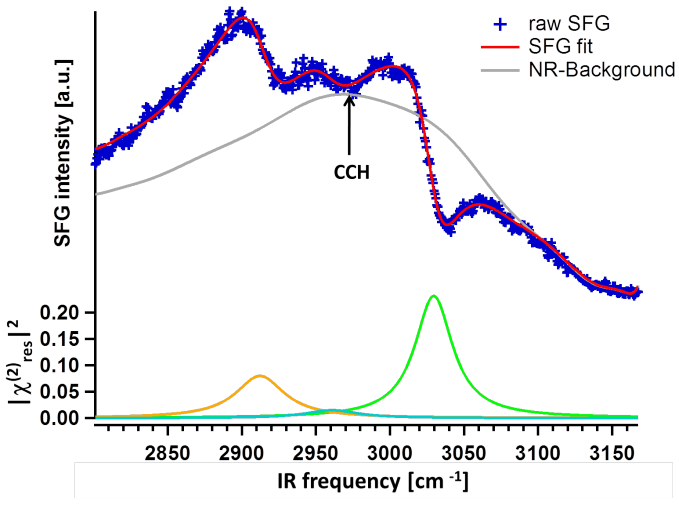

Figure 5.5: Sample from Figure 5.4 annealed to a temperature of 535 K in the absence of H_2. After this treatment, a small resonance off CCH at 2960 cm^{-1} appeared in the spectrum. From that we conclude that the observed CCH in our spectra is a product of CCH_2 dissociation.

Subsequent annealing of the sample produced again CCH being consistent with CCH production via CCH_2 dehydrogenation. This suggests the following formation mechanism (Figure 5.6). It should be possible with these insights in the formation

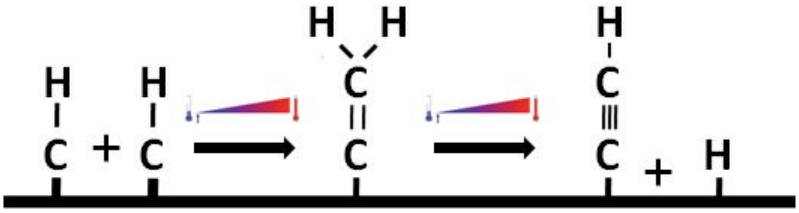

Figure 5.6: Assumed formation path for CCH_2 formation on Ru(0001). CH seems to polymerize by formation of CCH_2 which further dissociates to CCH

channels of CCH_2 and CCH, and giving appropriate temperature dependent data, to investigate CH coupling quantitatively.

5.2 Temperature dependent formation of CCH_2

For a more detailed investigation of CCH_2 generation we induced formation of CCH_2 by thermal treatment of a CH covered sample where CCH_2 was initially absent. These results of this treatment are shown in Figure 5.7. The graph shows a series of measurements of a CH covered sample with a carbon coverage of about 30 % of a ML carbon. It was flashed subsequently to higher temperatures e.g. 400 K, 425 K, 450 K.... . The sample itself was prepared at 350 K and showed at this temperature a single peak resulting from CH. Figure 5.7 shows how the vibrational spectra changes with increasing flashing temperature. As a little reminder: flashing means a fast increase of surface temperature to a certain level followed by a fast decrease to 110 K for characterization with SFG. Below 400 K flashing temperatures no CCH_2 was apparent. Higher flashing temperatures induced its formation. At temperatures above 500 K, CCH_2 and CCH once again disappeared. To show this behavior more qualitatively I integrated the fitted resonance of CCH_2 and extracted the relative population. I scaled the maximum intensity to 1 because we could not quantify the absolute number of CCH_2 present in any SFG spectra. We can suggest for our system that the relative amount of CCH_2 will be somewhere between 2-3% of a carbon monolayer which means about 1/10 of the total carbon coverage of the sample. This suggestion followed from the fact that we can see nearly no effect of the CCH_2 formation on the intensity of the CH signal (the decrease of CH signal at higher temperatures is discussed below). This means it must be within the experimental uncertainty for CH detection. The result of the CCH_2 population

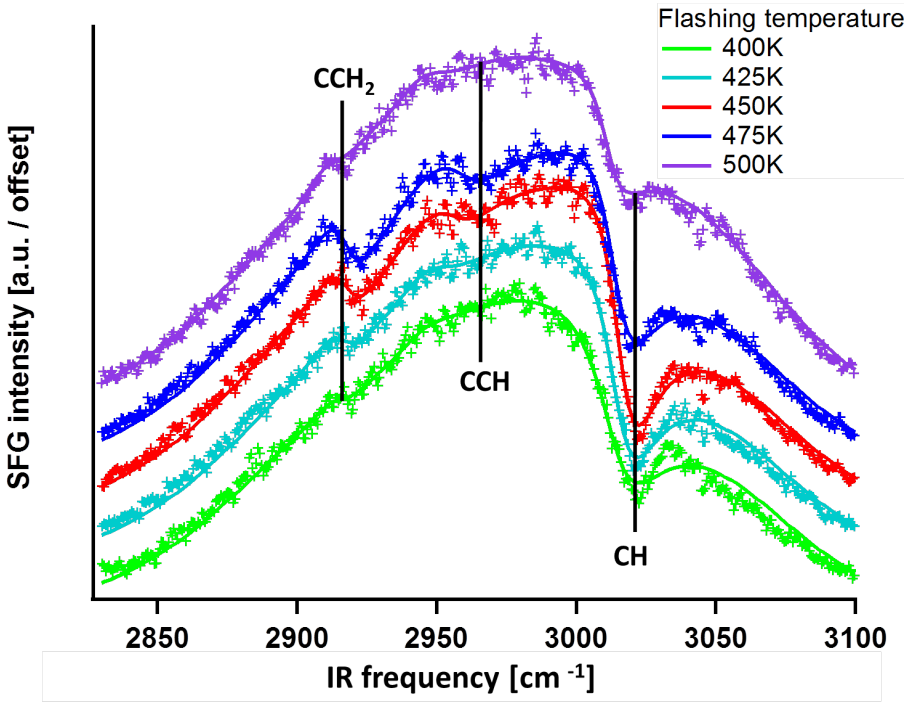

Figure 5.7: Series of measurements of a sample which had a coverage of about 30% of a ML of carbon. At temperatures below 400 K the vibrational spectrum just show a CH peak. With increasing temperatures two new peaks of CCH_2 and CCH were observed in the spectra. At temperature of 500 K or higher all higher hydrocarbon compounds disappeared again and just CH was left at the surface. The different datasets in the figure were offset to each other.

analysis is presented below in Figure 5.8. As clear from Figure 5.8 the measurements showed a maximum yield of CCH_2 between 460 K and 480 K. Above 480 K a strong decrease of the formed CCH_2 (and CH signal as well) was observed by dissociation and carbon production.

5.3 Data simulation by chemical rate equation

For a qualitative description of the system the already introduced chemical rate equation formalism of Chapter 2.4.1 will be applied on this problem. Therefore you must make some assumptions about the elementary reactions that determine the formation of CCH_2. In many theoretical work it has been reported that CH has compared to all the other hydrocarbon groups the highest adsorption energy on Ru(0001) [86, 18]. Taking this into account you possibly could assume, that the formation of CCH_2 is a diffusion controlled reaction. Reported values for the diffusivity of CH ranges from 60 to 100 kJ/mol. For simulation of our experimental data a conservative value of 100 kJ/mol in the reaction model was chosen. Then,

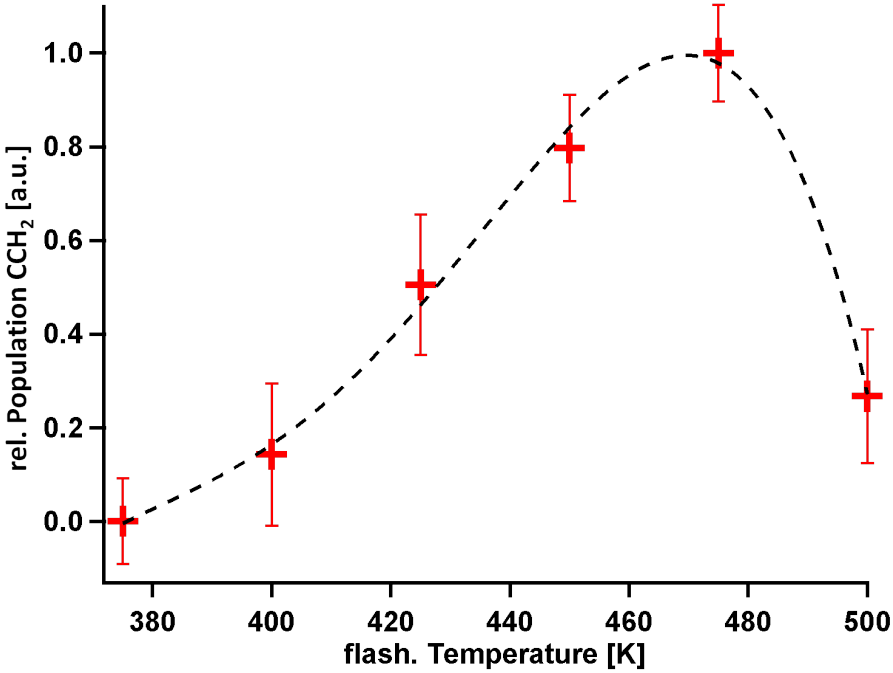

Figure 5.8: Figure shows the squareroot of the integrated CCH_2 resonance. The relative population was scaled to 1, because the absolute value of CCH_2 was not known at any temperature point. The attached fit to the data-points has no physical meaning. It should just catch the general trend of our data.

the increase in concentration of CCH_2 should be the result of following reaction

$$CH \; + \; CH \; \overset{k_D}{\rightarrow} \; CCH_2 \tag{5.5}$$

The important value for CCH_2 formation is the rate-constant k_D. Assuming it is diffusion controlled reaction [32] we could write the rate-constant as

$$k_D = 4\pi(D_{CH} \times D_{CH}) \; a \; N_a \tag{5.6}$$

where D_{CH} is the diffusion coefficient of a CH molecule on Ru, a the hcp- site distance of 2.7 Å and N_a the Avogadro number. D_{CH} is defined in [33, 32] as

$$D_{CH} = D_0 \times e^{\frac{-E_{act}}{RT}} \tag{5.7}$$

D_0 is the preexponential factor which can be approximated [33] by

$$D_0 = \frac{a^2\nu}{6} \tag{5.8}$$

ν is an attempt frequency of roughly $\nu = 1 \; \times \; 10^{13}$ s^{-1}[33]. It can be seen as the number of attempts per second of a molecule to "jump" to a neighboring adsorption site. It is normally assumed for this frequency to have a value similar to the lattice

vibrations of a solid ($\approx 10^{12}$ to 10^{13} Hz[33]) . By using Equation 5.5) with an activation energy for diffusion of E_{act} = 100 kJ/mol and a correct modeling of the thermal history of the sample by including the heating and cooling ramp between each flashing cycle, we get the following CCH_2 formation, as shown in 5.10.

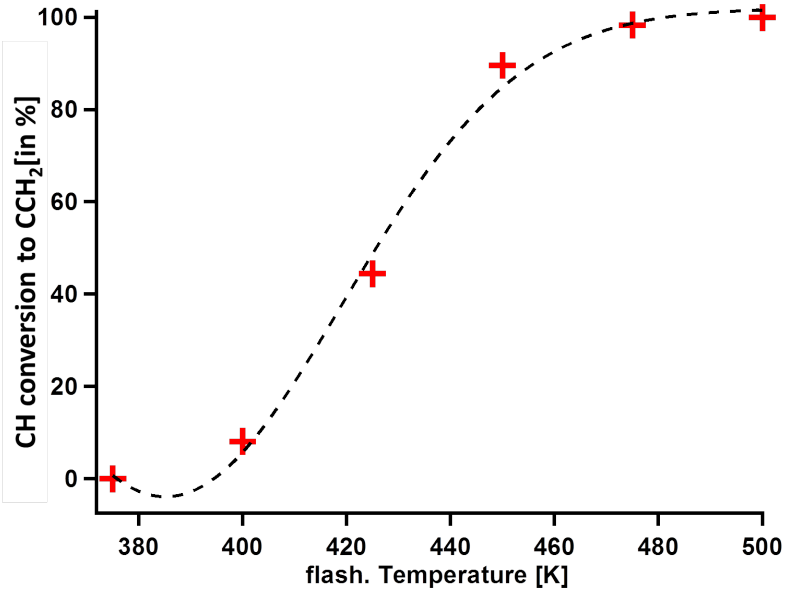

Figure 5.9: Qualitative simulation of a diffusion controlled CCH_2 formation. The calculated data points represents the total conversion of adsorbed CH into CCH_2. The attached fit to the data has no physical meaning and is just for emphasizing the general trend of the data. As obvious from the calculated conversion we would transform all CH into CCH_2 after a comparable thermal treatment as done in the experiment. This conclusion is inconsistent with our data.

As can be seen for the case of a diffusion controlled reaction, nearly every CH molecule would have been converted into CCH_2. This is clearly not the case from our experimental observation (see Figure 5.7). As discussed above our experimental observation suggests a transformation of possibly 10 % or lesser of CH into CCH_2 and not 100%. Therefore, it is comprehensible to assume other limiting factors for this process. From theory it is known that the coupling of two CH molecules to form CCH_2 has a not negligible barrier (as shown in Table 4.4). Therefore, a partially diffusion controlled reaction could be assumed[32]. The rate equation changes to:

$$CH + CH \overset{k_{CH}}{\rightarrow} CCH_2 \tag{5.9}$$

k_{CH} is the rate constant for CCH_2 formation. It is a combination of the rate constants for CH for diffusion and formation. k_{CH} is defined as [32]

$$k_{CH} = \frac{k_R}{1 + \frac{k_R}{k_D}} \tag{5.10}$$

with the formation rate constant k_R given as

$$k_R = A \times e^{\frac{-E_R}{RT}} \tag{5.11}$$

The critical point for this equation is the definition of the prexponential factor A. There are several possible ways to constrain it. One possibility is to apply an already measured or calculated prexponential factor of comparable coupling reactions to this system. In literature we find some work of Hardeveld and coworkers [179] about the coupling reaction of atomic nitrogen with ethylene on Rh(111). They found in their system experimentally a prexponential factor for the CN coupling of A_{CN}=$10^{11\pm1}\,s^{-1}$. This has been also supported by calculation. Furthermore, we find in some other publications about coupling reactions of long-chain hydrocarbons values for A between 10^9 to $10^{13}\,s^{-1}$ [158]. Another possibility of constraining this prexponential factor could be found in some work of Beatzold and Somorjai[66]. In their work about prexponential factors for surface reactions they give some formula for estimation of this value for simple reactions. Under assumption of having a bimolecular reaction where the possible amount of CH is always comparably large to the amount of converted CH, you could think about our reaction as a pseudo first order reaction instead of a second order reaction. The prexponential factor for a pseudo first order reaction could be given as

$$A = \frac{k_b\ T}{h} \tag{5.12}$$

In Equation 5.12,h corresponds to the Planck-constant. By using this equation you will get for A at room temperatures a value of $6\times10^{12}\ s^{-1}$. This value is in the regime of Hardeveld et al. and other reported values [179] . As an third approach to constrain the prexponential factor A, you can assume a model which describes it as the collision factor z_{AA} of molecules. Therefore, the collision number from the gas molecules in gas-phase was adopted, which has been found to describe with certain restrictions the absolute value acceptable . The collision number Z_{AA} is given in [32]:

$$Z_{AA} = 2N_{CH}^2 d^2 \left(\frac{\pi k_B T}{\mu}\right)^{1/2} \tag{5.13}$$

N_{CH} is the number of molecules per unit volume. Division of this quantity by N_{CH}^2 and multiplication by the Avogadro-number N_A gives

$$A \equiv z_{AA} = 2N_A d^2 \left(\frac{\pi k_B T}{\mu}\right)^{1/2} \tag{5.14}$$

d is the diameter of the molecules (1.3 Å) and m is the mass of a CH molecule. With this constraints z_{AA} can be calculated and has a value in the regime of $2 \times 10^{11}\ s^{-1}$.

This value is slightly depending on the surface temperature but it is within the range of the other reported values. By comparison of all results we decided to take a value for A of $5\times\ 10^{11}\ s^{-1}$ for further calculations. To test the sensitivity of simulation results also other values of A has been assumed. But as clear by inspection changes of A does not changes the relative population qualitatively but just quantitatively because it is just a scaling factor for the rate of conversion. For the activation barrier for formation E_R a value was chosen which is in the same range as the diffusion barrier E_D. With about 100 kJ/mol it is in acceptable agreement with the theoretical calculations for CH coupling on terraces [131]. With that you can calculate the rate-constant by Equation 5.10 and simulate the thermal induced formation of CCH_2 as observed in experiment. The in Figure 5.10 calculated formation by a

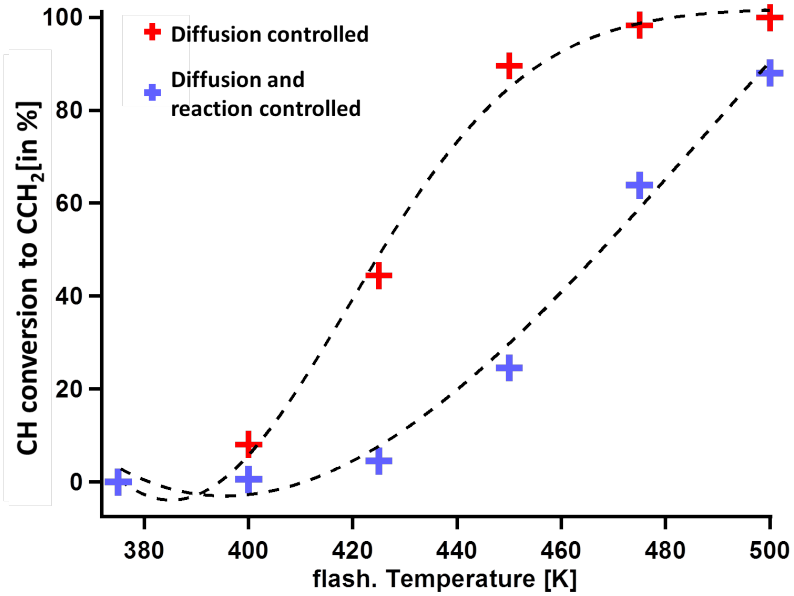

Figure 5.10: The graph shows the comparison between a total diffusion controlled reaction(RED) and a partial diffusion controlled reaction(BLUE) for CCH_2 formation. Both activation barriers have been assumed to be 100 kJ/mol. In case of a partial diffusion controlled reaction the CCH_2 formation shifted to higher temperatures, which is a better description of the system. Nevertheless, the total formation of CCH_2 by this model is still far to high compared to experiment.

combined reaction and diffusion rate constant could not describe the system properly. Simulation of the thermal treatment of our sample showed a conversion of about 80 % of the CH. This is clearly inconsistent with the experiment. Changes of 20 % or more in both activation energies does not change the result qualitatively. The total conversion rate just differs by 15-20 % which is still far to high to explain our observation. For a correct description of the general trend in the data it is necessary to take CCH_2 depletion channels into account. These could be a back reaction as well as a dissociation reaction reaction for CCH_2, because CCH_2 can be converted to

CCH by dissociation, as shown in Figure 5.6. Therefore we extended the existing rate model

$$CH + CH \overset{k_{CH}}{\rightarrow} CCH_2 \tag{5.15}$$

by the following two reaction pathways:

$$CCH_2 \overset{k_B}{\rightarrow} CH + CH \tag{5.16}$$

and

$$CCH_2 \overset{k_{Diss}}{\rightarrow} CCH + H \tag{5.17}$$

Then the overall reaction path could be seen as:

$$CH + CH \underset{k_B}{\overset{k_{CH}}{\rightleftharpoons}} CCH_2 \overset{k_{Diss}}{\rightarrow} CCH + H \tag{5.18}$$

For the reaction step of $CCH_2 \rightarrow CCH + H$ no back-reaction was assumed, because at surface temperatures above 400 K all produced Hydrogen would immediately desorb into gas-phase [114]. For the rate constants k_B and k_{Diss} the prexponential factors were assumed to be similar to those of k_R. Qualitative changes in the rate constant are clearly dominated by the exponential part and the prexponential factor just scales the rate. Then the back and the dissociation reaction could be given by a Arrhenius expression

$$k_{B,Diss} = A \times e^{\frac{-E_R}{RT}} \tag{5.19}$$

For the activation barriers of the different reaction channels we used a set of physical meaningful values which were found to fit the data best. For the back-reaction we assumed a barrier of E_B=76 kJ/mol and for the dissociation we chose E_{Diss}=72 kJ/mol. The assumed barrier for dissociation of CCH_2 followed from the experimental observation of CCH_2 dissociation in case of ethylene decomposition at low temperatures (see Section 3.2). There the depletion of CCH_2 was observed to finish at about 325 K. This means the value should be slightly higher than for CH_2, which had an observed barrier for dissociation of 65 kJ/mol. Therefore our assumption of 72 kJ/mol for getting the best fit for the system is an acceptable assumption. For the activation barrier of formation a value of E_R=107 kJ/mol was chosen which fitted the data in the best way. By taking these values you get a simulated formation of CCH_2, as shown in Figure 5.12. It is obvious from Figure 5.12 that the simulated data seemed to fit the observed trend in the experiments. Especially the strong decrease of the signal at higher temperature fitted the experimental observations quite well. Additionally the total conversion of about 8% of initial CH during the heating is in the expected range for the conversion. We assumed a maximum conversion of about 1/10 of the initial CH coverage. To compare simulated data to the experimental

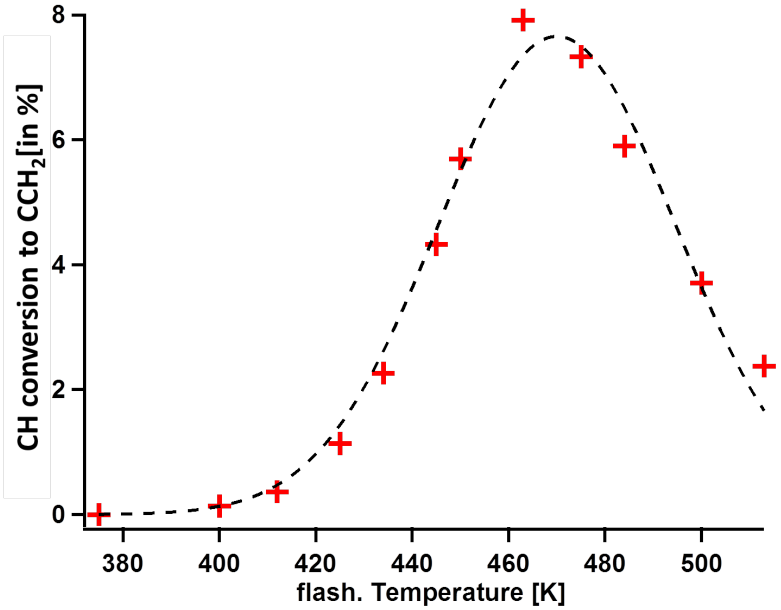

Figure 5.11: Simulated data for the fundamental reactions as shown in formula 5.18. The assumed barriers are 107, 76 and 72 kJ/mol for E_R, E_B and E_{Diss} respectively. The formation and depletion of CCH_2 at nearly all temperature ranges show a similar behavior compared to the experimentally observed formation of CCH_2 .

data directly, the simulated data were scaled down to 1 for the maximum intensity of CCH_2. The general trend in experiment is comparable to the simulation by our model. Especially the temperature for the maximum formation of CCH_2 fits very well. Just the experimentally observed initial signal increase was bigger than the simulated one. This deviation could have its origin in a comparable low signal to noise ratio of the data. This causes especially at lower flashing temperatures a higher uncertainty where the observed signal of CCH_2 was weak.

5.4 Discussion of CH coupling reactions

In Section 5.3 we investigated qualitatively the formation of higher hydrocarbons on the Ru(0001) surface e.g. CCH and CCH_2. Experiments with different seeding gases for the MBS suggested a reaction pathway for the coupling, which is shown in Figure 5.6. These fundamental reactions could be summarized up as $CH + CH \rightarrow CCH_2 \rightarrow CCH + H$. Assuming these fundamental reactions, in addition to the assumption of back reactions and diffusion, allowed us to set up a series of rate equations for the simulation of thermally induced CCH_2 formation. This is shown in Figure 5.7. Nevertheless, it is necessary to discuss the size of our suggested barriers and to compare them with the literature if possible. The assumed model suggests

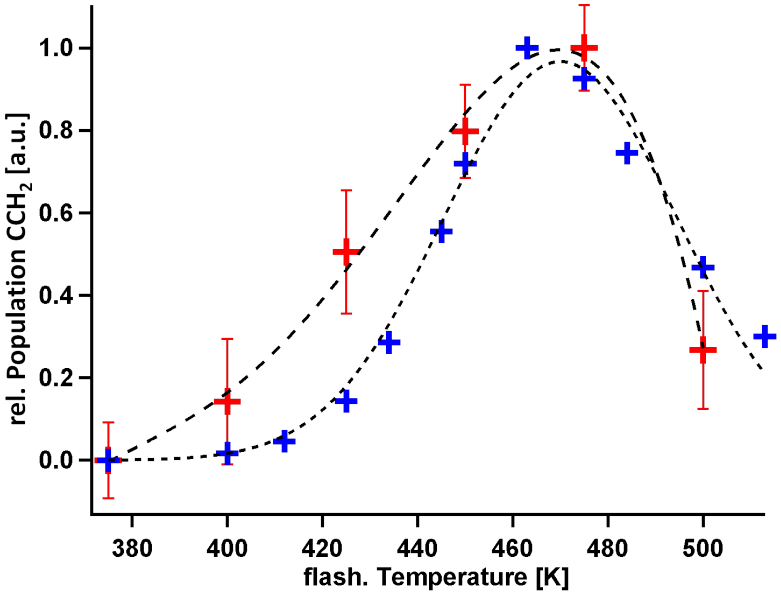

Figure 5.12: Direct comparison of simulated data with the experimentally obtained formation values. Simulation has been done assuming the in Equation 5.18 fundamental reactions. For a direct comparison the maximum intensity of the simulated data were scaled to 1. Beside the initial increase of the data the general trend of experiment and simulation is the same

that CH diffusion across the surface is not a rate limiting step for CCH_2 formation. Theoretically predicted values of 60-70 kJ/mol [86, 18] for diffusion just slightly influences the CCH_2 formation. The assumed barrier for the $CH + CH \rightarrow CCH_2$ reaction of 107 kJ/mol is slightly higher than prior theoretical work predicted[131, 16]. Liu and coworkers [131] calculated a coupling barrier for CH of 85 kJ/mol to form a HC-CH group. Actually, this molecule is not the same one, which was observed by us. To form CCH_2 from HC-CH an internal hydrogen transfer is necessary. Unfortunately, there is no possibility to constrain the barrier for this process, because there are no computational results available. We are assuming in our coupling model an effective coupling reaction which means a direct conversion two CH molecules to CCH_2 without intermediate states.This reaction could be composed of multiple elementary reactions with different barriers. If the barrier for hydrogen transfer is of order the barrier for the coupling we would see in such a scenario an "effective" barrier for CCH_2 generation which would be larger than the theoretically predicted value of 85 kJ/mol. The assumed barrier for dissociation of CCH_2 of 72 kJ/mol has been already discussed above and follows from our experimental observations (see Section 3.2). The last assumed value of 76 kJ/mol for the back-reaction between CH and CCH_2 followed from the constraints of the other values. If it would be 10 kJ/mol lower than 76 kJ/mol any formation of CCH_2 would not be possible, because the back-reaction would be comparably fast relative to the formation reaction. If it would

be 10 kJ/mol higher, the CCH formation would be the favored depletion channel of CCH_2. This would have a consequence. The formation of CCH as favored depletion channel would lead to coke formation by the reaction of CCH $\rightarrow$ CH+ C. But in the higher temperature region above 550K all rates increases but CH is still as single resonance apparent in the spectrum, while CCH not. This should be not the case if the formation channel of CCH would be the favored channel for CCH_2 depletion. Otherwise the whole coverage of CH would have been converted to coke already. As you can see the assumed values for setting up the rate equation followed from experimental constraints to the system and were physical meaningful. Furthermore, these values are simulating the CCH_2 formation qualitatively acceptable. This leads to the suggestion that the made assumption for the reaction channels/path were correct and that the chosen barriers for activation of the different processes were in certain range accurate.

Chapter 6

Adsorbate interaction effects on CH vibrational response

The main focus of the previous work in this thesis pointed towards the pure chemical interaction of adsorbate's and the influence of the surface on these chemical reactions. This chapter should focus more on the physics and chemistry of adsorption as well as their possible implications on experimental observations. Numerous examples in earlier investigation have shown that adsorbate energetics, geometry and configuration on solid surfaces could be influenced by lateral interaction between the adsorbates. We want to explore the influence of such interactions in CH on Ru(0001) on our SFG response and the possibility of using our observables to gain insight into such interactions.

6.1 Lateral interactions of adsorbate's on Ru(0001)

Generally, the influence of adsorbate coverage on vibrational frequencies, observed line-width and intensities of various spectroscopic techniques is known in physics and chemistry [151, 84, 161, 115]. One of the best investigated adsorbate regarding these effects is CO on numerous transition metal surfaces. Large shifts of the vibrational stretching frequencies have been observed of adsorbed CO in these systems. Also changes in intensity and line-width as a function of coverage have been reported. The first approach to explain this shift of CO's stretching frequency had been proposed by Hammaker and coworkers. They assumed for explanation of their observation a direct dipole-dipole interaction of adsorbed CO molecules. With this model they predicted the right sign of the shift but underestimated the magnitude of the shift by far [108]. Mahan and coworkers extended their model by considering an image charge screening of the metal substrate [139]. By this way of handling the system they were

able to explain 30-40% of the experimentally observed vibrational frequency shift. A suitable explanation why their model still failed was given later on by Scheffler[161]. They did not include correctly in their model the interaction of a dipole with its own image dipole. Scheffler however considered all contributions of the dipoles and image dipoles by assuming that the CO adsorption site did not change as a function of surface coverage. As a consequence Schefflers model quantitatively reproduced the experimental observed frequency shift of CO[161]. In his description of the system the total dipole moment of an adsorbed molecule is:

$$p(R_j, \omega, t) = p_{st} + \alpha(\omega) E^{local}(R_j, \omega, t) + [\beta(\omega) E^2 .....] \tag{6.1}$$

Scheffler was in his work only interested in the explanation of shifts observed by linear spectroscopy. Therefore, he focused on the first two terms in this equation and neglected higher order contributions. p_{st} is the static dipole moment of an isolated molecule, $\alpha(\omega)$ is the molecular polarizability and $E^{local}(R_j, \omega, t)$ is the local electric field at adsorption site R_j. It contains following contributions,

$$E_j^{local}(R_j, \omega, t) = E_j^0 \ + \ E_j^{otherdipoles} \ + \ E_j^{ownimage} \ + \ E_j^{otherimages} \tag{6.2}$$

As one could see Scheffler considered in his description of the electric field, which is interacting with a dipole, the electric field of the incoming laser beams, the reflected contribution E_j^0 from the metal surface, the field of the surrounding dipoles and their corresponding image dipoles and the electric field of the own image dipole. The indices follows from the surface site R_j where the field interacts with the molecules. The definition of the different field contributions is discussed intensively in Schefflers work [161] and allows the combination of Equation 6.1 and 6.2 to rewrite the total dipole moment of an adsorbed molecule as follows:

$$p(R_j, \omega, t) = \frac{p_{st}}{1 + \alpha(\omega)[S(\Theta) - 1/4 \ d^3]} + \frac{\alpha(\omega) E^0(R_j, \omega, t)}{1 + \alpha(\omega)[S(\Theta) - 1/4 \ d^3]} \tag{6.3}$$

In this equation d corresponds to the distance between the effective metal surface and the dipole. The polarizability $\alpha(\omega)$ is the given by

$$\alpha(\omega) = \alpha_e + \frac{\alpha_\nu}{1 - (\omega/\omega_0)^2 + i\Gamma(\omega/\omega_0)} \tag{6.4}$$

In Equation 6.4 α_e is the electronic polarizability, α_ν the vibrational polarizability, ω_0 the vibrational frequency of the normal mode and Γ the line width of this mode. Another important parameter is $S(\Theta)$ which is the sum of the contributions of the other dipoles and image dipoles to the local electric field at adsorption site R_j. It is

also often called sum dipole factor and contains the geometric information of the system. Θ reflects in this content the coverage dependence, because S(Θ) depends on the number of surrounding dipoles at the surface. S(Θ) is defined as

$$S(\Theta) = \sum_k \frac{1}{|R_k - R_j|^3} + \frac{1}{(|R_k - R_j|^2 + 4d^2)^{3/2}} - \frac{12d^2}{(|R_k - R_j|^2 + 4d^2)^{5/2}} \tag{6.5}$$

For a correct prediction of the vibrational shifts a correct calculation of the sum dipole is necessary. Unfortunately, it changes with increasing coverage. Scheffler found an elegant way to address this problem as long as the adsorbate (CO) is not changing its adsorption geometry. For CO on Ru(0001) it has been found that it adsorbs up to a coverage of 0.33 ML in an ordered $\sqrt{3}$ x $\sqrt{3}$ structure, which then gets saturated. Calculating the sum dipole at this saturation allows the prediction of the sum dipole at intermediate coverages of $\leq \Theta \leq$ 0.33ML. Therefore, Scheffler defined S(Θ)= C(Θ)S(0.33ML) where C(Θ) has the limits C=0 and C=1 between Θ=0 and Θ=0.33ML [161]. This way of addressing the problem is only valid at coverages of 0.33 ML or lower. If more CO would adsorb it would start to disorder, which causes changes in the sum dipole. Therefore, this model could not be applied properly at higher coverages.

Pfnuer and coworkers applied this formalism of Scheffler to explain the observed shift in their IR reflection adsorption spectroscopy of CO/Ru(0001) [151]. They investigated the relative shift of the center frequency and integrated IR adsorption peak intensity. By application of Scheffler's model they were able to explain their observed trends in their data. They observed up to the coverage of 0.33 ML CO a linear shift of the center-frequency and a linear increase of their integrated IR adsorption peak. Above this coverage the integrated peak area did not changed anymore. Furthermore, the frequency shift underwent a step change, which is in agreement with the picture of an adsorbate reordering above this coverage. For frequency prediction they defined the coverage dependent shift of the center-frequency as [151]

$$\omega = \omega_0 \left[1 + \frac{\alpha_\nu (S(\Theta) - 1/(4d^3))}{1 + \alpha_e (S(\Theta) - 1/(4d^3))}\right]^{1/2} \tag{6.6}$$

Equation 6.6 only holds for adsorption of the CO on one type of adsorption site and for a perfect ordered layer. In cases of small adsorbate islands or other ordered structures, the dipole sum at an edge of an island is different from those in the middle. This could therefore induce a splitting of the observed resonance. Nevertheless, this formalism has been found to describe the experimental observations acceptably in the coverage regime up to 0.33 ML.

Later on, Cho and coworkers [84] applied this formalism for description of coverage dependent frequency shifts of CO on Ru(0001) which they observed in sum frequency generation measurements. They found that the ν_s of CO shows a coverage dependent blue shift of 50 cm^{-1} for an increase of the coverage from 0-0.33 ML of CO in their SFG-spectra (together with an increasing intensity and decreasing bandwidth). Application of Scheffler's model quantitatively explained their results. This fact suggested that their data trends could be understood as the result of dipole-dipole coupling.

At low coverages the dipoles of the molecules could be interpreted as localized and each CO molecule had also localized vibration. With increasing coverage the averaged distance between molecules decreases and the stretch vibration is increasingly delocalized. That was due to dipole-dipole coupling[72]. For an understanding and simulation of these shift for the model-system of CO on Ru(0001),Cho et al. [84] took Schefflers and Persson formalism to express the nonlinear susceptibility $\chi^{(2)}$ in terms of polarizability, hyperpolarizability and sum dipole. The sum dipole includes the coverage dependency. They expressed $\chi^{(2)}$ for simulation of the data as,

$$\begin{aligned}\chi^{(2)}(\theta,\omega_{IR}) &= \frac{C(\Theta)\ \beta(\omega_{IR},\omega_{VIS})}{[1+C(\Theta)\alpha(\omega_{IR})S(0.33ML)][1+C(\Theta)\alpha(\omega_{Vis})S(0.33ML)]} \\ &\cdot \frac{1}{[1+C(\Theta)\alpha(\omega_{SFG})S(0.33ML)]}\end{aligned} \tag{6.7}$$

In this equation, $C(\Theta)$ contains the coverage dependency Θ. Thereby C ranges from 0<C<1 in the regime of $0 \leq \Theta \leq 0.33$ML, comparable to the function C in Schefflers work. $\beta(\omega_{IR},\omega_{VIS})$ is the molecular first hyperpolarizability, which will be defined later on. $\alpha(\omega)$ is the molecular polarizability. S is analog to Scheffler the sum dipole factor. The molecular polarizability α which appears in Equation 6.7 is already defined by Schefflers work in Equation 6.4 and contains a electronic and a vibrational contribution. α_e is the electronic polarizability and therefore independent of the frequencies in the frequency range of interest. α_ν is the vibrational polarizability and just for incoming IR field of interest. By this you can assume that $\alpha(\omega_{Vis})$ and $\alpha(\omega_{SFG})$ in Equation 6.7 can be approximated to be only α_e.

ω_0 is the center-frequency of an isolated molecule e.g. the center-frequency without coupling of dipoles. Furthermore Γ in Equation 6.4 is determined as the half FWHM of the SFG resonance. For simplification we define S(0.33ML)= S_0 because it is a fixed value. Than Equation 6.7 can be rewritten as follows:

$$\chi^{(2)}(\theta,\omega_{IR}) = \frac{C(\Theta)\ \beta(\omega_{IR},\ \omega_{VIS})}{[1+C(\Theta)\alpha(\omega_{IR})S_0][1+C(\Theta)\alpha_e S_0]^2} \tag{6.8}$$

The definition of the molecular first hyperpolarizability β is done in literature [84] analog to their definition of the polarizability α in Equation 6.4. The similarity of

their definitions will be more clear by going back to Equation 6.1. There α and β were defined as molecular properties for description of the dipole moment of a molecule in an applied electric field. Cho et al.[84] defined β as:

$$\beta(\omega_{IR}) = \beta_{non}\ e^{i\phi} + \frac{\beta_{res}}{1 - \omega_{IR}/\omega_0 - i\Gamma/\omega_0} \tag{6.9}$$

Following from Equation 6.9 the hyperpolarizability $\beta(\omega_{IR}, \omega_{VIS})$ contains a resonant β_{res} and a non-resonant part β_{non}. While β_{res} is the resonant hyperpolarizability of the adsorbed molecules, β_{non} is the non-resonant hyperpolarizability and is mainly contributed by the metal substrate. A phase factor $e^{i\phi}$ is attached to β_{non} with ϕ being the relative phase between the molecular response and that of the metal substrate[84].

By this developed formalism [84], Cho and coworkers showed that it is possible to explain qualitatively their experimental observed coverage dependent frequency shift as well as the intensity increase of the SFG resonance by lateral dipole-dipole interaction.

Our idea is to apply the developed model for coupling effects of CO on Ru(0001) to system of CH on Ru(0001). Thereby, the focus will set mainly on the effects of coverage on the observed center frequency. At the end the effect of coupling on the observed integrated SFG intensity will be also addressed as well. If the application of this model works, this would suggest that the model captures the essential physics. This would help to understand ongoing processes better. Generally, it would be useful to check, whether reproduction and therefore interpretation of coverage dependent spectral changes of CH is possible. If it is a result of dipole-dipole coupling we have to discuss the implications of our observation on the interpretation of vibrational data for these kinds of systems.

6.2 CH coupling on Ru(0001)

As mentioned above, the following sections will focus mainly on the effects of coverage on the observed center frequency. At the end there will be also a discussion of the effect of coverage on resonance intensity. To emphasize the observed shift in center-frequency for the system of CH on Ru(0001), I will show a data set of different coverages for samples, which were prepared at various temperatures and dosing times. We dosed for preparation between 5 - 120 min and produced coverages of 0.05 - 0.78 ML. In Figure 6.1 a) and b) we show as an example for the observed shift in the raw data two spectra, which were taken after dosing 5 minutes and 60 minutes at 400 K.

Figure 6.1 clearly shows the spectral shift of the CH-stretch response as well as

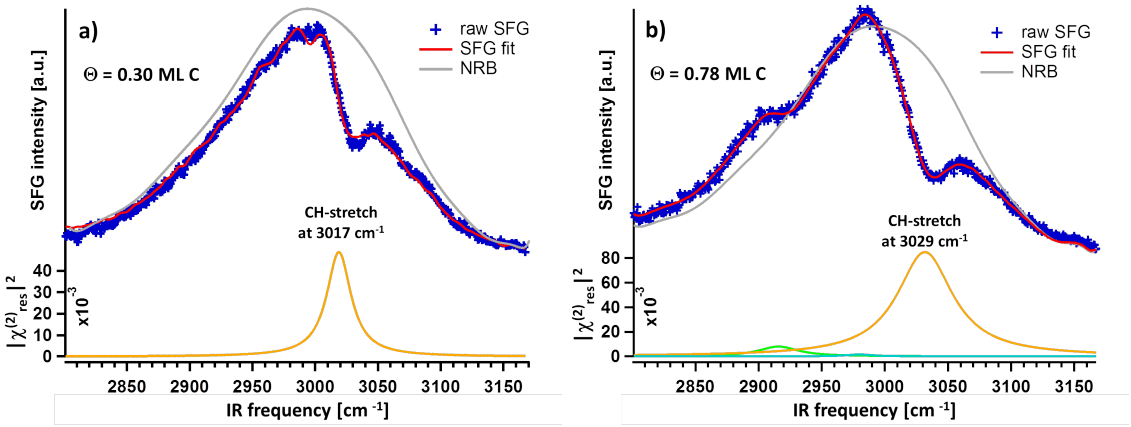

Figure 6.1: In both spectra the SFG intensity is plotted over the IR frequency. Figure a) shows the spectrum of a sample, created by dosing for 5 minutes at T_{Ru}= 400 K with methane seeded in helium. The spectrum is dominated by the ν_s of CH, which is centered at 3017 cm^{-1}. The coverage of the sample was 0.3 ML of carbon. Figure b) shows the spectral response of sample with 0.78 ML of carbon. Two peaks are now apparent, which attributable to the CH stretching modes of CCH_2 and CH. The center-frequency ν_s of CH is shifted to 3029 cm^{-1}.

an increase of the resonant intensity after increasing surface coverage from 0.3 to 0.9 ML[1].

Performing of a series of measurements with different coverages of carbon shows that the frequency shift is a smooth function of coverage (see Figure 6.2).

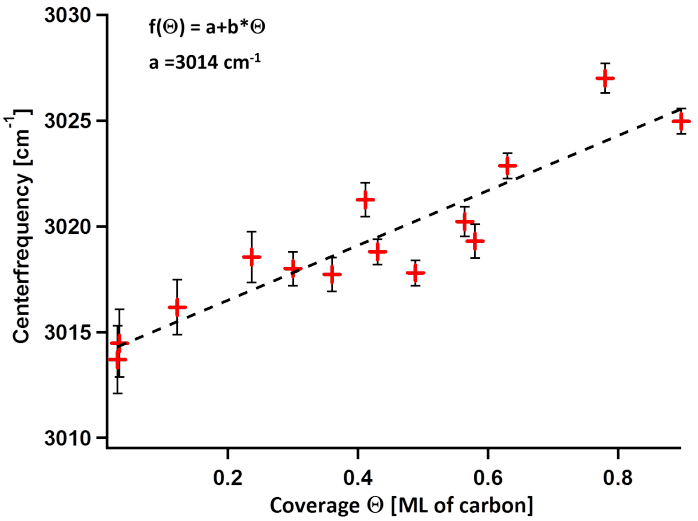

Figure 6.2: In this figure the extracted center frequency is plotted of the Coverage. The extracted center-frequencies show a linear shifting behavior with increasing coverage. The added fit to the data-points is a linear fit. This fit gives a zero-coverage frequency of about 3014 cm^{-1}, which is in good agreement with Goodman and coworkers [8, 9].

[1]The coverages were measured after the spectral characterization of the sample by the already introduced TPO method, as shown in section 3.1.1

Figure 6.2 emphasizes the clear dependence of center frequency on the coverage. The attached error to each data point followed from the dependence of the fitting results of the program on the initial guesses which were made. Nevertheless, the error in center frequency for each data point is relatively small. A linear fit of the data, as shown in Figure 6.2, gives a zero coverage center frequency of 3014 cm^{-1} which is in good agreement with Goodman and coworkers [8, 9]. This way of fitting suggests of course a linear behavior for the frequency which must not be correct. But even ignoring the fit result, $3014\,cm^{-1}$ is a valuable assumption because it is more or less the lowest by us observed frequency for the CH-resonance. It is our aim to predict with the model of Cho et al. by Equation 6.8 the frequency shift and learn by this method more about the molecular properties of CH. The simulation/calculation of the spectral response with the adopted model required several parameters. These parameters were found in literature or got physical meaningful constrained.

Determination of the zero-coverage center-frequency ω_0 was already done by us in Figure 6.2 with a value of $\omega_0 = 3014\,cm^{-1}$.

For the vibrational dephasing constant we can take an averaged value from our fitting model for the bandwidth of measured CH peaks. This gives for $\Gamma = 6\,cm^{-1}$. Because the choice of Γ does not infect the shift but only the amplitude this is a reasonable treatment.

It is not possible to get some values for the hyperpolarizability β from the literature but you can constrain it for following reasons. The hyperpolarizability β depends on two different unknown contributions, as shown in Equation 6.9. These are β_{non} and β_{res}. We have already discussed at this point that β_{non} is connected to the non resonant susceptibility of the metal substrate. Here we have to refer back to the discussion of our fitting model. In Chapter 2 it was shown that our fitting model separates the non resonant contribution of the signal and the resonant contribution. The extracted frequencies of the fitting model where therefore independent of the non resonant response of the substrate. Therefore, β_{non} can easily be set to 0 in our simulation. Furthermore, Equation 6.8 and 6.9 showed that β_{res} has just an influence on the amplitude of the generated signal but not on the shift of the center-frequency. Therefore, we can take an arbitrary value unequal zero for best simulation of the shift which was in our case β_{res}=0.00372.

For $\alpha(\omega)$ some values were found in literature, would be adopted. In literature[155] they investigated the molecular polarizability of CH_4 and CD_4. For the electronic polarizability α_e and the vibrational polarizability α_ν of methane they reported values of α_e=2.2146 $Å^3$ and α_ν= $0.124\,Å^3$. These values were calculated by Hartree-Fock wave-functions for assumed zero temperature. Unfortunately, it is not possible to get the exact value for a single CH-molecule but only for CH_4. But we will take these

values for simulation and will later on test the influence of changes in the values on the simulated shift. Comparison to experimentally derived values for the molecular polarizability of methane at around room temperature show comparable results of about 2.55 Å^3. [77, 185] This value contained both electronic and vibrational polarizability, which explain the differences to the polarizability values above[155].

For the last undetermined value is the sum dipole factor S_0. For this parameter no values for methane could be found in literature. But because all the other parameters in Equation 6.8 were constrained, the sum dipole factor will be left as a free fitting parameter. Later you will see that a value of S_0=0.081 Å^{-3} will give the best fit for the spectral shift in our system.

By using the listed parameters we can simulate the experimental observed shift in center frequencies, as shown in Figure 6.3.

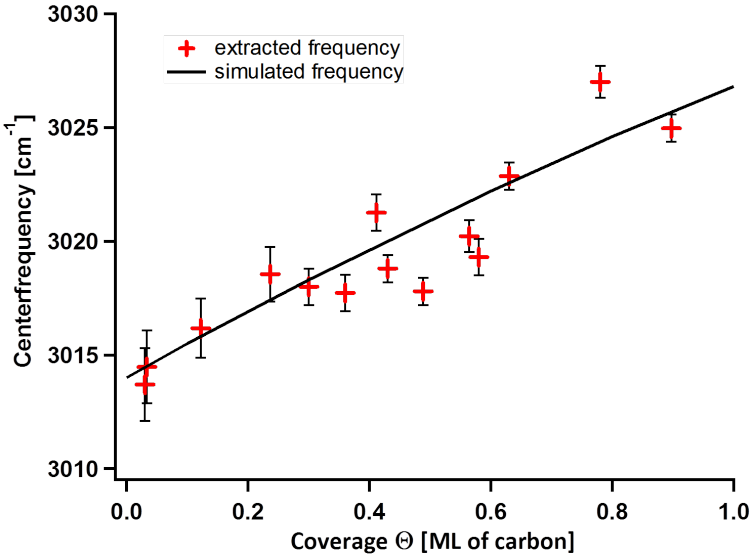

Figure 6.3: The figure shows the simulated frequency shift with increasing coverage (black line) by usage of the model given by Equation 6.8. The center frequency is plotted above the coverage. For calculation of the simulation the following parameter were chosen: α_e=2.2146 Å^3, α_ν= 0.124 Å^3, β_{res}=0.00372, β_{non}=0, ω_0 = 3014 cm^{-1}, Γ = 6 cm $^{-1}$ and S_0=0.081 Å^{-3}. Under the constraint of taking the values of methane for the polarizabilities and optimizing S_0 for the best overlap with the data, the dipole-coupling model described the spectral shift very well.

Figure 6.3 emphasized that the adopted dipole coupling model [84] can predict the observed spectral shift. This could suggests that the observed shift is the result of dipole-coupling effects at the surface.

However, CH on Ru(0001) is not CH_4 in vacuum. Therefore I will present in the following graphs the dependency of the simulated shifts on different parameters. This should give us some idea, whether our assumptions for all values are acceptable. As a first parameter, the dependency of the observed shift on the sum-dipole factor

S_0 will be shown. All following plots will be presented without an attached error bar for a better overview of the Graphs.

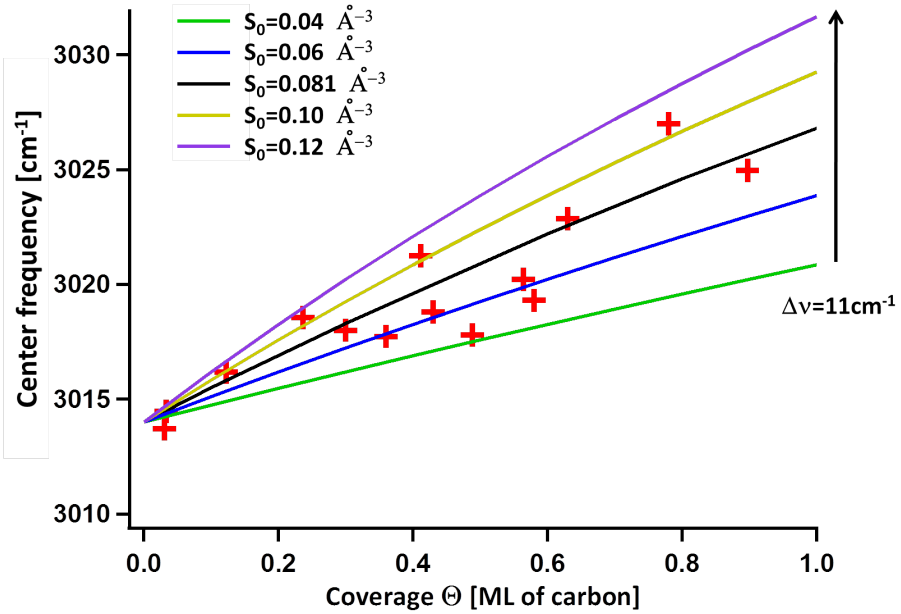

Figure 6.4: For this figure the frequency shift was calculated with the same values as for Figure 6.3, but the values for the sum dipole factor were varied. The center frequency is plotted above the coverage. As you can see, the frequency shift is highly sensitive to the value of the sum dipole. Even the small range from S_0 = 0.04- 0.12 Å^{-3} was enough to introduce changes in the observed shift of 11 cm^{-1} .

Figure 6.4 emphasizes the strong dependence of the frequency shift on the sum dipole moment. The value of S_0=0.081 Å^{-3} (black line) described the system as best. Small changes of the assumed sum dipole induces huge changes in the shift. This brings us to the conclusion that the real sum dipole at the surface must be within the range which was assumed.

The question whether the sum dipole changes with coverage is already answered in the last section. The assumed sum dipole S_0 is the sum dipole of a fully covered surface. The coverage dependence of the effective sum dipole is determined by the product $S(\Theta)$=$C(\Theta)$ S_0, where $C(\Theta)$ changes between 0 and 1 within the range of one monolayer.

The influence of the electronic and vibrational polarizability α_e and α_ν will be presented and discussed in the same way, as the dependence of the shifting on the sum dipole were presented. Their contribution to the spectral shift is shown Figure 6.5 and 6.6. The black line in the plots will always represent the best fit by using literature values.

The simulation emphasized that the literature values and the chosen value of the

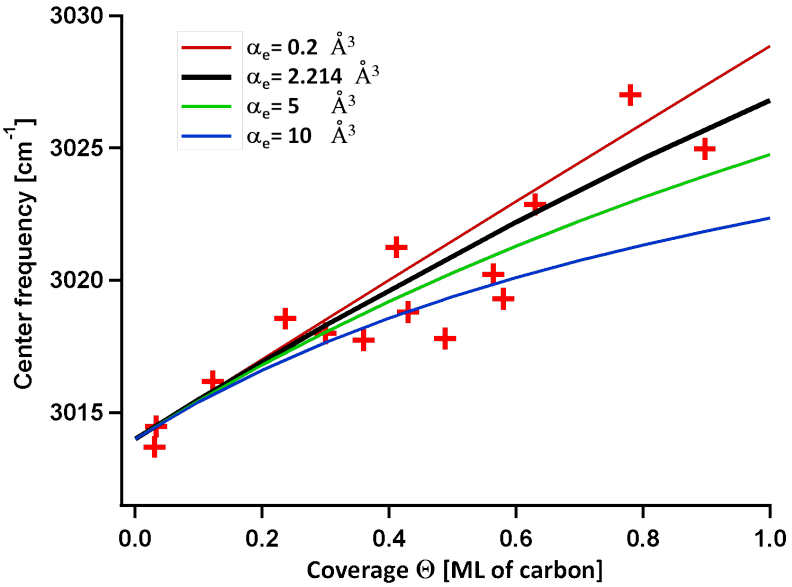

Figure 6.5: By comparison of the different vibrational shifts in order of the electronic polarizability it is obvious that this value does not influence the simulated shift dramatically. This gets even emphasized by the fact that changes between two lines in the graph were just possible to generate by changing α_e within the order of one magnitude. Beside the literature value (black line) the other lines were nearly not more physically meaningful.

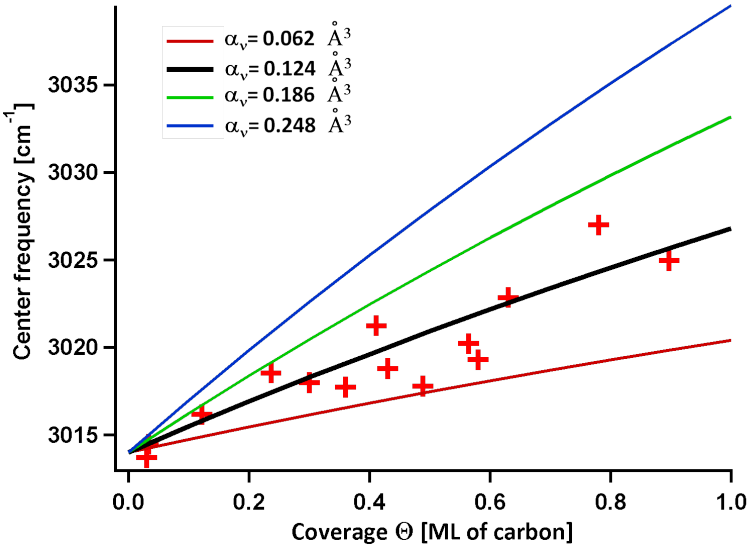

Figure 6.6: Clearly a strong dependence of the generated spectral shift onα_ν can be observed. Actually, the difference were even for smaller changes (factor of 2) so huge, that we assume the literature value for α_ν is the best or most meaningful value.

sum dipole factor seemed to describe our system accurately. This suggests that the observed spectral shift is the result of lateral interactions. All values were given in the subset of Figure 6.3.

Of course, the application of this model to our system contains a lot of other assumptions beside the fitting parameter. These are harder to constrain and will be discussed now. As mentioned in Section 6.1 several times, Schefflers model strongly depends on the ordering and adsorption sites of the molecules at the surface. While the ordering of CO on Ru(0001) up to a coverage of 0.33 ML is nearly perfect, there is no information about the distribution (means island growing) of CH molecules at the surface. The only available information is that CH prefers threefold hollow sites for adsorption. Pfnür and coworkers[151] already reported that island growing could create situations where different molecules see different sum dipole factors. This implies a different shift of these molecules in the spectrum which would cause in minimum case a broadening of the resonance. This effect has been observed by us experimentally for higher coverages. Comparison of the peak width in Figure 6.1 a) and b) clearly shows that. As long as we did not have any information about this adsorption behavior this problem could not be addressed in a detail. Nevertheless, this effect should mainly cause a broadening of the resonance in conjunction with a decreasing amplitude, but should affect the observed center frequency not so much.

An additional problem which needs to be discussed is the presence of different kinds of molecules at the surface. This gets important especially at higher coverages. While in comparison to Cho et al. [84] we have at higher coverages different molecular groups, such as CH, CCH_2 and CCH. This makes the application of this model problematic. We could not know if this induces changes in the sum dipole factor and if different molecules will have different polarizabilities and hyperpolarizabilities. On one hand we could make the assumption that all of these species will have comparable dipoles and polarizabilities. Therefore, co-adsorbed CCH_x groups will also have contributions on the spectral shift of CH. On the other hand it is clear that the presence of other species must have effects on the amplitude and the bandwidth of the CH-stretch resonance. We are unable to constrain these effects because we are unable to determine the exact coverages of CCH_x at each surface coverage. This is an additional reason why the application of this model on the prediction of the amplitude/intensity of a certain CH-resonance is a problem.

Regarding this amplitude prediction there is furthermore the problem of the unconstrained CH hyperpolarizabilty. This value is not of importance for the shifting simulation, because it influences the frequency shift only little. But it heavily influences the relative amplitude. Of course you could choose another value for

fitting but in addition to the already mentioned problems for the prediction of the amplitude this value would be arbitrary.

To emphasize the problem I will briefly discuss our data regarding the issue of amplitude prediction. Therefore, I extracted the integrated resonant intensities of the data-points in Figure 6.2 and plotted them over coverage.

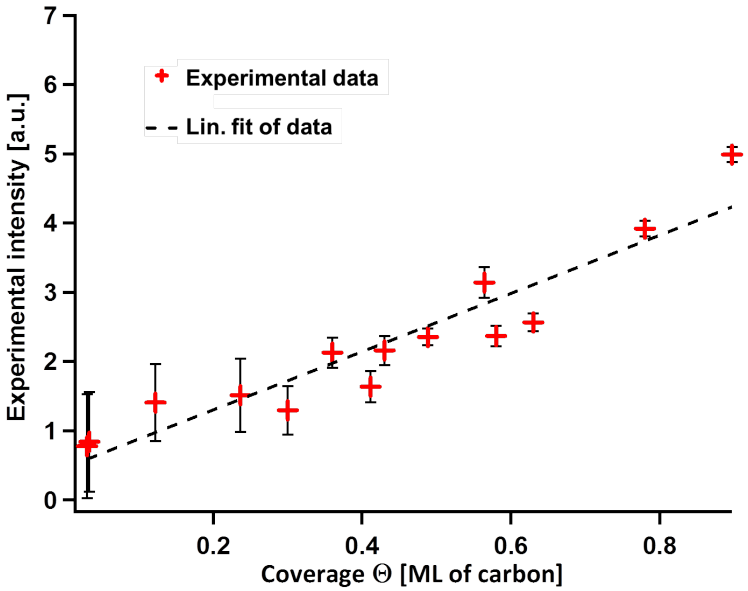

Figure 6.7: The graph show the integrated intensity of the CH-stretch resonance as function of coverage. The data suggest a linear behavior. Nevertheless as clear problem appears. The linear fit, attached to the data given a not negligible intensity of the SFG resonance in case of zero coverage, where the intensity should be zero. The origin of this could be found in an overestimation of the resonance by the fitting procedure in case of low coverages and will be discussed in the text.

You can see in Figure 6.7 a coverage dependence of the resonant intensity, as already expected. Unfortunately, the linear fit of the integrated intensity (to catch the trend) shows a resonant intensity in case of zero coverage which is unequal zero. This is not possible. This observation is caused by a low signal to noise ration in case of small resonances (due to low coverages). This induces an overestimation of the resonance by the fitting program. To cover this problem I attached an error to each data point. This error is in case for small coverages high and for high coverages small. Furthermore, there are the already mentioned additional problems for the high coverage region. We are just focusing on the CH-stretch mode of CH groups and therefore we neglect the contributions of other apparent higher hydrocarbons (CCH_2 and CCH) at higher coverages. This is clearly shown in Figure 6.1 b). This effect decreases the measured signal intensity of CH, because CH represents only parts of the coverage.

By usage of our already applied parameters for prediction of the frequency shift

in Figure 6.3 I simulated the coverage dependent amplitude changes in Figure 6.8.

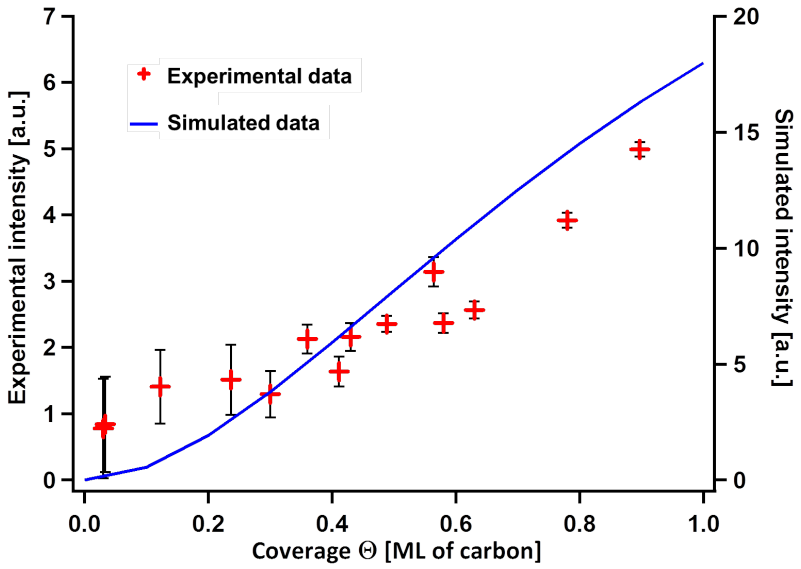

Figure 6.8: The graph show the integrated intensity of the CH-stretch resonance as function of coverage. The attached curve is generated by usage of the dipole coupling model with the already discussed parameters, derived for the prediction of frequency shift.

You can see from Figure 6.8 that the data trend is not reproduced by the model. The first problem is, that the total predicted intensity by the model for high coverages is nearly three times higher than the measured on. But even in case of a comparable intensity, the general data trend is still not really covered by this model. This is due to already mentioned reasons.

The mentioned facts as well as the data allows the suggestion that the application of the dipole coupling model on the prediction of the spectral CH shift is reasonable within the range of the assumptions we made. The prediction of the relative amplitude is not reasonable because of the unknown amounts of higher hydrocarbons, the correct distribution of the molecules at the surface and the hyperpolarizability of the molecules.

6.3 Discussion of CH-coupling

The prior shown graphs have demonstrated quite well that by the given parameters from literature and the assumptions for the sum dipole factor it is possible to reproduce the spectral shift in CH frequency with changing carbon coverage. The value for the sum dipole factor contained the assumption of a well ordered structure (as required from Scheffler for this model) of our CH-species on our surface. This could unfortunately not be checked. Of course, it is clear that small changes in the

sum dipole could be possibly compensated by the α_ν and the other way around. But the range where this is possible is relatively small. By comparison of our value for the sum dipole to other investigated systems to get a feeling for it, you find in [84] for their system of CO on Ru(0001) a sum dipole of S_0= 0.082 Å^{-3} for a coverage of 0.33 ML. Our value is nearly the same. But you should have in mind that we assumed a maximum coverage of 1 ML of CH and not 0.33 ML(as it was the case for CO). The sum dipole of 1 ML CO on Ru(0001) would have been much larger. Unfortunately, there have been to the best of our knowledge no values for sum dipoles of hydrocarbons published yet. Therefore, it is hard to get some feeling whether the value for S_0 is over- or underestimated. On the other hand, the fact that these values described our system more or less accurate clearly hints that the dipole shifting model is, under certain constraints, applicable to the system of C_xH_x on Ru(0001).
Let us discuss now more general the effects of dipole coupling with focus on the understanding and interpretation of vibrational responses of adsorption systems.

Within the last decades, the effects of dipole coupling have been the focus on many investigations. One general aim in these studies were the understanding of dipole-dipole interaction of adsorbed molecules (normally CO on various metal surfaces). This were done by observation of spectral shifts. Another aim was to get a better insight into morphological aspects and adsorption geometries of molecules. These effects have been observed in case of electro-chemistry (Pt(111)/CO system [163]) as well as in UHV on metal surfaces[151, 161]. The influence of coupling on the investigated systems can be described as follows: if a molecule changes its adsorption site this will have effects on the vibrational frequency of the internal molecular bonds. Therefore, two identical molecules which are adsorbed at different adsorption sites will have different observable frequencies in the vibrational spectrum. This is a wonderful tool for the understanding of adsorption geometry in ordered ad-layers. But if the adsorption geometry is a function of coverage [151] and lateral interactions happen, you will have multiple effects on your spectral observables that can have a similar influences. Clearly, the understanding of geometrical aspects will be hindered in such a case. A detailed knowledge about the coupling mechanisms in combination with a model which enables the prediction of dipole shifts allows therefore a better insight into the geometrical aspects and substrate contributions.

Another important topic, where a detailed understanding of coupling effects would be helpful is the investigation of energy dissipation in chemical reactions. For a detailed understanding of chemical reactions it is of crucial importance to understand the kinetics and therefore the rates and timescales of energy dissipation during a reaction. In case of no coupling or isolated molecules these parameters were

just controlled by the substrate-adsorbate interaction. If a reaction takes place at a by other molecules surrounded molecule, intermolecular coupling could open new channels for energy dissipation. Parts of the reaction energy could be transferred to the surrounding molecules. This would change the kinetics of the whole process. In such a situation a detailed understanding of the occurring reactions requires without doubt some constraining of the intermolecular coupling strength.

However, there is a last point which is more related to this thesis. A model which allows the prediction of shifts in the vibrational frequencies of hydrocarbons would be a useful extension for identification and interpretation of CH-groups in the CH-stretching region. Also a more detailed understanding of occurring chemical reactions would be possible. This thesis has shown in detail that the correct identification of different ν_s resonances of C_xH_x molecules is a challenging topic, because of the huge amount of different modes in a spectrally narrow region (2880-3050 cm^{-1}). Even small shifts in observed frequencies could thereby lead to a misleading interpretation of experimental observation, because the dipole coupling induced shifts could be 10-30 cm^{-1}. This is within the order of relative frequencies shifts between the ν_s of different CH-containing molecules.

This observation of dipole-dipole interaction for hydrocarbons could therefore open new ways for the understanding of chemical interaction of hydrocarbons on surfaces.

Chapter 7

Water Interaction with α-$Al_2O_3(0001)$

After investigating methane on Ru(0001) in previous chapters I will introduce in the following chapter the next important topic of this thesis: water adsorption on Alumina surfaces. In this chapter we will focus on the interaction of heavy water with the basal plane of α-$Al_2O_3(0001)$. This is done because of its character as a model system for water dissociation and its importance for industrial applications and environmental chemistry. [75, 23, 76]

7.1 Introduction into water/Alumina interaction

Much work has shown that Alumina change surface properties dramatically in interaction and reaction with water [60, 21, 23]. While a lot of effort has been spent to gain molecular level insight into these changes, it has been found to be surprisingly challenging to reach this goal. For example, α-$Al_2O_3(0001)$, in contact with liquid water and studied as a function of pH, appears to react significantly different when studied by different groups using the same methods [96, 192, 152]. The origin of this challenge could be based on two possibilities: on the one hand the preparation of well defined surface under ambient conditions without any pollution seems challenging. On the other detection and interpretation of experimental parameters like the OH-stretch and bending modes, which are important for the characterization and understanding of interfacial liquid water, can be hard to perform[168]. Our approach to overcome both potential problems is to move the investigation of the water/alumina interface into the UHV. Actually, the movement of investigations into UHV has an additional benefit. While investigations under ambient conditions were nearly always

performed at fully hydroxylated samples (because the humidity of air will always cause hydroxylation), the investigation in UHV allows us to control water coverage at the interface. This improvement of experiments is of a particular interest and will be clear later on. The majority of prior investigations probing water/Alumina interaction in UHV have focused on the α-Al_2O_3(0001), because this crystal is the most stable of the α-Alumina surfaces [89, 58, 111, 127, 143, 175, 93, 59, 60]. It has been experimentally shown that the (1×1) 1-Al-terminated surface of α-Al_2O_3(0001) is the most stable configuration of the crystal interface in vacuum [125]. Unfortunately, many experimental attempts, which wanted to investigate not only the clean sample surface, but also its interaction with water, observed that the probability of water's dissociative adsorption (i.e. water's sticking coefficient) is strongly pressure dependent varying over seven orders of magnitude by moving from low to high water pressures at the interface [175, 127, 93, 60]. Therefore the dissociative sticking coefficient for H_2O at a surface temperature of 300 K in UHV was low. To overcome this problem they transferred the sample for hydroxylation into an attached high pressure cell (HPC) where they exposed the sample to mbar pressures of water and explored the surface water by thermal desorption experiments afterwards. Therefore, I want to refer to some TDS measurements of the hydroxylated α-Al_2O_3(0001) surface which was performed by Elam et al [143, 58]. In their TDS signal they observed a long high temperature desorption tail for water. Elam et al. interpreted this tail as resulting from recombinative desorption of water from more than 20 different adsorption sites, at which the adsorption energies differ by more than 100 kJ/mol [143, 58]. In contrast, only two mechanisms of dissociative adsorption have been identified theoretically [111, 110, 21]. Clearly experiment and theory disagree.

A possible origin of this misfit between experiment and computational observation could be that investigated coverages of the systems differed widely. Theoretical studies have investigated mainly the interaction of limited amounts of water (0.25 ML [21]) with surfaces. Many scientist are interested in the basic reactions at the surface, which is the single molecular dissociation of water. However, this is also a question of the costs for calculation, because the calculations use density functional approaches which gets more expensive for more complicated (more molecules in a unit cell) and bigger systems (bigger unit cells). Therefore theoretical approaches normally tried to use small unit cells (2x2-cells) with less water (one molecule per cell) which ends up by an investigated coverage of 0.25 ML. In contrast to theory, experimental approaches for investigation of this system under UHV conditions hydroxylated their samples by first exposing them to mbar pressures of water. If the kinetics and thermodynamics of water/α-Al_2O_3(0001) interaction changes as a function of water pressure/coverage as implied from the pressure dependent sticking coefficient, you

could possibly expect to observe different chemistry at the surface than for isolated water. This suggestion gets supported by some computational studies, which reported the activation barrier of water dissociation to be lower for the case of additional coadsorbed water at surface. [111]

An additional explanation for the deviations could be that many experimental tools for investigation of this system were not a preferred choice for getting a detailed insight into the dissociated adsorption mechanisms of water in UHV. The great majority of the experimental tools, which were used for investigation of H_2O/ α-Al_2O_3(0001) in UHV, did not allowed a direct insight into the different adsorbed OH/OD groups . TDS measurements for example give only insight into what desorbs from the surface. For x-ray and electron based techniques it is not possible to detect hydrogen atoms adsorbed on a surface[127, 93]. In principle photon based vibrational spectroscopy (*e.g.* reflection absorption infrared) could overcome this problem by probing of the OH-stretch vibration. But to the best of our knowledge there has been no work along these lines so far for this system. This could be caused by the low infrared reflectivity(causes weak signals) from the oxide surface [186].

By using our experimental setup for investigation of this system I close the gap between theory and experiments. This could be the case because of two reasons. On the one hand I can use as a tool for hydroxylation of the sample our molecular beam source, which should hopefully allows the dissociation of D_2O directly under UHV conditions. To our knowledge nobody else had employed such a source of water to the system in such a way so far. Therefore, one could hardly make any predictions for the dissociation probability. On the other hand, I have a surface sensitive tool by usage of SFG for optical spectroscopy and in situ identification of adsorbate layers to probe the OD-stretch responses of interfacial species.

In this chapter I will attempt to get insight into the physics and chemistry of adsorbed water and identify all different occurring OD-species. A correct spectroscopically identification of the occurring OD-species allows furthermore the comparison with theoretical calculated values of our coworkers of the University of Potsdam from the working group of Prof. Saalfrank. By comparison of the measured SFG-spectra with calculated frequencies and geometries one could possibly verify the theoretically predicted dissociation pathways. These pathways will be introduced below. In addition to that I will also use our spectroscopy methods to get insight into the relative populations of different OD-groups. By doing this one could be able to get some insight into the kinetics, which controls the population of the different dissociation channels. This will be of certain interest, because my coworkers also had spend some effort on calculation of the kinetics which controls the populations of their theoretical predicted adsorption states. Details of their computational methods

were given in the Appendix.

Before presentation of the spectroscopic results I will discuss the computational results for the different dissociation and adsorption channels on the surface.

7.2 Calculating Frequency and Orientation of Surface OD fragments

As mentioned above, prior theoretical work has shown that the dissociative adsorption of D_2O/H_2O is occurring via two mechanisms (see Figure 7.1, taken from [21]).

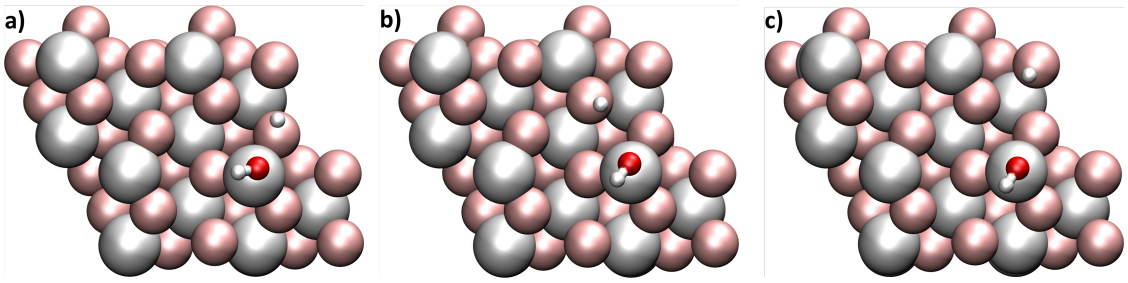

Figure 7.1: (1×1) Al-terminated α-Al_2O_3(0001) surface with D_2O adsorbed via the 1-2 (left) and 1-4 (center) dissociation channels. The 1-4′ configuration (right) was considered in the calculations as representative for various configurations featuring adsorbed deuterons in larger distance from residual OD groups. Different colors denote aluminum (large grey balls), surface oxygen (large red), water oxygen (small red), and hydrogen atoms (small white), respectively.

Figure 7.1 a) shows the first of these mechanisms, which is the so-called 1-2 dissociation channel. An OD fragment (I term it as OD_{ads}) of a D_2O molecule is covalently bound to a surface Al-atom. The corresponding deuterium atom binds to the nearest surface oxygen atom and forms of a new OD group (hereafter called OD_{surf}). The second dissociation channel, shown in Figure 7.1 b), is called the 1-4 channel. The position of the OD_{ads} group is the same but the OD_{surf} group is adsorbed on a surface oxygen one further away from the OD_{ads} group. At this point we have to mention, that further diffusion of the D-atom at the surface can happen, since its diffusivity is quite high[21]. This surface diffusion can lead to adsorption situations, where the D-atom is adsorbed further away from the corresponding OD_{ads}, than its is the case for the 1-4 channel. Calculations of our coworkers addressed this issue by including an additional adsorption state, called 1-4′. Thereby they neglected, whether the D-atom is attached to an Oxygen atom which is one site further away compared to the 1-4 channel or more. It has been shown by calculations that the vibrational frequencies of the corresponding OD-stretch modes were insensitive to this further diffusion. This means that changes in the frequencies were not more resolvable

OD fragment	ν (cm^{-1})	ν_{01} (cm^{-1})	θ (degrees)
OD_{surf}^{1-2}	2629	**2523**	37
OD_{surf}^{1-4}	2647	**2541**	26
$OD_{surf}^{1-4'}$	2686	**2583**	29
OD_{ads}^{1-4}	2795	**2696**	45
$OD_{ads}^{1-4'}$	2796	**2697**	53
OD_{ads}^{1-2}	2810	**2713**	49

Table 7.1: Calculated harmonic frequency ν, anharmonic frequency ν_{01} and bond vector angle (θ) with respect to the surface normal for each type of OD fragment in the 1-2, 1-4 and 1-4′ dissociation state. Data published in [22].

in my setup. After geometry optimization of the (2x2)-cell, theory performed for comparison with my experiments normal mode calculations for the frequencies of each possible OD fragment in the 1-2, 1-4 and 1-4′ state. These harmonic frequencies, the corresponding anharmonic frequencies and the orientation of the corresponding OD-groups with respect to the surface normal are shown in Table 7.1.

Several trends of Table 7.1 are immediately apparent. First of all, it should be possible to resolve 5 distinct resonances of the different OD-groups at the surface (OD_{ads}^{1-4} and $OD_{ads}^{1-4'}$ presumably indistinguishable). The second observation is that the OD_{surf} groups are closer to the surface normal and their frequencies are red-shifted relative to those of OD_{ads}. As a last point one can see that the anharmonicity induces shifts of all frequencies towards lower frequencies by approximately 100 cm^{-1}.

Before coming to the in-situ investigation of the different predicted adsorption states it needs to be clarified whether it is possible with the experimental setup to dissociate D_2O under UHV conditions on α-$Al_2O_3(0001)$. As mentioned before, all prior work in UHV on α-$Al_2O_3(0001)$ used a HPC for hydroxylation. Therefore it is not clear whether the usage of a MBS for dosage of high kinetic energy water molecules enhances dissociative adsorption of water in UHV.

7.3 Dissociative adsorption of D_2O on α-$Al_2O_3(0001)$

To understand whether it is possible to enhance dissociative adsorption of D_2O it is necessary to distinguish molecularly from dissociatively adsorbed water. Below will be some TDS data for D_2O desorption presented which should give more insight into this question. For dosing of D_2O, helium as the seeding gas was bubbled through a deuterated water reservoir. This gives the helium a certain humidity. All tubings

of the gas system were heated to 120°C to minimize subsequent adsorption of D_2O on the stainless steel tubes between the reservoir and the nozzle. All measurements were performed using a nozzle temperature (i.e. T_{Nozzle}) of 860 K.

Initially, a series of measurements were conducted where the sample temperature was fixed at 160 K and the sample was dosed with D_2O/He for different times. After each dosing Thermal Desorption Spectroscopy spectra of water were taken. For taking the TDS spectra a heating ramp of 100 K/min was applied to the sample. By doing this, you get a series of spectra as shown in Figure 7.2. The aim of these series was to get insight into the multi- and monolayer desorption spectrum of D_2O from α-Al_2O_3(0001). In case of molecular adsorption, we expect a desorption spectrum which shows two desorption peaks, where the low temperature peak will correspond to the multilayer and the high temperature peak corresponds to the monolayer. If adsorption happens only molecularly, you also expect a relatively sharp desorption tail in the high temperature region[31].

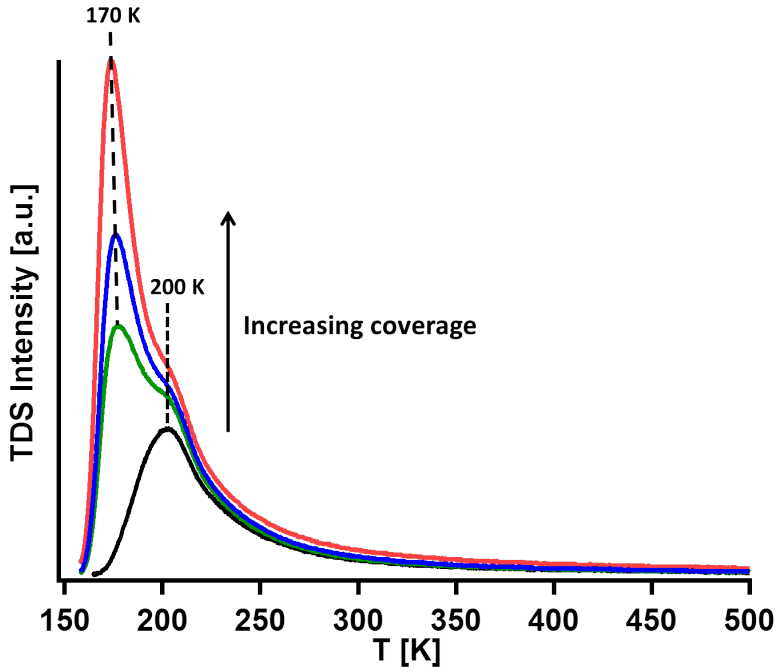

Figure 7.2: TDS spectra of α-Al_2O_3(0001) dosed with D_2O using the MBS and with $T_{Al_2O_3}$ = 160 K. Plotted is the desorbed mass 20 over the surface temperature. Dosing time increases from black→green→blue→red curve. You can observe a desorption feature in the spectrum which is centered around 200K. After saturation of this peak a second peak appears in the spectrum. This is centered around 170 K and increases with increasing dosing time.

Figure 7.2 suggests that D_2O adsorbs at low temperatures($<$ 200K) on α-Al_2O_3(0001) by formation of multi- and monolayer peaks. The peak centered at

170 K corresponds to multilayer adsorption of D_2O, because the peak could not be saturated. The shoulder which is centered at 200 K corresponds to the monolayer of molecular adsorbed water. Keeping the sample temperature of 180 K while dosing should therefore end up in saturation of the water monolayer. This could be used as monolayer preparation-way for a reference spectrum what will be described later. For all following discussions I will define the peak centered around 200 K, which corresponds to the black desorption curve in Figure 7.2, to a monolayer of molecularly adsorbed water.

Interestingly, the desorption signals in Figure 7.2 show a high temperature tail for D_2O desorption. The long desorption tail to high temperatures suggests that there are already small amounts of dissociatively adsorbed water at the surface. You can assume (and later on verify this assumption using SFG measurements) that desorption of D_2O at > 250 K have its origin in dissociatively adsorbed water.

Because the aim of this work is the investigation of dissociated water, I want to increase the amount of dissociatively adsorbed water at the surface by changing the preparation conditions. Comparison of the TDS spectra of modified preparations ways with the monolayer spectrum(black curve in Figure 7.2) allows the decision if a certain way of preparation is successful. Therefore, the surface temperature while dosing was changed in a special way that we found to give the highest desorption signal of D_2O at > 250 K. To prepare such a sample I followed a five step procedure: 1.) Start dosing with the MBS at $T_{Al_2O_3}$= 450 K and cool it with a 10 K/min ramp to 300 K while dosing 2.) Dose 20 minutes at $T_{Al_2O_3}$= 300 K 3.) Continue dosing during the sample is cooled by 20 K/min to 150 K and stop dosing when this temperature is reached 4.) Align the SFG setup on the large free OD signal of ice by overlapping the visible and infrared beams spatially and temporally (a precondition for the SFG measurement) 5.) Anneal the surface with a ramp of 100 K/min to 250 K to remove the great majority of all molecularly adsorbed water and return the sample to 150 K for characterization.

If the five step procedure enhances dissociative sticking there should be a higher desorption signal of D_2O in the high temperature region observable. Preparation of a sample as described above and plotting the measured TDS spectrum together with the desorption spectrum of the above defined monolayer of D_2O, should clarify the possibility of enhanced dissociation. This was the case, as clear from Figure 7.3.

The thermal desorption spectrum of a five step procedure prepared sample(shown Figure 7.3) shows several important features. First of all, one can observe in nearly the full temperature range a higher desorption signal for D_2O than in the monolayer spectrum. This higher intensity must have its origin in enhanced dissociative water adsorption at the surface, which clearly shows MBS preparation

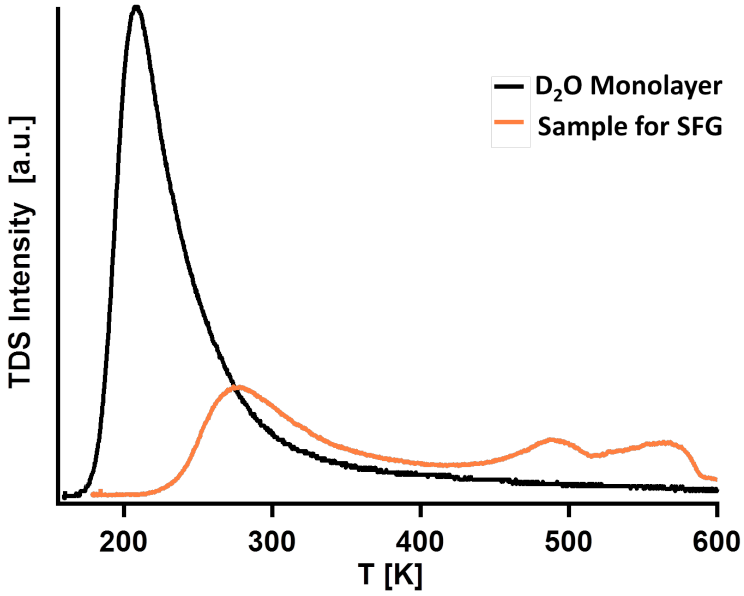

Figure 7.3: TDS spectra of α-Al_2O_3(0001) dosed with D_2O using the MBS and with $T_{Al_2O_3} = 180$ K: monolayer preparation (black curve). TDS of sample as prepared for SFG analysis.

is successful. Three desorption maxima in the TDS signal are apparent: at 280 K, at 480 K and at 560 K. The two high temperature peaks are clearly the result of dissociatively adsorbed D_2O and have not been observed in prior UHV studies of water/α-Al_2O_3(0001) reactivity[143]. The desorption maximum at a temperature of 280 K is a function of the maximum temperature in the final annealing step: if the sample get instead annealed to 220 K before beginning the TDS scan this peak would be centered at lower temperatures. But as discussed above, this desorption peak is expected to be dominated by the desorption of dissociatively adsorbed D_2O.

To crosscheck if dissociatively adsorbed water dominates the desorption spectrum, you can apply SFG-spectroscopy for the detection of molecular water at the surface. TDS data suggests that at temperatures of $\approx$ 170 K and below the crystal surface is ice covered. By annealing the sample to 200 K the ice and molecular water should be desorbed and only the OD fragments from the dissociation should be left. From this point of view, the spectral response at temperatures of 170 K and below should be dominated by a significant population of hydrogen bonded OD groups: those OD's (of D_2O) at the ice/vacuum interface that donates a hydrogen bond. If molecular water is largely absent above 200 K this population is expected to disappear. Therefore, I prepared a sample by just performing the first four steps of the five step process (no final annealing step). Afterwards SFG spectra in the D-bonded region (2400 cm^{-1}-2550 cm^{-1}) were taken. Figure 7.4 shows a series of measurements with different

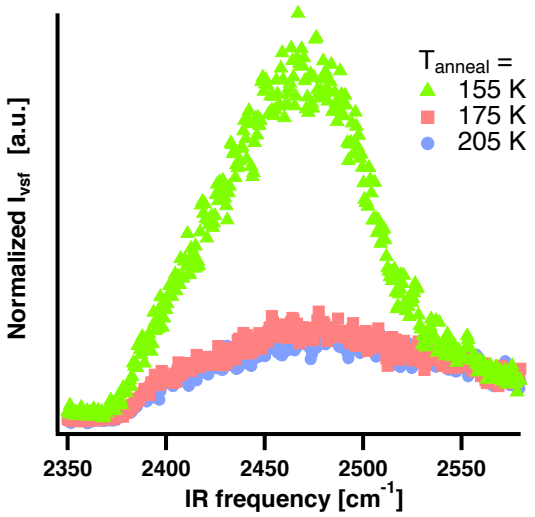

Figure 7.4: SFG spectra of the D-bonded region of D_2O ice as a function of annealing temperature. The sample was prepared in the five step routine without the last annealing step to 250 K. Subsequent heating removes the ice from the surface and the D-bonded signal vanishes at temperatures > 200 K. The width of the spectral feature is determined by the FWHM of our IR pulse: $\approx 150\,\mathrm{cm}^{-1}$.

annealing temperatures. At 155 K a huge D-bonded signal of the ice multilayer can be observed, in good agreement with prior studies of ice in this frequency region [183, 184]. By annealing the sample to 175 K approximately a monolayer of water should be left at the surface. This monolayer still shows a small D-bonded signal, implying that Deuterium bonding in the monolayer between the molecularly adsorbed water at the surface is occurring. Annealing to 205 K leads to the complete disappearance of the D-bonded signal. This is consistent with our conclusion that above 200 K surface temperature mainly dissociatively adsorbed water will be present at the surface. Most of the later on taken SFG spectra will be performed on samples which got annealed to 250 K, to be confident that no contribution of molecular waters is apparent. To summarize: both SFG and TDS analysis is consistent with the picture that the α-$Al_2O_3(0001)$ surface is dominantly covered by dissociated water in case of dosing with the MBS at elevated surface temperatures.

7.4 Influence of OD orientation on the measured I_{SFG}

Given the possibility to dissociate the D_2O, I next discuss how molecular orientation of the different OD-groups influences the SFG response. It was already shown in

Chapter 2 that molecular orientation with respect to the surface normal, as well as the experimental geometry, influences the relative intensity of generated SFG from different OD-groups. The in Table 7.1 shown computational results of our coworkers find that different types of OD fragment have different orientations. Therefore, you can predict the relative I_{SFG} of each OD fragments depending on its calculated tilt with respect to the surface normal in our experimentally accessible beam geometries. The mathematical background for calculation of the SFG intensity as a function of different polarization combinations, molecular orientations and beam geometries was already derived in the Section 2.3.4. Insertion of the molecular angle and chosen polarization combination into to Equation 2.34 enable the calculation of the effective $\chi^{(2)}$. This allows the calculation of I_{SFG} by Equation 2.28 in order of the incident angles of the used IR and VIS beams. There are two possible geometries to use for SFG spectroscopy. Geometry 1 has as incident angles 75°/70° for Vis/IR. Geometry 2 has as incident angles 37°/35° for Vis/IR. Calculation of the relative I_{SFG} for geometries 1 and 2 gives the results shown in Figure 7.5.

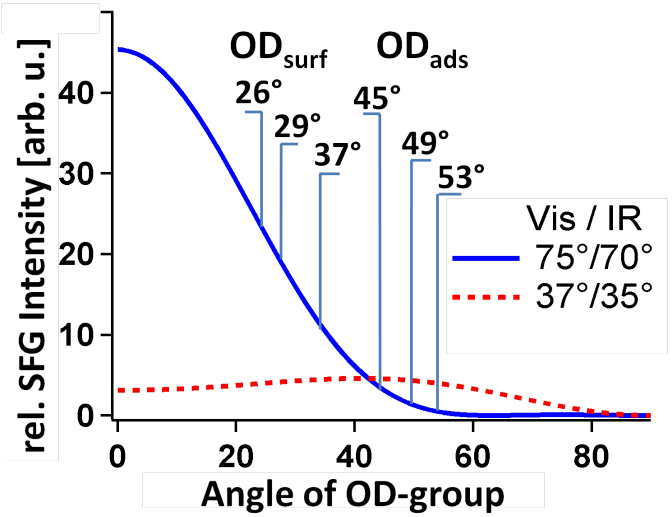

Figure 7.5: Calculated relative I_{SFG} as a function of molecular orientation for geometry 1 and 2. In case of an incident angle of 75°/70° for Vis/IR (geometry 1), the solid blue line is the relative resonance intensity for the *ppp* polarization combination. The dotted red line is the relative resonance intensity for *ssp* polarization(s) given incident angles of 37°/35° (geometry 2) for Vis/IR. The spectral response of the OD_{ads} fragments should slightly be more intense under *ssp* with the second set of incident angles.

As is clear from inspection, the calculated responses for different types of OD-groups differs dramatically in intensity. The graph includes the calculated response for *ppp* polarization condition in geometry 1 and the *ssp* polarization condition in geometry 2, which were in the both geometries those with the highest intensity.

Other polarization combination for the geometries could be neglected because of the dramatically lower expected signals. Comparison of the relative I_{SFG} as a function of the computed orientations of each OD fragment (Table 7.1) emphasizes, that under *ppp* polarization conditions in geometry 1 one should see the spectral response from the OD_{surf} groups $2-10\times$ more intense than those of the OD_{ads}. In comparison, changing to geometry 2 should increase the relative intensity of the OD_{ads} resonances (employing *ssp*) although still with lower signal intensity.

7.5 SFG characterization of dissociatively adsorbed D_2O

Given this background, I will focus on the SFG response of a sample prepared in the five step way. This will be done by a series of temperature dependent SFG spectra, where the response of the surface will be monitored under different coverages. For this initial measurements geometry 1 with *ppp* polarization of the beams was chosen because of its expected higher SFG intensity. By performing these kinds of measurements it has been found to be necessary, to align both IR and VIS beam in UHV on the strong OD-stretch response of ice. Presentation of the data in an ordered temperature dependence will also verify the prior conclusion for the composition of the adsorbate layer at different annealing temperatures (molecular vs. dissociative adsorption). As a starting point, I will present the spectral response of a sample, which has been prepared in the five step way without the final annealing step. This means the hydroxylated surface was covered by ice multilayer. By doing this, we found a single peak corresponding to the free-OD of Ice at $2725\,cm^{-1}$, which is shown Figure 7.6

As could be seen, Figure 7.6 shows the single peak of ice at $2725\,cm^{-1}$ in the OD stretching region. For a better presentation of the data we divided the resonant signal by the non-resonant signal. All following SFG spectra will be presented in this way. Comparison of the peak in Figure 7.6 to literature shows us that the center-frequency agreed well with the ice-peak in prior studies of others in UHV[39]. After alignment, we annealed the surface to a temperature of 180 K and cooled it again to 150 K (at this temperature all SFG measurements for this adsorption system were performed). As suggested in the TDS response, after heating to 180 K the ice should be removed and just a monolayer of water (containing both molecular and dissociated water) remains. The spectral response of a sample, treated in such a way shows a dramatically different response(see Figure 7.7) As clear by inspection, there is still a single resonance in the spectrum, but it shifted lower by $5\,cm^{-1}$ to

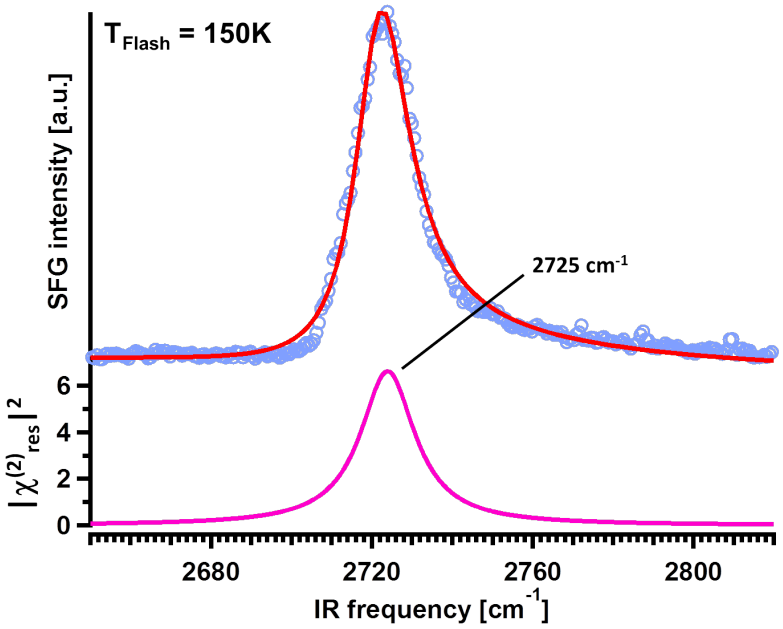

Figure 7.6: The graph shows a single peak in the OD stretching region , which could be attributed to the OD-stretch vibration of ice in vacuum. Plotted is the SFG intensity over the IR frequency. The resonant spectrum got divided by the non resonant background, to emphasize the resonant part of the spectrum. All following data are presented in this way. The measured center-frequency of 2725 cm^{-1} agreed well with prior work by others [39]. Data were taken at geometry 1 and *ppp* polarization. The pulse energy was $\approx$ 12 μJ for the IR and 40 μJ for the VIS.

2720 cm^{-1} compared to ice and had a much weaker signal intensity. Under such preparation conditions (annealing to 180 K), there should be still valuable amounts of molecular water on the surface. It seems likely to assume that the peak at 2720 cm^{-1} corresponds to molecular water. From TDS measurements we know that annealing to 200 K should remove most of this molecular water. If this is true, this suggests that by continuing to heat to 200 K we should see the SFG response continue to evolve. Indeed, as shown in Figure 7.8, at 200 K new features appears in the high frequency region. The spectrum changed dramatically, because now three peaks appears in the spectrum at 2725, 2765 and 2790^{-1}. The low frequency peak, before at 2720 cm^{-1}, seemed to have shifted again to higher frequencies for 5 cm^{-1}, but we could not be sure whether it is still contributed to molecular water. To exclude this, we annealed the sample once again to 250 K , 300 K and 400 K. From TDS we know that at these temperature the surface must be dominated by dissociated water, what is also reported by literature [143]. Therefore I will present several higher annealing steps at once an will discuss their implication afterwards.

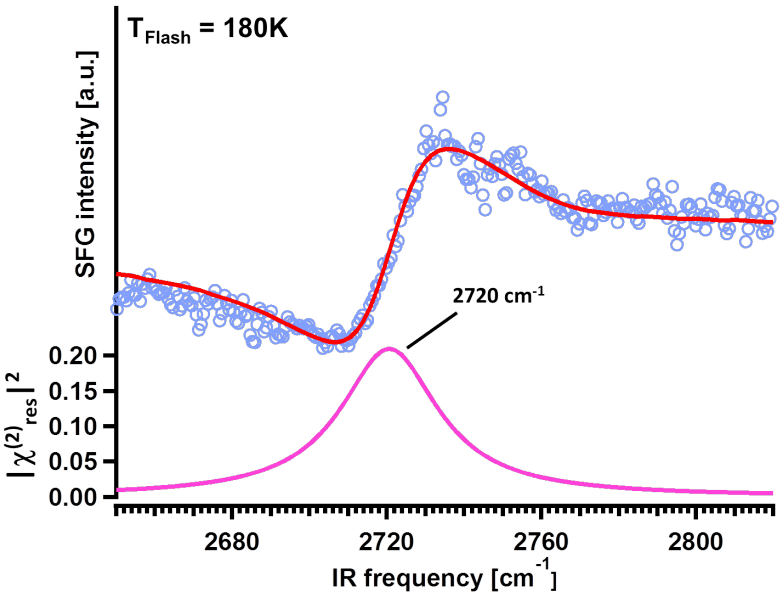

Figure 7.7: The spectral response of the sample, annealed to 180 K dramatically changes from that annealed to 150 K (see Figure 7.6). We can see still one resonace at the surface, but the signal intensity decreased by one order of magnitude and shows a different shape. The center-frequency has been found to be red-shifted for $5\,\mathrm{cm}^{-1}$ compared to the ice layer. I assume, the peak at $2720\,\mathrm{cm}^{-1}$ has its origin in molecular water.

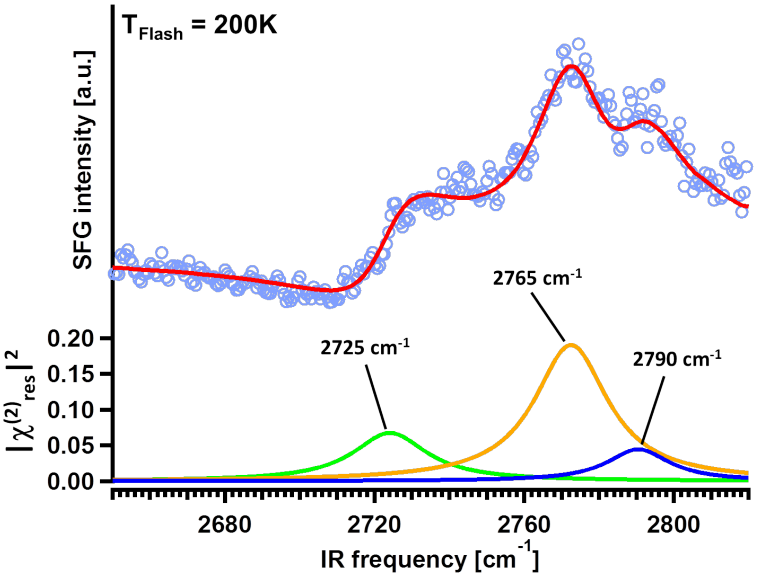

Figure 7.8: The spectral response of the sample, annealed to 200 K shows dramatic changes compared to that annealed to 180 K. In the spectrum, we observe three distinct features. The low frequency mode shifted back to higher frequencies for $5\,\mathrm{cm}^{-1}$.

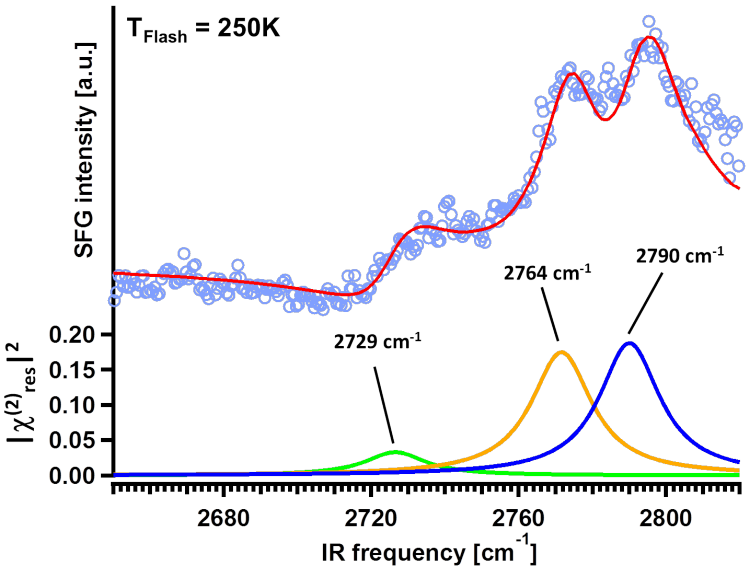

Figure 7.9: The spectral response of the sample, annealed to 250 K. At this temperature we were still able to observe 3 distinct features. The low frequency mode shifts again blue for $4\,\mathrm{cm}^{-1}$ to $2729\,\mathrm{cm}^{-1}$. From their thermal stability, we can conclude that they must have their origin by dissociated water.

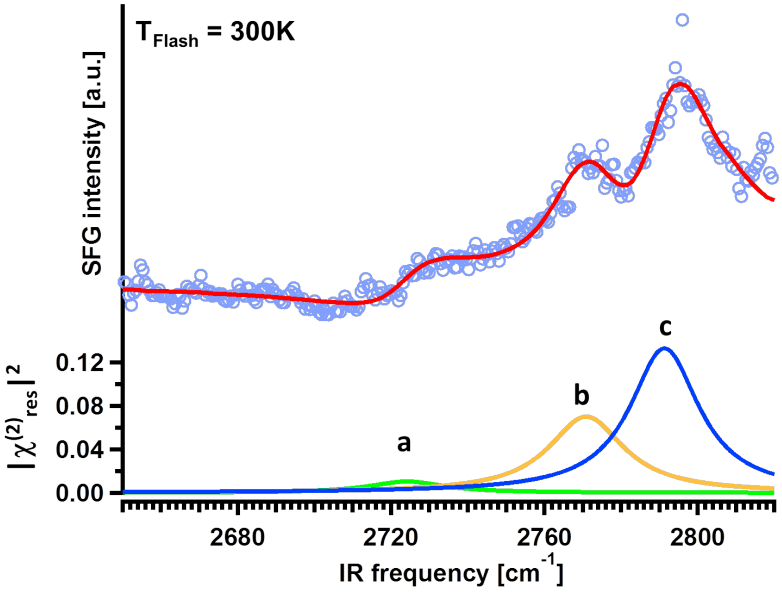

Figure 7.10: The spectral response of the sample, annealed to 300 K. As we can see, the three features are still observable. The frequencies of a, b and c are 2729, 2764 and $2790\,\mathrm{cm}^{-1}$. All modes stayed at these frequencies and does not shift anymore.

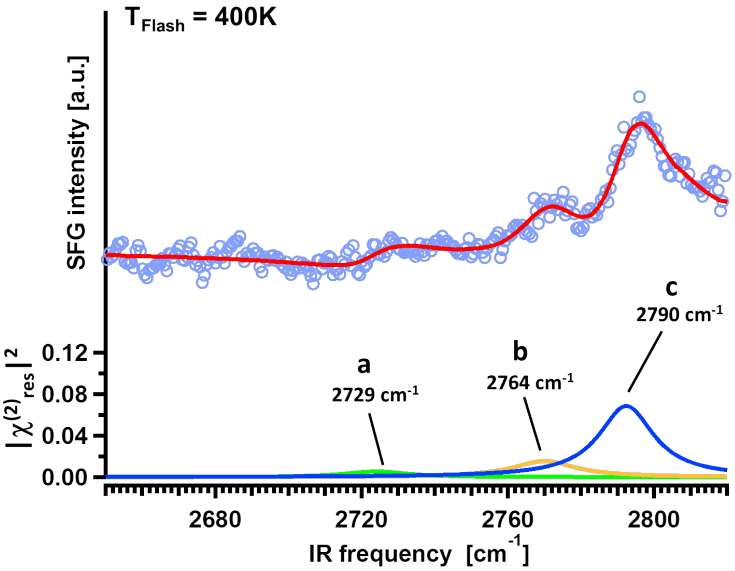

Figure 7.11: The spectral response of the sample, annealed to 400 K. Clearly the spectral response is now dominated by the high frequency resonance.

In Figure 7.9, 7.10 and 7.11 we can follow the temperature dependent decrease of the resonances in the spectrum. The highest temperature, where at least one of the resonances was resolved, was 450 K. From the high thermal stability of the resonances even under the UHV conditions we can conclude that these resonances must have their origin in dissociated water. In the series of measurements shown before we can see three resonances in the spectrum. Above 250 K they did not changed their center frequencies anymore. I defined these peaks as *a*, *b* and *c*. Their corresponding frequencies where 2729, 2764 and 2790 cm^{-1}. The observable relative intensities of the peaks clearly depend on the annealing temperature. This characteristic will be addressed in a following section. Right now, we want to focus on the correct assignment of the observed peaks. By shifting the wavelength of the IR to higher as well as to lower frequencies, we were not able to observe any other resonance in the spectrum.

Comparing the frequencies of these resonances to the theoretical calculated values in Table 7.1 does not show any obvious overlap between the values. From simulation of our SFG intensity we conclude that under this geometry and polarization the resonances of the OD_{surf}-species should be dominant. The intensity of the OD_{ads}-species should be much weaker relative to them. The fact that we were able to observe only three distinct features suggests, that these are the OD_{surf}-species. Comparison of the observed frequencies to the anharmonic frequencies from our collaborators shows an offset of 200 cm^{-1} between computation and experiments.

On the other hand it has been observed that DFT calculated frequencies often show red-shifts compared to the measured experimental values [22]. Nevertheless, it is clear that observation of the remaining resonances would clearly identify the species. Therefore we changed the geometry of our setup to geometry 2 and chose a polarization combination of *ssp*. By scanning the frequency region from 2500 - 3000 cm^{-1} we were able to observe the resonance *c* at 2790 cm^{-1} (as the strongest resonance of *a*,*b* and *c*), but its total intensity was about one order of magnitude lower. This is in agreement with our calculation, if resonance *a*, *b* and *c* would have their origin in OD_{surf}-species. Their orientation dependence is shown in Figure 7.5.

While the molecular orientation of the different groups allowed to predict for the OD_{surf}-species much more intensive resonances in geometry 1, than for the resonances of the OD_{ads}-species, this turns around in geometry 2. There the OD_{ads}-species should be the more intensive ones. These prediction actually fits perfectly in our observation. Additionally to resonance *c*, we found two additional resonances in the high frequency region at around 2900 cm^{-1}. The resonances of *a* and *b* were possibly also apparent, but the lower signal intensity with its corresponding higher signal to noise ratio hindered correct identification, as shown in 7.12.

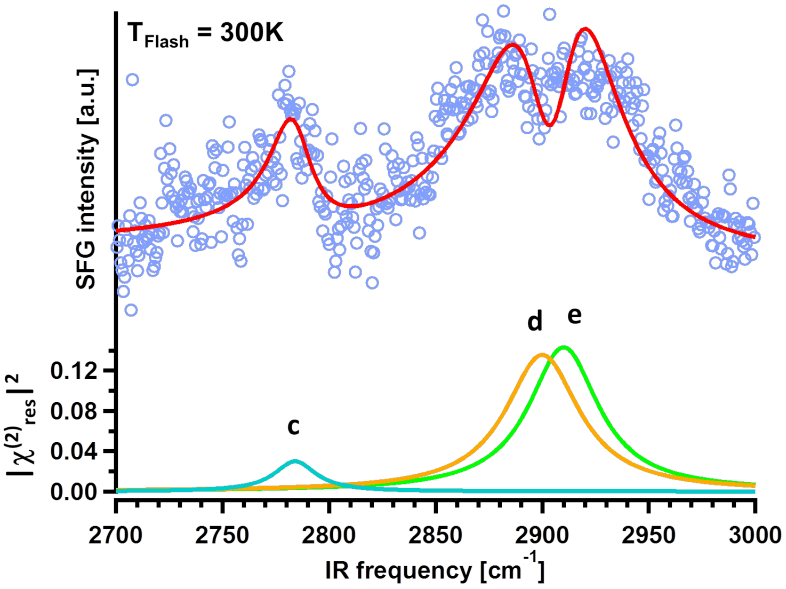

Figure 7.12: The spectral response of the sample, annealed to 300 K, measured in geometry 2 with *ssp* polarization combination. Resonace c has been observed before in geometry 1. Resonance d and e at 2900 and 2910 cm^{-1} have not been observed before.

We can see beside resonance c two additional resonances, called d and e, which appear in the spectrum at 2900 and 2910 cm^{-1}. The other resonances a and b were not resolvable in this graph because of the high signal to noise ratio this measurement. Under the assumption that a, b and c belong to the OD_{surf}-species, the relative frequencies of d and e fits in good agreement to the calculated frequencies of the OD_{ads}-species, listed in Table 7.1. This will become more clear by inspection of Table 7.3 in the next section, where we compared the relative frequency shifts between theory and experiment. All experimentally derived frequencies were listed once again in Table 7.2.

$\tilde{\nu}_q$ **(cm^{-1})**	**Assignment**
2729 ± 5	$\mathrm{OD}^{1-2}_{\mathrm{surf}}$
2764 ± 5	$\mathrm{OD}^{1-4}_{\mathrm{surf}}$
2790 ± 3	$\mathrm{OD}^{1-4'}_{\mathrm{surf}}$
2900 ± 7	$\mathrm{OD}^{1-4}_{\mathrm{ads}}$, $\mathrm{OD}^{1-4'}_{\mathrm{ads}}$
2910 ± 7	$\mathrm{OD}^{1-2}_{\mathrm{ads}}$

Table 7.2: Frequencies of resonances in the experimental data and their suggested assignments.

7.6 Interpretation of SFG Analysis

The listed frequencies in Table 7.2 allow, to test the preliminary assignment of the observed resonances by comparison with the computational derived modes. Since it is clear that the calculated and the measured frequencies seems to have an offset between each other, we will focus for the final assignment of the resonances on the frequencies shifts between the modes. These relative shifts should not be affected by the offset.The offset can base on a model error or incorrectly accounted anharmonicity. Normally, theory compensates observed frequency offsets by multiplying a constant correction factor to all derived frequencies. Because our observed resonances are in a comparable small frequency region such a factor should not affect the relative shift a lot. Therefore we listed the differences $\Delta\tilde{\nu}_q$ between different species for the OD_{surf} and OD_{ads}-species in Table 7.3.

Resonances	$\Delta\tilde{\nu}_q$ **comp.**	$\Delta\tilde{\nu}_q$ **exp.**
$\tilde{\nu}^{1-4}_{\text{surf}} - \tilde{\nu}^{1-2}_{\text{surf}}$	18	35
$\tilde{\nu}^{1-4'}_{\text{surf}} - \tilde{\nu}^{1-2}_{\text{surf}}$	60	61
$\tilde{\nu}^{1-4}_{\text{ads}} - \tilde{\nu}^{1-2}_{\text{surf}}$	173	171
$\tilde{\nu}^{1-4'}_{\text{ads}} - \tilde{\nu}^{1-2}_{\text{surf}}$	174	171
$\tilde{\nu}^{1-2}_{\text{ads}} - \tilde{\nu}^{1-2}_{\text{surf}}$	190	181

Table 7.3: Calculated and experimentally derived frequencies relative to the lowest frequency mode: the $\tilde{\nu}^{1-2}_{\text{surf}}$.

We can see from Table 7.3 that the measured frequency shifts between different modes are in good agreement between calculated and measured values. The main discrepancy between experiment and computation appears to be, that $\tilde{\nu}^{1-4}_{\text{surf}} - \tilde{\nu}^{1-2}_{\text{surf}}$ is slightly larger and $\tilde{\nu}^{1-2}_{\text{ads}} - \tilde{\nu}^{1-2}_{\text{surf}}$ slightly smaller in experiment than in computation. Here we have to take into account that the in Table 7.1 presented frequencies are calculated for a perfectly periodic quarter of a monolayer of adsorbates. Clearly, this situation likely differs from that in the experiment. At (locally) higher surface coverages dipole/multipole coupling between OD groups may influences the resulting calculated frequencies. This could cause a shifting of them by $\approx 20 - 30$ cm^{-1} to lower frequencies, as discussed by us in [22]. Absent more detailed insight in the spatial relationship between 1-2, 1-4 and 1-4$'$ fragments, it seems plausible that such coupling may explains the observed experiment/computation difference.

To summarize up: 15 years of various experimental investigations always reported different results for the water dissociation on α-Al_2O_3(0001) than predicted by

theory. This emphasizes the amazing experimental challenge to get insight into the molecular processes of water on this surface. However, our experimental approach of in-situ preparation of dissociated water in combination with high resolution optical spectroscopy overcomes this hurdle. By comparison of the relative frequency shifts between the different modes, in combination with comparison of the relative geometry dependent intensities, we are able to conclude that we have identified the different OD-species spectroscopically in nearly perfect agreement with theoretical prediction. This verified the theoretically predicted single molecular water dissociation channels on α-Al_2O_3(0001) for the first time experimentally! [22]

7.7 Temperature dependent population

Within the last sections I have identified the theoretical predicted dissociation channels of water on this surface. An interesting question would be, if the kinetics which are controlling the dissociation channels are also in agreement with theoretical prediction. Therefore it is the plan to use SFG as a quantitative tool for getting insight into the population of the different states. The relative populations are controlled by the kinetics of the system. Studying the flashing temperature dependent populations of the different species allows qualitative comparison to theoretical prediction. Wirth and al. [21], our coworkers, investigated in their work the kinetics of interconversion between the different adsorption states at the surface. Their work has shown that the 1-2-channel of adsorption is from the theoretical point of view the most favorable, which means the most populated one. This could be better explained by Figure 7.13.

Figure 7.13 shows the interconversion rates for diffusion and dissociation between molecular water and the different adsorption states. The attached numbers to the arrows in the figure corresponds to the order of magnitude of the rates. For calculation of the rates, our coworkers first derived the barriers for interconversion by a nudged elastic band method. Then the rates were calculated by quantum tunneling corrected Transition State Theory (details of calculation were given in [21]). Seen from these calculations, the 1-2 adsorption state is the most favorable. Rates into the 1-2 state are several orders of magnitude higher than rates out. If the calculated rate model is accurate, we should see in our spectra the 1-2-state as the most populated one. Let us compare this to our data.

As clear from the last chapters, SFG spectroscopy is an analytical tool that allows insight into the relative populations of the different adsorption states. To extract the relative population of a certain adsorption state in order of the temperature from our data, we have to take care for several contributions in the spectra. Because we need for such a kind of analysis a high signal to noise ratio, we just focused for

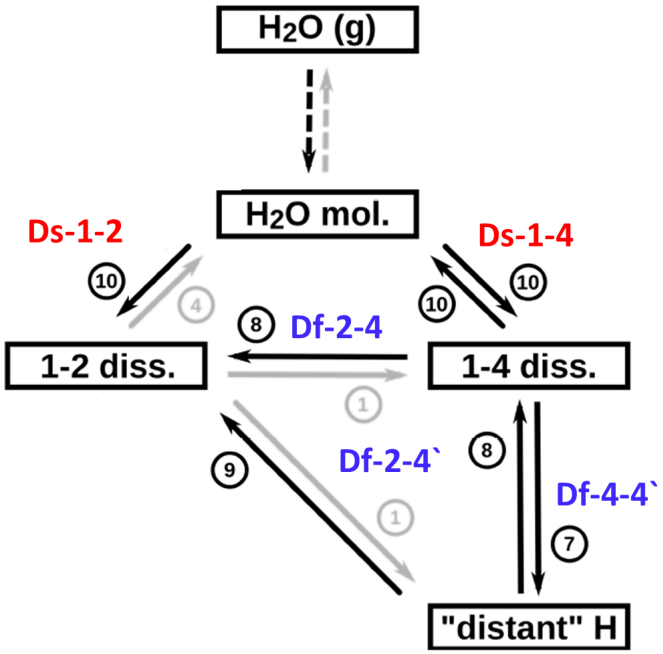

Figure 7.13: Computational developed rate model at 300 K for interconversion between the different adsorption states. **Ds** corresponds in this context for dissociation reactions and **Df** for diffusion reactions. The numbers attached to the arrows corresponds to the order of magnitude of the rate for certain reaction coordinate. Dominant or equal coordinates were black arrows, unfavored coordinates were gray. Rates were calculated for H_2O, but it has been shown that the corresponding rates for D_2O do not differ quantitatively. Figure was taken from literature [21] and modified.

this analysis on the measured intensities of the OD_{surf}-species in geometry 1. These had the larger signal and therefore the better resolution. Since each OD_{surf}-group requires one OD_{ads}-group at the surface, this should be an acceptable approach.

From theory we know that different OD groups should have different molecular orientations. We can assume that at 140 K surface temperature, where SFG measurements were performed, the calculated geometries are valid for our system. Furthermore, we assume that subsequent heating of the sample followed by cooling to 140 K for characterization does not affect the geometries. With these reasonable assumptions we can correct the extracted SFG intensities for the orientation dependent factor, shown in Figure 7.5. These scaled intensities should then reflect the real relative population of the different states.

For this analysis I performed a series of measurements, were I prepared a sample and flashed it afterwards to various temperatures in the range of 200- 450 K. Beyond 450 K the resonances were no longer resolvable. By extracting the resonance intensity from the fitted SFG spectra and multiplying it by its scaling factor to compensate for the orientation (and take the squareroot of it, because $I_{SFG} \propto n^2$), I extract the

temperature dependent relative population of the three OD_{surf}-groups.

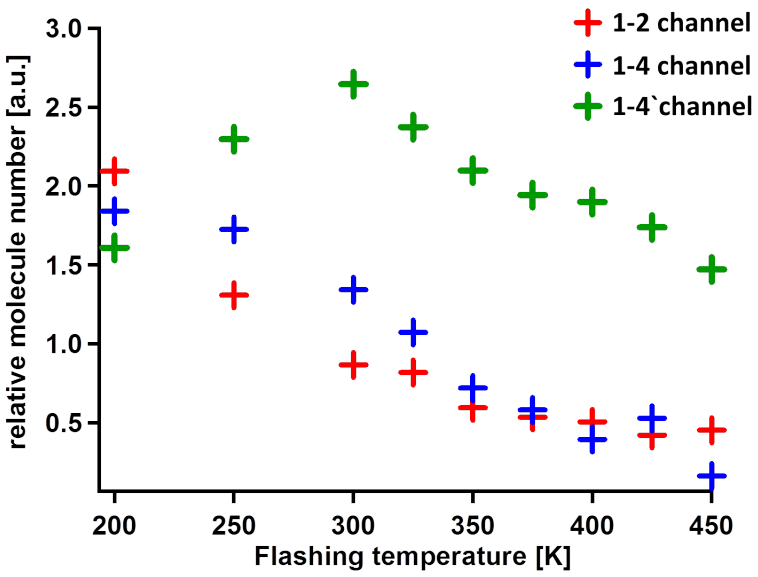

Figure 7.14: Experimentally derived and orientation dependency corrected populations of the different OD_{surf} species. At temperatures of 200 K, the 1-2-dissociation channel is most populated, while the 1-4‘-channel has the lowest population. With increasing subsequent flashing temperature, the 1-2 and 1-4-channel decrease, while the 1-4‘-channel goes through a maximum before decreasing also.

The results are shown in Figure 7.14. Clearly, at 200 K the 1-2-channel is the most populated, as predicted by theory. This relative population inverts with increasing temperature and the 1-4‘-channel is larger, by reaching a maximum at approximately 300 K. Afterwards all populations gradually decrease with subsequent flashing.

To test the assumption that all intensities (after correction for experimental parameters such as IR power, overlap molecular angles etc.) can be directly compared and that the total number of molecules is decreasing with increasing temperature, I added the data point of each temperature together and compared it with integrated TDS measurements of the system for different flashing temperatures. Of course, the absolute values of both techniques were different. For comparison, I scaled the SFG data and TDS data at a flashing temperature 300 K to each other. Then the population decrease should show a similar behavior to the integrated TDS spectra if the quantitative analysis of the SFG is correct .

Figure 7.15 shows the total population decrease by desorption, derived out of TDS and SFG data. At higher temperatures (>300 K) all water should be dissociated at the surface. At these temperatures TDS and SFG data show the same trend. This correspondence strongly suggests the relative populations derived from SFG are accurate in this temperature region. The deviations in the low temperature

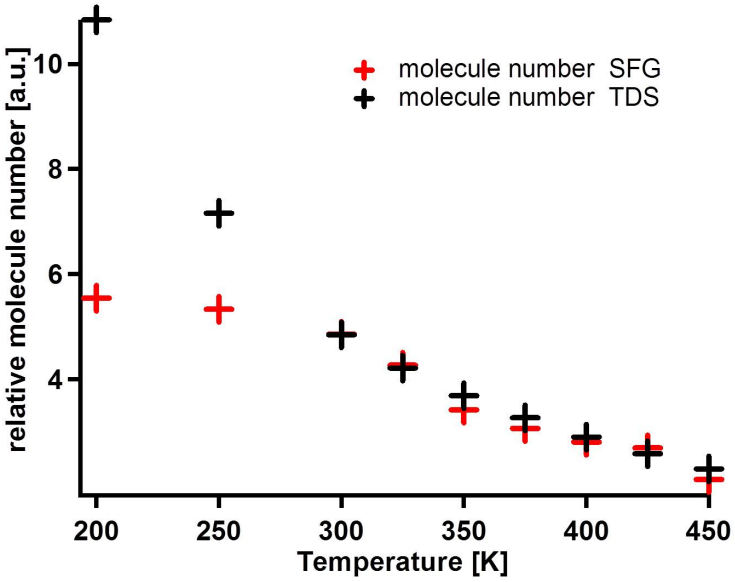

Figure 7.15: Population decrease by subsequent flashing derived out of SFG and TDS data. Absolute populations plotted over flashing temperature. For comparison both were scaled on the same value at 300 K. Beyond 300 K, the population of SFG and TDS behave similar. Below 300 K, both dataset show differences. The origin for this could be explained by the influence of molecular water at the surface. While in TDS data it will be detected equally to dissociated water, it will show a different intensity in the spectral response in SFG. This is not compensated by our model in Figure 7.5. That is the reason why both data got scaled on their intensity at 300 K. At this temperature, no molecular water should be left at the surface.

region may indicate the contribution of molecular water to the SFG spectra, for which we are unable to correct. Nevertheless, this data trend beyond 300 K shows that the derived populations of the different adsorption states are quantitatively correct. The result that there is a population inversion at 300 K, is in contrast to the theoretical model, shown in Figure 7.13. They predict that at 300 K the 1-2-state is the most populated one. The question is whether our experimental observation and the theoretical treatment could be compared directly. By our experimental treatment, we are flashing the sample up to a certain temperature and cooled it afterwards to 140 K to perform SFG measurements. Clearly, this additional cooling step was not reflected in the rate model. To test whether this cooling induces changes in relative populations, I performed a measurement while holding the sample temperature at 300 K. From an experimental perspective measurements at > 140 K are extremely hard to perform. The different sample temperature changes slightly the sample orientation and therefore the overlap of the both VIS and IR beams. Nevertheless, I was able to make this measurement and found no significant difference in population relative to samples cooled before measurements. Therefore, this effect could not

explain the misfit between theory and experiment.

Another possibility to explain the difference between theory and experiment could be different water coverages. For the theoretical calculation, Wirth et al.[21] fixed the water coverage to 25 % of a ML and excluded the possibility of desorption. This assumption is important, because the relative population of different states should be a function of surface coverage. To see this we first consider a 2x2-cell of α-Al_2O_3(0001) and a coverage of 25 % of a ML (e.g. one water molecule per cell). For this system there could be only three different adsorption states (1-2, 1-4 and 1-4‘) possible at the surface. Summing the total number of adsorption sites in each state gives three 1-2, three 1-4 and six 1-4‘. If we now have only 12.5 % of a ML (two 2x2-cells next to each other but still only one water molecule), there will be a huge amount of possible adsorption states, where the D-atom is even further away from its OD_{ads}-group than in the 1-4‘-site.

These new adsorption sites could be collectively called the 1-4$'_{far}$- sites. Therefore you will have three 1-2-sites, three 1-4-sites, six 1-4‘-sites ,and twelve 1-4$'_{far}$- sites. Spectroscopically, the 1-4$'_{far}$- sites and the 1-4‘- site could not be distinguished (theory calculated the frequency shift with $1\,cm^{-1}$), which implies that you should see an overlap between of these two states in our spectrum as the 1-4‘-state. As a try to constrain the effect of surface coverage on the relative populations of the different states, our coworkers from Potsdam spend some effort on simulation of the populations by kinetic Monte-Carlo simulations. Since I do not want to go into detail into their results I have to mention, that there are not negligible effects on the relative populations of the states, depending on the surface coverage and temperature. By decreasing the amount of water in their system and increasing the temperature, they were able to observe an inversion of the population. Nevertheless, this topic is still in focus of investigations and ongoing work and will be hopefully better understood in the near future.

7.8 Surface phonon modes of α-Al_2O_3(0001)

In the preceding sections of this chapter it should have become clear that there is intensive interaction between water and α-Al_2O_3(0001). Up to now, I only focused on the effect on the water during this interaction: how water dissociates. On the other hand, it would be interesting to monitor also the effect of water adsorption and dissociation on the substrate. Ideally for this purpose, we would like to use a spectroscopic tool, which allows characterization of both the dissociated water and the interfacial structure. I have already shown in the last section that SFG is a powerful tool for probing water dissociation. In this section I will demonstrate

that SFG is also an appropriate tool for gaining insight into water induced surface reconstruction through probing surface phonons.

Other techniques for phonon spectroscopy have often been used but SFG allows to overcome some of their limitations. Therefore I will briefly explain some disadvantages of prior used techniques regarding our particular system. Typically, investigations of single crystals in presence of small amounts of water are performed by electron based techniques like EELS spectroscopy. Unfortunately, all electron based techniques are limited to usage in UHV because of electron adsorption in the gas-phase. Furthermore, even the usage in UHV for this system is found to be challenging. It has been shown that the electron impact on a hydroxylated surface cause electron induced desorption processes.[58] Investigation of oxide surfaces in presence of high water pressures in UHV and in the presence of liquid water can be straightforwardly performed using scanning probe microscopies (SPM) or x-ray scattering/diffraction based approaches[103, 156]. Unfortunately, both techniques are insensitive to hydrogen (or deuterium) at the surface, as discussed by us in detail in [174]. In contrast, Shen and coworkers[129] have recently demonstrated the application of SFG spectroscopy to probe interfacial phonon modes of silicon-oxide at the air/α- SiO_2(0001) and air/fused silica interfaces.[129] The application of this technique to our specific system allows surface sensitivity by inversion symmetry of α-Al_2O_3(0001) and is therefore an ideal approach for our purpose.

For characterization of hydroxylation processes by monitoring phonon modes, we started with a surface prepared in UHV. The preparation way is described in Section 2.5.2. As mentioned above, the thermodynamical favored coordination of α-Al_2O_3(0001) under UHV conditions is the (1x1) 1-Al-termination, which gets also supported by LEED (LEED picture of our sample is shown in Figure 2.11). Al-termination means, that the top layer of the surface contains of Al-atoms, which are slightly above the first layer of surface oxygen. Actually, there are existing several possible Al-termination, such as the 1-Al-termination and others. The difference between those depends on which different crystal layer of Al is on top. As an example, I show a side view of a crystal in following figure. As clear from Figure 7.16, there are different possibilities for surface terminations, but only the 1-Al in UHV and the 1-O in ambient were thermodynamical stable. The 1-Al-termination has been found to be the most stable surface in vacuum and all calculation for water dissociation and phonon modes have been performed on this surface. It is reasonable to assume that our UHV preparation of the α-Al_2O_3(0001) creates such a 1-Al-termination.

If now a (1x1) 1-Al-terminated surface gets in contact with bulk water, the top layer of Al-atoms gets dissolved and water dissociatively adsorbs[93] (Figure 7.17 a) and b))

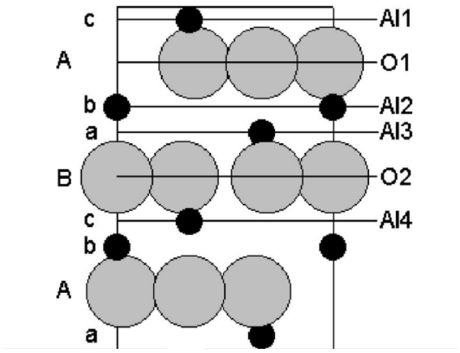

Figure 7.16: Graph shows a side view of an α-Al_2O_3(0001). The lines in the graph corresponds to different kinds of surface terminations. The Al-1 or 1-Al termination is the most stable in vacuum. Under ambient conditions, the O-1 or 1-O-termination has been found to be the thermodynamical stable phase. Figure taken from literature[166].

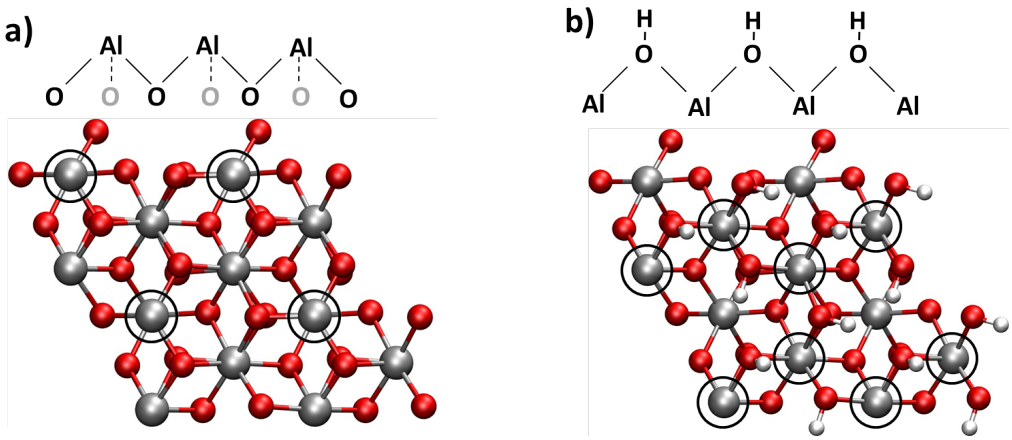

Figure 7.17: Shown are a schematic side view of the surface(top) and calculated structures for the different surface terminations. a) is thermodynamically most stable surface structure under UHV conditions, the (1x1) Al-termination, while b) is the fully hydroxylated surface that is most stable under ambient conditions. The uppermost layer of Al-atoms is marked by circles, but now below the surface oxygen atoms.

Figure 7.17 a) shows the Al-terminated surface structure with four Al-atoms as the top layer in a 2x2-cell (marked by circles). In case of contact with bulk water these atoms will dissolve and the subsurface oxygen layer becomes the top layer. As shown in Figure 7.17 b), subsequent dissociative adsorption of water leads to a fully hydroxylated surface. Nevertheless, it is quite obvious that if SFG spectroscopy of the surface phonon's of α-Al_2O_3(0001) works, the phonon spectra of the different cases in Figure 7.17 a) and b) should differ from each other, because the surface coordination of the atoms in the top-layer has changed. In one of our used setups the generation of IR light even in range of phonon modes is possible, so we tried to investigate the different cases by spectroscopy of the frequency range between 700-1000 cm^{-1}. These frequency range was defined, because in the frequency range between 700-1000 cm^{-1} Al-O-stretch modes in other systems have been reported[142, 89, 129, 174]. A detailed description of the methodology and the setup is also given in our paper [174]. Unfortunately there is no UHV system connected to this laser setup, therefore investigations of the Al-terminated samples were restricted to samples, which were prepared in UHV and afterwards transported into ambient for the performance of the measurement.

Additionally to the UHV prepared and Al-terminated crystal, fully hydroxylated samples were investigated. To prepare the fully hydroxylated surface we took the as received sample, cleaned it in a sonication bath with acetone for 15 min, ethanol for 15 min and Milli-Q water (18.3 MΩ·cm) for 45 min. The sample was then etched using a 15 mM solution of HNO_3 under sonication for 30 min. After thoroughly rinsing with Milli-Q water, the sample was dried by blowing with nitrogen gas. No C-H or C=O stretch peaks were observed in SFG for the cleaned surface (as described in [174]).

By preparation of such samples, we observed interesting features in the phonon spectral region. As expected, SFG generated on a fully hydrated and an Al-terminated surface differed drastically, as shown in Figure 7.18.

As you can see in Figure 7.18, the UHV prepared sample shows a sharp resonance at 980 cm^{-1} and a broad feature centered at 640 cm^{-1}. In contrast to this, the fully hydrated sample shows a broad resonance at 875 cm^{-1} with a dip 750 cm^{-1}. The different x-axis between the extracted resonances from the fitting program and the SFG data depends on a huge noise in the SFG data below 700 $^{-1}$. Nevertheless, it was possible to fit the data appropriate, as clear from the graph. For correct interpretation of the data, our coworkers from Potsdam performed a harmonic normal mode analysis of the different surface structures and predicted resonances at frequencies, shown in the lower panel of Figure 7.19

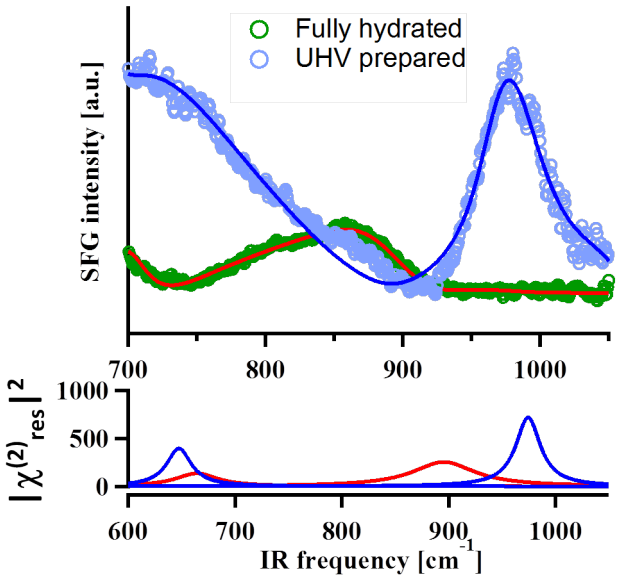

Figure 7.18: Phonon spectra of fully hydroxylated and UHV prepared, Al-terminated, α-Al_2O_3(0001). Phonon intensity is plotted over the frequency. Both spectra show dramatic differences in their spectral response. The extracted resonances from the fitting program in the lower panel have a different scaling for the x-axis than the SFG spectrum because of strong noise below 700 cm^{-1} in the SFG data.

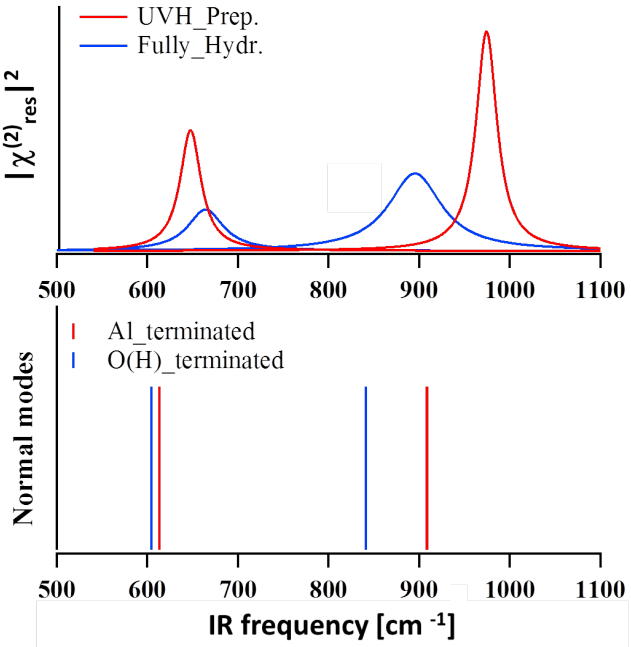

Figure 7.19: Comparison of measured phonon resonances (upper panel) to normal model calculation (lower panel). Theoretical predictions are in good agreement with measurements, despite the offset of $\approx$ 80 cm^{-1}.

As clear from comparison, the theoretical predicted resonances are in qualitative good agreement for the two different surfaces, despite an offset of $\approx 80\,cm^{-1}$. These observation helped us to understand our spectral observations. It seems that those observed modes are the characteristic surface phonon modes for both surfaces.

In addition to that, the observation of the characteristic modes of an Al-terminated surface under ambient conditions (we took the sample out of UHV and characterized it in ambient) opens some new questions regarding the timescales of hydroxylation. Prior investigators of α-Al_2O_3(0001) water interaction have argued that a short time exposure of water (below 1 mbar gas-pressure) to an Al-terminated surface induces a full hydroxylation of the surface within minutes[58, 89]. On the other hand we observed that the spectral response of the Al-termination seems to be stable on macroscopic timescales on our lab bench, where we expect to have a vapor pressure of H_2O of approximately 5 mbar. From this observation you can infer that the surface structure is stable, what is in contrast to prior reports.

To test our assumption of the higher stability we also investigated the OH-stretch region of both samples. If this by us observed stability is the case, we should see in the OH stretching region different SFG responses generated from the Al-terminated and the fully hydroxylated crystal. In the OH stretching region we should see the fr-OH of the hydrated surface.

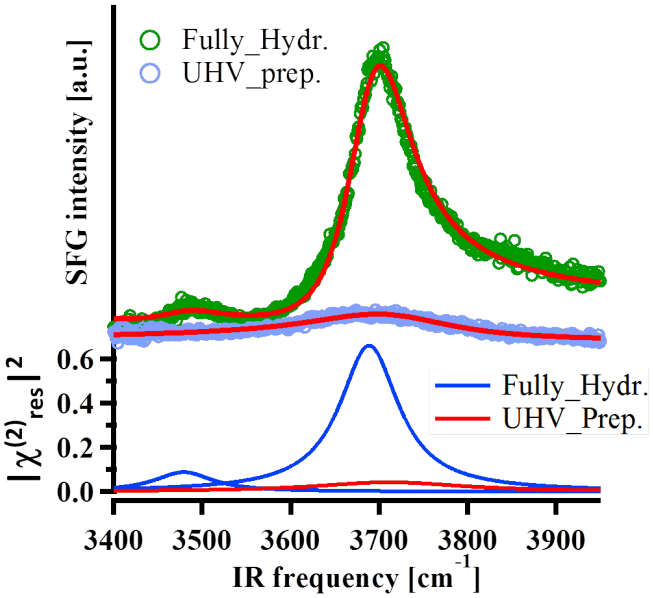

Figure 7.20: Direct comparison of the OH-stretching signal of the hydrated and the Al-terminated surface. As could be seen, dramatic differences could be observed in the intensity of the observed OH stretching signals. The generated signal of the UHV prepared surface is one order of magnitude lower.

Figure 7.20 underlined the conclusion, made before by investigation of the surface phonon region. The UHV prepared sample shows a resonant signal in the OH stretching region, which is about one order of magnitude lower in intensity, than that signal of the fully hydrated sample. Furthermore, we observed timescales for hydroxylation of the Al-terminated surface of 20 days. In contrast to that, Coustet et al. and others [89, 58] reported a full hydroxylation of the surface at short timescales (minutes) and lower water pressures(< 1 mbar). Evidently, the kinetics of water dissociation and surface reconstruction of our UHV prepared α-Al_2O_3(0001) surface are slow compared to prior reports.

There are several possible explanations for these different observations. One reason could be hydrocarbon contamination of our UHV prepared sample, which hindered water adsorption. To investigate this possibility we performed control experiments to check for the C-H, C=O and C=C modes. Actually, up to 24 hours on the lab bench no contaminations were detected.

Another possible explanation for the differences could be based on different defect concentrations. Defects on oxides have been found to drive various kinds of dissociations reaction, including water dissociation[70]. It is therefore acceptable to assume, that the presence of defects on this particular surface will enhance water dissociation. We prepared our Al-terminated surface in UHV by sputtering and annealing cycles, followed by characterization of the surface termination with LEED. Our procedure ended up with observable sharp LEED pattern, which argue for a comparable low defect concentration. On possible explanation for the differences between our and previous work is that the samples probed in prior work had a higher defect density. This would enhance the water dissociation and explain these obvious differences. Especially the fact that many investigators did not sputter their samples could be important at this point[58, 89, 143]. After mounting their sample into UHV they only annealed the sample to elevated temperature in an oxygen ambient (for the removal of carbon) or by oxygen plasma cycles, which could even induce more damages of crystal surface.

A last explanation is that the stoichiometric composition of the first layer could not reach the ideal 1-Al-termination without removal of surface oxygen atoms. If the starting condition of a sample is an OH-terminated surface, e.g. fully hydroxylated, some oxygen must leave the surface to reach the 1-Al-termination. We are inducing this removal by sputtering of the surface by Ar^+-ion. Whether this is possible just by annealing, is not clear. It has been reported, that surface oxygen can partially evaporate at temperatures above 1300 K [125], but at these temperature also a reordering of the lattice happens from a 1x1-structure to a $\sqrt{3}$ x $\sqrt{3}$-structure. Therefore, removal of oxygen just by annealing is problematic, if the aim of investigations is

the (1x1)-1-Al-terminated surface. Unfortunately, we can not make a final statement which explains the deviations between our observations and those of others. But the observations above clearly suggest a direction of further investigations. Up to this point, we have characterized only the two "extreme" surfaces with respect to their surface phonon modes: the Al-terminated (nearly dehydroxylated) and the fully hydroxylated. Since we are interested in understanding the chemical and morphological processes during the hydroxylation of a surface, the investigation of intermediate states in all spectral regions would be useful. Our first experimental approach for these kinds of investigations is by starting with the fully hydroxylated surface. We expect this surface to be covered by a combination of aluminol groups and molecularly adsorbed H_2O in ambient. Based on prior infrared studies of alumina powders [129], we expect that brief heating of such a surface should cause a decrease of the adsorbed OH-groups by desorption. Assuming these partially hydroxylated samples have no macroscopic domains, these intermediate surfaces presumably have a spectral response that is a linear combination of a Al-terminated and hydroxylated sample (the removal of OH-groups will create some sites, where the Al-atom should be on top). In minimum case the phonon spectra of a hydroxylated sample, where water have been partially removed, should show some different spectrum. To verify this assumption, we baked a fully hydroxylated sample in ambient for 24 h at $\approx$ 625 K and characterized it afterwards in the phonon spectral region(Figure 7.21)

As clear from inspection of Figure 7.21, heating of a hydroxlated surface causes a partial dehydroxylation of the surface and a reappearance of the characteristic peak for an Al-terminated surface. A quantitative analysis of the relative peak intensities suggest a composition of the surface being 40% Al-terminated and 60% hydroxylated. Interestingly, investigation of the OH-stretch intensities for the same sample (as done for the "extreme" situations in Figure 7.20) suggests a different surface composition by comparison to OH-intensity of full hydroxylated sample. This will be clear by inspection of Figure 7.22.

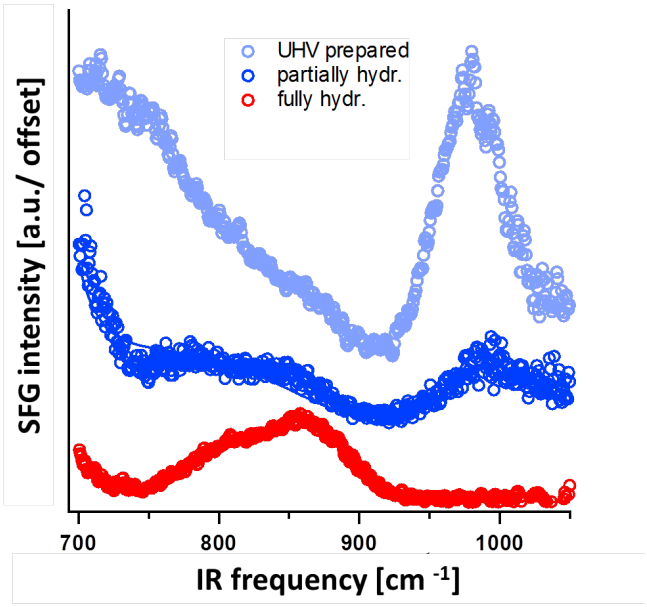

Figure 7.21: Comparison of phonon resonances for the dehydroxlated(upper curve), partial hydroxylated (middle curve) and the fully hydroxlated (lower curve). As expected, the gained spectrum for the partially dehydroxylated surface seems to be an intermediate state between both surfaces.

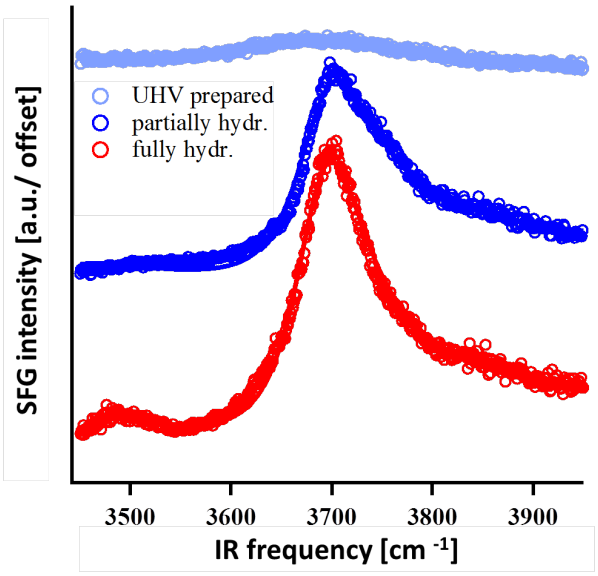

Figure 7.22: Comparison of OH- resonances for the dehydroxlated(upper curve), partial hydroxylated (middle curve) and the fully hydroxlated (lower curve). The spectrum of the partially dehydroxylated surface seems to be an intermediate state between both surfaces. But the intensity decrease in comparably low, compared to the increase of the corresponding mode in the phonon region.

The observed intensity decrease of the OH-stretch mode for the partially dehydroxylated in Figure 7.22 is much weaker than the increase of the characteristic Al-terminated mode in Figure 7.21. The comparison of the relative OH-mode intensities suggest a surface composition being 10% dehydroxylated and 90% hydroxylated.

This implies that the hydroxylation (or dehydroxylation) process (including the morphological changes) contains different steps, which are not fully understood. This needs more investigations from experimental, as well as from the theoretical side. Possibly there are more observable surface specific modes in the low frequency region, which are necessary for a full description of the surface structure. Also the question of surface stoichiometry can play a role. It is clear that starting from a hydroxylated surface and remove water creates a stoichiometrically different surface, than coming with the sputtered sample out of UHV (due to additional oxygen atom at the surface). This will be the topic of further investigations.

At this point we could summarize, that we were able to observe and identify some surface specific characteristic phonon modes of Al_2O_3(0001). This clearly opens new channels for investigation of the water/oxide interaction. These new channels can allow an up to now unknown level of insight into the interaction of water with oxides. This insight opens new levels of understanding the influence of hydroxylation on various important fields like heterogeneous catalysis or environmental chemistry.

7.9 Summary of water/α-Al_2O_3(0001) interaction

Within the last sections it has become clear that the interaction of water with oxide surfaces in general, and α-Al_2O_3(0001) in particular, induces dramatical changes of a variety of surface properties. These changes are of interest for many fields, e.g. catalysis, environmental chemistry or material science. The adsorption of water on α-Al_2O_3(0001) is a coupled process, where on one side water dissociates and and on the other this dissociation induces structural changes in the surface. These changes have been found to influence subsequent reactivity. In this chapter I have shown that investigation of water/oxide interaction from these different perspectives is possible by combination of sum frequency generation (SFG) spectroscopy and plane-wave based density functional theory. Theoretical work for this surface by our colleagues[21] and others[111] predicts for water adsorption on α-Al_2O_3(0001) two dissociation channels, which produces three different adsorption states. Calculation of normal mode frequencies for these adsorption states have found (under the assumption that all adsorbed water (D_2O)dissociates) OD fragments with five unique (two are indistinguishable) frequencies: the OD_{surf} and OD_{ads} fragments associated with the 1-2, 1-4 and 1-4$'$ dissociation channels. Since it has been proven challenging to dissociate water on

α-Al_2O_3(0001) in UHV, we applied our molecular beam source. By this approach we were able to dissociate water successfully as shown by TDS (and additionally by SFG). In the TDS response we observed two unreported desorption peaks in the high temperature region, which were assigned to two associative desorption channels. We demonstrated the presences of five stretching frequencies, which could be attributed to the stretching modes of the expected OD fragments. Comparison of our derived stretching frequencies with calculated ones by our coworkers from Potsdam clearly identified them (despite an constant offset of $\approx 100\,\mathrm{cm}^{-1}$ for the harmonic modes) as the expected modes of the different OD-groups.

Therefore, the application of our sample preparation technique in combination with our vibrational spectroscopic tool allowed for the first time the experimental verification of the heretofore theoretically suggested single molecular dissociation channels of water on the α-Al_2O_3(0001) surface [21]. We could say, that the recent work is an experimental benchmark of computational models for this relatively simple system, which is of general importance for the following more complex systems like α-Al_2O_3(0001) in ambient conditions, e.g. the fully hydroxylated surface.

Furthermore we demonstrated the capability of SFG for investigation of structural changes, happening at the surface with water adsorption. Comparison of our measured SFG-response from these samples in the frequency region of surface phonon modes ($600\,\mathrm{cm}^{-1}$ - $1000\,\mathrm{cm}^{-1}$), in addition with normal mode calculations from our collaborators from Potsdam, clearly illustrates the capability to probe surface structure and water adsorption. In these measurements we observed the surface phonon modes of Al-terminated (in UHV prepared) and fully hydroxylated crystals. Comparison of our results to the computational results for the normal mode analysis, clearly identified the characteristic phonon modes of the different surface structures. This gives an additional tool for understanding of kinetics and thermodynamics of water adsorption. Our first approach for investigation of intermediate hydroxylation levels of a surface has shown the reversibility of the characteristic phonon modes for Al-termination by ambient heating of a hydroxylated surface. Interestingly the quantitative analysis of the characteristic phonon modes and the OH-stretch spectral response are in disagreement to each other. This implies, that possibly additional observables (especially in the lower phonon region) are necessary for a detailed understanding of morphological changes. But because such modes exist, we now seem to have a tool that allows probing of structural intermediates.

One additional result from our measurements was, that even though dissociative water adsorption is thermodynamically favored, the kinetics of this process seems to be quite slow. This is in contrast to prior reports[58, 89, 143]. One possible explanation for this observation based on different sample preparations. Some investigators

proclaimed for their investigated α-Al_2O_3(0001) to see the (1x1) 1-Al-terminated surface already after transferring the hydroxylated sample into UHV, followed by high temperature annealing 1200 K, without oxygen annealing or sputtering [127]. This is hard to believe, as long as you are starting with a fully hydroxylated, e.g. an OH-terminated, surface. In this case dehydroxlation by H_2O desorption would end up in an oxygen terminated surface. Indeed, it has been reported by others that such a treatment of the sample results in an O-terminated surface will also show a (1x1)-structure [166]. As I mentioned before, oxygen desorption (from surface oxygen atoms) is possible at elevated temperatures (> 1300 K), but this would also cause lattice reconstruction. You would not get an (1x1) 1-Al-terminated surface[125]. Nevertheless, as long as the surface dehydroxylates without removal of surface oxygen, it will be an O-terminated surface and the LEED pattern should show a (1x1)-structure[166]. Possibly just the spot intensities will be different compared to those of an Al-terminated surface. On the other hand, sputtering of a sample without annealing in oxygen (as it has been done by others, who reported a high reactivity for water dissociation) could induce oxygen vacancies. These could act as highly reactive sites for the water dissociation, which is known for various oxides [70, 127, 95]. Of course, it is hard to define what is the best way to end up in a thermodynamical stable (1x1) 1-Al-termination, respectively if others did not had this Al-termination. But we must have in mind, that our prepared sample showed after sputtering followed by annealing in an oxygen background pressure of 1×10^{-6} mbar the characteristic (1x1) LEED pattern and our characterization of the water dissociation channels highly supported the picture of an1-Al-terminated picture. Otherwise the predicted dissociation channels by theory would not have fitted our experimental observations. Nevertheless, further investigation of the specific phonon modes for the different types of samples, in UHV as well as in ambient, should help to understand this question of surface termination better. Also it could answer the question of reactivity dependence for water dissociation on surface morphology.

Chapter 8

Water Interaction with α-Al_2O_3(1102)

After the detailed investigation of the water/α-Al_2O_3(0001) interaction within the last chapter, I will transfer the gained insight about the water dissociation from the (0001)-surface to a more environmentally abundant surface, the α-Al_2O_3(1102)[176]. The performed studies are somehow an outlook on the useful applications of knowledge and techniques, used and developed before, on more complicated but realistic system. Especially investigation of the chosen α-Al_2O_3(1102) is useful for understanding of the more complex environmental processes. While it is still a single crystal with all its advantages and disadvantages for handling, the exposed surface sites of the hydroxylated α-Al_2O_3(1102) crystal are a model for naturally abundant aluminum-hydroxide phases, such as gibbsite and the aluminol layer of clay minerals. For those, the exposed surface sites are postulated to have similar local structure and reactivity for water chemistry.

8.1 Surface structure and hydroxylation of α-Al_2O_3(1102)

During the end of the last chapter I already addressed the question, what kinds of surface terminations were apparent for the different prepared α-Al_2O_3(0001) samples (by us and others) and what is the relationship of termination and reactivity. Here I will continue with this topic, because one of the main differences between the α-Al_2O_3(0001) and α-Al_2O_3(1102) are their surface terminations. For α-Al_2O_3(0001) the Al-termination has been suggested by theory and experiment to be the most stable surface structure in UHV[21, 60]; a conclusion verified by comparison of our phonon measurements with computational derived phonon modes for this structure.[21, 89, 58,

111] Nevertheless, this preferred termination changes for α-Al_2O_3(1102). The crystal surface has been suggested to be oxygen terminated under all conditions (ambient as well as UHV) [176, 140]. This observation has been made by Crystal truncation rod diffraction, which is a X-ray diffraction method [176]. In literature[170] we find two schemes which shows the suggested surface morphology in case of ambient and UHV conditions.

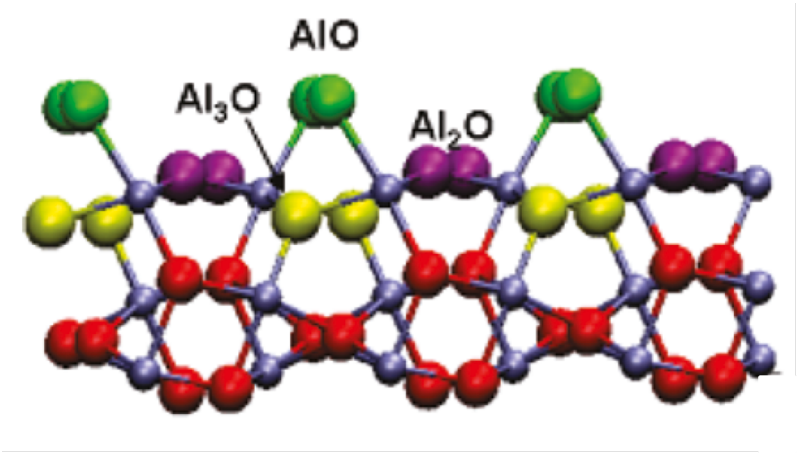

Figure 8.1: Schematically side view of the oxygen terminated α-Al_2O_3(1102) surface under ambient conditions. Different kinds of surface coordination of the oxygen groups are given by different colors. Single (AlO, Green), double (Al_2O, Purple) and triple (Al_3O, Yellow) coordinated oxygen. Figure taken from [170]

Figure 8.1 shows the different kinds of surface oxygen groups of the O-terminated crystal under ambient conditions, as it has been observed by experiments [176]. This termination has been also found by DFT calculation to be the most stable surface under ambient conditions[140]. Clearly, there are three different kinds of surface oxygen groups, namely 1-fold, 2-fold and 3-fold coordinated oxygen. These are shown in different colors in Figure 8.1. We have to mention that under ambient conditions protons should be also attached to the surface, which are not shown in Figure 8.1. That based mainly on the reason that X-ray diffraction techniques are insensitive to detection of protons.

Under UHV conditions, another kind of O-termination has been found by Trainor and coworkers [176] and by DFT calculations [140]. A scheme, describing this oxygen termination is given in literature [170] and shown below in Figure 8.2. As could be seen in this Figure for the case of UHV conditions, only two different kinds of top layer oxygen atoms are suggested: 1-fold and 3-fold coordinated oxygen atoms. Interestingly, for both cases the thermodynamical favorable surface layer is an oxygen termination. This makes the (1102)-surface interesting for investigation for several

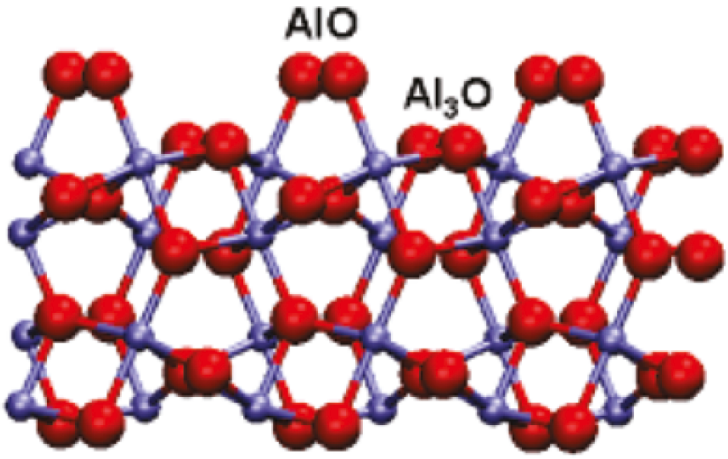

Figure 8.2: Schematically side view of the oxygen terminated α-Al_2O_3(1102) surface under UHV conditions. In case of this termination, just 1-fold and 3-fold coordinated oxygen is apparent. Figure taken from [170]

reasons. First of all, this oxygen termination gives the surface some similarity to the hydroxylated, oxygen terminated gibbsite structures of x-$Al(OH)_3$ under ambient conditions, which are naturally abundantly existing[176]. Therefore, understanding of its reactivity and chemical behavior possibly helps to understand in a simplified way some kinds of environmental chemistry.

Secondly, prior work on this surface reported a similar reactivity for water dissociation as for α-Al_2O_3(0001)[176]. This will be an interesting point for comparison to our prior results (see Chapter 7). There we found (as discussed in Section 7.9) the kinetics of hydroxylation of the α-Al_2O_3(0001) surprisingly slow on timescales of days. In contrast to that, literature [58, 89, 143] reported for α-Al_2O_3(0001) a high reactivity (hydroxylation within minutes) for water dissociation. I have already given in the last chapter a potential explanation of this obvious deviations: the possibility that prior investigators of the α-Al_2O_3(0001) prepared samples in a way, which created an oxygen terminated surface (for detailed discussion of this point see Section 7.9).

Investigation of the water/ α-Al_2O_3(1102) interaction will address both mentioned points and will be supported by additional phonon mode measurements. For the first investigation we chose the water/ α-Al_2O_3(1102) interaction under UHV conditions, because of its well defined preparation conditions. The investigation was performed by usage of same techniques, we used before for investigation of the (0001)-surface, e.g. TDS and SFG spectroscopy.

To test the ability to hydroxylate α-Al_2O_3(1102) under UHV conditions, we ap-

plied thermal desorption measurements. This proves the general ability of dissociative water adsorption at this crystal surface under UHV. Furthermore, it quantifies the amount of water at the surface. Comparison with the results from the (0001) surface should allow a first comparison of surface reactivity regarding water dissociation. For dosing we used D_2O seeded in Helium for our MBS (a detailed description of the sample preparation and dosing procedure is given in Section 7.3 of the last chapter and in the method section). The settings of the MBS were the same as for the (0001)-surface. Initially, we dosed for 5 minutes on the crystal at a certain surface temperature, then cooled it to 120 K to perform afterwards the TDS measurement. For different measurements we varied only the surface temperature while dosing. After each TDS measurement the sample was annealed to 1040 K to remove all D_2O[60]. By performing this cycle for several surface temperatures, we generated the data set as shown in Figure 8.3.

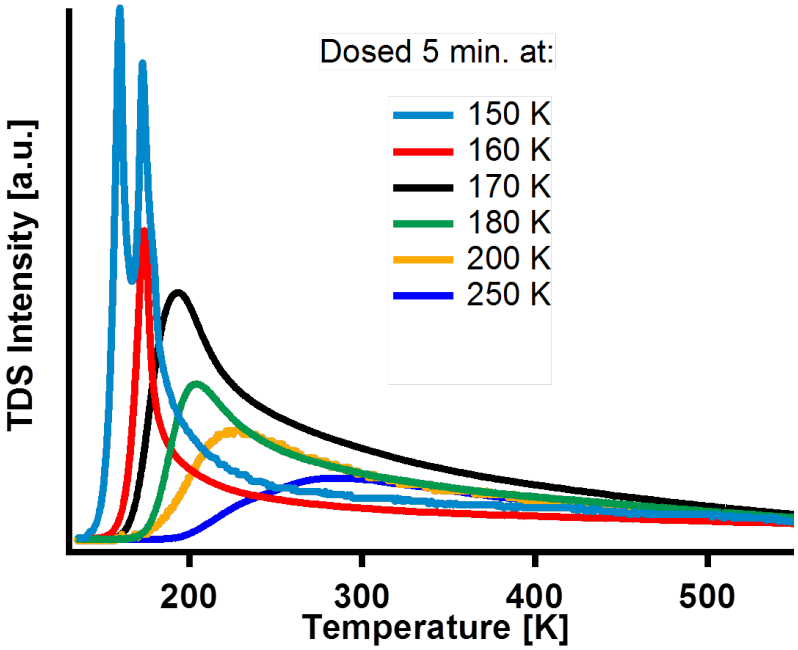

Figure 8.3: Series of TDS measurements at different surface temperatures. The spectrum shows the desorption signal of D_2O in order of the surface temperature.

This figure gives us several informations. As a starting point we will discuss the adsorption behavior at surface temperatures below 160 K. Dosing at surface temperatures below 160 K creates a desorption signal, which can be attributed to a mono and multilayer desorption of molecular water. The desorption maximum of the monolayer is centered at approximately 170 K and of the multilayer at 160 K. Furthermore we can see in the high temperature desorption region ($> 250\,K$) a

long desorption tail. This contributes to dissociated water. Nevertheless, in case of doing at < 160 K D_2O seems to adsorb mainly molecular. That follows from the observation of a relatively small desorption signal in the high temperature region (compared to the multi- and mono-layer desorption signal).

This changes for the case of surface temperatures more than 170 K while dosing. As we can see from the black curve in Figure 8.3, dosing at 170 K with the same nozzle settings (temperature, pressure) generates a desorption signal in the high temperature region, which is dramatically increased. Beyond 250 K, the desorption signal of the 170 K measurement has an intensity, which is twice of the intensity of the 150 K and 160 K data. It seems, that there is some kind of a transition in water adsorption (leading to a change in the desorption mechanism) between 160 K and 170 K. At the lower temperature D_2O adsorb molecularly, while above 170 K it seems to favor dissociative adsorption.

A similar observation for a transition between molecular and dissociative adsorption has been also made for the (0001) surface. But that happened at much higher surface temperatures while dosing and with much lesser intensity. As a reminder at this point: on the (0001) surface, adsorption at temperatures above 250 K lead to an enhanced dissociative adsorption. Additionally, much more dissociative water is adsorbed at the α-Al_2O_3(1102) surface, than on the (0001) surface. This allows the suggestion, that the barrier for water dissociation on α-Al_2O_3(1102) is smaller, due to the lower required temperature for enhanced dissociation (170 K on (1102) vs 250 K on (0001)).

By comparison of this thermal behavior one can conclude that the α-Al_2O_3(1102) surface is more reactive for water dissociation than the α-Al_2O_3(0001) surface.

8.2 Computational results for D_2O dissociation on α-Al_2O_3(1102)

For understanding of the TDS and SFG measurements, we once again cooperated with our coworkers from Potsdam. By usage of the same techniques for calculation as for the (0001)-surface, they modeled adsorption of D_2O on (1102). In contrast to the α-Al_2O_3(0001) surface, they predict only one type of OD_{surf} and OD_{ads} groups. Also the difference in energy between molecular and dissociative adsorption is quite small from their calculation. The energetics will be shown later. The similar adsorption states of molecular and dissociative adsorption becomes more clear by inspection of Figure 8.3 a) and b):

Figure 8.4 a) shows the dissociated and b) the molecular adsorption state. As

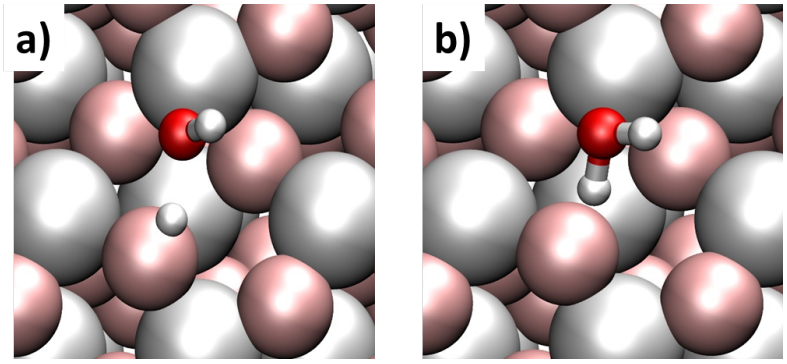

Figure 8.4: Theoretical predicted adsorption states of molecular and dissociated heavy water on α-Al_2O_3(1102). In this figure the silver balls correspond to surface Al-atoms, the red balls to surface O-atoms. Figures taken from Wirth et al. [188].

could be seen, the two states principally just differ in the distance between the oxygen and one deuterium atom of the water molecule. The orientation of the remaining OD-group (OD_{ads}) between both adsorption states changes only minimally. The small differences between both states are also reflected in the calculated energetics(see Figure 8.5):

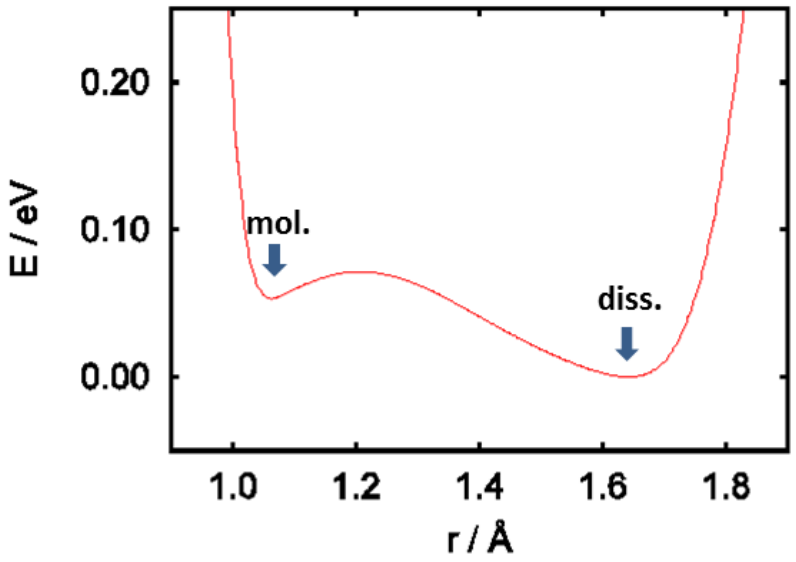

Figure 8.5: Energy diagram along the on OD bond length (of the bond, which dissociates) on α-Al_2O_3(1102). The state of dissociative adsorption is energetically slightly more favorable, than molecular adsorption. Figure from Wirth et al. [188].

The potential curve, plotted in Figure 8.5 reflects the standard change in internal energy of the molecule along the OD-axis parallel to the surface. The lowest energy in this curve is set to zero and corresponds to the most favorable adsorption condition,

which is in this case dissociative adsorption. The local minimum at an O-D length of approximately 1.1 Å correspond to the bond length of an OD-group of molecular water. However, this system has two distinct minima. The dissociated state is energetically slightly favored. The barrier for dissociation of molecular water is thereby quite small ($\approx$ 4 kJ/mol).

Complementary to the calculation of bonding geometry and energetics, our coworkers calculated via DFT additionally the characteristic vibrational frequency modes of the different kinds of molecules and OD-groups on the surface. These are listed in Table 8.1. One consequence of the calculation is, that we expect only two

$\tilde{\nu}_q$ **(cm^{-1})**	**Assignment**
2779	OD_{ads}
1958	OD_{surf}
2737	mol. D_2O-(free)
1651	mol. D_2O-(D-bond)

Table 8.1: Calculated harmonic frequencies of different OD-groups on α-Al_2O_3(1102). Values calculated by our coworkers from Potsdam. [188]

resonances in the stretching region between 2600-2800 cm^{-1}. To be clear at this point: OD_{ads} corresponds in this table to the remaining OD group from dissociated water, which is attached to an surface Al-atom. As in the discussion of the (0001)-surface, the OD_{surf}-group is formed by a deuteron, adsorbed on a surface oxygen atom. The stretching frequency of this group is approximately 800 cm^{-1} lower, than on the (0001) surface.

For the molecular water, theory had interesting result. Normally, as on the (0001)-surface, symmetric and asymmetric vibrational modes are expected, as well as a bending mode of the molecule. This is on the (1102)-surface not the case, because the OD-bonds in a water molecule are uncoupled on this surface. The reason for this contrast to the (0001)-surface could be found in the fact, that molecular water on the (0001)-surface does not donate a D-bond to the surface, which implies that both OD-bonds in the water molecule experience the same local environment and remain coupled. On the (1102)-surface water donates one D-bond to the surface and an one is free. Therefore the OD-bonds see a different local environments and remain uncoupled. The OD mode of molecular water, which is pointing out and not D-bonded, as could be seen in Figure 8.4, is the high frequency mode and called $mol.D_2O-(free)$, while the mode of the deuteron is called mol. D_2O-(D-bond). Even though four different modes were calculated, we only expect to observe the both high frequency modes at around 2700 cm^{-1}. The modes at 1700-1900 cm^{-1}

corresponds to OD-groups, which are nearly parallel to the surface. These modes will be SFG inactive. This behavior is already shown and discussed in chapter 7 in Figure 7.5. With this background knowledge we will start to investigate the D_2O/α-Al_2O_3(1102) interaction by vibrational sum frequency generation.

8.3 OD-stretching spectra of hydroxylated α-Al_2O_3(1102)

For initial SFG measurements we created an ice covered surface by dosing at a sample temperature of 150 K. By doing so, we can straightforwardly overlap the incoming beams spatially and temporally at the sample on the strong SFG signal of ice. The TDS measurements in Section 8.1 already showed, that there are drastic differences for water adsorption below and above 170 K surface temperature. Therefore we started with a sample, dosed at 150 K surface temperature and performed a series of measurement with different annealing temperatures. The aim of these measurements was to investigate the surface speciation at temperatures below 200 K, where possibly molecular water can be resolve. The SFG spectra an ice covered surface at 150 K is shown in Figure 8.6. The spectrum of ice on the (1102)-surface is qualitatively the

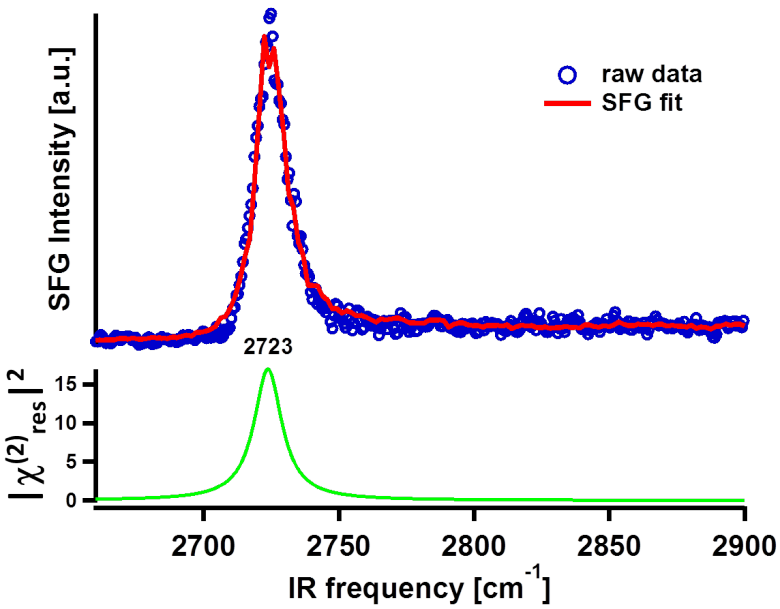

Figure 8.6: SFG spectra of ice on α-Al_2O_3(1102) crystal in UHV. The spectrum shows the expected resonance of ice at 2723 cm^{-1}, in perfect agreement with the results of the (0001)-surface and literature [39].

same as for the (0001)-surface. It shows a single peak, identical in shape and center

frequency at 2723 cm^{-1}, as known from the Al_2O_3(0001) surface. We can assume from the TDS data that annealing of the surface to 180 K should remove the ice layer and only parts of the monolayer remains. Characterizing such a surface, we get the spectra shown in Figure 8.7.

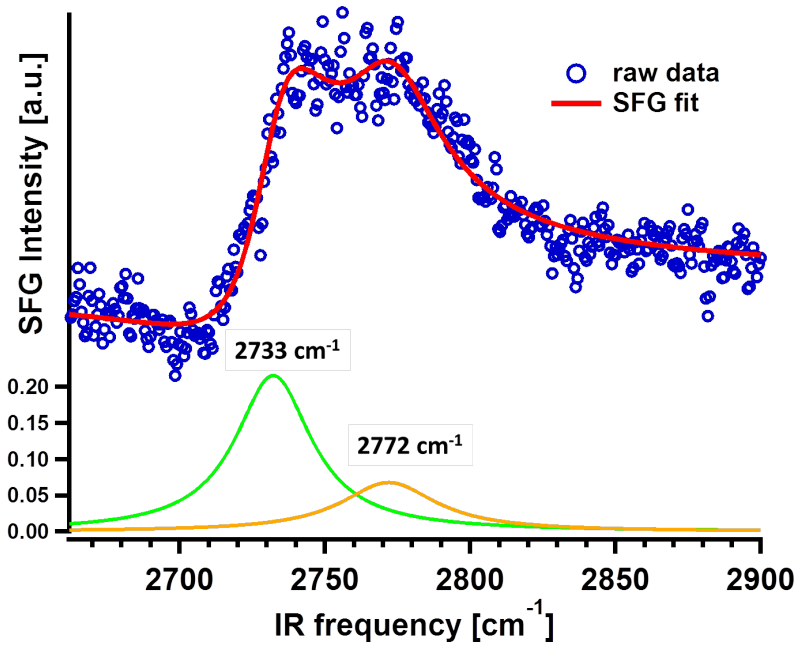

Figure 8.7: SFG spectra D_2O on α-Al_2O_3(1102) in UHV. The coverage of the characterized surface was below one monolayer of water. The spectral response splits into two resonance at 2733 cm^{-1} and 2772 cm^{-1}.

Annealing the surface to 180 K results in a spectrum, which shows two distinct resonances with center frequencies of at 2733 and 2772 cm^{-1}. Interestingly the center frequency of the low frequency mode is apparently different from that of ice. That is in agreement with TDS data, suggesting that at 180 K annealing temperature the surface is in a (sub)monolayer regime. The relative frequency shift between both modes suggests the observation of the $mol.D_2O - (free)$ mode of molecular water at 2733 cm^{-1} and the OD_{ads} mode of dissociated water at 2772 cm^{-1} (the computational values are 2737 and 2779 cm^{-1}, shown in Table 8.1). Comparison of the relative shift between both experimentally observed modes and the calculated shift emphasizes this conclusion. The shift is with $\Delta\nu_{Theo}$=42 cm^{-1} and $\Delta\nu_{Exp}$=39 cm^{-1} nearly identical.

A a prove of this assumption is, to increase the population of dissociated water on the surface by adoption of the five step dosing procedure from the α-Al_2O_3(0001) surface (dosing at 300 K before decreasing the surface temperature). After this way of preparation the crystal was annealed to 300 K surface temperature and cooled

again to 150 K for spectroscopic characterization. The TDS data suggested for such a case of preparation an enhanced amount of dissociated water, which should dominate the spectrum. The signal of molecular water should be much weaker or absent. The gained SFG spectra of such a surface is shown in Figure 8.8 :

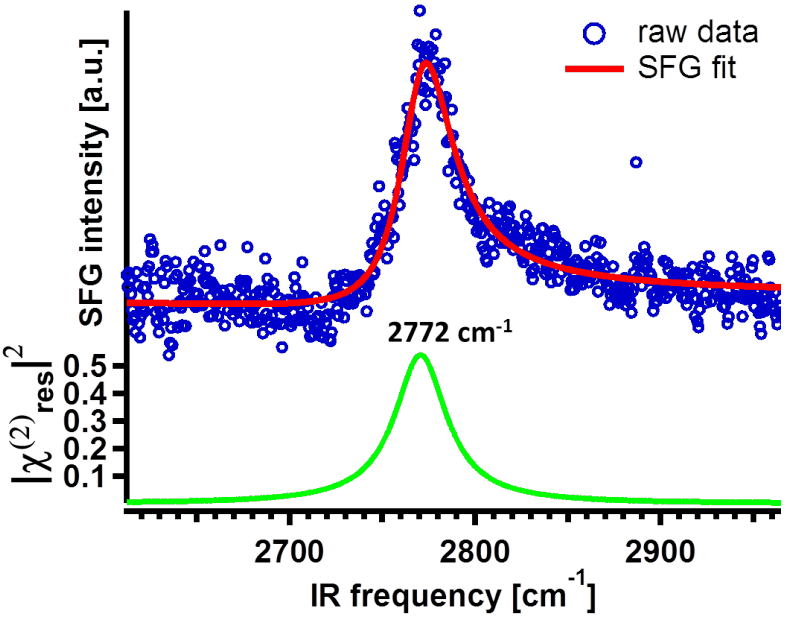

Figure 8.8: SFG spectra of a hydroxylated α-Al_2O_3(1102) crystal in UHV. The spectrum shows only one resonance at 2972 cm^{-1}. No other resonances could be observed. Scanning of the high and low frequency region did not bring up any other resonance.

These kind of sample preparation results in a surface, whose SFG spectrum is dominated by a single resonance in the OD-stretching region. This suggests that such a treatment of the sample produces samples with dissociated water as the dominant species. This observation could be seen as a verification that the peak in Figure 8.8 at 2772 cm^{-1} has its origin in dissociated water. This observation is in qualitative agreement with theoretical prediction. Because the dissociated state is energetically slightly favored, it should be more populated. Therefore it is expected to be dominant in the spectrum. A quantitative discussion of this experimental result with the theoretical prediction will follow later on.

The observation of the corresponding low frequency modes would have been a nice test for the this qualitative overlap between theory and experiment. But as I mentioned before the corresponding molecular excitation is parallel to the surface which prohibit detection by SFG for this system.

A last proof for the single resonance at 2772 cm^{-1} to have its origin in dissociated water was to test the thermal stability of this mode. For this purpose the

sample was flashed subsequently to elevated temperatures and cooled afterwards for characterization by SFG. Doing that we got following set of measurements:

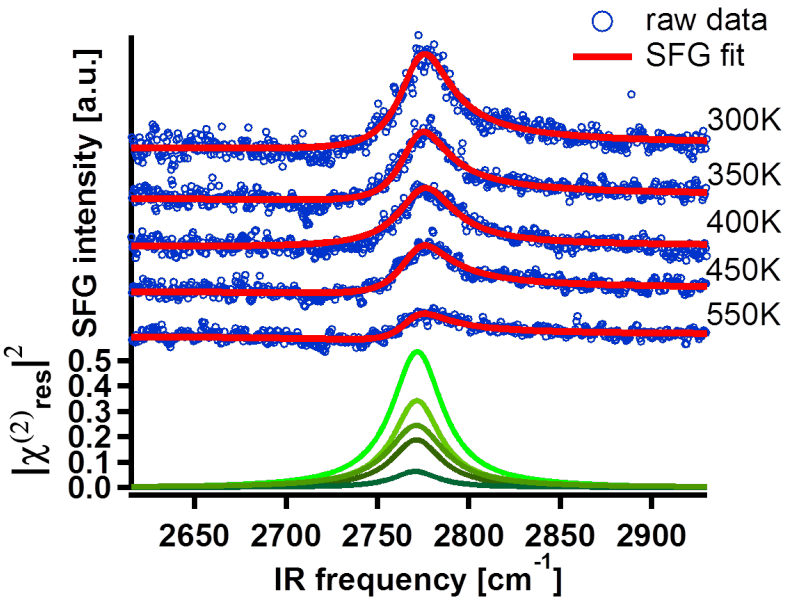

Figure 8.9: Series of SFG spectra of an hydroxylated α-Al_2O_3(1102) crystal in UHV at different flashing temperatures. The data got an offset to each other for a better overview. The resonance at 2770 cm^{-1} is observable up to temperatures of 550 K with decreasing intensity, which clearly supports the assumption of dissociated water being responsible for this peak.

As expected, the resonance intensity is a function of flashing temperature, as it was the case already on the (0001)-surface. Additionally, no shifting or splitting of the peak could be observed with increasing flashing temperature. This is in agreement with the theoretically prediction for the surface.

Nevertheless, we have to discuss the quantitative overlap between theory and experiment. From calculation it is known that dissociative adsorption is 8.2 kJ/mol more favorable than the molecular adsorption. Under the rough assumption, that the barrier between both states does not affect the relative population of the two states (because it is extreme small with 4 kJ/mol), one can calculate the concentration equilibrium constant and by this the expected relative population. For a system which is controlled by following reaction

$$[D_2O]_{mol} \leftrightarrow [D_2O]_{diss} \tag{8.1}$$

the concentration equilibrium constant K_c between both species is given as [32],

$$K_c = e^{\frac{-\Delta U_0}{RT}} \tag{8.2}$$

ΔU_0 is thereby the standard change in internal energy between the two states which is in our case the 8.2 kJ/mol. Equation 8.2 described the temperature depend

change of the equilibrium constant. K_c is also defined by the relative population of both states to each other. This results for the reaction of Equation 8.1 in following definition

$$K_c = \frac{[D_2O]_{diss}}{[D_2O]_{mol}} \tag{8.3}$$

With these formulas we are able, within a certain frame, to predict the relative populations of both states at different temperatures.

Of course this simplification requires several assumptions, which we have briefly to discuss at this point. First of all, we neglected the small barrier between both states. Furthermore K_c is formally defined as $K_c = e^{\frac{-\Delta G}{RT}}$ with ΔG as the Gibbs energy change. ΔG is defined as $\Delta G = \Delta H - T\Delta S$ with ΔS as standard entropy change. If we assume that the change in enthalpy ΔH dominates ΔS and we furthermore suggest, that the volume change while dissociation is small (since $\Delta H = \Delta U_0 + P\Delta V$), our assumption for K_c in Equation 8.2 is acceptable. For Equation 8.3 assumes that the process is a unimolecular reaction, otherwise the equation would look like

$$K_c = \frac{[OD][D]}{[D_2O]_{mol}} \tag{8.4}$$

what would slightly changes the relative populations especially at higher temperatures. The reason why we did not chose Equation 8.4, based on the system which was chosen by theory for calculation. In the theoretically description the proton (after dissociation) could not be seen independent of the remaining OD-groups, because it is still hydrogen bonded. This implies for their model that the proton is somehow fixed to its own OD-groups and can not recombine with a neighboring OD-group. Because of this reduced degree of freedom (which certainly must not reflect reality), we used Equation 8.3 for simulation of the population.

By using these set of equations theory would predict following relative populations at the different states: Clearly Table 8.2 shows, that molecular adsorption is in all

Temperature (K)	$\mathbf{K}_c$	$[D_2O]_{mol}$ (%)
100	22000	0.005%
200	147	0.7%
300	28	3.5%
400	12	7.5%
500	7	12%
600	5	16%

Table 8.2: Calculated population of molecular water at different temperatures on α-Al_2O_3(1102).

situations not favored. Especially at low temperatures the dissociative adsorption

should be dominant. Only at higher surface temperatures small amounts of molecular water should be present. In our experiments we observed an opposite behavior. What could be the reason for this observation?

One reason for this deviations could be, that theory describes a system of an isolated molecule in thermal equilibrium. The explanation for our observation could be in this case, that the rates for equilibration would be especially at low temperatures to slow. If we dose at 150 K molecular water and characterize the surface after removal of the ice, it could be that the system has not equilibrated yet. On the other hand one should assume that after a the sample treatment where molecular water was observed (flashing to 180 K), the system should be equilibrated. This explanation seems not plausible.

Another more plausible explanation is the neglected role of higher coverages. As I sad before, theory focused on isolated molecules. When we observed molecular water we are in the regime of a monolayer. That means, many molecules are coadsorbed nearby. It is reasonable to assume that higher coverages stabilizes molecular water. This has been also reported for the (0001)-surface [21]. with increasing flashing temperature the water coverage will decrease in our system by desorption. Then the stabilization effect and therefore the spectral feature of molecular water disappears.

A third explanation for our observation could be that theory underestimated the barrier(4 kJ/mol) for dissociation. Possibly, molecular water is at low surface temperatures kinetically stabilized, but with higher flashing temperatures it equilibrates into its more favored dissociated state.

Finally theory neglect the possible role of surface diffusion of the proton. If a proton diffuses away (especially at low coverages), this would favor once again the dissociated state.

Nevertheless, by inspection of Table 8.2 one could ask, why we see in our high temperature data (see. Figure 8.9) no contribution of molecular water in the SFG spectrum. This could be explained by the fact, that even in case of a 10 % population of molecular relative to dissociated water the spectral response would be smaller than the signal to noise ratio, because the SFG is proportional to n^2 of the molecules. Furthermore we should have in mind, that flashing to 500 K is always followed by cooling to 140 K. At this temperature we performed the SFG measurements. Even if small amounts of molecular water would be populated by heating, it would equilibrate while cooling of the sample and we should not see in the spectrum.

To summarize: In case of high flashing temperatures (and corresponding low coverages), our experimental observation is in agreement with theory. Only at low temperatures and high coverages, experiment and theory mismatches. This could be explained by coverage effects and/or kinetic stabilization of the molecular water.

Generally, we have shown once again the useful combination of theory and experiment for understanding of a complex adsorption system. By this approach we verified the theoretical predicted dissociation model of D_2O on α-Al_2O_3(1102). Comparison of the theoretically predicted and experimentally observed relative frequency shift between molecular and dissociated water clearly identified both states. Additionally it has been shown that α-Al_2O_3(1102) is more reactive for water dissociation than the (0001)-surface (which followed from TDS and SFG). This observation will be addressed in the final discussion of the chapter once again[170].

8.4 Surface phonon spectroscopy of α-Al_2O_3(1102)

At this point we will switch to the application of SFG on the detection of surface phonon modes in ambient conditions. This could help to understand, respectively identify the correct surface termination. As mentioned at the beginning of this chapter, the surface termination under ambient conditions is thought to be O-terminated, by containing three different kinds of oxygen atoms in the surface layer, which differs by their coordination (see Figure 8.1). If this coordination of the different oxygen atoms is correct (what is not totally clear and topic of ongoing investigations), we should be able to observe in minimum case three different kinds of surface phonon modes in the SFG spectrum. Analog to α-Al_2O_3(0001) within the last chapter we applied SFG as our spectroscopic tool for this purpose. By scanning the same frequency region as we did for the α-Al_2O_3(0001) crystal, we found following modes apparent in the spectrum:

Figure 8.10 clearly shows three different resonances in the surface phonon spectral region. This would fit very well with the prior suggested surface termination, as supposed by Sung and coworkers. [176, 170, 140] But its not clear what kind of modes we are really observing. On the one hand Al_x-O stretch modes are plausible. On the other hand also AL-O-H bending modes for different terminated oxygens are highly reasonable. The measurements were performed in ambient with a hydroxylated surface which implies the presence of OH-groups. On the (0001)-surface similar bending modes have been observed in ambient. Unfortunately, there are no computational derived values by normal mode analysis for this surface structure available to compare. This makes is hard to define, respectively to connect each observed resonance to a certain mode. One possibility to test their origin would be measurements with focus on the azimuthal dependence of the different resonances. These could be compared to measurements of the azimuthal dependence of OH-vibration modes in ambient. Especially for AL-O-H bending modes an overlap for the azimuthal dependence to corresponding OH-stretching modes should exist.

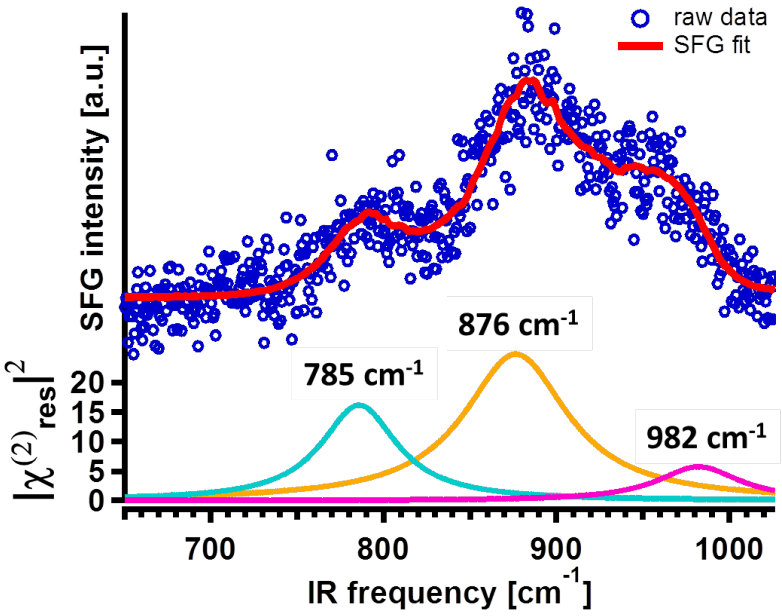

Figure 8.10: Phonon spectra of hydroxylated α-Al_2O_3(1102) under ambient conditions. The SFG intensity is plotted over vibrational frequency. Prior experimental and theoretical work by others suggested three different types of oxygen atoms at the surface [170, 140]

Furthermore, three observed modes are possibly not the final number of expected modes to describe this structure. There could especially in the low frequency region more resonances be apparent which we do not know. The reason for this could be found by bonds of Al-atoms to subsurface O-atoms, which should be also SFG active. Although the bulk Al_2O_3 has centrosymmetric structure which makes the Al-O stretch modes SFG inactive, however, due to the surface relaxation the bond length between Al and O atoms in the surface 3-5 layers can be quite different from that of the bulk. This breaks the centrosymmetry of the Al_2O_3 unit cell at the surface and gives rise several new SFG active mode in the lower frequency region (400-700 cm^{-1}). Unfortunately, we cannot access this frequency region with the current setup. A possible way to address the question of surface termination to corresponding Al_x-O mode will be given in the discussion.

Nevertheless, this measurements are once again a wonderful proof of principle for wide application of SFG spectroscopy on the interesting field of phonon spectroscopy. It opened new channels of understanding adsorbate/substrate interaction.

8.5 Discussion of spectroscopic results for α-Al_2O_3(1102)

This chapter has shown that by combination of experimental and computational results, a deeper understanding of the thermodynamics and kinetics of water adsorption on α-Al_2O_3(1102) can be obtained. Theory predicts for the interaction of water with this surface several results. First, dissociative adsorption of water is thermodynamically favored compared to molecular adsorption because of several reasons. On the one hand, the barrier of 4 kJ/mol for dissociation of an adsorbed D_2O molecule is relatively small. Furthermore, the dissociative adsorption is energetically more favorable, as clear from inspection of Figure 8.5. This suggests, that water should dissociate even at lower surface temperatures on this surface. This observation is different from those of the α-Al_2O_3(0001) surface, where enhanced dissociative adsorption of water occurs at elevated temperatures of more than 250 K. On the recent surface enhanced dissociative adsorption in the TDS data is observed at a surface temperature of 170 K. An interesting observation of these TDS measurements was, that at surface temperatures of T_{surf} <160 K the desorption of water in the high temperature region (> 200 K) was much lower than by dosing at T_{surf} > 170 K. That suggests preferred molecular adsorption at lower temperatures. It also suggests that the barrier for desorption is presumably lower than those for dissociation of water, otherwise the heating ramp for the TDS would induce dissociation (means in this case stabilization) instead of desorption.

Our vibrational spectroscopic results for these surface at different flashing temperatures verified this assumption, since we were able to clearly distinguish the vibrational stretching modes of molecular and dissociated water at flashing temperates of about 180 K. With a frequency of 2733 cm^{-1} the mode of molecular water is distinguishable from those of the ice covered surface (2723 cm^{-1}). The OD_{ads} mode of dissociated water has been found at 2772 cm^{-1}. Also the relative shift between the molecular and the dissociated water is in perfect agreement with theoretical prediction for both modes ($\Delta\nu_{Theo}$= 42 cm^{-1} $\approx$ $\Delta\nu_{Exp}$ 39 cm^{-1}). At temperatures above 300 K the molecular contribution in the spectra vanishes and just the stretching mode of dissociated water at 2772 cm^{-1} is left. As discussed in Section8.3, this could be explained by coverage dependent stabilization effects for molecular water at low temperatures (which disappears at higher flashing temperatures because of reduced coverage due to desorption), or by kinetic stabilization of molecular water at lower temperatures, which equilibrate to the energetically favored dissociative state at higher temperatures.

From a purely theoretical perspective, the observation of molecular water at

each temperature was unexpected, as shown by our calculation of the relative populations in Section 8.3. While the question of coverage effects on stabilization should be addressed by the theory, the idea of higher kinetic barrier for dissociation could eventually be addressed by experiments. Therefore we plan to investigate the temperature dependence of dissociative adsorption more quantitatively by SFG spectroscopy, because we are be able to distinguish the vibrational response of molecular D_2O from those of dissociated one. An experimental approach you could imagine for this would be to dose water at the surface for a fixed time (5 minutes) at different surface temperatures followed by cooling and SFG characterization. Therefore we would monitor spectral assignment of dissociated water at 2772 cm^{-1} after each dosing. After each SFG characterization, we would remove all water from the surface by annealing at 1040 K and dose again at a different surface temperature. In the temperature region between 160 k-190 K we should see a huge change of this peak intensity, depending on the surface temperature while dosing. Because it is possible to derive relative populations out of SFG data, one can apply an Arrhenius analysis on this population change in order of surface temperature. This treatment can give eventually insight into the kinetics for dissociation.

An additional approach of further investigation is the correct assignment of the observed phonon modes. For a more detailed understanding of the spectra, it is necessary to reduce complexity of the system or probing other characteristic modes. A possible experimental approach of doing this will be to transfer the phonon measurements from ambient into vacuum. If some of our observed modes have their origin in Al-O-H bending modes, they should disappear in UHV, since we are able to produce clean, dehydroxylated surfaces. Additionally, the termination of the α-Al_2O_3(1102) in UHV is still an O-termination but instead of having three different coordinated of O-atoms, as in ambient, you will have just two in UHV. While in ambient you have Al_1-O, Al_2-O and Al_3-O, you will have in UHV only Al_1-O and Al_3-O coordinated surface oxygen atoms. This means we will decrease the amount of possible modes in UHV, which will decrease the complexity of system. Together with measurements of the azimuthal dependency of the observed modes in ambient, a correct identification of their origin seems possible. In addition to these experimental phase space for investigation, further computational work is planned to understand the ongoing structural changes during water adsorption.

Nevertheless, this work, together with the work performed on the α-Al_2O_3(0001) could act as benchmark for computational models, which will help to understand and even predict more complex system, such as the role of hydroxylation of supporting materials in catalysis, as well as the function of surface termination on the reactivity of oxide surfaces for various reactions.

Chapter 9

Summary

The purpose of this study was to gain insight into complex reaction mechanisms, kinetics and thermodynamics of various chemical processes on three single crystal surfaces under ambient and UHV conditions.

Therefore, the systems of methane adsorption on Ru(0001) and water adsorption on α-Al_2O_3(0001) and α-Al_2O_3(1102) were investigated. Despite their obvious differences, it has been shown that all systems are controlled by similar physical and chemical processes and that they could be described and investigated by equal methods and techniques.

In the CH_4/Ru(0001) work methane was dissociated in UHV on a single crystal using a molecular beam source(MBS) and the produced methane fragments and higher hydrocarbons were investigated as a function of different parameters. These were the gas mixture for dosing, the kinetic energy of impinging CH_4-molecules, the adsorbate coverage and the surface temperature of the ruthenium. The produced samples were characterized by Thermal Desorption Spectroscopy and by vibrational Sum Frequency Generation (SFG). Using these methods it was possible to identify various adsorbed CH containing groups on the surface, including CH, CH_2, CCH, CCH_2 and CCH_3. Therefore CH_2, CCH and CCH_3 have been observed for the first time by methane decomposition. The identification of these species has been done by monitoring the thermal stability and the characteristic vibrational symmetric CH-stretch frequencies.

Investigating thermal stability of CH_2 by an Arrhenius plot method allowed the experimental determination of the $CH_2 \rightarrow CH$ dissociation barrier: 65 kJ/mol. This value is the first experimental determination of this barrier and is in dramatic disagreement with the prior computational results of 16 kJ/mol [18]. Cooperation with theory enabled us to show that this deviation is the result of co-adsorbed hydrogen coverage. After including of a sufficiently high hydrogen coverage into the

calculation (as was present in the experiment), theoretical and experimental values were in quantitative agreement. This opens new channels of understanding and interpretation of the reaction mechanisms during Fischer-Tropsch (FT) synthesis. Additionally, the effect of defects on CH_2 stabilization have been observed and discussed within the frame of this study. The results have been related to the general understanding of the FT mechanism as well.

In addition to the FT process, higher hydrocarbon formation via low temperature methane coupling were investigated by spectroscopy of the temperature dependent surface speciation. Simulation of the relative C_xH_y-group populations were done by modeling the reaction pathway with chemical rate equations. A rate equation model with the following reactions as the elementary reaction steps was assumed:

$$CH + CH \underset{k_B}{\overset{k_{CH}}{\longleftrightarrow}} CCH_2 \xrightarrow{k_{Diss}} CCH + H \tag{9.1}$$

With application of this pathway it was possible to qualitatively reproduce the formation and depletion of the different hydrocarbon groups in order of the thermal treatment of the sample. Therefore, this model allowed to gain insight into the up to now experimentally undiscovered energetics of these processes. For this investigation the application of a High-Resolution spectroscopy method has been found to be extreme important, because the stretching frequencies of different C_xH_x groups varied only for 10'th of wavenumbers.

Observed coverage dependent shifts in stretching frequencies even increases the problem of a correct molecular identification. The stretching frequencies of various hydrocarbon groups have been observed to be effected by surface coverage of the sample, inducing a blue shift of the resonances with increasing coverage. To explain this dependence a dipole coupling model was applied and demonstrated for the CH molecule that lateral interaction between coadsorbed CH molecules could explain qualitatively the observed frequency shift. This observation demonstrates the importance of including lateral interactions into the interpretation of vibrational spectra for hydrocarbons, because the observed shifts were of the order of relative frequency shifts between different CH-containing molecules.

The second part of this thesis focused on water/oxide interaction by studying the D_2O/α-Al_2O_3 interface in vacuum and ambient. This interaction is dominated by dissociation of the water, what induces hydroxylation (means adsorption of OD-groups) of the α-Al_2O_3. The understanding of this hydroxylation of processes is of high interest, since the dissociative adsorption of water changes the surface morphology of oxides drastically and clearly infect changes in reactivity. The morphological influence of water adsorption, regardless whether it is molecular or

dissociatively adsorbed, is important to understand because oxides and water are ubiquitous in the environment and in technology. Unfortunately, getting insight into these interaction has been found be extremely challenging to attain.

For investigation of this system the MBS for purpose of sample preparation was applied, which allowed the direct dissociation of D_2O on (1x1) Al-terminated α-Al_2O_3(0001) in UHV. By combining plane-wave based density functional theory (by our coworkers from the University of Potsdam) and vibrational SFG, the observation and identification of the theoretically predicted single molecular water dissociation channel products were shown experimentally for the first time. In addition to the two distinct dissociation channel products these measurements also proved the existence of one additional diffusion controlled adsorption state. These three states should create six distinct resonant frequencies where five of them should be resolvable by our setup. These five resonances have been clearly identified.

To explore also the water/oxide-relationship from the oxides point of view probing of surface phonon modes of α-Al_2O_3(0001) via SFG have been been performed. The experimentally observed resonances have been again compared with normal mode calculations performed by our coworkers. Doing this clearly identified the characteristic phonon modes of an UHV prepared Al-terminated sample and a fully hydroxylated sample. Interestingly, the kinetics of hydroxylation of the Al-terminated surface under ambient conditions was surprisingly slow, which is in contradiction to prior results . This could be potentially explained by different surface termination of the samples used by us and prior investigators.

To address the role of surface termination on hydroxylation more in detail the interaction of heavy water with another alumina surface, namely α-Al_2O_3(1102), was explored. This surface is reported to have a more complicated surface structure, but prior work of others in ambient suggested the exposed surface sites of α-Al_2O_3(1102) to have similar local structure and reactivity as gibbsite. This makes this system a good model system for the understanding of environmental chemistry processes. A reason for this could found in its surface termination, which is under each condition (ambient and UHV) an O-termination. This is different to α-Al_2O_3(0001) surface (Al-termination for (0001) vs. O-termination for(1102) in UHV).

The α-Al_2O_3(1102) system was studied using the same techniques which have been found already useful for understanding of the D_2O/α-Al_2O_3(0001) system. Furthermore, the observations have been again compared with plane-wave based density functional theory calculations of our coworkers. By performing these measurements and calculations the α-Al_2O_3(1102) surface was found to be more reactive for water dissociation under equal conditions than the (0001)-surface. The dissociation process is, in contrast to the (0001)-surface, the result of only one dissociation channel which

leads to a single adsorption state.

The prior results suggested that surface the termination of $Al_2O_3(0001)$ plays an important role for water reactivity. Understanding these role of surface termination on reactivity is still part of ongoing research. The spectroscopic observation of surface phonon modes for this crystal in ambient (as already done) and in UHV as well as their correct interpretation will help to understand the limiting steps in surface reconstruction. Because of the experimental observation and therefore confirmation of the different dissociations channels and adsorption states for the first time, our work could be seen as benchmark for computational models, which are describes water reactivity on structures. Such benchmarking is necessary for the transfer of computational models for well constrained surfaces to more naturally abundant and complicated structures like gibbsite surfaces in ambient.

Summarizing, this thermal desorption and vibrational spectroscopy study provided detailed insight into the reaction mechanism of methane decomposition and higher hydrocarbon formation on Ru(0001) as well as water adsorption and dissociation on alumina surfaces in ambient and UHV. A useful extension of this work regarding our methane studies would be to transfer our knowledge about the limiting factors of reaction kinetics to investigations of more realistic reaction conditions. These could be in-situ characterization of surface populations while reaction of $(CO+H_2)$/Ru(0001) in a high pressure cell. This measurements possibly answer the controversial discussion about the role of CH_2 as the chain building reaction while FT-synthesis.

For the work of D_2O on both alumina surfaces one can say, that static investigations of the OD-stretching region in UHV reaches the limit of getting more insight with further work. The step would be higher water pressures as well as the spectroscopy of all observable phonon modes which determine the water/alumina interaction while this interaction. Also the application of time-resolved vibrational spectroscopy would be helpful for the investigation of the different molecular states. In combination, this would enable the next level of understanding the complex process of hydroxylation and surface reconstruction. Furthermore, the understanding of the mechanisms in this model system will be an important step in understanding heterogeneous chemistry on oxides in general.

Chapter 10

Appendix

10.1 Reaction order and temperature dependence of Arrhenius analysis

The aim of this discussion is to show that the choice of the reaction order in our adsorbate system is a valuable assumption. We want to emphasize that the choice of reaction order on the Arrhenius analysis does not change the kinetics of the dissociation process in way, which could influence the general result of our observation. As you can see in Figure 10.1, Arrhenius analysis of the data under assumption of a zero order reaction changes the activation energy of the dissociation process by about 6 kJ/mol. The general statement that the gained result is still 4 times higher than the calculated value by theory [18, 65], is still correct.

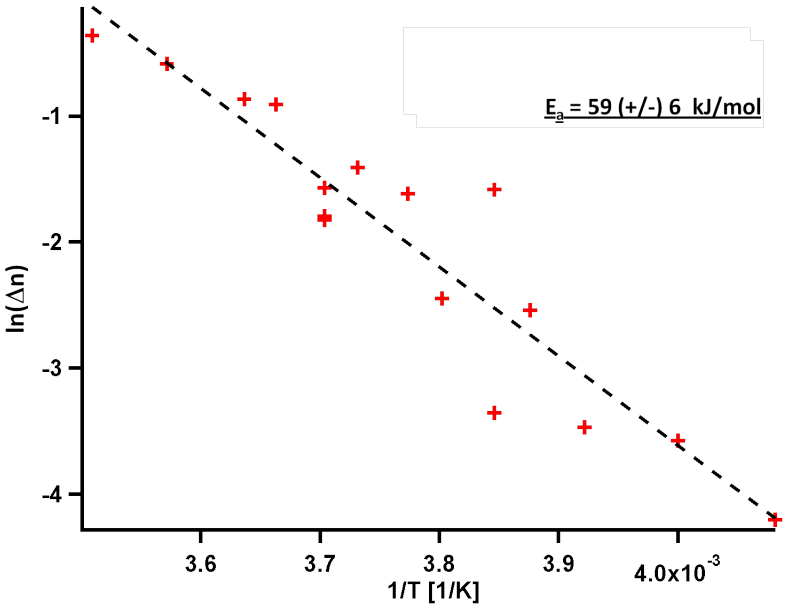

Figure 10.1: Arrhenius analysis of $CH_2 \rightarrow$ CH dissociation process assuming a zero reaction order

Nevertheless, it is important to mention that the choice of a first order reaction for dissociation is scientifically more reliable. As shown in [32], reactions of zero's order could only be reactions of A→B type, where the reaction speed is independent of the concentration of reactant A. That is clearly not the case in our system. Furthermore we have a A→B+C reaction type in our system, which should be described by [32]as a first order reaction.

Another assumption which were made for the analysis of our data was the presumption of a temperature independent pre-exponential factor in the Arrhenius equation. This temperature independence is actually only a approximation for a easier handling of the data. In a real system, the pre-exponential factor has a temperature dependence, which could be normally formulated as follows[32]:

$$A = u\ \sqrt{T} \tag{10.1}$$

A is thereby the pre-exponential factor, u a temperature independent factor. As quite clear from inspection, the change of the factor for the investigated temperature region of 245K-290K is only a few percent and could induce only marginal changes in our calculated value for the dissociation barrier. The assumption of a temperature independent factor is therefore an acceptable approximation.

10.2 Computational Methods for calculation of D_2O dissociation

As mentioned in the thesis, there will be a brief introduction of the methods for calculations, done by our cooperation group from Potsdam. The following part has been taken from our published paper [22]. Periodic first-principles total energy calculations were performed within the framework of Kohn-Sham density functional theory (DFT) [120] applying the projector augmented wave (PAW) method [71, 124] as implemented in the Vienna ab initio simulation package (VASP) [122, 123, 121]. Electron exchange and correlation was treated according to the generalized gradient approximation (GGA) using the PBE functional [147, 146]. Total energies were corrected for dispersion interaction by using Grimme's semiempirical D2 scheme [101].

Total energies and vibrational frequencies were evaluated using a plane-wave basis set truncated at a kinetic energy cutoff of 400 eV and a Γ-point centered ($3 \times 3 \times 1$) Monkhorst-Pack grid [141] (resulting in a set of 5 irreducible k-points) for sampling the Brillouin zone of the hexagonal supercell. Self-consistent field convergence was considered to have occurred for a total energy difference of less than 10^{-4} eV between iterations; ionic relaxation was stopped when the forces acting on ions dropped below 0.01 eV/Å.

The bulk structure of α-alumina can be described by a hexagonal unit cell with alternating layers of aluminum and oxygen atoms stacked along the [0001] direction, as shown in Fig. 10.2(a). The lattice constants were optimized as $a = b = 4.83$ Å and $c = 13.09$ Å, exceeding experimental values [172] by a GGA-typical amount of $\approx 1\%$. The Al-terminated (0001) surface was modelled by a slab consisting of nine atomic layers (see Fig. 10.2(a)), following a similar approach as in ref. [21]. To improve convergence of observables with the size of the vacuum gap between neighbouring slabs, a dipole/quadrupole correction to the total energy was calculated applying the built-in VASP routine. A vacuum gap of approximately 26 Å was found to ensure convergence of total energies within 20 meV; pairwise dispersion interactions were limited to distances smaller than 20 Å to avoid interference between adjacent slabs. During ionic relaxations as well as for normal mode analyses the lowermost four atomic layers, *i*.e., three aluminum layers and the intermediate oxygen layer, were kept fixed at their bulk positions. To account for a low-coverage situation of 1/4 with respect to the surface Al adsorption sites, a (2×2) supercell of the Al-terminated α-Al_2O_3(0001) surface featuring a single adsorbed D_2O molecule was used in this study (see Fig. 10.2(b)).

Molecular vibrations were calculated by normal mode analysis, *i*.e. by diago-

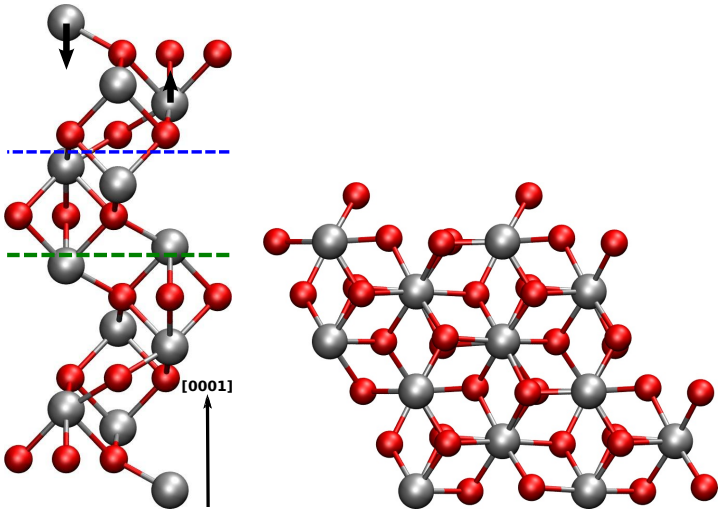

(a) (b)

Figure 10.2: α-Al_2O_3 bulk and surface structures used in this work (red = oxygen, grey = aluminum). (a) Bulk unit cell. Layers above the green dashed line were included in the surface model, layers between both dashed lines were kept fixed at the bulk positions during geometry optimizations and normal mode analyses. The bold black arrows indicate the major ion movements during surface relaxation. (b) Surface structure. The (2×2) surface supercell (top view) used in this study, featuring four surface Al sites for D_2O adsorption.

nalization of the dynamical (Hessian) matrix; energy derivatives with respect to the nuclear coordinates were evaluated numerically using centered finite differences. We corrected these frequencies for anharmonicity using a previously described anharmonic correction scheme that assumes each mode is an uncoupled anharmonic oscillator (see Supporting Information for additional detail).

Bibliography

[1] A. Mittasch *Dpr*, vol. 254, p. 437, 1910.

[2] G. Ertl, "Primary steps in catalytic synthesis of ammonia," *Journal of Vacuum Science & Technology A: Vacuum, Surfaces, and Films*, vol. 1, no. 2, pp. 1247–1253, 1983.

[3] J. H. Lunsford, "The catalytic oxidative coupling of methane," *Angewandte Chemie International Edition in English*, vol. 34, no. 9, pp. 970–980, 1995.

[4] H. Dietrich, P. Geng, K. Jacobi, and G. Ertl, "Sticking Coefficient for Dissociative Adsorption of N_2 on Ru Single-Crystal Surfaces," *Journal of Chemical Physics*, vol. 104, pp. 375 – 381, 1996.

[5] D. M. Smyth, "The defect chemistry of metal oxides," *The Defect Chemistry of Metal Oxides, by DM Smyth, pp. 304. Foreword by DM Smyth. Oxford University Press, Jun 2000. ISBN-10: 0195110145. ISBN-13: 9780195110142*, vol. 1, 2000.

[6] J. A. Anderson, *Supported metals in catalysis*. World Scientific, 2011.

[7] C. Bolm, J. Legros, J. Le Paih, and L. Zani, "Iron-catalyzed reactions in organic synthesis," *Chemical reviews*, vol. 104, no. 12, pp. 6217–6254, 2004.

[8] D. W. G. M.-C. Wu, "High-Resolution Electron Energy-Loss Measurements of Sticking Coefficients of Methane Decomposition on Ru(0001)," *Surface Science Letters*, vol. 306, pp. 529–533, 1994.

[9] M.-C. Wu and D. W. Goodman, "High-Resolution Electron Energy-Loss Studies of Hydrocarbon Formation from Methane Decomposition on Ru(0001) and Ru(1120) Catalysts," *Journal of the American Chemical Society*, vol. 116, pp. 1364–1371, 1994.

[10] M.-C. W. P. Lenz-Solomun and D. W. Goodman, "Methane Coupling at Low Temperatures on Ru(0001) and Ru(1120) Catalysts," *Catalysis Letters*, vol. 25, pp. 75–86, 1994.

[11] D. W. G. M.-C. Wu, P. Lenz-Solomun, "Two-Step, Oxygen-Free Route to Higher Hydrocarbons from Methane Over Ruthenium Catalysts," *Journal of Vacuum Science and Technology A*, vol. 12, pp. 2205–2209, 1994.

[12] R. C. Egeberg, S. Ullmann, I. Alstrup, C. B. Mullins, and I. Chorkendorff, "Dissociation of CH_4 on Ni(111) and Ru(0001)," *Surface Science*, vol. 497, p. 183Â–193, 2002.

[13] D. W. G. M.-C. Wu and G. W. Zajac, "The Characterization of Carbonaceous Species from CO Hydrogenation on Single Crystal Ru(0001) andRu(1120) Catalysts with High-Resolution Electron Energy-Loss Spectroscopy," *Catalysis Letters*, vol. 24, pp. 23–30, 1994.

[14] I. Ciobîcă, G. J. Kramer, Q. Ge, M. Neurock, and R. Van Santen, "Mechanisms for Chain Growth in Fischer–Tropsch Synthesis over Ru (0001)," *Journal of Catalysis*, vol. 212, no. 2, pp. 136–144, 2002.

[15] S. G. Shetty, I. M. Ciobîcă, E. J. Hensen, and R. A. van Santen, "Site regeneration in the Fischer–Tropsch synthesis reaction: a synchronized CO dissociation and C–C coupling pathway," *Chemical Communications*, vol. 47, no. 35, pp. 9822–9824, 2011.

[16] E. v. S. R. A. van Santen, I. M. Ciobîcă and M. M. Ghouri, "Mechanistic Issues in Fischer-Tropsch Catalysis," *Advances in Catalysis*, vol. 54, pp. 127–187, 2011.

[17] R. C. Brady and R. Pettit, "Mechanism of the Fischer-Tropsch reaction: The chain propagation step," *J. Am. Chem. Soc., 103:1287-1289,1981*, vol. 103, pp. 1287–1289, 1981.

[18] I. M. Ciobîcă, F. Frechard, R. A. van Santen, A. W. Kleyn, and J. Hafner, "A DFT Study of Transition States for C-H Activation on the Ru(0001) Surface," *Journal of Physical Chemistry B*, vol. 104, pp. 3364 – 3369, 2000.

[19] V. P. Mm Neurock and R. A. van Santen, "The Importance of Transient States at Higher Coverages in Catalytic Reactions," *J. Am. Chem. Soc.*, vol. 122, 2000.

[20] M. Bäumer, J. Libuda, K. M. Neyman, N. Rösch, G. Rupprechter, and H.-J. Freund, "Adsorption and reaction of methanol on supported palladium catalysts: microscopic-level studies from ultrahigh vacuum to ambient pressure conditions," *Physical Chemistry Chemical Physics*, vol. 9, no. 27, pp. 3541–3558, 2007.

[21] J. Wirth and P. Saalfrank, "The Chemistry of Water on α-Alumina: Kinetics and Nuclear Quantum Effects from First Principles," *J. Phys. Chem. C*, vol. 116, no. 51, pp. 26829–26840, 2012.

[22] H. Kirsch, J. Wirth, Y. Tong, M. Wolf, P. Saalfrank, and R. K. Campen, "Experimental Characterization of Unimolecular Water Dissociative Adsorption on α-Alumina," *The Journal of Physical Chemistry C*, vol. 118 (25), p. 13623–13630, 2014.

[23] M. Sterrer and H.-J. Freund, "Towards Realistic Surface Science Models of Heterogeneous Catalysts: Influence of Support Hydroxylation and Catalyst Preparation Method," *Catal. Lett.*, vol. 143, pp. 375–385, 2013.

[24] O. Dietrich, M. Heun, J. Notroff, K. Schmidt, M. Zarnkow, and M. Carver, "The role of cult and feasting in the emergence of Neolithic communities. New evidence from Göbekli Tepe, south-eastern Turkey.," *Antiquity*, vol. 86, no. 333, 2012.

[25] W. Ostwald, "Referat zur Arbeit F. Strohmann : Ueber den Waermegehalt der Bestandteile der Nahrungsmittel," *Z. phys. Chem.*, vol. 15, p. 705, 1896.

[26] F. Schüth, "Heterogene Katalyse. Schlüsseltechnologie der chemischen Industrie," *Chemie in unserer Zeit*, vol. 40, no. 2, pp. 92–103, 2006.

[27] P.-Y. Lin, M. Skoglundh, L. Löwendahl, J.-E. Otterstedt, L. Dahl, K. Jansson, and M. Nygren, "Catalytic purification of car exhaust over cobalt-and copper-based metal oxides promoted with platinum and rhodium," *Applied Catalysis B: Environmental*, vol. 6, no. 3, pp. 237–254, 1995.

[28] M. P. Elsner, M. Menge, C. Müller, and D. W. Agar, "The Claus process: teaching an old dog new tricks," *Catalysis Today*, vol. 79, pp. 487–494, 2003.

[29] V. Smil, "Global population and the nitrogen cycle," *Scientific American*, vol. 277, no. 1, pp. 76–81, 1997.

[30] M. Henzler and W. Goepel, *Oberflaechenphysik des Festkoerpers*. Teubner Studienbuecher, 1994.

[31] A. de JONG and J. NIEMANTSVERDRIET, "THERMAL DESORPTION ANALYSIS: COMPARATIVE TEST OF TEN COMMONLY APPLIED PROCEDURES," *Surface Science*, vol. 233, 1990.

[32] K. J. Laidler, *Chemical Kinetics*. Harper and Row, 1994.

[33] T. Zambelli, J. Trost, J. Wintterlin, and G. Ertl, "Diffusion and atomic hopping of N atoms on Ru (0001) studied by scanning tunneling microscopy," *Physical review letters*, vol. 76, no. 5, p. 795, 1996.

[34] Kolasinski, *Surface Science*. John Wiley and Son Ltd, 2007.

[35] R. Boyd, *Nonlinear Optics*. Academic Press, 1992.

[36] P. Magnan, "Detection of visible photons in CCD and CMOS: A comparative view," *Nucl Instrum Meth A*, vol. 504, no. 1, pp. 199–212, 2003.

[37] Y. Shen, *The principles of nonlinear optics*. Wiley & Sons, 1984.

[38] H. Arnolds and M. Bonn, "Ultrafast surface vibrational dynamics," *Surf. Sci. Reports*, vol. 65, p. 45, 2010.

[39] J. Bdzoch, *Ultrafast Energy and Charge Transfer in D_2O/Ru(0001)*. PhD thesis, Freie Universitaet Berlin, 2010.

[40] P. G.-S. J.H. Hunt and Y. Shen, "Observation of C-H stretch vibrations of monolayers of molecules optical sum-frequency generation," *Chemical Physics Letters*, vol. 133, p. 189, 1987.

[41] Y. S. I. T. H. und M. Inguscio, "Proceedings of the International School of Physics Enrico Fermi, Course No. CXX," vol. 194, 1984.

[42] Y. R. Shen, "Surface-Properties Probed by 2^{nd}-Harmonic and Sum-Frequency Generation," *Nature*, vol. 337, no. 6207, pp. 519–525, 1989.

[43] M. B. und M. Himmelhaus, "Vibrational spectroscopy of interfaces by inrared–visible sum frequency generation," *Journal of Vacuum Science and Technology*, vol. 19, p. 2717, 2001.

[44] G. L. Richmond, "Molecular Bonding and Interactions at Aqueous Surfaces as Probed by Vibrational Sum Frequency Spectroscopy," *Chemical Reviews*, vol. 102, no. 8, pp. 2693–2724, 2002.

[45] Y. R. Shen, "A Few Selected Applications of Surface Nonlinear Optical Spectroscopy," *Proceedings Of The National Academy Of Sciences Of The USA*, vol. 93, no. 22, pp. 12104–12111, 1996.

[46] D. K. X. Zhuang, P. B. Miranda and Y. R. Shen, "Mapping molecular orientation and conformation at interfaces by surface nonlinear optics," *Phys. Rev. B*, vol. 59, 1999.

[47] W. C. P. Guyot-Sionnest and Y. R. Shen, "General Considerations on Optical Second-Harmonic Generation from Surfaces and Interfaces," *Physical Review B*, vol. 33, pp. 8254–8263, 1986.

[48] X. D. Zhu, H. Suhr, and Y. R. Shen, "Surface Vibrational Spectroscopy by Infrared-Visible Sum Frequency Generation," *Phys. Rev. B.*, vol. 35, no. 6, pp. 3047–3050, 1987.

[49] T. F. Heinz, "Second-Order Nonlinear Optical Effects at Surfaces and Interfaces," in *Nonlinear Surface Electromagnetic Phenomena* (H. E. Ponrath and G. I. Stegeman, eds.), pp. 353–416, Elsevier Science Publishers, 1991.

[50] C. D. Bain, P. B. Davies, T. H. Ong, R. N. Ward, and M. A. Brown, "Quantitative Analysis of Monolayer Composition by Sum-Frequency Vibrational Spectroscopy," *Langmuir*, vol. 7, no. 8, pp. 1563–1566, 1991.

[51] H.-F. Wang, W. Gan, R. Lu, Y. Rao, and B.-H. Wu, "Quantitative Spectral and Orientational Analysis in Surface Sum Frequency Generation Vibrational Spectroscopy (SFG-VS)," *International Reviews in Physical Chemistry*, vol. 24, no. 2, pp. 191–256, 2005.

[52] S. Funk, *Ultraschnelle Reaktionsdynamik an Oberflaechen: Desorption und Oxidation von CO auf Ru(001) induziert durch Femtosekunden–Laserpulse.* PhD thesis, FU Berlin, 1999.

[53] S. T. Ceyer, "Dissociative Chemisorption: Dynamics and Mechanisms," *Annual Review of Physical Chemistry*, vol. 39, pp. 479–510, 1988.

[54] P. R. McCabe, L. B. F. Juurlink, and A. L. Utz, "A Molecular Beam Apparatus for Eigenstate-Resolved Studies of Gas-Surface Reactivity," *Review of Scientific Instruments*, vol. 71, pp. 42–53, 2000.

[55] L. Chen, "Development of a supersonic molecular beam chamber for surface dynamics research," Master's thesis, Hochschule Karlsruhe Technik und Wirtschaft, 2010.

[56] T. K. Shimizu, A. Mugarza, J. I. Cerdá, M. Heyde, Y. Qi, U. D. Schwarz, D. F. Ogletree, and M. Salmeron, "Surface species formed by the adsorption and dissociation of water molecules on a Ru (0001) surface containing a small coverage of carbon atoms studied by scanning tunneling microscopy," *The Journal of Physical Chemistry C*, vol. 112, no. 19, pp. 7445–7454, 2008.

[57] S. Funk, M. Bonn, D. N. Denzler, C. Hess, M. Wolf, and G. Ertl, "Desorption of CO from Ru(001) induced by near-infrared femtosecond laser pulses," *J.Chem.Phys.*, vol. 112, 2000.

[58] J. W. Elam, C. E. Nelson, M. A. Cameron, M. A. Tolbert, and S. M. George, "Adsorption of H_2O on a Single-Crystal α-Al_2O_3(0001) Surface," *J. Phys. Chem. B*, vol. 102, pp. 7008–7015, 1998.

[59] C. Niu, C. Shepherd, D. Martini, J. A. Kelber, D. R. Jennison, and A. Bogicevic, "Cu interactions with α-Al_2O_3(0001): Effects of Surface Hydroxyl Groups vs Dehydroxylation by Ar Ion Sputtering," *Surface Science*, vol. 465, pp. 163–176, 2000.

[60] J. A. Kelber, "Alumina Surfaces and Interfaces Under Non-Ultrahigh Vacuum Conditions," *Surface Science Reports*, vol. 62, no. 7, pp. 271–303, 2007.

[61] D. N. Denzler, *Zur ultraschnellen Reaktionsdynamik von Wasserstoff und Grenzflächenstruktur von Wasser auf der Ru (001)-Oberfläche*. PhD thesis, Dissertation, Freie Universität Berlin, 2003.

[62] W. Koechner and M. Bass, *Solid-State Lasers: A Graduate Text*. Springer, 2003.

[63] A. Amariglio, M. Belgued, P. Paréja, and H. Amariglio, "Oxygen-free Conversion of Methane to Higher Hydrocarbons through a Dual-Temperature Two-Step Reaction Sequence on Platinum and Ruthenium: 1. Chemisorption of CH4at a Fixed Temperature," *Journal of Catalysis*, vol. 177, no. 1, pp. 113–120, 1998.

[64] A.-F. An, A.-H. Lu, Q. Sun, J. Wang, and W.-C. Li, "Gold nanoparticles stabilized by a flake-like Al_2O_3 support," *Gold Bulletin*, vol. 44, no. 4, pp. 217–222, 2011.

[65] G.-C. W. B. Xing, X.-Y. Pang, "CÂ–H Bond Activation of Methane on Clean and Oxygen Pre-Covered Metals: a Systematic Theoretical Study," *Journal of Catalysis*, vol. 282, pp. 74–82, 2011.

[66] R. Baetzold and G. Somorjai, "Preexponential factors in surface reactions," *Journal of Catalysis*, vol. 45, no. 1, pp. 94–105, 1976.

[67] M. Belgued, H. Amariglio, P. Pareja, A. Amariglio, and J. Saint-Just, "Low temperature catalytic homologation of methane on platinum, ruthenium and cobalt," *Catalysis today*, vol. 13, no. 2, pp. 437–445, 1992.

[68] M. Belgued, P. Pareja, A. Amariglio, and H. Amariglio, "Conversion of methane into higher hydrocarbons on platinum," *Nature*, 1991.

[69] F. Benthaus, *Rohstoff Kohle: Eigenschaften, Gewinnung, Veredelung*. Verlag Chemie, 1978.

[70] O. Bikondoa, C. L. Pang, R. Ithnin, C. A. Muryn, H. Onishi, and G. Thornton, "Direct visualization of defect-mediated dissociation of water on TiO2 (110)," *Nature materials*, vol. 5, no. 3, pp. 189–192, 2006.

[71] P. E. Blöchl, "Projector Augmented-Wave Method," *Phys. Rev. B.*, vol. 50, pp. 17953–17979, 1994.

[72] M. Bonn, C. Hess, J. H. Miners, T. F. Heinz, H. J. Bakker, and M. Cho, "Novel surface vibrational spectroscopy: Infrared-infrared-visible sum-frequency generation," *Physical review letters*, vol. 86, no. 8, p. 1566, 2001.

[73] J. van den Brand, P. C. Snijders, W. G. Sloof, H. Terryn, and J. H. W. de Wit, "Acid-Base Characterization of Aluminum Oxide Surfaces with XPS," *J. Phys. Chem. B*, vol. 108, no. 19, pp. 6017–6024, 2004.

[74] B. Braunschweig, S. Eissner, and W. Daum, "Molecular Structure of a Mineral/Water Interface: Effects of Surface NanoRoughness of α-Al_2O_3(0001)," *J. Phys. Chem. C*, vol. 112, no. 6, pp. 1751–1754, 2008.

[75] G. E. Brown, V. E. Henrich, W. H. Casey, D. L. Clark, C. Eggleston, A. Felmy, D. W. Goodman, M. Gratzel, G. Maciel, M. I. McCarthy, K. H. Nealson, D. A. Sverjensky, M. F. Toney, and J. M. Zachara, "Metal Oxide Surfaces and their Interactions with Aqueous Solutions and Microbial Organisms," *Chem. Rev.*, vol. 99, no. 1, pp. 77–174, 1999.

[76] M. A. Brown, E. Carrasco, M. Sterrer, and H.-J. Freund, "Enhanced Stability of Gold Clusters Supported on Hydroxylated MgO(001) Surfaces," *J. Am. Chem. Soc.*, vol. 132, no. 12, pp. 4064–4065, 2010.

[77] A. Buckingham and B. Orr, "Kerr effect in methane and its four fluorinated derivatives," *Trans. Faraday Soc.*, vol. 65, pp. 673–681, 1969.

[78] B. Busson and A. Tadjeddine, "Non-Uniqueness of Parameters Extracted from Resonant Second-Order Nonlinear Optical Spectroscopies," *J. Phys. Chem. C*, vol. 113, no. 52, pp. 21895–21902, 2009.

[79] C.-F. N. C.-T. Au and M.-S. Liao, "Methane Dissociation and Syngas Formation on Ru, Os, Rh, Ir, Pd, Pt, Cu, Ag, and Au: A Theoretical Study," *Journal of Catalysis*, vol. 185, pp. 12–22, 1999.

[80] E. Carrasco, M. A. Brown, M. Sterrer, H.-J. Freund, K. Kwapien, M. Sierka, and J. Sauer, "Thickness-Dependent Hydroxylation of MgO(001) Thin Films," *J. Phys. Chem. C*, vol. 114, no. 42, pp. 18207–18214, 2010.

[81] M. Ceriotti, J. Cuny, M. Parrinello, and D. E. Manolopoulos, "Nuclear Quantum Effects and Hydrogen Bond Fluctuations in Water," *P. Natl. Acad. Sci. USA*, vol. 110, no. 39, pp. 15591–15596, 2013.

[82] A. Chauvel and G. Lefebvre, "Petrochemical Processes: Synthesis-Gas Derivative and Major Hydrocarbons," vol. 1, 1989.

[83] J. Cheng, P. Hu, P. Ellis, S. French, G. Kelly, and C. M. Lok, "Some understanding of Fischer–Tropsch synthesis from density functional theory calculations," *Topics in Catalysis*, vol. 53, no. 5-6, pp. 326–337, 2010.

[84] M. Cho, C. Hess, and M. Bonn, "Lateral interactions between adsorbed molecules: Investigations of CO on Ru (001) using nonlinear surface vibrational spectroscopies," *Physical Review B*, vol. 65, no. 20, p. 205423, 2002.

[85] T. Choudhary and D. Goodman, "Methane activation on ruthenium: the nature of the surface intermediates," *Topics in Catalysis*, vol. 20, 2002.

[86] I. Ciobîcă, F. Frechard, R. Van Santen, A. Kleyn, and J. Hafner, "A theoretical study of CH_x chemisorption on the Ru (0001) surface," *Chemical physics letters*, vol. 311, no. 3, pp. 185–192, 1999.

[87] I. Ciobîcă and R. van Santen, "Carbon monoxide dissociation on planar and stepped Ru (0001) surfaces," *The Journal of Physical Chemistry B*, vol. 107, no. 16, pp. 3808–3812, 2003.

[88] I. Ciobica and R. Van Santen, "A DFT Study of CH x Chemisorption and Transition States for CH Activation on the Ru (1120) Surface," *The Journal of Physical Chemistry B*, vol. 106, no. 24, pp. 6200–6205, 2002.

[89] V. Coustet and J. Jupille, "High-Resolution Electron-Energy-Loss Spectroscopy of Isolated Hydroxyl Groups on α-Al_2O_3(0001)," *Surf. Sci.*, vol. 307-309, pp. 1161–1165, 1994.

[90] S. Dahl, A. Logadottir, R. C. Egeberg, J. H. Larsen, I. Chorkendorff, E. Toernqvist, and J. K. Norskov, "Role of Steps in N_2 Activation on Ru(0001)," *Physical Review Letters*, vol. 83, p. 1814, 1999.

[91] L. Danielson, M. Dresser, E. Donaldson, and J. Dickinson, "Adsorption and desorption of ammonia, hydrogen, and nitrogen on ruthenium (0001)," *Surface Science*, vol. 71, no. 3, pp. 599–614, 1978.

[92] M. E. Dry, "The Fischer–Tropsch process: 1950–2000," *Catalysis today*, vol. 71, no. 3, pp. 227–241, 2002.

[93] P. J. Eng, T. P. Trainor, G. E. B. J. andG. A. Waychunas, M. Newville, S. R. Sutton, and M. L. Rivers, "Structure of the Hydrated α-Al_2O_3(0001) Surface," *Science*, vol. 288, p. 1029, 2000.

[94] L. M. Falicov and G. A. Somorjai, "Correlation Between Catalytic Activity and Bonding and CoordinationNumber of Atoms and Molecules on Transition Metal Surfaces: Theory and Experimental Evidence," *Proceedings of the National Academy of Sciences of the USA*, vol. 82, pp. 2207–2211, 1985.

[95] D. Ferry, S. Picaud, P. Hoang, C. Girardet, L. Giordano, B. Demirdjian, and J. Suzanne, "Water monolayers on mgo (100): structural investigations by leed experiments, tensor leed dynamical analysis and potential calculations," *Surface science*, vol. 409, no. 1, pp. 101–116, 1998.

[96] M. Flörsheimer, K. Kruse, R. Polly, A. Abdelmonem, B. Schimmelpfennig, R. Klenze, and T. Fanghänel, "Hydration of Mineral Surfaces Probed at the Molecular Level," *Langmuir*, vol. 24, no. 23, pp. 13434–13439, 2008.

[97] M. Frank, K. Wolter, N. Magg, M. Heemeier, R. Kuehnermuth, M. Baeumer, and H.-J. Freund, "Phonons of Clean and Metal-Modified Oxide Films: an Infrared and HREELS Study," *Surf. Sci.*, vol. 492, pp. 270–284, 2001.

[98] B. G. Frederick, G. Apai, and T. N. Rhodin, "Electronic and Vibrational Properties of Hydroxylated and Dehydroxylated Thin Al_2O_3 Films," *Surf. Sci.*, vol. 244, no. 1, pp. 67–80, 1991.

[99] Q. Ge, M. Neurock, H. Wright, and N. Srinivasan, "A first principles study of carbon-carbon coupling over the {0001} surfaces of Co and Ru," *The Journal of Physical Chemistry B*, vol. 106, no. 11, pp. 2826–2829, 2002.

[100] C. Greenlief, P. Radloff, X.-L. Zhou, and J. White, "The formation and decomposition kinetics of ethylidyne on Ru (0001)," *Surface science*, vol. 191, no. 1, pp. 93–107, 1987.

[101] S. Grimme, "Semiempirical GGA-type Density Functional Constructed with a Long-Range Dispersion Correction," *J. Comput. Chem.*, vol. 27, no. 15, pp. 1787–1799, 2006.

[102] L. Guczi, R. A. van Santen, and K. Sarma, "Low-temperature coupling of methane," *Catalysis Reviews*, vol. 38, no. 2, pp. 249–296, 1996.

[103] P. Guenard, G. Renaud, A. Barbier, and M. Gautier-Soyer, "Determination of the α-Al_2O_3(0001) Surface Relaxation and Termination by Measurements of Crystal Truncation Rods," *Surface Rev Lett*, vol. 5, no. 01, pp. 321–324, 1998.

[104] A. K. B. H. Ahlafi, M. Nawdali and D. Bianchi, "Isothermal Hydrogenation of Carbonaceous Adsorbed Species on a Ru/Al_2O_3 Catalyst After the Adsorption of CO and the CO/H_2 Reaction," *Bulletin des Société Chimiques de Belgique*, vol. 106, pp. 245–252, 1997.

[105] I. H. H. L. Abbott, "Methane Dissociative Chemisorption on Ru(0001) and Comparison to Metal Nanocatalysts," *Journal of Catalysis*, vol. 254, pp. 27–38, 2008.

[106] A. B. H. Mortensen, L. Diekhoener and A. C. Luntz, "CH_4 Dissociation on Ru(0001): A View From Both Sides of the Barrier," *Journal of Chemical Physics*, vol. 116, 2002.

[107] D. R. Hamann, "H_2O Hydrogen Bonding in Density-Functional Theory," *Phys. Rev. B.*, vol. 55, pp. R10157–R10160, 1997.

[108] R. Hammaker, S. Francis, and R. Eischens, "Infrared study of intermolecular interactions for carbon monoxide chemisorbed on platinum," *Spectrochimica Acta*, vol. 21, no. 7, pp. 1295–1309, 1965.

[109] Z. R. S. V. L. M. W. M. S. Harald Kirsch, Xunhua Zhao and R. K. Campen, "Controlling CH_2 Dissociation on Ru(0001) through Surface Site Blocking by Adsorbed Hydrogen," *Journal of catalysis*, 2014.

[110] K. C. Hass, W. F. Schneider, A. Curioni, and W. Andreoni, "First-Principles Molecular Dynamics Simulations of H_2O on α-Al_2O_3(0001)," *J. Phys. Chem. B*, vol. 104, no. 23, pp. 5527–5540, 2000.

[111] K. C. Hass, W. F. Schneider, A. Curioni, and W. Andreoni, "The Chemistry of Water on Alumina Surfaces: Reaction Dynamics from First Principles," *Science*, vol. 282, no. 5387, pp. 265–268, 1998.

[112] A. Hassanli, F. Giberti, J. Cuny, T. D. Kuehne, and M. Parrinello, "Proton Transfer Through the Water Gossamer," *P. Natl. Acad. Sci. USA*, vol. 110, no. 34, pp. 13723–13728, 2013.

[113] C. Hess, M. Bonn, S. Funk, and M. Wolf, "Hot-Band Excitation of CO Chemisorbed on Ru(0001) Studied with Broadband-IR Sum-Frequency Generation," *Chemical Physics Letters*, vol. 325, p. 139Â–145, 2000.

[114] M. M. Hills, J. E. Parmeter, C. B. Mullins, and W. H. Weinberg, "Interaction of Ethylene with the Ru(001) Surface," *Journal of the American Chemical Society*, vol. 108, pp. 3554–3562, 1986.

[115] P. Hobza and Z. Havlas, "Blue-shifting Hydrogen Bonds," *Chem.Rev.*, vol. 100, pp. 4253–4264, 2000.

[116] A. Holmen, "Direct conversion of methane to fuels and chemicals," *Catalysis Today*, vol. 142, no. 1, pp. 2–8, 2009.

[117] P. M. H. J. H. Larsen and I. Chorkendorff, "Dissociative Sticking of CH_4 on Ru(0001)," *Journal of Chemical Physics*, vol. 110, pp. 2637–2642, 1999.

[118] G. Jones, J. G. Jakobsen, S. S. Shim, J. Kleisa, M. P. Andersson, J. Rossmeisl, F. Abild-Pedersen, T. Bligaard, S. Helveg, B. Hinnemann, J. R. Rostrup-Nielsen, I. Chorkendorff, J. Sehested, and J. K. Norskov, "First Principles Calculations and Experimental Insight into Methane Steam Reforming over Transition Metal Catalysts," *Journal of Catalysis*, vol. 259, pp. 147–160, 2008.

[119] D. T. R. K. A .Tillman, R. R. J. Maier and E. D. McNaghten, "Mid-Infrared Absorption Spectroscopy ofMethane using a broadband FemtosecondOptical Parametric Oscillator Based on a Periodically Poled Lithium Niobate," *Journal of the Optical Society of America A: Pure and Applied Optics*, vol. 7, pp. 408–414, 2005.

[120] W. Kohn and L. J. Sham, "Self-Consistent Equations Including Exchange and Correlation Effects," *Phys. Rev.*, vol. 140, pp. A1133–A1138, 1965.

[121] G. Kresse and J. Hafner, "*Ab initio* Molecular-Dynamics Simulation of the Liquid-Metal-Amorphous-Semiconductor Transition in Germanium," *Phys. Rev. B.*, vol. 49, pp. 14251–14269, 1994.

[122] G. Kresse and J. Hafner, "*Ab initio* Molecular Dynamics for Liquid Metals," *Phys. Rev. B.*, vol. 47, pp. 558–561, 1993.

[123] G. Kresse and J. Hafner, "*Ab initio* Molecular Dynamics for Open-Shell Transition Metals," *Phys. Rev. B.*, vol. 48, pp. 13115–13118, 1993.

[124] G. Kresse and D. Joubert, "From Ultrasoft Pseudopotentials to the Projector Augmented-Wave Method," *Phys. Rev. B.*, vol. 59, pp. 1758–1775, 1999.

[125] T. Kurita, K. Uchida, and A. Oshiyama, "Atomic and Electronic Structures of α-Al_2O_3 Surfaces," *Phys. Rev. B.*, vol. 82, no. 15, p. 155319, 2010.

[126] J. B. B. S. J. V. LA. Ransley, L.M. Ilharco and M. Chesters, "Adsorption and thermal decomposition of ethene and propene on Ru(0001), studied by RAIRS," *Surface Science*, vol. 198, pp. 187–194, 1993.

[127] P. Liu, T. Kendelewicz, G. E. Brown, Jr., E. J. Nelson, and S. A. Chambers, "Reaction of Water Vapor with α-Al_2O_3(0001) andα-Fe_2O_3(0001) Surfaces: Synchrotron X-ray Photoemission Studies and Thermodynamic Calculations," *Surf. Sci.*, vol. 417, pp. 53–65, 1998.

[128] W. T. Liu and Y. R. Shen, "Sum-frequency Phonon Spectroscopy on α-Quartz," *Phys Rev B*, vol. 78, no. 2, p. 024302, 2008.

[129] W. T. Liu and Y. R. Shen, "Surface Vibrational Modes of α-quartz(0001) Probed by Sum-Frequency Spectroscopy," *Phys Rev Lett*, vol. 101, no. 1, p. 016101, 2008.

[130] Z.-P. Liu and P. Hu, "General Rules for Predicting Where a Catalytic ReactionShould Occur on Metal Surfaces: A Density Functional Theory Study of C-H and C-O Bond Breaking/Making on Flat, Stepped, and Kinked Metal Surfaces," *Journal of the American Chemical Society*, vol. 125, p. 1953, 2003.

[131] Z.-P. Liu and P. Hu, "A new insight into Fischer-Tropsch synthesis," *Journal of the American Chemical Society*, vol. 124, no. 39, pp. 11568–11569, 2002.

[132] T. Livneh and M. Asscher, "The Adsorption and Decomposition of C_2H_4 on Ru(001): A Combined TPR and Work Function Change Study," *Journal of Physical Chemistry B*, vol. 104, pp. 3355–3363, 2000.

[133] E. Lundgren, J. Gustafson, A. Mikkelsen, J. N. Andersen, A. Stierle, H. Dosch, M. Todorova, J. Rogal, K. Reuter, and M. Scheffler, "Kinetic hindrance during the initial oxidation of Pd (100) at ambient pressures," *Physical review letters*, vol. 92, no. 4, p. 046101, 2004.

[134] J. H. Lunsford, "Catalytic conversion of methane to more useful chemicals and fuels: a challenge for the 21st century," *Catalysis Today*, vol. 63, no. 2, pp. 165–174, 2000.

[135] J. Q. B. M. A. Barteau and D. Menzel, "Vibrational Spectroscopy of Hydrocarbon Intermediates on Ru(001)," *Application of Surface Science*, vol. 19, pp. 92–115, 1984.

[136] S. T. C. M. B. Lee, Q. Y. Yang, "Dynamics of the Activated Dissociative Chemisorption of CH_4 and Implication for the Pressure Gap Catalysis: a Molecular Beam-High Resolution Electron Energy Loss Study," *Journal of Chemical Physics*, vol. 87, pp. 2724–2740, 1987.

[137] J. E. P. M.M. Hills and W. H. Weinberg, "Coadsorption of Hydrogen and Ethylene, and Carbon Monoxide and Ethylene on the Ru(001) Surface," *J.Am Chem. Soc.*, vol. 108, pp. 7215–7221, 1986.

[138] G. J. MacDonald, "The future of methane as an energy resource," *Annual Review of Energy*, vol. 15, no. 1, pp. 53–83, 1990.

[139] G. Mahan and A. Lucas, "Collective vibrational modes of adsorbed CO," *The Journal of Chemical Physics*, vol. 68, no. 4, pp. 1344–1348, 1978.

[140] S. E. Mason, C. R. Iceman, T. P. Trainor, and A. M. Chaka, "Density functional theory study of clean, hydrated, and defective alumina (1 1^{-} 02) surfaces," *Physical Review B*, vol. 81, no. 12, p. 125423, 2010.

[141] H. J. Monkhorst and J. D. Pack, "Special Points for Brillouin-Zone Integrations," *Phys. Rev. B.*, vol. 13, pp. 5188–5192, 1976.

[142] C. Morterra and G. Magnacca, "A case study: surface chemistry and surface structure of catalytic aluminas, as studied by vibrational spectroscopy of adsorbed species," *Catal Today*, vol. 27, no. 3, pp. 497–532, 1996.

[143] C. E. Nelson, J. W. Elam, M. A. Cameron, M. Tolbert, and S. M. George, "Desorption of H_2O from a hydroxylated single-crystal α-Al_2O_3(0001) surface," *Surf. Sci.*, vol. 416, pp. 341–353, 1998.

[144] W. H. W. P. M. George, N. R. Avery and F. N. Tebbe, "Formation and Identification of Methylene on Ru(001)," *Journal of the American Chemical Society*, vol. 105, pp. 1393–1394, 1983.

[145] F. Paesani, S. Yoo, H. J. Bakker, and S. S. Xantheas, "Nuclear Quantum Effects in the Reorientation of Water," *J. Phys. Chem. Lett.*, vol. 1, no. 15, pp. 2316–2321, 2010.

[146] J. P. Perdew, K. Burke, and M. Ernzerhof, "Generalized Gradient Approximation Made Simple [Phys. Rev. Lett. 77, 3865 (1996)]," *Phys. Rev. Lett*, vol. 78, pp. 1396–1396, 1997.

[147] J. P. Perdew, K. Burke, and M. Ernzerhof, "Generalized Gradient Approximation Made Simple," *Phys. Rev. Lett*, vol. 77, pp. 3865–3868, 1996.

[148] P. Pereira, S. Lee, G. A. Somorjai, and H. Heinemann, "The conversion of methane to ethylene and ethane with near total selectivity by low temperature ($< 610°$ C) oxydehydrogenation over a calcium-nickel-potassium oxide catalyst," *Catalysis Letters*, vol. 6, no. 3-6, pp. 255–262, 1990.

[149] B. Persson and R. Ryberg, "Vibrational interaction between molecules adsorbed on a metal surface: The dipole-dipole interaction," *Physical Review B*, vol. 24, no. 12, p. 6954, 1981.

[150] H. Pfnür, P. Feulner, and D. Menzel, "The influence of adsorbate interactions on kinetics and equilibrium for CO on Ru (001). II. Desorption kinetics and equilibrium," *The Journal of chemical physics*, vol. 79, no. 9, pp. 4613–4623, 1983.

[151] H. Pfnür, D. Menzel, F. Hoffmann, A. Ortega, and A. Bradshaw, "High resolution vibrational spectroscopy of CO on Ru (001): The importance of lateral interactions," *Surface Science*, vol. 93, no. 2, pp. 431–452, 1980.

[152] R. Polly, B. Schimmelpfennig, M. Flörsheimer, K. Kruse, A. Abdelmonem, R. Klenze, G. Rauhut, and T. Fanghänel, "Theoretical Investigation of the Water/Corundum (0001) Interface," *J. Chem. Phys.*, vol. 130, no. 6, p. 064702, 2009.

[153] V. A. Ranea, I. Carmichael, and W. F. Schneider, "DFT Investigation of Intermediate Steps in the Hydrolysis of α-Al_2O_3(0001)," *J. Phys. Chem. C*, vol. 113, no. 6, pp. 2149–2158, 2009.

[154] V. A. Ranea, W. F. Schneider, and I. Carmichael, "DFT characterization of coverage dependent molecular water adsorption modes on α-Al_2O_3(0001)," *Surf. Sci.*, vol. 602, pp. 268–275, Jan. 2008.

[155] W. Raynes, P. Lazzeretti, and R. Zanasi, "Vibration-rotation effects on the polarizabilities of CH4 and CD4 calculated from an ab initio polarizability surface," *Molecular Physics*, vol. 64, no. 6, pp. 1061–1071, 1988.

[156] G. Renaud, "Oxide surfaces and metal/oxide interfaces studied by grazing incidence X-ray scattering," *Surf Sci Rep*, vol. 32, no. 1, pp. 5–90, 1998.

[157] G. L. Richmond, "Structure and Bonding of Molecules at Aqueous Surfaces," *Annual Review Of Physical Chemistry*, vol. 52, pp. 357–389, 2001.

[158] M. K. Sabbe, M.-F. Reyniers, V. Van Speybroeck, M. Waroquier, and G. B. Marin, "Carbon-Centered Radical Addition and β-Scission Reactions: Modeling of Activation Energies and Pre-exponential Factors," *ChemPhysChem*, vol. 9, no. 1, pp. 124–140, 2008.

[159] R. A. ávan Santen *et al.*, "A low temperature reaction sequence for methane conversion," *Journal of the Chemical Society, Chemical Communications*, no. 18, pp. 1281–1283, 1991.

[160] L. F. Scatena, M. G. Brown, and G. L. Richmond, "Water at Hydrophobic Surfaces: Weak Hydrogen Bonding and Strong Orientation Effects," *Science*, vol. 292, no. 5518, pp. 908–912, 2001.

[161] M. Scheffler, "The influence of lateral interactions on the vibrational spectrum of adsorbed CO," *Surface Science*, vol. 81, no. 2, pp. 562–570, 1979.

[162] A. P. Scott and L. Radom, "Harmonic Vibrational Frequencies: An Evaluation of Hartree-Fock, Moller-Plesset, Quadratic Configuration Interaction, Density Functional Theory, and Semiempirical Scale Factors," *J. Phys. Chem.*, vol. 100, no. 41, pp. 16502–16513, 1996.

[163] M. W. Severson, C. Stuhlmann, I. Villegas, and M. J. Weaver, "Dipole–dipole coupling effects upon infrared spectroscopy of compressed electrochemical adlayers: Application to the Pt (111)/CO system," *The Journal of chemical physics*, vol. 103, no. 22, pp. 9832–9843, 1995.

[164] M. W. Severson and M. J. Weaver, "Nanoscale island formation during oxidation of carbon monoxide adlayers at ordered electrochemical interfaces: A dipole-

coupling analysis of coverage-dependent infrared spectra," *Langmuir*, vol. 14, no. 19, pp. 5603–5611, 1998.

[165] T. Shimanouchi, *Tables of Molecular Vibrational Frequencies. Consolidated volume I.* National Bureau of Standards, 1972.

[166] E. Soares, M. Van Hove, C. Walters, and K. McCarty, "Structure of the α-Al 2 O 3 (0001) surface from low-energy electron diffraction: Al termination and evidence for anomalously large thermal vibrations," *Physical Review B*, vol. 65, no. 19, p. 195405, 2002.

[167] G. A. Somorjai and A. L. Marsh, "Active Sites and States in the Heterogeneous Catalysis of Carbon-Hydrogen Bonds," *Philosophical Transactions of the Royal Society A*, vol. 363, pp. 879–900, 2005.

[168] M. Sovago, R. K. Campen, G. W. H. Wurpel, M. Müller, H. J. Bakker, and M. Bonn, "Vibrational Response of Hydrogen-Bonded Interfacial Water is Dominated by Intramolecular Coupling," *Phys. Rev. Lett*, vol. 100, no. 17, p. 173901, 2008.

[169] I. Stará, D. Zeze, V. Matolín, J. Pavluch, and B. Gruzza, "AES and EELS Study of Alumina Model Catalyst Supports," *Appl. Surf. Sci.*, vol. 115, no. 1, pp. 46–52, 1997.

[170] J. Sung, L. Zhang, C. Tian, G. A. Waychunas, and Y. R. Shen, "Surface Structure of Protonated R-Sapphire (1102) Studied by Sum-Frequency Vibrational Spectroscopy," *Journal of the American Chemical Society*, vol. 133, no. 11, pp. 3846–3853, 2011.

[171] P. Thissen, G. Grundmeier, S. Wippermann, and W. G. Schmidt, "Water Adsorption on the α-Al_2O_3(0001) Surface," *Phys. Rev. B.*, vol. 80, no. 24, p. 245403, 2009.

[172] P. Thompson, D. E. Cox, and J. B. Hastings, "Rietveld Refinement of Debye-Scherrer Synchrotron X-Ray Data from Al_2O_3," *J. Appl. Crystallogr.*, vol. 20, no. 2, pp. 79–83, 1987.

[173] Y. Tong, A. Vila Verde, and R. K. Campen, "The Free OD at the Air/D_2O Interface Is Structurally and Dynamically Heterogeneous," *J. Phys. Chem. B*, vol. 117, no. 39, pp. 11753–11764, 2013.

[174] Y. Tong, J. Wirth, H. Kirsch, M. Wolf, P. Saalfrank, and R. K. Campen, "Concurrent Characterization of α-Al_2O_3(0001) Surface Structure and Reactivity on Interaction with Water via Surface Specific Vibrational Spectroscopy," 2014.

[175] J. Toofan and P. R. Watson, "The termination of the α-Al_2O_3(0001) surface: a LEED crystallography determination," *Surf. Sci.*, vol. 401, pp. 162–172, 1998.

[176] T. P. Trainor, P. J. Eng, G. E. Brown Jr, I. K. Robinson, and M. D. Santis, "Crystal truncation rod diffraction study of the α-Al 2O3(1102) surface," *Surface science*, vol. 496, no. 3, pp. 238–250, 2002.

[177] P. Ugliengo, F. Pascale, M. Mérawa, P. Labéguerie, S. Tosoni, and R. Dovesi, "Infrared Spectra of Hydrogen-Bonded Ionic Crystals: Ab Initio Study of $Mg(OH)_2$ and β-$Be(OH)_2$," *J. Phys. Chem. B*, vol. 108, no. 36, pp. 13632–13637, 2004.

[178] G. Van der Zwet, P. Hendriks, and R. Van Santen, "Pyrolysis of methane and the role of surface area," *Catalysis today*, vol. 4, no. 3, pp. 365–369, 1989.

[179] R. Van Hardeveld, R. Van Santen, and J. Niemantsverdriet, "CN Coupling in Reactions between Atomic Nitrogen and Ethylene on Rh (111)," *The Journal of Physical Chemistry B*, vol. 101, no. 40, pp. 7901–7907, 1997.

[180] B. Wang, H. Hou, Y. Luo, Y. Li, Y. Zhao, and X. Li, "Density Functional/All-Electron Basis Set Slab Model Calculations of the Adsorption/Dissociation Mechanisms of Water on α-Al_2O_3(0001) Surface," *J. Phys. Chem. C*, vol. 115, no. 27, pp. 13399–13411, 2011.

[181] S.-G. Wang, D.-B. Cao, Y.-W. Li, J. Wang, and H. Jiao, "CH_4 Dissociation on Ni surfaces: Density Functional Theory Study," *Surface Science*, vol. 600, pp. 3226Â—-3234, 2006.

[182] X. Wang and L. Andrews, "Infrared Spectroscopic Observation of the Group 13 Metal Hydroxides, $M(OH)_{1,2,3}$(M =Al, Ga, In, and Tl) and $HAl(OH)_2$," *J. Phys. Chem. A*, vol. 111, no. 10, pp. 1860–1868, 2007.

[183] X. Wei, P. B. Miranda, and Y. R. Shen, "Surface Vibrational Spectroscopic Study of Surface Melting of Ice," *Phys. Rev. Lett*, vol. 86, no. 8, pp. 1554–1557, 2001.

[184] X. Wei and Y. R. Shen, "Vibrational Spectroscopy of Ice Interfaces," *Appl. Phys. B*, vol. 74, no. 7-8, pp. 617–620, 2002.

[185] H.-J. Werner and W. Meyer, "PNO-CI and PNO-CEPA studies of electron correlation effects: V. Static dipole polarizabilities of small molecules," *Molecular Physics*, vol. 31, no. 3, pp. 855–872, 1976.

[186] E. L. Wilson and W. A. Brown, "Low Pressure RAIRS Studies of Model Catalytic Systems," *J. Phys. Chem. C*, vol. 114, no. 15, pp. 6879–6893, 2010.

[187] S. Wippermann, W. G. Schmidt, P. Thissen, and G. Grundmeier, "Dissociative and Molecular Adsorption of Water on α-Al_2O_3(0001)," *Phys Status Solidi C*, vol. 7, no. 2, pp. 137–140, 2010.

[188] J. Wirth and P. Saalfrank, "D_2O dissociation on α-Al_2O_3(1102)." Private communiaction.

[189] W. Xiong, J. E. Laaser, R. D. Mehlenbacher, and M. T. Zanni, "Adding a Dimension to the Infrared Spectra of Interfaces using Heterodyne Detected 2D Sum-Frequency Generation (HD-2D-SFG) Spectroscopy," *P. Natl. Acad. Sci. USA*, vol. 108, no. 52, pp. 20902–20907, 2011.

[190] W. M. F. Y. Zhou, M. A. Henderson and J. M. White, "Decomposition of Methyl Iodine on Ru(001)," *Surface Science*, vol. 224, pp. 386–406, 1989.

[191] Q. Y. Yang, K. J. Maynard, A. D. Johnson, and S. T. Ceyer, "The Structure and Chemistry of CH_3 and CH Radicals Adsorbed on Ni(111)," *Journal of Physical Chemistry*, vol. 102, pp. 7734–7749, 1995.

[192] L. Zhang, C. Tian, G. A. Waychunas, and Y. R. Shen, "Structures and Charging of α-Alumina(0001)/Water Interfaces Studied by Sum-Frequency Vibrational Spectroscopy," *J. Am. Chem. Soc.*, vol. 130, no. 24, pp. 7686–7694, 2008.

[193] Z. Zhang, L. Piatkowski, H. J. Bakker, and M. Bonn, "Ultrafast Vibrational Energy Transfer at the Water/Air Interface Revealed by Two-Dimensional Surface Vibrational Spectroscopy," *Nat. Chem.*, vol. 3, no. 11, pp. 888–893, 2011.

Publications

Related to this Thesis

1. H. Kirsch, J. Wirth, Y. Tong, M. Wolf, P. Saalfrank, R.K. Campen *Experimental Characterization of Unimolecular Water Dissociative Adsorption on α-Alumina*, J. Phys. Chem. C, 118 (25), pp 13623-13630 (2014)

2. H. Kirsch, X. Zhao, Z. Ren, S. V. Levchenko, M. Wolf, M. Scheffler and R. K.Campen *Controlling CH_2 Dissociation on Ru(0001) through Surface Site Blocking by Adsorbed Hydrogen*, submitted

3. Y. Tong, J. Wirth, H. Kirsch , M. Wolf, P. Saalfrank, R.K. Campen *Concurrent Characterization of α-Al_2O_3(0001) Surface Structure and Reactivity on Interaction with Water via Surface Specific Vibrational Spectroscopy*, submitted

4. H. Kirsch, Z. Ren, M. Wolf, R.K. Campen *Vibrational characterization of surface indermediates during Methane and Ethylene decomposition on Ru(0001) in UHV*, in preparation

5. H. Kirsch, J. Wirth, Y. Tong, M. Wolf, P. Saalfrank, R.K. Campen *Temperature dependent population of single molecular dissociation products on α-Alumina(0001)*, in preparation

6. H. Kirsch, S. Wlosczyk, J. Wirth, Y. Tong, M. Wolf, P. Saalfrank, R.K. Campen *Water dissociation on α-Al_2O_3(1102)*, in preparation

Not related to the thesis

1. P. Giese, H. Kirsch, M. Wolf and C. Frischkorn. *Reduction of N_2O on MgO/Ag(001) via UV-Photoinduced Trapped Electrons*, J. Phys. Chem. C 115, 10012-10016 (2011)

Danksagungen

Ich danke Herrn Professor Martin Wolf die Überlassung des Themas der vorliegenden Dissertation, sowie den vielen Diskussionen über die Interpretation und die Analyse der Meßdaten, was nicht nur hilfreich und essentiell war, sondern zuweilen auch recht amüsant.

A special thanks goes to Dr. Kramer Campen, who was my advisor and the leader of my working group for the last three years. Without his enthusiastic help and effort, this work would not have been, what it is right now.

Furthermore I want to thank Dr. Yujin Tong, who spent a lot of his time on my thesis to discuss some technical and scientific questions or, in the worst case, helped me to repair all the broken stuff in the lab.

Ebenfalls danke ich Jonas Wirth, einem Doktoranden aus der Arbeitsgruppe von Prof. Peter Saalfrank an der Universität Potsdam. Von ihm stammen all die wundervollen Berechnungen zu den Wasser/Oxid Systemen und die vielen Diskussion über unsere gemeinsame Thematik haben ganze Nachmittage gefüllt.

Ich danke meinem Diplomanden Sebastian Wlosczyk für seinen Einsatz im Labor und die gute Zusammenarbeit während der letzten 9 Monate.

Ich danke den Herren Marcel Krenz, Willi Krauss und Frank Quadt für ihren unermüdlichen Einsatz, die Laser, die UHV-Aufbauten und all die Computer in meinem Labor am Leben zu erhalten. Ohne sie hätte ich das nicht geschafft.

Erklärung gemäß der Promotionsordnung

Hiermit versichere ich, dass diese Arbeit von niemandem anderen als mir angefertigt wurde. Alle verwendeten Hilfsmittel wurden angegeben. Zitate und Abbildungen aus fremden Arbeiten sind als solche kenntlich gemacht. Diese Arbeit wurde bisher in gleicher oder ähnlicher Form keiner anderen Prüfungskommission vorgelegt und auch nicht veröffentlicht.

Berlin, den

(Datum, Unterschrift)

Lebenslauf von Karl Harald Kirsch

Der Lebenslauf ist in der Online-Version aus Gruenden
des Datenschutzes nicht enthalten.